LIFETIME ANALYSIS OF A COMPOSITE FLYWHEEL ENERGY STORAGE SYSTEM.

Robert J. Neumann

A thesis submitted for the degree of Doctor of philosophy in the Faculty of Engineering at the University of London.

Department of Materials
Mile End Road,
London, E1 4NS

2001

TEXT BOUND INTO THE SPINE

"If YOU'RE not living on the edge, YOU'RE taking up too much space"

, Inc.

2251 Faraday Av.

Carlsbad, California 92008

Acknowledgements

Firstly I would like to express my thanks to Professor Paul. J. Hogg for all the help, comments, suggestions and encouragement offered during the programme, although we will never agree when it comes to football.

Equally, I would like to thank URENCO for supporting the research, particularly Dr. Lesley Lewis and Colin Tarrant whose input has been invaluable over the years.

My thanks also go to all the secretarial staff particularly Cath and Sandra. I would also like to thank all the academic staff in both the materials and engineering departments who taught me during my undergraduate years.

I would also like to mention all the technical staff who helped at one time or another, these guys make the departments tick: Kevin, Mike, Dougie, Dave, Colin, Mick (The Peoples Champion), Tony, John, Roger and Bob.

May I also thank all the other postgraduates, research assistants and undergraduates who have made the time here very enjoyable. I would like to specifically mention those whom I shared an office with over the years. Silv'n' Chulee, Alan and Caroline and The Bridgestone Boys! Those who started out on the long road at the same time as me, Simon, Chris, we all nearly there. I would also like to those who have passed into legend, Ata, Ali, Gary, Gus, Jamie, Bethan and Stelios.

Finally I would like to thank my family, Mum, Dad and Chas and also friends outside QM, Matt, Ron, Marcus, Pete, Jen, Tony, Sharon, Lawrence, Prav, Jack, Kyne, Anil, Chimen, Will, Frankie (The), Colin, James, Simona, Steve, Astrid, Patrick, Valerio, Big Mig and many others who I've missed, sorry you guys.

Oh yes, where would I be without Sati.

Abstract

This thesis is concentrates on the long-term fracture of thick unidirectional glass and carbon fibre composites subjected to transverse stress. The objective was to develop a methodology for predicting the long term lifetime of a composite rotor used as part of a flywheel based energy storage system. The flywheel design is based on accommodating high hoop stresses induced during the high speed rotation. However, the different Poisson's ratios of the constituent materials in the rotor result in a complex stress distribution with significant stresses introduced in a direction transverse to the fibres. The possibility has been raised that the lifetime of the rotor will be limited by crack growth in this transverse direction, originating from defects (pores, cracks etc) that can be introduced into the rotor during its manufacture.

The approach explored in this work has been to adopt a fracture mechanics based methodology whereby the rate of crack growth in a thick composite is measured as a function of an applied stress intensity. The basic fracture parameters for the material were measured such that the time taken for a crack to grow to a size sufficient to cause failure under an operating stress could be calculated. The materials were also examined to characterise the nature, size and extent of inherent defects. The stress distribution in the rotor under operating conditions was modelled using finite element analysis. The combination of information on inherent defects, stress directions and crack growth rates enable predictions to be made concerning the likely lifetime of the composites. Proof stress diagrams were also constructed in order to demonstrate an approach to product quality assurance testing.

The end point of the work was to identify critical manufacturing defect sizes that could be tolerated under the specified operating conditions. The methodology developed for lifetime predictions was critically assessed and considered to be generally acceptable. The work did however raise some concerns regarding the applicability of a conventional fracture mechanics approach applied to heterogeneous composite systems where the size of the cracks are very small. It is recommended that future work should concentrate on studying this area with an emphasis on crack nucleation studies rather than on further crack propagation work.

Strategy

The objective of this work was to develop a preliminary framework for assessing the structural integrity of a thick composite rotor. This would take the form of both a guide to determining the maximum allowable size of any defect in the rotor that could be tolerated and still allow an acceptably low probability of failure in the specified operating lifetime, and a route to validating the integrity of a final component to ensure that this maximum flaw size had not been exceeded.

The approach adopted has made a number of assumptions, many of which are validated during the study. The primary assumption is that the entire problem of predicting the lifetime of the rotor can be addressed by taking a fracture mechanics approach. The fracture nechanics treatment is predicated on the further assumptions that cracks will grow in a self-similar manner and, that the fracture toughness of the material remains constant over time.

On this basis the first step is to determine a value for the fracture toughness of the different layers in the composite rotor and to determine the relationship between allowable operating stress and defect size. This specifies the size of defect that would cause instantaneous failure in the rotor (operating at a given stress) and also the size that a sub-critical flaw would have to achieve through slow crack growth in order to cause a failure in service. The subsequent step involves measuring the rate of crack growth in each composite layer as a function of applied crack tip stress intensity. Once the relationship between crack growth rate and K has been determined it becomes possible to calculate the time required for sub-critical cracks of different sizes to grow to the critical flaw size over a range of operating stresses. This becomes the base for the determination of maximum allowable flaw sizes in the rotor. Stress analysis of the rotors under assumed operating conditions provides a value for the maximum stresses experienced by the rotor at any given point and this maximum value of stress can be used to calculate the critical flaw size. If the service life is specified then it is possible to work backwards to calculate the maximum initial flaw size that can be tolerated such that the rotor lifetime is equal to the time required for a sub-critical crack to grow to critical dimensions.

This situation represents a worst-case scenario assuming that the largest flaw in the rotor is situated at the position of maximum operating local stress. The probability of finding a flaw at this position can be addressed and standard limit state design approaches used to determine the probability of rotor failure. It may be that an acceptable probability of failure can then be achieved by tolerating slightly larger flaws.

The second part of the methodology relates to how a real rotor could be tested to ensure that its structural integrity is within the acceptable bounds for the application. The initial design would have resulted in a calculation of the allowable flaw size. Proof testing can then be used to ensure that the rotor does not have flaws that exceed this limit. In the extreme case a proof test would take a rotor to destruction, measure the ultimate speed, calculate the peak operating stress and determine the flaw size from that data. This unfortunately destroys the rotor. The proof testing approach therefore adopts the principle that if a rotor is tested to a stress level below that required to cause failure, it must contain flaws that are equal to or smaller than the flaw size that would just have caused failure at that proof stress. This provides a value for a maximum flaw size present in the rotor which can be used to calculate a safe operating life. Charts can be developed based on equations that determine the time for cracks to grow from the maximum possible flaw derived from the proof test, to the size of the critical flaw (which depends on the service stress). The higher the proof test imposed on a rotor the longer the lifetime that can be guaranteed. The plots can be developed further to provide information on the maximum conceivable lifetime for rotors operating at specific service stresses.

This outline methodology will need to be developed further in order to provide a safe approach for use by industry. Factors such as the influence of superimposed fatigue loads, operation in vacuum and at slightly elevated temperatures, the effects of multiple cracks, the importance of defect geometry as well as size, are all important but outside of the scope of this work. The intention at this time is to provide an initial methodology which can form the basis for the ultimate development of an industrial tool.

The approach outlined above specifies the key stages in the work with the need to generate:

1. Elastic data for modelling of the rotor.
2. Fracture toughness values for each constituent layer.
3. Crack growth relationships for each layer.
4. Stress distribution information for the rotor as a function of rotation speed.
5. Data on flaw size and flaw distribution in a real rotor.

It is also important to validate the assumptions that crack growth is self-similar in nature, and to investigate the mechanisms of crack growth, in order to ensure that crack growth relationship would not change.

Table of Contents

Table of figures

Table of Tables

1 INTRODUCTION

1.1 BACKGROUND

Increased consumption of electrical power and the need for a higher quality, more efficient electrical supply, has lead many companies to investigate the possibilities of the development of a power handling energy storage device. Of the many companies involved in this research, Urenco [61], [70] have designed a commercially viable energy storage/handling device based upon the principle of a spinning mass, known as a flywheel. This technology was developed from high speed centrifuges manufactured and used, by the company for uranium enrichment. The principal advantages that flywheels have over conventional energy storage devices are summarised in table 1-1.

Table 1-1 Comparison of energy storage devices.

	Batteries	Flywheels
Efficiency	40%	95% +
Maintenance	Normal	Very Low
Service Life	5 Years	20 Years +
Chemicals	Hazardous	None
Emissions	Yes	None
Environmental Tolerance	Narrow	Wide
Mobility	Excellent	Poor

The flywheel design has the capability to provide a reliable source of backup power without any of the drawbacks associated with traditional energy storage equipment, such as batteries. The device is particularly suited for applications where a high number of cycles at high loads are required and also where power quality is a concern. An energy storage capacity in excess of 3 kWh was desired. To achieve this very high rotational speeds would be required. It was also proposed, at an early stage that the flywheel would be a sealed, maintenance free unit which should have a minimum

service life expectancy of no less than 20 years. As a result, material selection was of key importance to the success of the Urenco design.

1.1.1 Materials selection for large scale industrial flywheels. [1]

Logic dictates that the most efficient flywheel design will store the maximum energy per unit mass as possible, without failure. Any body exposed to a rotation will experience forces as a result of the centripetal acceleration and the mass. When the centripetal acceleration increases or the mass, the induced forces also increase and hence so do the stresses within the rotor. We call this stress the centrifugal stress, when these stresses reach the tensile strength of the material, the rotor will break down and fly apart. For example, with a steel rotor the mass will increase the forces quickly which will result in low speed before failure.

Thus, failure within the hoop direction this being caused by the centripetal acceleration is of primary concern since this term is governed by a squared term, where the mass is not. This implies that the maximum energy per unit mass is constrained by its angular velocity.

There is also a constraint on the outer radius of the rotor, assuming that it will fit into a confined space.

Consider a solid disk, radius r, thickness t, rotating at an angular velocity ω. The energy U it stores is:

$$U = \frac{1}{2} J\omega^2$$

Where $J = \frac{\pi}{2}\rho r^4 t$ which is the polar moment of inertia a disk (rotor) and ρ is the density.

Therefore:

$$U = \frac{\pi}{4}\rho r^4 t\omega^2$$

The mass of the disk is $m = \pi r^2 t\rho$

To maximise the energy per unit mass, the ratio of the last two equations must be taken:

$$\frac{U}{m} = \frac{1}{4} r^2 \omega^2$$

Since it isknown that as the angular velocity increases so does the centrifugal stress. The maximum principal stress of a spinning disk of uniform thickness is:

$$\sigma_{max} = \left(\frac{3+\upsilon}{8}\right)\rho r^2 \omega^2$$

Where υ is the Poisson's ratio. This stress must not exceed the failure stress of the disk material. It is also likely that during the flywheel' lifetime, it will be repeatedly spun charged and discharged. Thus, an endurance limit must be imposed on the material σ_e which is a measure of the material strength. This is the stress below which the fatigue life of the material is infinite. Hence, an upper limit to the angular velocity ω and the radius R are set(the remaining free variables).

Eliminating R and ω from the last two equations, with $\sigma_{max}=\sigma_e$:

$$\frac{U}{m} = \left(\frac{2}{3+\upsilon}\right)\left(\frac{\sigma_e}{\rho}\right)$$

Since Poisson ratio is approximately a third for most materials, the first term can be treated as a constant. Therefore, the best materials for efficient flywheels are those with highest values of:

$$\frac{\sigma_e}{\rho}$$

This quantity has the units kJ/kg, and is also the definition of specific strength. To avoid failure due to fast fracture, the disk must also have adequate toughness. Thus, another requisite is that the fracture toughness K_{IC} should be as large as possible, as a guide it must be greater than 20 $MPam^{1/2}$

The maximum specific strength for various materials can be compared using Cambridge Material Selector (CMS) software. Figure 1-1 plot compares σ_e against ρ. Those which perform best on this chart (upper left hand corner) will be by definition the best materials for flywheels. It can be seen that there are a few high specific strength materials from which to choose.

I. Engineering Ceramics

II. Carbon/Glass fibre reinforced plastics

III. Magnesium alloys.

IV. Beryllium Alloys

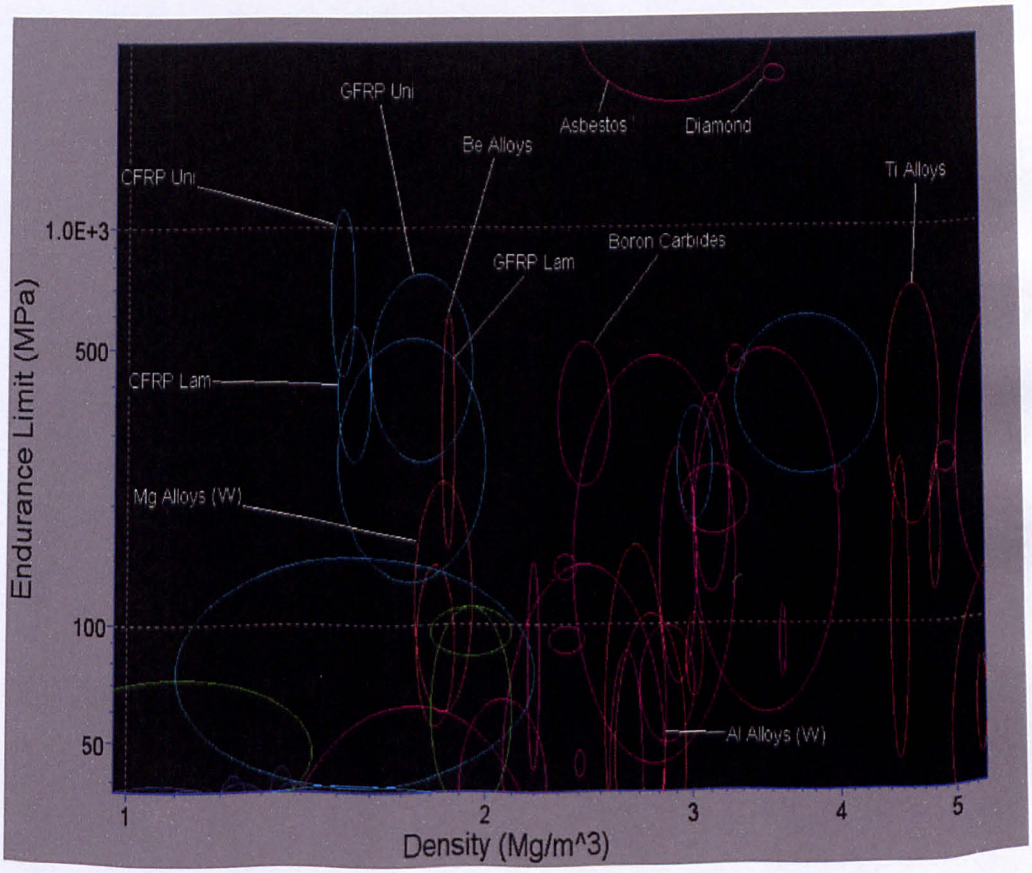

Figure 1-1 Density vs. Endurance limit [2]

Table 1-2 Comparison of CMS[2] results.

Material	KJ/Kg	Comment
Ceramics e.g. Boron Carbide	200-2000 (compression only)	Weak in tension, brittle and low Fracture toughness
Magnesium alloy	100-200	Good performance
Beryllium alloys	300	Good performance, expensive, difficult to form, toxic
Composites CFRP	200-500	Best Performance
Composites GFRP	100-400	Almost as good as CFRP, but cheaper

Engineering ceramics can be ruled at this stage, they meet every criteria except the ability to withstand radial cracks, i.e. they do not have adequate fracture toughness in the hoop direction (>20 MPa $m^{1/2}$). In the future, a successor to the current flywheel designs may involve a hybrid carbon/glass fibre reinforced ceramic flywheel. Beryllium alloys may also be ruled out on cost and environmental concerns.

This leaves high strength magnesium alloys and engineering composites as direct competitors. There is a performance differential between the two materials. The composites offer a higher energy density. However, there are other factors that influence the decision of any viable industrial project including issues of cost and manufacturing.

1.1.2 Flywheel Design.

With materials selection decided, the next relevant step was to design a flywheel. Many different designs have been proposed and are currently under development.

The design and development of a commercial flywheel was undertaken by Urenco in the mid 1990's. Urenco has many years experience with very high speed composite centrifuges for Uranium enrichment. The value of this experience is clear, and as a result composite materials were chosen for the flywheel rotor.

The rotor is based upon a large cylinder, a cylinder was chosen since its design is inherently safer than a disk, the principles behind this choice are clear. When a composite material is subjected to a cyclic load properties of the composite degrade. Thus, in a disk the inner layers of the flywheel will relax and transfer load to the outer layers, which themselves will have reduced properties. Hence the disc will fail catastrophically by failure of the outer layers.

With a cylinder, the reduction in mechanical properties causes a reduction in the critical flexural speed. This reduction in speed causes the rotor to bend. As the rotor deforms it will contact the central shaft and begin to precess As the precession increases the central shaft itself will deform. This deformation will allow the rotor to contact the containment system walls. The cylinder will then grind to a halt (Figure 1-2).

The final chosen dimensions of the rotor cylinder are summarised in table 1-3.

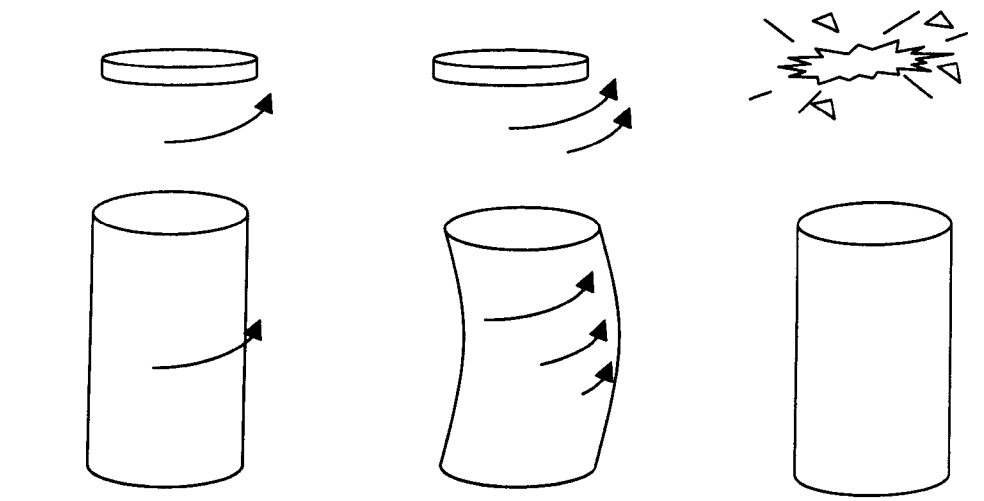

Disc and cylinder spin faster

Disc spins faster still, while cylinder deforms.

Disc finally explodes, while cylinder grinds to a halt.

Figure 1-2 Failure Management.

Table 1-3 Rotor Dimensions.

Dimension	Value (mm)
Internal Diameter	170
External Diameter	330
Overall Length	898

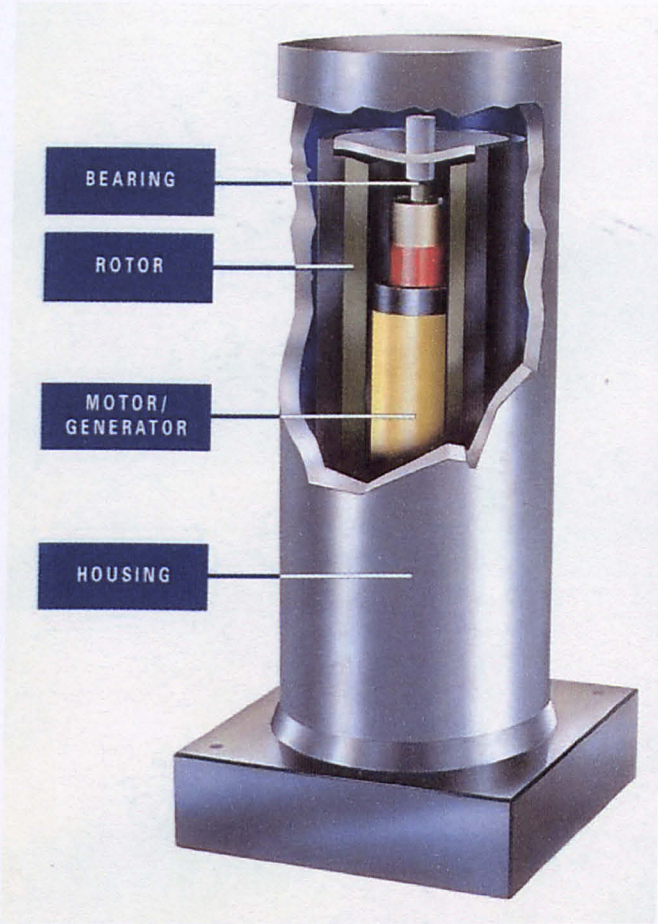

Figure 1-3 General layout of flywheel

The rotor composite is a high volume fraction filament wound GFRP/CFRP composite. The inner two thirds (46mm) of the rotor are GFRP, which gives increased energy density, and the outer third (25mm) is high strength CFRP, which significantly augments the burst strength in the hoop direction. The inner 8mm of the GFRP layer contains a particulate magnetic filler. It was found that the introduction of this filler into the composite did not significantly deteriorate the properties up to contents of around 20% [57]. When this filler is magnetised with specific patterns, it allows it to act as both a bearing and the motor generator. This inner layer is referred to as the NdFeB layer.

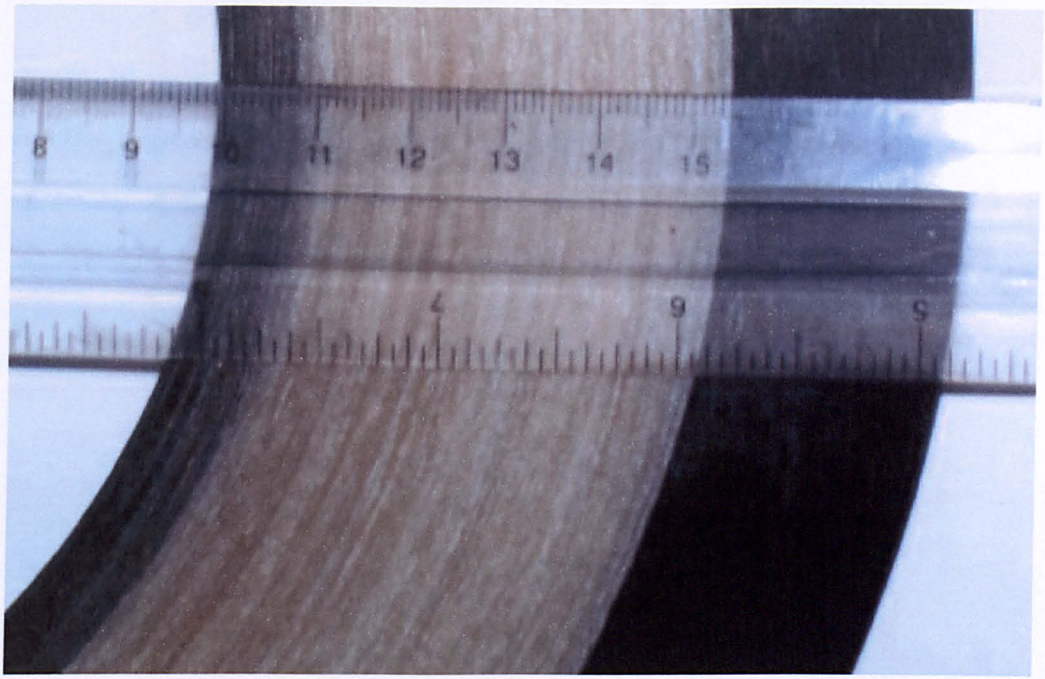

Figure 1-4 Section through rotor

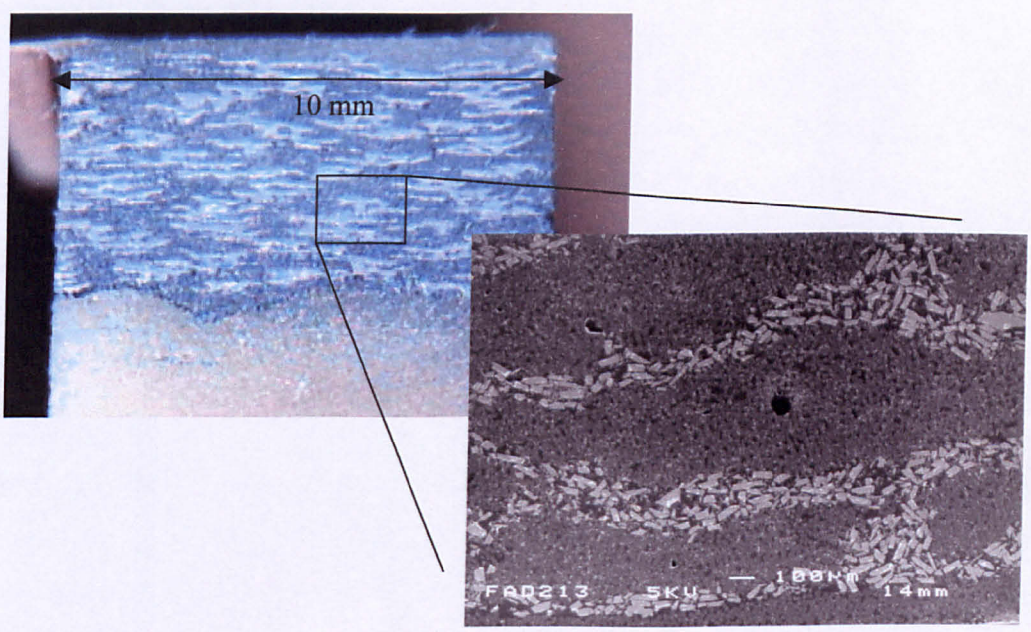

Figure 1-5 Cross section through the NdFeB Layer

A clear requirement for qualification of the rotor design is a full understanding of both the static and dynamic material properties, along with their long-term behaviour.

1.1.3 Project.

Although other flywheel projects have been, and are being undertaken, the vast majority of these are purely research projects developed in academic institutions with perhaps an industrial collaborator. The feature that sets the Urenco project apart is its production and commercial aims were already nearly realised when the work was initiated. However, although the design was very nearly ready to go to market, not enough was known about the long term behaviour of various components.

1.1.4 Research Aims

The rotor is the only component of the system under scrutiny in this project. The aim of which is to design and develop a tensile test method that will allow qualification of the material properties, leading to a detailed analysis of the rotor stress state within the rotor and finally investigating the long term properties of the composites. The culmination of these research fields would be the development of a simplified method for predicting the lifetime of the rotor, under simplified conditions.

Initial design analysis by Urenco forecast a stress state within the rotor where the GFRP and CFRP receive tensile loading in the axial direction. The magnitude of these predicted tensile loads is high and significantly approaching the materials transverse strength. With these concerns in mind, the through-thickness static and dynamic response of the composite needs to be determined with the emphasis on through-thickness crack growth, known as creep rupture.

Since the flywheel rotor is manufactured from GFRP/NdFeB and CFRP, the properties of each composite layer, along with the crack growth characteristics of the various materials, may be investigated. These will ultimately be decisive in determining the manner in which rotors are most likely to fail.

1.2 Conventions.

For the purposes of this thesis, the sign convention is defined as in figure 1-6 and co-ordinate system used to categorise the various material orientations. Thus, the 1 direction represents the hoop direction, the 2 direction is the radial axis and the 3 direction denotes the axial direction.

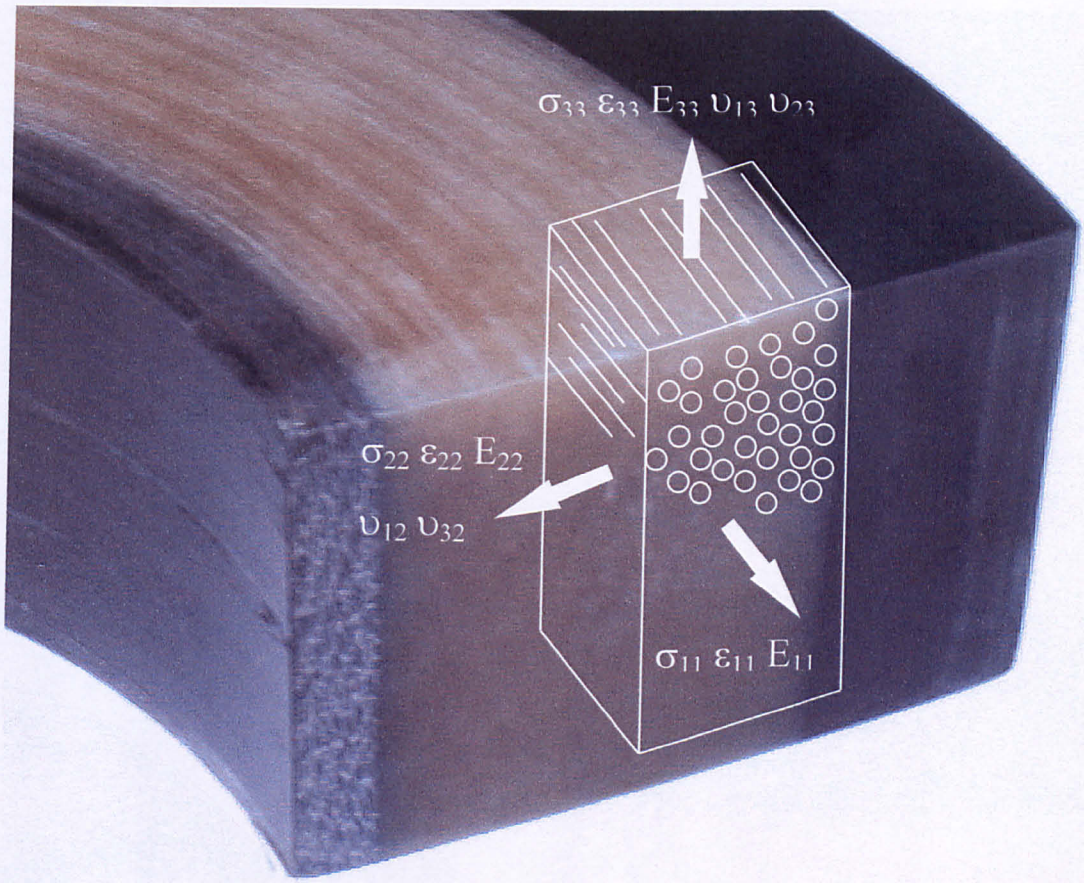

Figure 1-6 Sign Convention.

In keeping with tradition developed by Urenco, angular velocities are referred to in Hz rather than rpm, $rads^{-1}$ or $°s^{-1}$. Thus, 1 Hz is defined as 1 complete revolution of the rotor (cycle) per second.

2 LITERATURE REVIEW

2.1 Introduction

Composite materials are now widely used in many industries. Traditional uses are now being accompanied by more diverse applications such as flywheel rotors. Many institutions and companies are investigating the feasibility of composite flywheels, the published results of these projects must be examined. This, in conjunction with other published data relating to the testing and mechanical properties of composites, combine to highlight the material parameters concerning flywheel design.

The proof of the suitability of composites has already been illustrated. The principle concerns for using composites for flywheels, lies mainly in the high degree of anisotropy exhibited. Thus, the ability to accurately quantify these properties is important and a large amount of research has been conducted, that will ultimately lead to a recognized adopted standard. Thus, a review of the proposed methods was necessary. Exactly how these materials perform over a longer time period was also to be studied and hence, background regarding the ability to predict the life of a given stressed component was crucial.

Predictive methods for a variety of different components were studied for example, composite marine pipes, and there suitability to flywheels was assessed.

2.2 Composite Materials.[23]

2.2.1 Longitudinal properties

The longitudinal properties of composites are well documented. The specific performance of these materials is exceptional, hence the applicability to flywheel

rotors (Section 1.1). In order to predict the properties of the material in this direction, the simplest model has proved very effective (Figure 2-1).

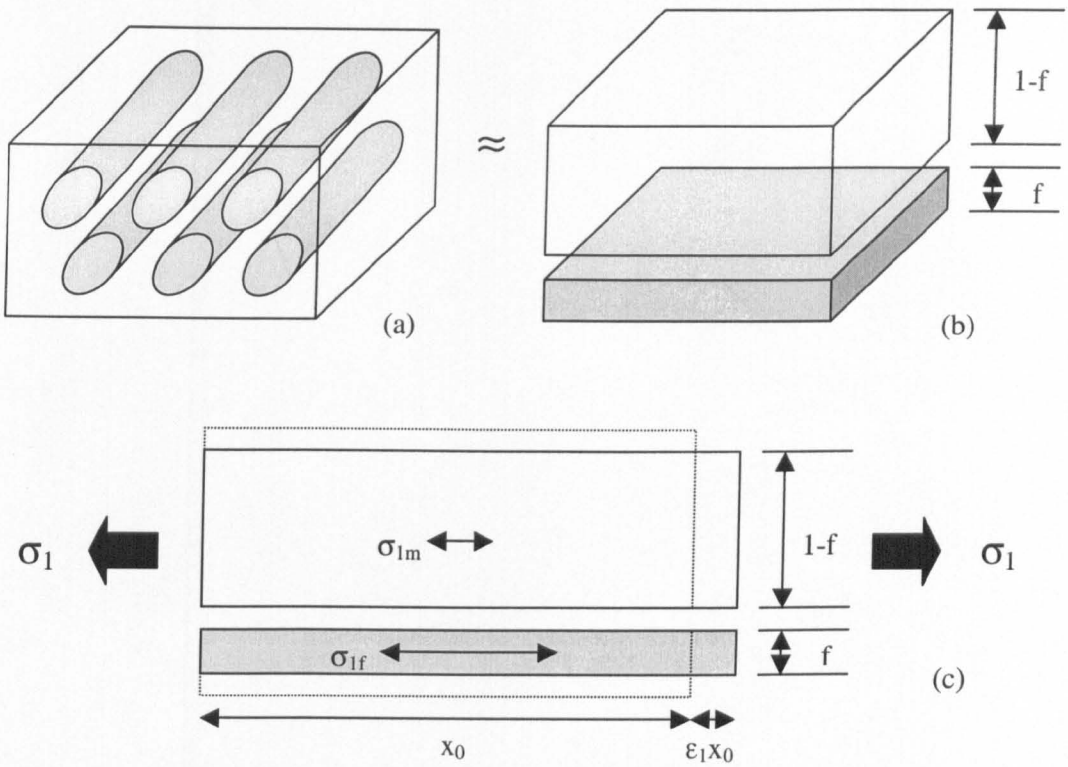

Figure 2-1 Schematic of simplification process for the rule of mixtures.

Part (a) shows a composite containing aligned long continuous fibres. This is simplified to part (b) where the composite is regarded as a bonded block of fibre and matrix, this is known as the 'slab' model. When a load is applied parallel to the fibre direction (c) they deform together with identical axial strain.

Thus, what essentially results is a weighted average of the constituents. This model is very effective, with a high degree of accuracy. It has been shown that the effects of the differing Poisson ratios on the materials in the model has little significant effect upon this, the Voigt model.

$$\sigma_l = v_f \sigma_f + (1 - v_f)\sigma_m$$

2.2.2 Transverse properties

The understanding of transverse properties is important in any application of thick composite parts. The ability to successfully predict these properties is much more difficult than for the longitudinal direction.

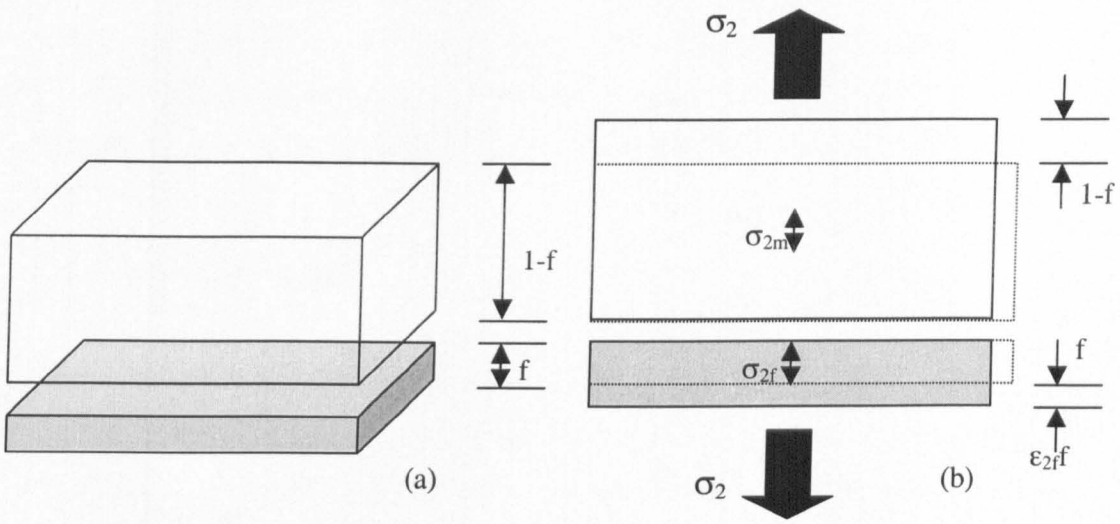

Figure 2-2 Schematic of the simplified transverse loading conditions.

Again the 'slab' model (Figure 2-2) can be seen (a), this time it is exposed to transevrse loading (b) resulting in the equal stress assumption. In this model the approach is one of equal stress, i.e.

$$\sigma_2 = \sigma_{2f} = \varepsilon_{2f} E_f = \sigma_{2m} = \varepsilon_{2m} E_m$$

The component strains can be expressed in terms of applied stress. Hence the overall strain is:

$$\varepsilon_2 = f\varepsilon_{2f} + (1-f)\varepsilon_{2m}$$

So the composites modulus is:

$$E_2 = \frac{\sigma_2}{\varepsilon_2} = \frac{\sigma_{2f}}{[f\varepsilon_{2f} + (1-f)\varepsilon_{2m}]}$$

Substitute expressions for ε_{2f} and ε_{2m}:

$$E_2 = \left[\frac{f}{E_f} + \frac{(1-f)}{E_m}\right]^{-1}$$

This model is simple, the primary concern is that it does not represent E_2 accurately in terms of value and volume fraction variation. To better predict the transverse modulus, a more detailed approach should be used, where the modelling of the true stress and strain distributions is undertaken. Thus, the next level of complexity replaces the slab of reinforcement with actual fibres. This model breaks the composite into regions where the matrix is in series with the fibres, in the line of the loading direction.

2.2.3 Halpin-Tsai Model

The most successful and hence accepted model for transverse modulus is the Halpin-Tsai model developed in 1967. The model is not based upon rigorous elastic theory, such as the Reuss model described previously. The Halpin-Tsai model significantly takes into account enhanced fibre loading, relative to the equal stress assumption.

$$E_2 = \frac{E_m(1+\xi\eta f)}{(1-\eta f)}$$

where $$\eta = \frac{\left(\frac{E_f}{E_m} - 1\right)}{\left(\frac{E_f}{E_m} + \xi\right)}$$

E_2=transverse modulus

E_m=Modulus of matrix (6 GPa)

E_f=Modulus of fibre (70 GPa)

F=Fibre volume fraction

And ξ= an adjustable parameter.

The Halpin-Tsai model is very useful for predicting the elastic composites. Once the adjustable parameter has been determined, usually experimentally, the elastic properties of a given composite may be predicted with some confidence.

2.3 Through thickness testing.

2.3.1 Introduction

There are many proposed test methods available for through thickness testing, however, as yet no fixed standard exists. This is principally due to the design engineer regarding the properties of this direction as weak and introducing a suitable safety factor. For the flywheel rotor application this direction is critical.

The principle issues with through thickness testing concerns the manufacture of suitably thick material. Thus, a great deal of work has focused on producing meaningful results from smaller specimens. The problem with this is the ability to expose a relatively thin specimen to a uniform transverse tensile stress. The solution to this problem can be divided into two categories:

1. Direct introduction of a through thickness load.
2. Indirect loading, i.e. a load is introduced into the specimen such that a resultant through thickness stress will exist in the specimen.

2.3.2 Direct through thickness tests [5-8].

The load is introduced into the specimen directly along the through thickness axis. This is the simplest and most logical form of test. With the use of strain gauges this type of test will yield accurate results for elastic properties.

2.3.2.1 Gripped un-tabbed specimens.

In 1984 Kitching [43] produced very thick (229mm) E-glass chopped strand mat and polyester laminates. This was cut into specimens for transverse testing. Two types of specimen were evaluated (Figure 2-3). Grips were also manufactured to allow the best contact to be made with the round type b specimen.

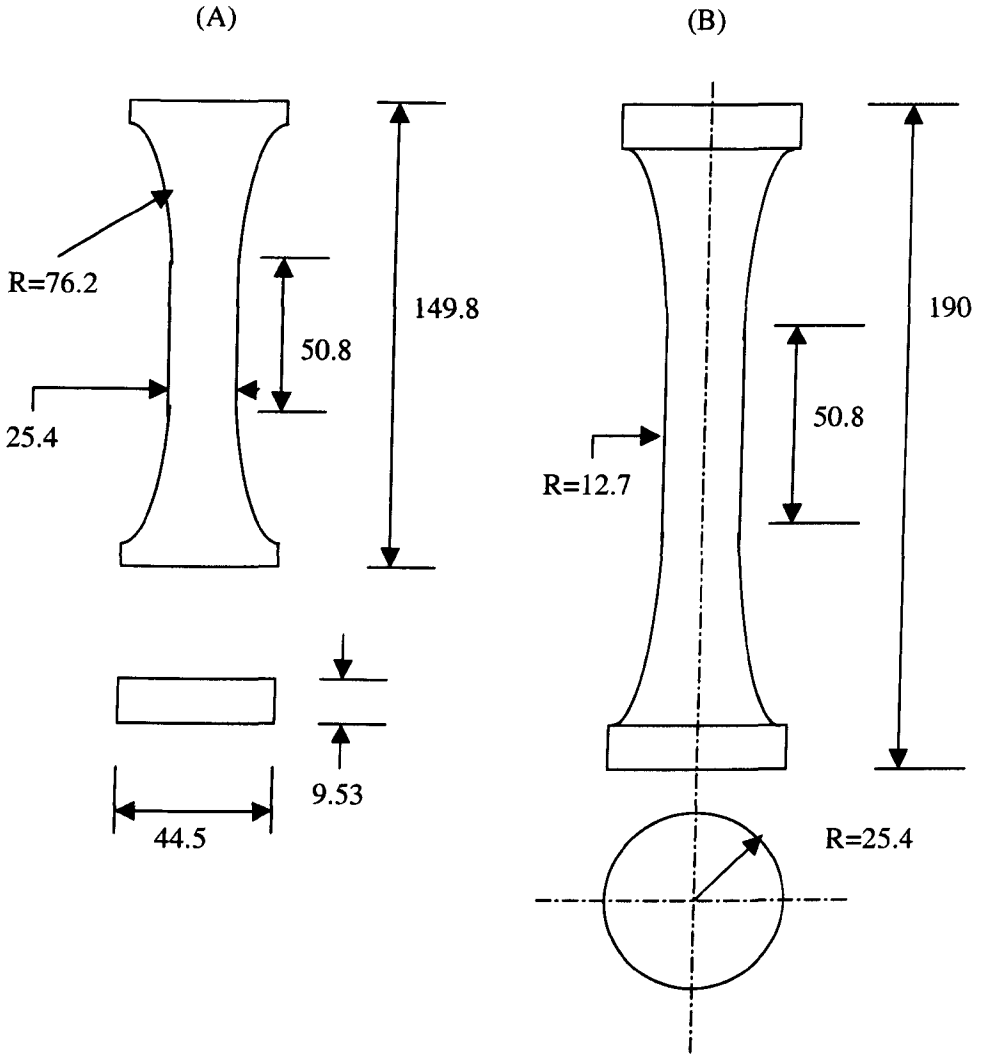

Figure 2-3 Gripped un-tabbed wasted specimens. Dimensions in mm.

The results of these tests (Table 2-1) are reasonable with the exception of υ_{31} measured on the circular specimen. This is due to the difficulty in bonding a strain gauge onto a curved surface. The modulus and strength results are very similar. No mention was made of polishing the specimens after the machining. This is a particular concern with cylindrical specimens, since the only way to manufacture these is to turn them down on a lathe, which inevitably will lead to damaged surfaces that will promote premature failure.

Table 2-1 Tensile properties of glass/polyester.

Quantity	Type (A)		Type (B)	
	Value	C_v (%)	Value	C_v (%)
Modulus (GPa)	5.0	8.9	5.3	6.4
υ_{31}	0.18	7.8	0.17	21
σ_{utts} (MPa)	9.0	8.9	8.8	12

2.3.2.2 Tabbed Block Specimens

The use of tabbed block specimens was used by Roy [44] who developed the method for use with carbon fibre reinforced epoxies. The goal was to determine the stiffness and strength of AS4/3501-6. The specimens were constructed as shown in figure 2-4. The use of a brass shim soldered to the specimens was implemented in order to minimise any problems with alignment since they would act as a hinge joint, which also reduced the possibility of bending being introduced. The thickness of the specimens was varied, with t =1, 1.4, 2.5 and 5.7mm.

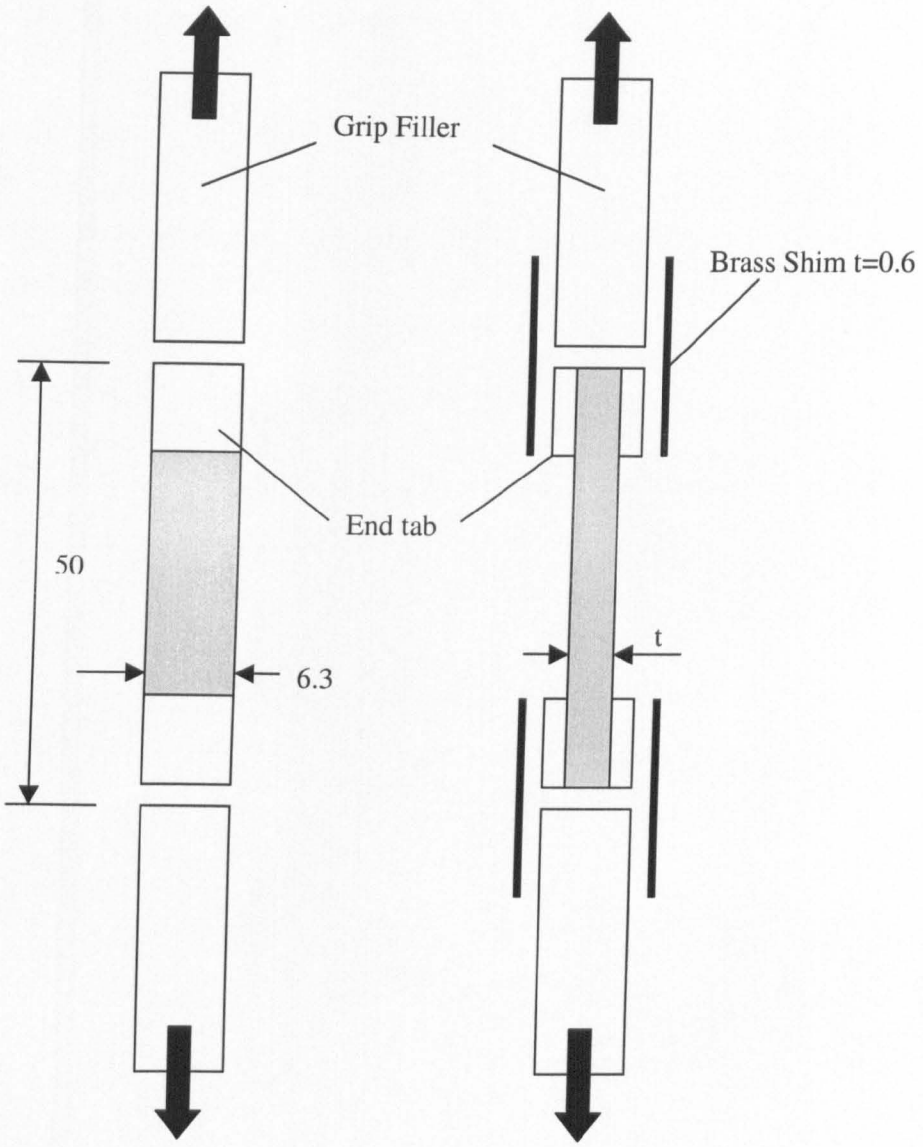

Figure 2-4 Tabbed hinge block specimens, dimensions in mm.

Two types of lay-up were tested, cross-ply and quasi-isotropic. It was found that the modulus of the cross ply laminates was constant with respect to specimen width. The author noted that the modulus reduced with specimen width for the quasi-isotropic specimens. Although, because only a 6% drop was recorded, these claims are unwarranted, since the amount of specimens tested was not mentioned. No strength values were quoted. The reason behind this being that failure consistently occurred at the end tabs, obviously suggesting high stress concentration in this region.

2.3.2.3 Tabbed waisted specimens

Initially Ishai [45] used similar specimens to those described in the previous section. However, the loading method was modified to use pins as an alternative to gripping the end tabs. Pins improved the load transmission and the uniformity of the stress state in the gauge section.

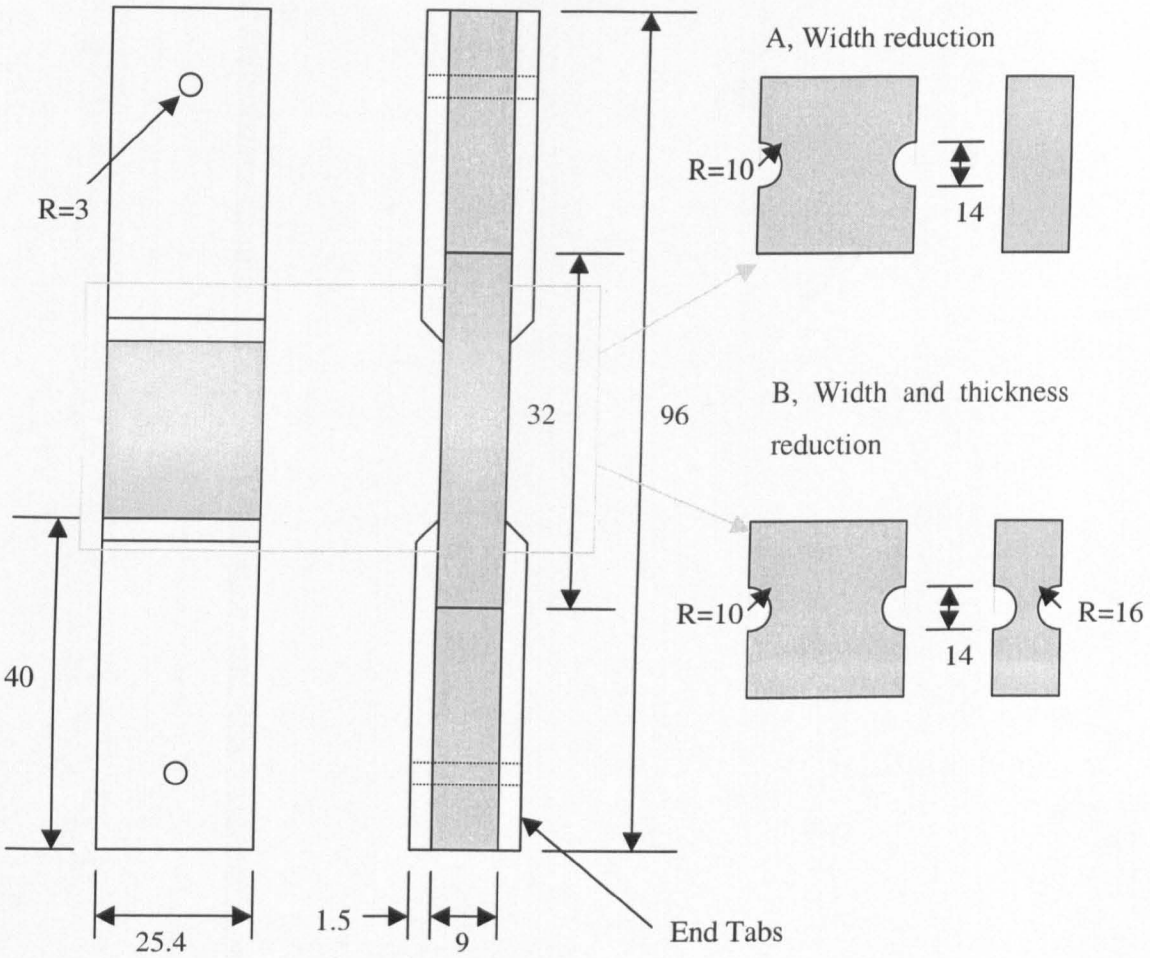

Figure 2-5 Tabbed Pin loaded specimens, with further wasting profiles. Dimension in mm

Strain gauges were attached at the centre of all four faces. The modulus results for the unidirectional carbon fibre materials tested are good 10.1 and 10.6 GPa for the two transverse moduli. The volume fraction of the materials was not measured, although

by the moduli results, it is safe to assume that they were reasonably high. As with Roy no strength values were quoted, due to failure around the end tab.

Ishai proposed necking down of the block test section. This would promote failure in the gauge region and he suggested two strategies, A and B (Figure 2-5). The first, Type A would only require machining down in one plane to produce a 1D waisted specimen. The alternative was to then further waste the profile down in the other direction to produce a 2D waisted profile. Again the specimens were loaded using the pin configuration. Ishai modelled the stress concentration that would take place in the 2D specimen and found that a stress concentration factor of 1.25 would be present with this geometry. He corroborated the FE results by monitoring the strains closely in the curved and straight portions of the specimen. Good agreement between the predictions and experimental work was noted.

The wasted profiles proved successful, all specimens broke in the waisted zone. The 1D specimens produced failure strengths of 40.3 MPa with a C_v=35%. Again this was for UD AS4/3501-6 material. When this same material was tested in the other transverse direction, a higher value of 64.4 MPa (C_v=31%) was achieved. Thus, the assumption that UD materials may be transversely isotropic is not always accurate.

The 2D specimens produced higher results still, a strength of 70.0 MPa was observed with C_v=16%. This result was measured in the same direction as the first result for the 1D specimen. The suggestion would be that the stress concentration factor is indeed higher the initially anticipated, or there is a volume effect present.

2.3.2.4 Bonded Block specimens

The simplest approach to measuring the transverse properties is to bond straight sided block type specimens directly to the loading jig. Kim [46] tested such specimens manufactured from AS4/3501-6. The v_f of the composite panel was 55% and some 17.8mm thick. Strain gauges were bonded to the surfaces of the specimens. Table 2-2 shows the results of this testing programme. The Moduli are very constant with exceptional C_v's. The values also correlate well with other published data. Further, the

strength values compare well with other data. In addition, it should again be noted that no special specimen architecture was used.

Table 2-2 Transverse properties of AS4/3501-6 [46].

Fibre direction	Modulus [GPa] (C_v)	Strength [MPa] (C_v)
2 (Figure 1-6)	9.7 (4.5%)	51.4 (8.7%)
3 (Figure 1-6)	9.0 (2.1%)	61.2 (16%)

2.3.2.5 Bonded waisted specimens

The approach used by Martin and Sage [47] was to produce several laminates 16 ply's thick. 24 of these were then bonded together, in a layered structure to produce a composite 48mm thick. The material was XAS/914 carbon fibre/epoxy. The laminate was then processed into the specimen form illustrated in figure 2-6, Aluminium end tabs were bonded onto the waisted specimen. No values were quoted for the width(W) of the specimens.

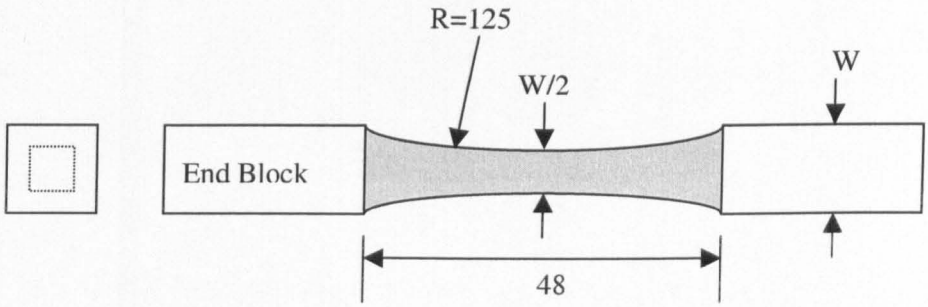

Figure 2-6 Bonded block type specimen. Dimension in mm

The strength of these specimens was found to be 75 MPa. No indication of scatter was presented. The authors explained that failure often occurred at or near the interface between laminates. The reason presented for this being that the Poisson ratio in the bond layer was approximately 50 times higher that that in the fibre direction. Hence, considerable stress concentrations arose from this disparity. Although the results seem

reasonable, the author concluded that due to this bond line behaviour, the test method is inappropriate for continued research.

Similarly, Lagrace and Weems [48] design a square waisted specimen (Figure 2-7). The specimen was small and thus could be cut from a thick laminate without the problems experienced by Martin and Sage [47]. The specimens were then bonded to long(125mm) loading arms. The material tested was AS4/3501-6 with three different lay-ups. No difference was observed in the results for these lay-upswhen compared with the scatter. A strength of 43 MPa was measured with a variance of 15.6 %. This is not an unreasonable value, certainly within expected range for this material. In all cases failure was confined to a single ply surface, i.e. no broken fibres were seen.

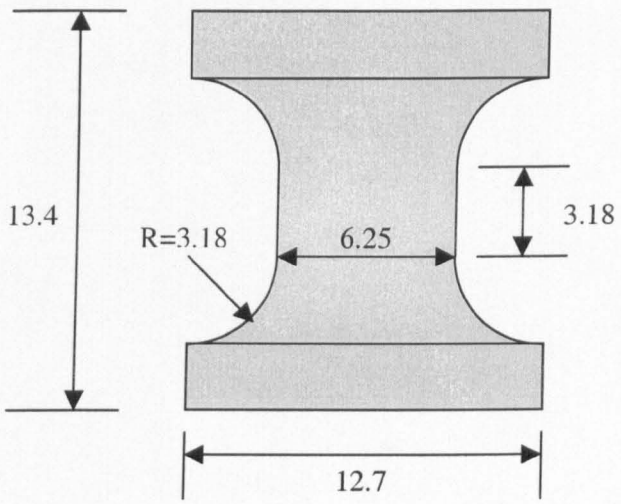

Figure 2-7 Bonded waistedspecimen. Dimension in mm.

The greatest difficulties reported with these types of specimens, was the need to very accurately bond them to the end tabs to avoid misalignment. A jig was proposed to ensure the correct alignment, although not used. Secondly, the amount of intricate machining required to fabricate these specimens, makes the test method expensive.

However, even with these problems addressed, specimens with short gauge lengths will suffer from stress concentrations. These inhibit development of the true transverse

stresses. This would certainly be compounded by the proximity of the resin end tab interface.

At DERA, Ferguson [49] progressed this test method further, using a larger specimen. His goals included development of this specimen to universally measure the transverse properties. The modified specimen architecture is shown in figure 2-8. The specimen no longer has a square gauge section but instead is waisted down to a rectangular profile.

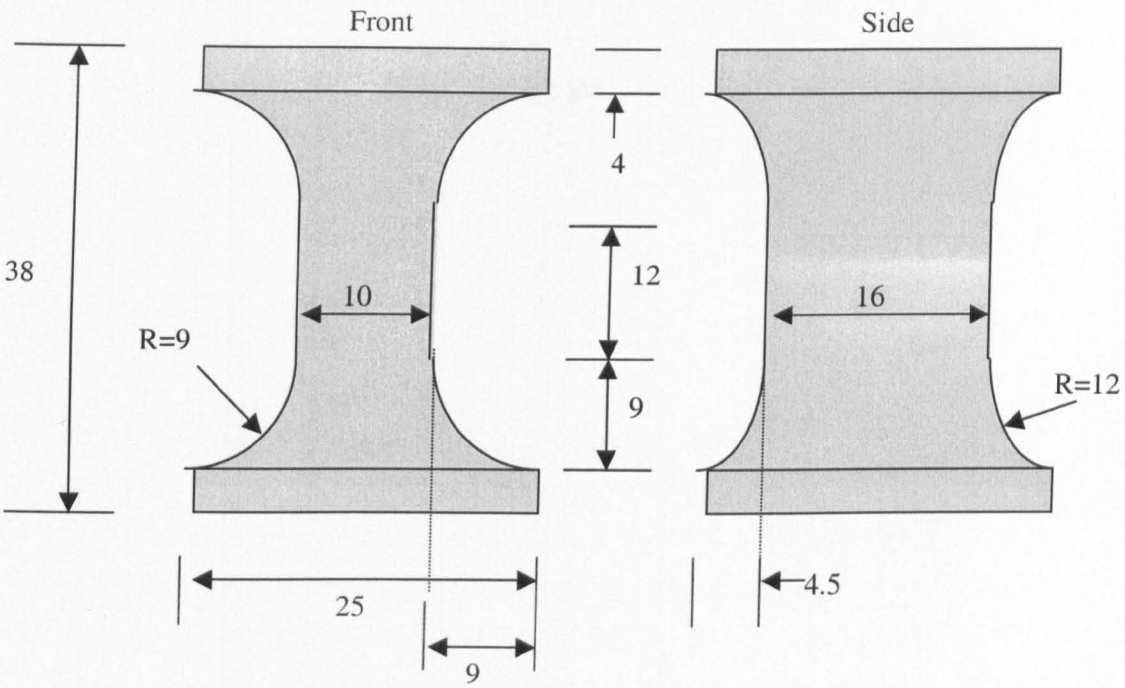

Figure 2-8 DERA waisted specimen. Dimensions in mm.

The research programme conducted at DERA was comprehensive. A wide variety of materials were used in both tension and compression. The results for the carbon tests, in tension were good. The strength was measured at 70.7 MPa (C_v=8.1). The modulus value of 9.52 GPa is also comparable with other research, however the variance of 0.7% is exceptional. The majority of the tests conducted showed very small variances, typically around 9% for strength and 2% for moduli. The Poisson ratio measured were also very consistent when compared to other published values.

This specimen geometry is complex, again requiring considerable expertise to machine accurately. Hence, the costs of these tests are high. However, the authors refer to an NPL report [6] which highlights that specimen machining and testing costs are relatively unimportant, in comparison with the production of accurate strength and stiffness data.

2.3.3 In-direct through thickness tests [49]

With in-direct tests, the specimen design and loading orientation result in a transverse tension force being exerted upon a specific region the specimen. Many different tests methods of this kind have been proposed and used. The most common of these are reviewed here. In the majority of cases the resultant specimen architecture and loading jig are very elaborate, hence costly to fabricate.

2.3.3.1 Compression disc.

This test method involves applying a compressive load to a disc of composite. This compressive load induces a tensile force perpendicular to the loading axis (Figure 2-9). The magnitude of the induced force is 1/3 of the applied load, for isotropic materials, and is constant across the diameter of the specimen [24]. For anisotropic materials, further analysis was conducted by Okubo [25]. His work concluded that if the material is significantly weaker in the transverse direction, then failure will occur in this region. The method obviously adapts itself well to pulltruded rods. Otherwise, the method again involves the production of a relatively thick specimen (the diameter of the disc)

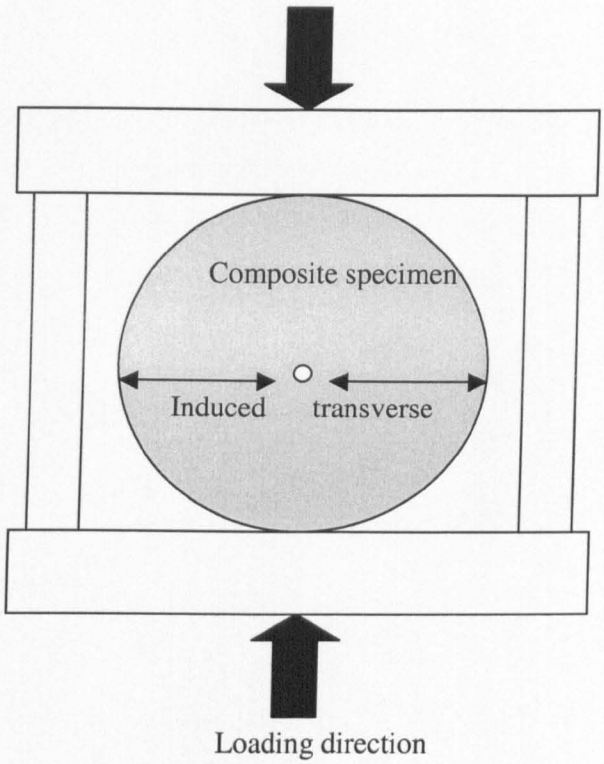

Figure 2-9 Schematic of the compression disc set-up.

The test method was used on woven GFRP materials by Mao and Owen [26]. In conclusion, although varying thickness and diameters were used these were found to have no effect. The results were also highly scattered, this was due to the mixed stress state across the diameter of the disc. This test method does not allow the determination of the elastic constants of the material.

2.3.3.2 Curved specimens

Much work has been conducted upon the use of curved specimen geometries. This type of test may only be performed upon UD laminates, any angle ply laminate would be subjected to interlaminar shear at the free edges.

Initial studies by Lekhnitskii **[27]** centred around the elastic equations controlling the stresses in a semi circular specimen (Figure 2-10). Consequently he found that these

were linked to the angle θ and the coefficient of anisotropy, $k = \sqrt{\frac{E_\theta}{E_r}}$. In 1993 Jackson and Martin [28] published further work on this specimen geometry. They examined the influence of the transverse modulus on the stress state and discovered that a 30% uncertainty in this value had virtually no effect upon the predicted strength value.

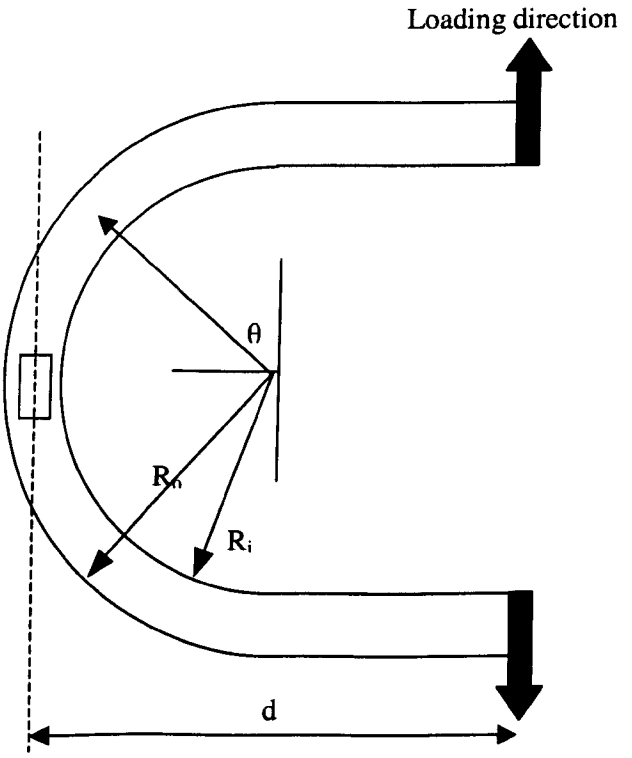

Figure 2-10 Semi-circular bend specimen.

This geometry may also be approached from a simpler standpoint addressed by Kedward [29]. He assumed that failure consistently occurred in the same area, and used beam theory to calculate a value for the maximum transverse strength.

$$\sigma_{T\,max} = \frac{3Pd}{2wt\sqrt{R_i R_o}}$$

Where w is the specimen width and t is the thickness.

σ_{Tmax} has a peak at $\theta=90°$ and is located at a point $r=\sqrt{R_i R_o}$. This study also concluded that the errors resulting from the use of this equation increased with the degree of anisotropy and also when R_m/t decreases. Since Carbon fibre composites exhibit very high degrees of anisotropy, R_m/t must be high enough to counter balance this, if the simple solution to the specimen architecture is to be used. 2D finite element analysis performed by Shivakumar [30] on CFRP specimens of this type found that the difference between the exact elastic solution and the beam disagreed by only 1.5% for $R_m/t=1.75$. For any value higher than this, the beam theory is more than acceptable to use.

Actual results of tests using this type of specimen are not easily compared, since no standard for specimen dimensions has been set. Thus, by displaying all the parameters based upon the geometries, the data can in part be normalised.

The experiments Hiel [31] conducted used three separate test designs. After the initial specimens with the conventional geometry were conducted, it was felt that more should be done to promote failure in the curved section. Therefore, in further tests the gauge section was narrowed to 6.35mm. In this set the result could be split into two distinct categories, strong and weak values. It was believed that the weak specimens failed due to the presence of large defects. The author does not mention how the specimen were treated post machining of the wasted section.

In order to further promote failure in this region, Hiel [31] reduced the radius of curvature. This led to the elliptical specimen design (Figure 2-11).

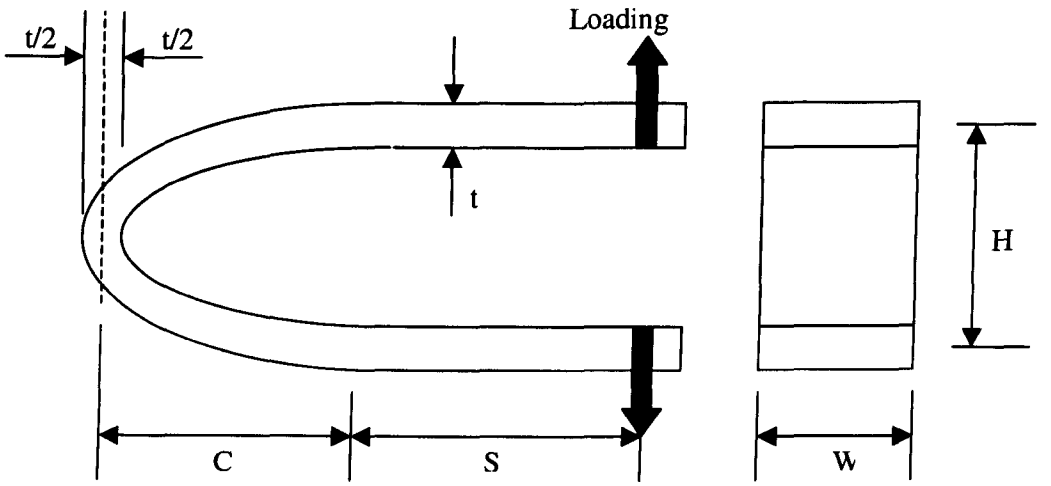

Figure 2-11 Elliptical curved beam specimen.

The specimens were then machined and tested by Sumich [32]. The values reported for the transverse strength were very high. This may be due to either, and/or the following effects:

- The same equations were used as for semi-circular specimens
- The stressed volume is very small, O'Brien and Salpekar [36] demonstrated that strengths decrease with increasing stressed volume.

In continuation, Matthews and Ellis [33] designed a rig that eliminated the need to drill and screw the specimens in order to introduce loads onto them. This had the effect of reducing the stress concentrations as the load was applied. Unfortunately, the specimens frequently slipped out of the jig as it began to extend. The results obtained were reasonable. However, again very high values for the second batch of tests using the elliptical specimens confirms the fallacy of using this method with the conventional analysis.

Gower [34] conducted extensive experiments using the Matthews jig and another jig developed by Ige [38]. The jig designed by Ige was intended to put the specimen in pure bending. Gower's results using these two jigs were reasonable for the semi-circular specimens. The results for the elliptical specimens were poor. No explanation was offered for this low value.

Notes for table 2-3

1, All test were conducted on CFRP composites of the type listed.

2, Specimens were necked down to 6.35 mm at the apex of the semi circle

3, σ_{utts} as measured by Wu and Springer [35].

4, These specimens did not fail in the intended location, and exhibited a great deal of matrix cracking.

5, σ_{utts} as measured byHexcelComposites [36].

6, No value for % of σ_{utts} was given.

Table 2-3 Results of Semi-circular/elliptical test programs.

Material[1]	Type, SC or E	H (mm)	C (mm)	S (mm)	t (mm)	W (mm)	Strength (MPa)	C_v %	%of σ_{utts}	Notes	Reference
G40-600/5245C	SC	61	30.5	19.1	9.1	25.4	36.8	23	63		[31]
G40-600/5245C	SC	61	30.5	19.1	9.1	6.35	57.8	7.6	99	2	[31]
G40-600/5245C	SC	61	30.5	19.1	9.1	6.35	32.5	11.8	55	2	[31]
T300/934	E	40	50.8	25.4	2.8	25.4	107.1	10.1	194	3	[32]
XAS/913	SC	24	12	43.5	10	25	-	-	-	4	[33]
XAS/913	E	39	48	21.5	3	10/25	99.5	9.8	175	5	[33]
T300/913	SC	91	45.5	175	3-5	23	50.9	25	-	6	[34]
T300/913	E	91	91	175	3-5	23	62.0	15	-	6	[34]

2.3.3.3 L-shaped specimen [28]

Jackson and Martin proposed and tested L shaped specimens as shown in figure 2-12. The loads were applied to the AS4/3501-6 specimens via bonded hinges. Several geometric parameters were varied and the results compared (Table 2-4)

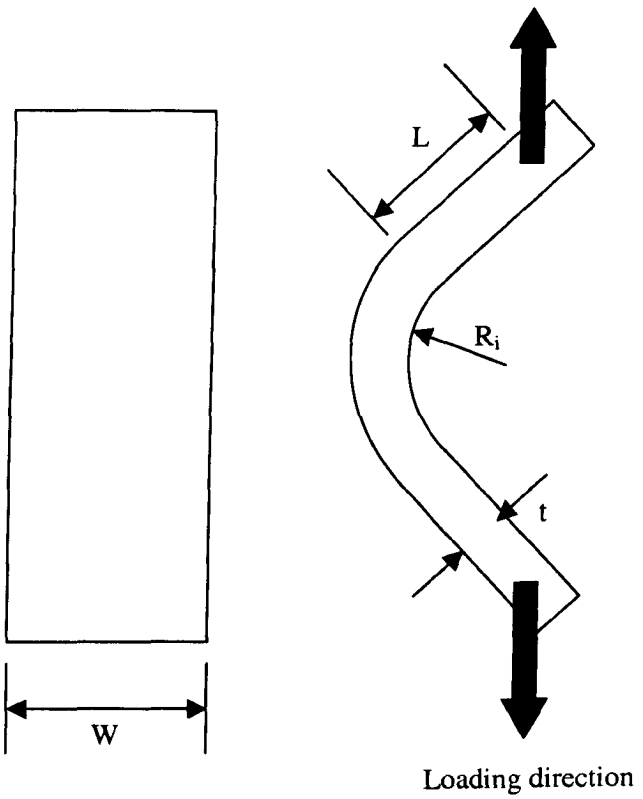

Figure 2-12 Schematic of L-shaped beam specimen

Table 2-4 Transverse strength of AS4/3501-6 [28]

No. plies	R_i (mm)	L (mm)	W (mm)	σ_T (MPa)	C_v (%)
16	5	25.4	12.7	81.4	13.3
			25.4	81.1	16.2
24	3.2	25.4	12.7	75.5	14.3
			25.4	47.4	41.4
	5	25.4	12.7	30	20.7
			25.4	35.7	7.3
		50.8	12.7	37	27.5
			25.4	40.8	15.3
	8.5	25.4	12.7	39.7	28.8
			25.4	29.2	42.6
48	5	25.4	12.7	16.7	5.5
			25.4	17.1	5.3

It was observed that the thicker specimens yield much lower strength values This was attributed to increased probability of a significant defect being present in the gauge region. The influence of specimen width could not be clearly established. The results for the 16 ply specimens, represented values that were clearly in excess of the transverse strength of this material ~140%. This was believed to be due to the same effects as seen in the earlier results reported by Sumich [32] and Matthews [33].

2.3.3.4 Humpback specimen.

In 1995 Winsom and Jones [40] tested specimens of glass fibre/epoxy using a humpbacked specimen configuration. Large displacements were observed which prevented the calculation of the bending moment directly from the applied load and initial geometry. As an alternative, the bending moment was estimated from the measurement of surface strains and the results of 2D analysis. Three different geometries were used to combat the volume effects suspected to have an influence on the transverse strength, The standard specimens (small) dimensions were, t=2mm, $S_2=2S_1=60$mm, $R_1=4$mm, $R_2=3$mm and W=5mm. The other geometries (medium and

large) used were exactly 2 or 4 times larger, in every dimension. Uniquely the void content was also measured for the different specimens and was quoted as 3.3%, 0.3% and 1.3% for the small, medium and large specimens.

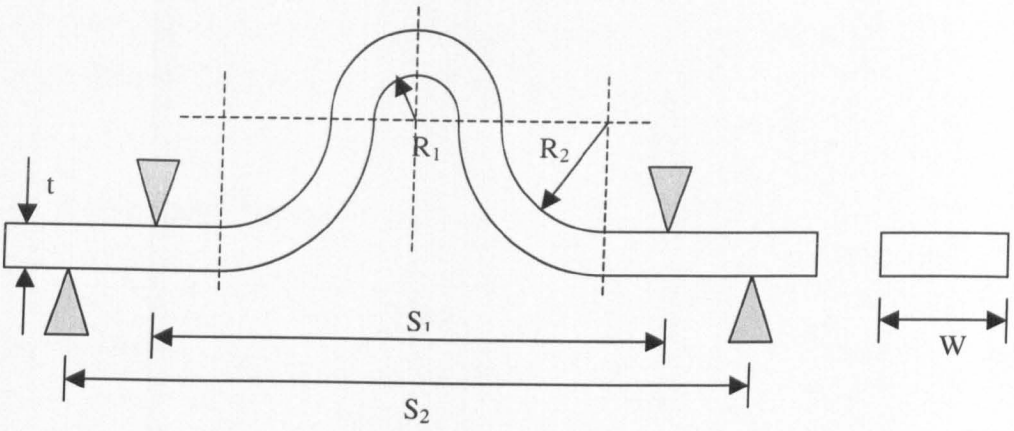

Figure 2-13 Humpback specimen architecture

In every test, failure occurred in the intended location. Six specimens of each size were tested, the results were consistent (Table 2-5). Interestingly, these results do confirm the argument that the transverse strength of composites is volume dependant. However, the magnitude of this effect is far lower than most other researchers claim.

Table 2-5 Humpback specimen results.

Specimen	Strength (MPa)	C_v %	Void content %
Small	97	4.9	3.3
Medium	90.4	4.3	0.3
Large	85	3.1	1.3

2.3.3.5 3-Point bending.

Less complex and thus the most useful of these methods, for testing the strength of composites, is the ASTM D790. This is a flexural test method for polymers, either 3 or 4 point, on a simple rectangular beam specimen. This test is applicable to fibrous

composites. Like the other test methods, only a very small amount of the specimen is actually exposed to pure transverse stress. However, recent research by a group of European Universities [41] in transverse properties, has highlighted this feature as an advantage. The conclusion being that since only a small volume is exposed to the transverse force, there is less likelihood of an inherent flaw being present. Thus, the figures represent the true value of the transverse strength.

2.4 Long Term Properties

2.4.1 Creep

Creep is defined as the progressive deformation of materials exposed to a continuous load. The fact that materials deform over a time period under load poses problem to design engineers. Over a large time frame very large strains may develop in a component. Creep in components is often exaggerated by elevated temperatures, typical 0.4-0.5 of the melting temperature. Thus, the primary mechanism active is a diffusion process, allowing molecular rearrangements and associated straining.

Since fibre composites are fabricated from two distinct components, the fibre and matrix, the behaviour will be governed by some combination of the constituents. The creep resistance of carbon fibre is known to be excellent [79]. Carbon fibre generally can sustain loads approaching the tensile strength of the carbon strand for an indefinite period of time, in either air or water. Glass fibres do not perform so well. The rupture times, at equivalent strain levels are several orders of magnitude greater for carbon over glass fibres.

The matrix of composite systems plays an important role in the creep behaviour. Thermosetting resins have fairly vague melting temperature, but they do tend to chemically and mechanically degrade at 100-200°C above ambient temperatures. Thus, at room temperature they are fairly resistant to creep. Thermoplastic polymers, in contrast, have well defined glass transition and melt temperatures, above these they

become viscous liquids. These temperatures are relatively low, and thus make them prone to creep at room temperature.

2.4.1.1 Axial creep

In the case of axial creep of composites, so long as the fibres remain elastic, which in the case of glass and carbon fibres they do, the analysis is relatively simple. As creep occurs in the matrix, which it does since we know the fibres are creep resistant compared to the matrices, then the applied stress will gradually be transferred to the fibre. As the fibres strain elastically, the stress will also increase. Thus, the limit of creep is reached when the fibres carry all the applied load. The amount of creep will actually drop off with time since as the fibres carry more load, the stress in the resin reduces, and hence the amount of creep declines. This situation is useful to designers since the load fibres carry may be easily calculated and thus a limit for creep imposed. This, of course, assumes that the fibres do not fail. This simple analysis gives a good approximation of experimental results.

For example, Endo [85] conducted tests on Al/SiC. These tests showed clearly the progressive load transfer and the fall off in matrix creep (Figure 2-14). This behaviour is also seen in polymer composites. It is also possible to predict the rate at which this limit strain is approached. Analysis was conducted by McLean in 1983 [86] which related this rate to the creep characteristics of the matrix.

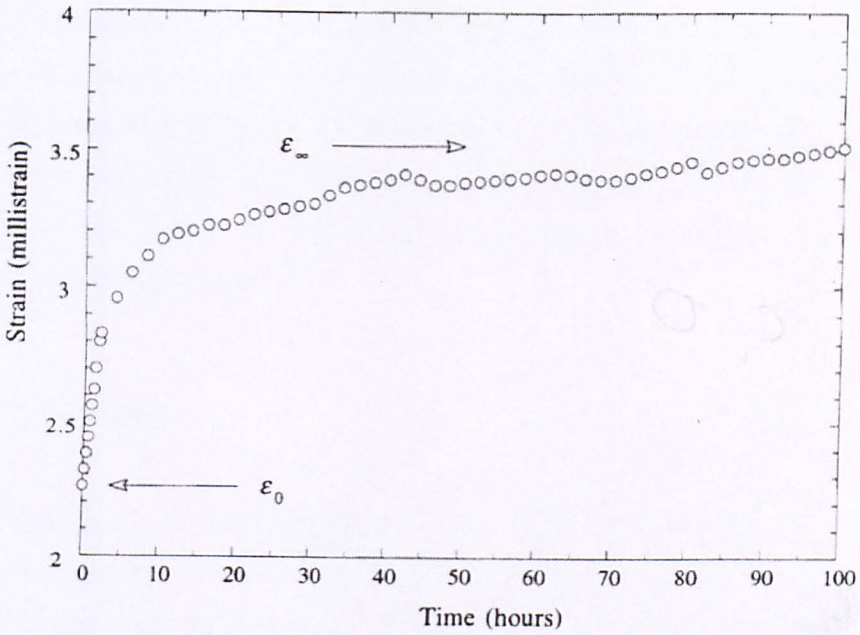

Figure 2-14 Axial creep behaviour of Al/SiC composite at 673°K [85].

2.4.1.2 Transverse creep

In the transverse directions, the situation is very different. In this case due to the lack of reinforcement, creep is often more acute. This is because the transverse behaviour of composites is highly resin dependant. Thus, since it is known the primary influence on creep is the matrix, thus the transverse creep of composites is largely dependant upon the creep characteristics of the matrix. It is possible to achieve steady state creep in the transverse directions with composites.

In theory, any of the previously outlined through thickness test methods that could successfully measure modulus may be used to determine the transverse creep. However, preference would be biased towards those specimen designs where the loads are introduced directly to the specimen.

In 1995 Scott [88] performed a series of off-axis tensile tests that showed that the creep behaviour of 45° and 90° laminates is almost identical. He also found that this behaviour was very similar to that of the neat resin.

When the issue of transverse creep rupture is considered, very little research has been conducted. Since the use of very thick composites is still in its infancy, designers are only beginning to understand the significance of the transverse properties, and making calculations accordingly. Thus, the notion of transverse creep rupture has barley been considered. However, it is very important to address this issue with regards to the flywheel rotor, as we shall see.

2.5 Toughness

The toughness of a material is regarded as the resistance of that material to fracture and crack propagation [90]. Phillips and Tetelman [91] mentioned that any toughness value must relate the response of a material, in terms of fracture characteristics, to the applied stresses and strains. Thus, a useful way of establishing the toughness of a material is by analysis of the fracture surface energies (γ). This is a measure of the resistance of the material to crack propagation, and is defined empirically as the minimum amount of energy required in creating a unit area of fracture surface. Thus, a great deal of work was has been conducted in relating such parameter into a useful engineering quantity.

2.5.1 Fracture Mechanics

2.5.1.1 Introduction.[23]

The origins of fracture mechanics can be traced back to the work by Inglis, published in 1913. He realised that the stresses around a crack tip would be significantly higher than those in the bulk (σ_B) of the material. He derived expressions to show the stress at the tip of a crack of length c (or 2c if internal) and tip radius r were:

$$\sigma = \sigma_B\left(1+2\sqrt{\frac{c}{r}}\right)$$

Hence, this predicts that the stress concentration factor around a hole=3. This is entirely feasible. However, with a sharp crack, as r tends to 0, the stress concentration approaches infinity. This implies that any scratched material will fail when loaded. Clearly evolution of the theory was required.

2.5.1.2 Griffith theory.

The breakthrough came in 1920 when Griffith pioneered the concept that for a crack to propagate the energy in the system would reduce, i.e. energy would be consumed in the creation of new surfaces. Thus, the energy released when the crack advanced, came from the stored strain energy in the surrounding material plus any work done by the loading medium. If this amount of energy is insufficient to balance the energy used to create the new surfaces and other deformation mechanisms, the crack will not advance. In many materials, damage mechanisms are stimulated by the high stress gradients at the crack tip, and these are often enough to balance the energies. In metallic materials this is often the case, where dislocation movements can absorb significant amounts of energy.

Griffith primarily considered brittle materials, where the effectiveness of such mechanisms are greatly reduced. Thus, the assumption can be made that all energy in the system was converted into the new fracture surfaces. Consequently, he showed that the change in stored energy of a loaded plate of unit thickness, caused by the introduction of a crack of length 2c was:

$$U = -\frac{\sigma^2 \pi c^2}{E}$$

where:

σ=applied stress.

E=Young's modulus.

The other constituent of the total energy is that required to create the new surface area, which is positive and has a value of $4c\gamma$, where γ is the surface energy. The

dependence of these two factors on the crack length (Figure 2-15), shows that only cracks of a length $<c_*$ will grow spontaneously.

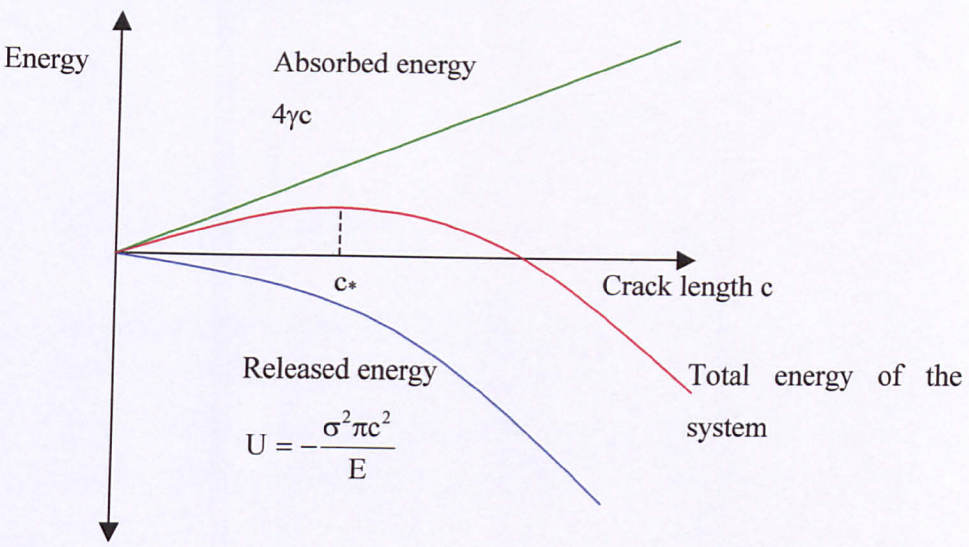

Figure 2-15 Energy vs. crack length for a crack in a brittle material.

The critical length was found by differentiating the total energy with respect to crack length and equating it to zero, hence:

$$c_* = \frac{2\gamma E}{\sigma^2 \pi}$$

In the late 1940's this approach was further evolved by Irwin to apply to tougher materials. He modified the 2γ term to encompass other contributions to the energy absorbed by the advancing crack tip. Thus, for a given applied stress and pre existing crack size, an expression was obtained for the strain energy release rate G.

$$G = \frac{\sigma^2 \pi c}{E}$$

In the same manner as before, for fracture to occur a critical value of G must be exceeded. This critical value is the total energy absorbed per unit crack surface area.

Subsequent further research by Irwin through the 1950's led to the development of the stress intensity factor, K. This material parameter allowed a link between energy and stress field approaches to be established.

$$K = Y\sigma\sqrt{\pi c}$$

Where Y is a geometric factor.

This expression couples the effects of the applied load and the pre existing crack size, with the relative weighting these parameters have in determining G. Hence, this expression characterises the stress field around the crack tip. Again a critical value may be identified which corresponds to the associated critical value of G.

$$K_c = Y\sigma_*\sqrt{\pi c} = \sqrt{EG_c} \qquad \text{for plane stress conditions}$$

$$= \sqrt{\frac{EG_c}{(1-\nu^2)}} \qquad \text{for plane strain conditions}$$

This value is referred to as the fracture toughness of a material.

2.5.2 Modes of crack opening.

Three modes of crack opening exist, mode I tension, mode II shear and mode III tearing (Figure 2-16). All crack growth may be expressed as one or combinations of these modes.

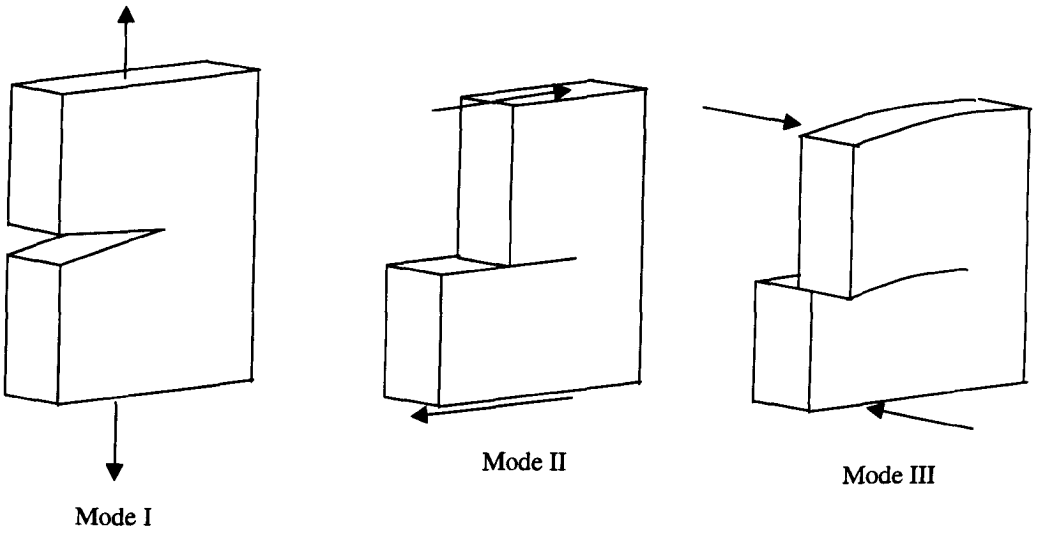

Figure 2-16 Crack growth modes.

2.5.3 Are these theories appropriate for composite materials?

Considerable research has been conducted by establishments to asses the suitability of simple fracture mechanics to composite materials. Principally the bulk of this has focused on the fracture mechanics of composites in the fibre direction. It has been shown that the compliance relationship for a fibre reinforced material in the fibre direction is significantly different to an isotropic elastic continuum. However, it was found that simple corrections may be used to allow for this. Barnby and Spencer [74] addresses this problem in the 1970's. They conducted tests upon glass fibre composites in which they grew cracks transverse to the fibres. They used numerical techniques to construct a K-calibration curve. The K-calibration curve is essentially related to the elastic strain energy content of a body which was measured by compliance methods, or as here with stress analysis methods. The conclusion of this work was that the appropriate K-calibration curve for a composite specimen must be used rather than one derived for an isotropic material. Thus, it is important to repeat this procedure when determining K_c for a composite.

Similar research has also proposed the use of various correction factors to account for the crack growth in composites. The problems associated with crack growth transverse to the fibre are illustrated in figure 2-17. Here it can be seen that the interference of the

fibres to crack growth is significant, when the crack grows perpendicular to the fibres. In the second schematic the crack is growing parallel to the fibres, thus, the interference of the fibres on the crack growth is greatly reduced. In this situation, for simplicity, composite materials may be regarded as being transversely isotropic.

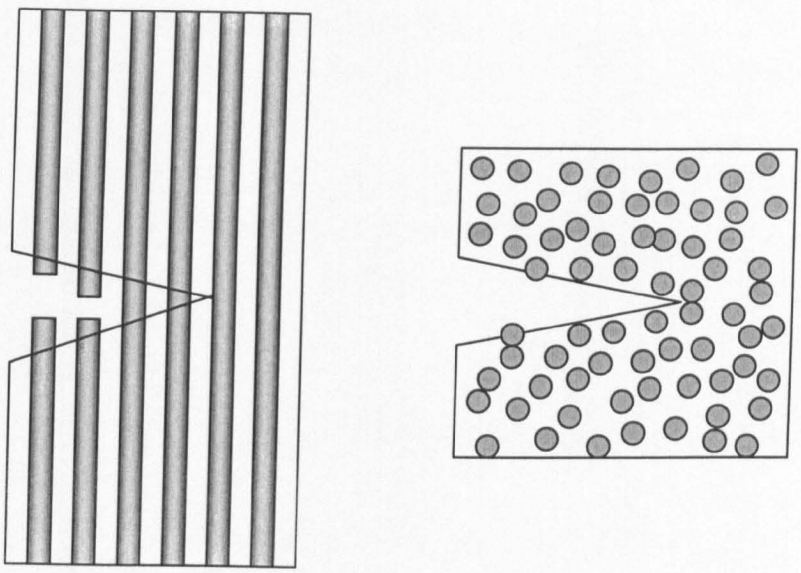

Figure 2-17 Schematic of crack opening types in unidirectional composites.

Notwithstanding the above conditions where it can be seen that we may relate simple fracture mechanics to composite materials, it is prudent to consider the various mechanisms that are present in composite systems. It is not surprising that the dominant mechanism is not the same for all composites, and it may be difficult to determine which is the dominant mechanism in a specific system. This dominant mechanism will be not only a function of the materials but also the loading and environmental conditions.

The fracture process of a composite material involves both macroscopic as well as microscopic failure mechanisms. Some of these mechanisms will be dealt with in more detail later. However, all these mechanisms are important to enhance the energy dissipation in composite materials. On the microscopic level, the actual failure modes occurring within the crack tip, damage zone can appear in the form of fibre pull-out, matrix micro-cracking, fibre-matrix interfacial failure, fibre breakage. On the macroscopic level, the major failure modes are delamination, matrix cracking along

the fibre direction in the individual plies, and failure of individual plies. The relative contribution of each failure mode during fracture will depend upon a large number of parameters.

An overview of the various modes of fracture in composite laminates was published by Dharan in 1978. Figure 2-18 schematically illustrates the various mechanisms and processes in composite fracture. The following list is a description of the numbers in the diagram:

1. This region shows the characteristic failure of brittle fibres.
2. Fibre pull-out occurs when the fibre fails within the matrix.
3. Debonding between the fibre and the matrix indicative of a weak interface.
4. Matrix microcracking.
5. Ductile failure of the fibre.
6. Fibre fracture at a flaw and the associated plastic strain distribution (or craze) in the matrix.
7. This area indicates the plastic strain distribution at the tip of the main crack.
8. This area corresponds to the plastic shear strain distribution.
9. Longitudinal matrix or interfacial crack caused by the influence of the σ_x stress distribution.
10. The dotted outline shows a possible zone of interlaminar shear failure between the ply shown and an adjacent off-axis lamina.

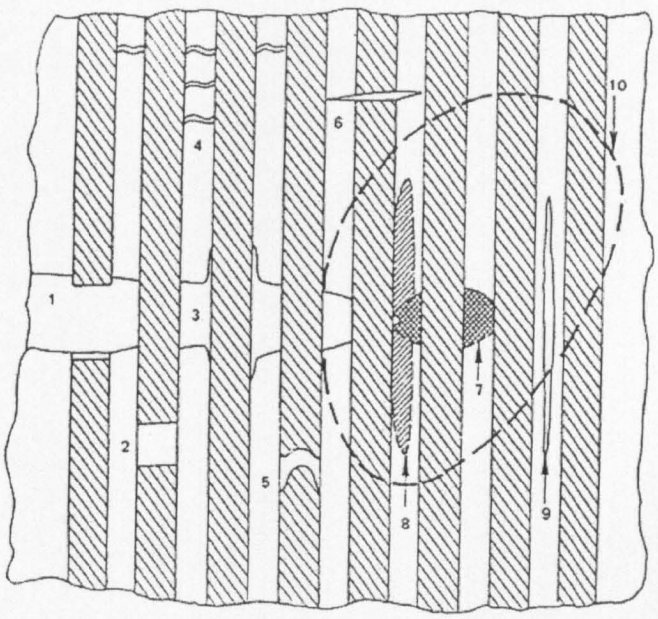

Figure 2-18 Schematic representation of possible failure mode in fibre reinforced composites [92].

2.5.4 Evaluation of G_C and K_C

A wide variety of test methods exist to experimentally determine these parameters. The project was only concerned with those that are suitable for testing the transverse toughness of composites.

2.5.4.1 ASTM Standards

2.5.4.1.1 E399

This thesis is focused solely on Mode I opening (tension). It is relatively straight forward to experimentally determine G_{IC} and K_{IC} for isotropic materials. ASTM standards exist, principally E399 [14], which covers the spectrum of testing required to determine these properties. Although the standard is written only for isotropic

materials, as previously discussed, it may, in theory be used for the determination of the transverse fracture toughness, if the material is as expected transversely isotropic.

Two types of specimen architecture exist in the standard: Compact tension (CT) and single edge notch beam (SENB). These specimens are illustrated in figure 2-19. The SENB specimens are more practical for composite test since it is very simple to manufacture. These tests are not readily used for composites since other, more accurate tests have already been developed for composite.

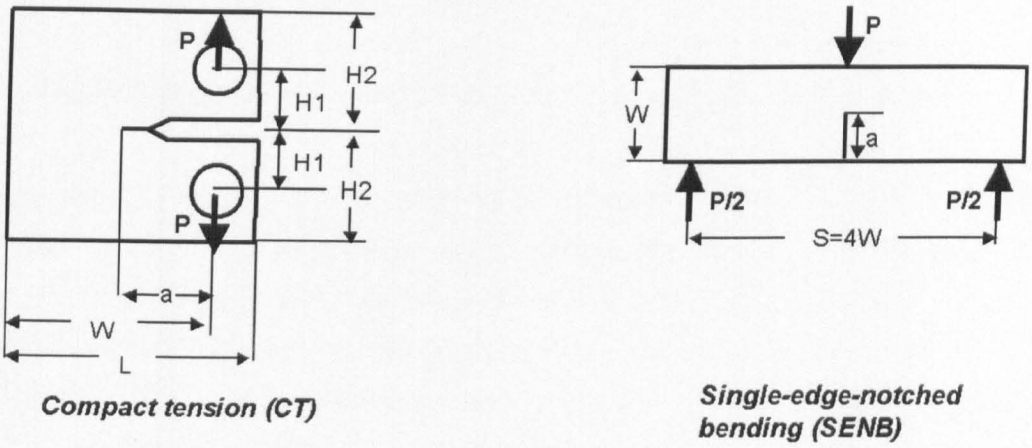

Figure 2-19 ASTM E399 Specimen geometries.

2.5.4.1.2 D5528

Standards [50] also exist for the determination of the Mode I Fracture toughness of composites. This ASTM standard uses a double cantilever beam (DCB) specimen cut from laminates fabricated with a pre-crack introduced using a release agent between the centre ply's, e.g. release film. The specimens then have loading blocks or hinges attached to them (Figure 2-20).

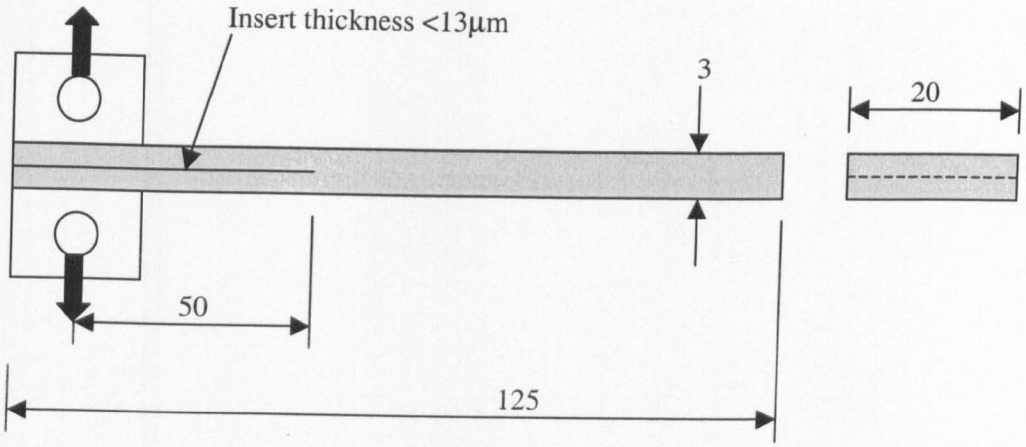

Figure 2-20 DCB specimen, minimum dimensions shown. Dimensions in mm

The results of the tests may be processed in a number of ways. The most frequently used is the modified beam theory and the compliance calibration method. Research conducted internally [51] has concluded that the modified beam theory is too simplistic, principally not enough corrections are made to counter the bending in the specimen. The preferred method is to use a compliance calibration to determine G_{IC}. The point at which the crack initiates should be taken as visual, as opposed to other methods quoted in the standard which rely on the force/displacement chart or the maximum load achieved. The results of a round-robin test programme presented in the standard show that with this method, typically, C_v' of 15% are expected with values of G_{IC} ranging from 1.1 to 1.7KJ/m^2 for AS4/PEEK.

2.5.4.1.3 E1922

This is a standard designed to for testing the translaminar fracture toughness of laminated composite panels. The specimen (Figure 2-21)is a simple panel of material into which a notch is introduced. The specimens size is controlled by the thickness of the panel. The method was developed from a series test programmes and allows the determination of K_{IC} for laminates with various fibre orientations., and multiple layers.

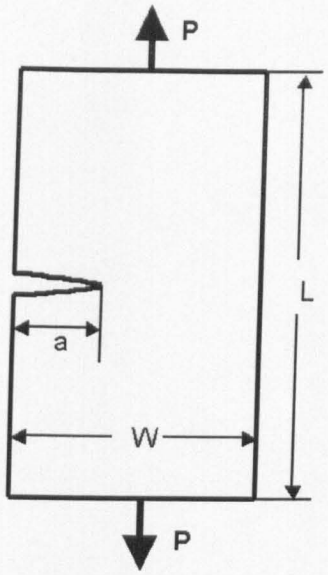

Figure 2-21 ASTM E1922 Single edge notched tension specimen.

2.5.4.2 Circular specimens.

Kunmar [52] developed a test method based upon a circular specimen geometry (Figure 2-22). He found that the limitation of the DCB specimen was that the edges of the specimen were exposed to modes II &III loading. Thus, only a small proportion of the crack front which was away from the edges was exposed to pure mode I, resulting in non uniform crack growth.

Other advantages of this method included the ability to test angle-ply laminates. The analysis became more complex since the crack front would grow elliptically, with its major axis running along fibre at the interface.

Tests were conducted using this method and the DCB specimen on GFRP laminates. The DCB specimens yielded 445 J/m^2 while the circular test method resulted in values of 264 J/m^2. No mention was made of variance, however it is reasonable to conclude that the embedded crack methods results are more representative of the material property due to the pure loading. The magnitude of the difference in results ~40% does however seem high.

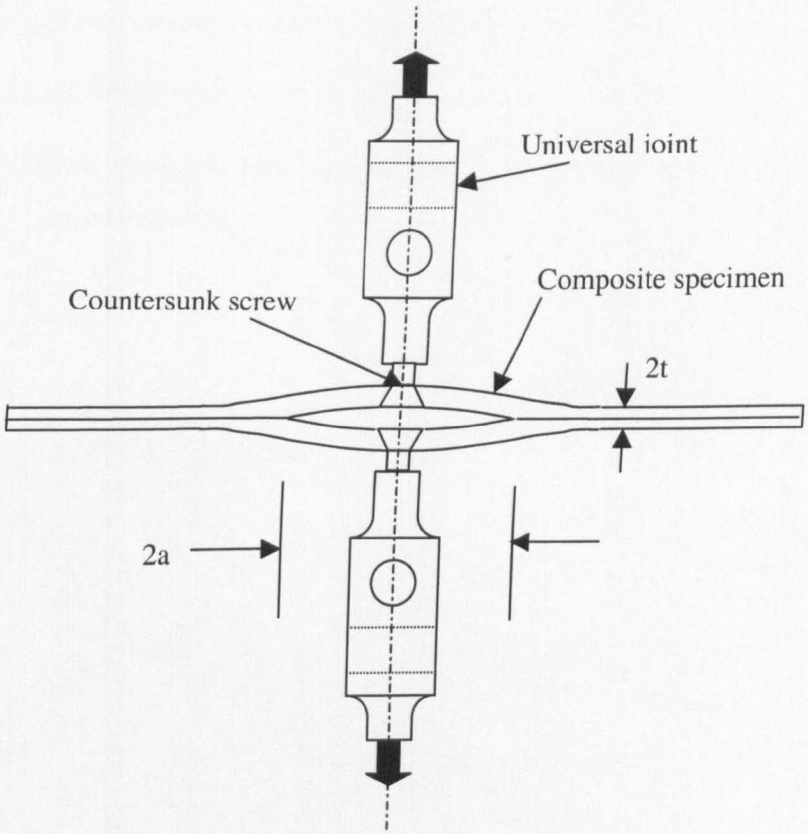

Figure 2-22 Circular fracture toughness specimen.

2.5.5 Compliance calibration.

The compliance calibration technique has been mentioned already with regards to the ASTM DCB specimen, the theory can however be applied to any specimen geometry.

Compliance is defined as the amount of displacement per unit of applied force, the reciprocal of stiffness. Bubsey [54] described a compliance coefficient as a particular kind of flexibility influence coefficient, A ratio of displacement to force that represents the linear elastic static response of a body to the action of a pair of equal and opposite collinear forces.

The method is straightforward. The stiffness of a sample, or a series of samples with progressively increasing crack length are measured. A plot of the compliance versus the crack length can be constructed and hence the relationship of $\frac{dc}{da}$ may be determined. From this plot the strain energy release rate may be calculated using the following expression:

$$G_{IC} = \frac{P^2}{2\ b}\left(\frac{dc}{da}\right)$$

Where: P=Load

b= specimen width.

The compliance method is not valid for orthotropic materials, if the crack does not advance along the original crack direction. This is because this technique is based upon the principles of LEFM, which assumes the crack will continue to grow along the original direction.

The method has proved itself as reliable. The advantages of this method were outlined by Parhizgar [55].

I. Only one specimen is needed for the determination of the fracture toughness.
II. By defining toughness in terms of load and compliance rather than load and crack length, it is not necessary to introduce a plasticity correction. The damage zone is automatically accounted for by the compliance measurements, which is associated with an effective crack length rather than the actual crack length.
III. The results can easily be checked by repeating the above steps for different crack lengths.

2.5.6 Effect of Matrix toughness on transverse toughness.

Clearly the matrix plays a very important role in the transverse fracture properties of composite materials. Some of the most comprehensive work on this subject was

conducted by Bradley at Texas A&M university. He has published some 7 papers on the subject, these were summarised for a book chapter [75]. The studies conducted covered various aspects of crack growth.

This research was centered around analysis of transverse crack growth in composites, both mode I and II. The work focused around in-situ study using electron microscopy techniques. In mode I experiments, it was predicted that two factors would dominate the fracture behaviour, the resin ductility and the interfacial bonding strength. A series of specimens with increasing resin fracture toughness were examined. The fibre type was not however kept constant.

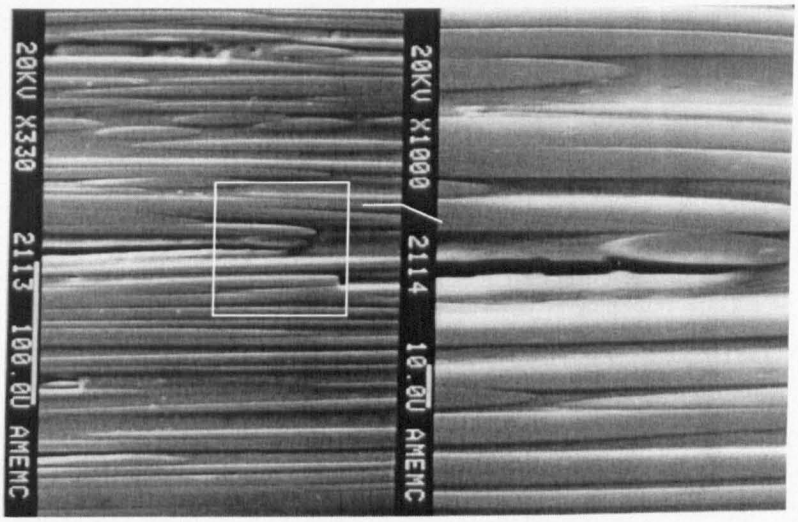

Figure 2-23 Crack growth in AS4/3502 [75].

Figure 2-23 represents the sample with the lowest fracture toughness (G_{IC}=0.19 kJm^{-2}) . It was observed that the deformation zone around the crack tip is very small. The crack path was also found to be along the fibre interface rather than through the matrix. Thus, in system crack growth is primarily associated with the interfacial bond strength. Bradley confirmed these findings with post-mortem fractography.

In the next figure, (Figure 2-24), matrix cracking is more evident. This resin was an epoxy, but without any rubber additions. It was noted that the deformation extends some distance into the material ahead of the crack tip. It is however confined to the resin rich area between the fibres. The toughness of the composite is higher

(G_{IC}=0.335 kJm^{-2}). It was concluded that the crack advances using a combination of void formation in the matrix and interfacial de-bonding.

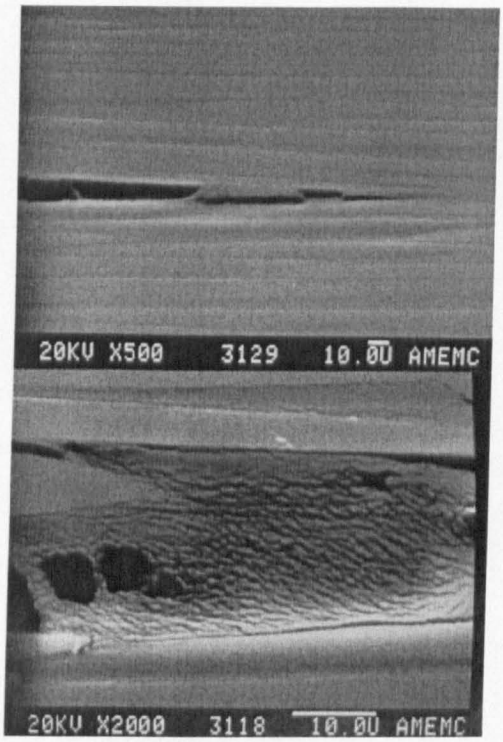

Figure 2-24 Crack growth in Hexcel T6T145/F155 (without rubber additions) [75].

Figure 2-25 shows a T300/BP907 composite, the fracture toughness G_{IC}=0.38 kJm^{-2} is only marginally higher than the toughness of the neat resin (G_{IC}=0.325 kJm^{-2}). The failure in this composite was again primarily attributed to interfacial failure. The reason proposed for the increase in toughness over the neat resin were:

1. With neat resin, the failure surface was relatively smooth. The failure surface in the composite is far rougher, by simple calculation some 57% more fracture surface area in present in the failed composites.
2. A degree on fibre bridging and pull-out is also evident. This has the effect of dissipating additional energy.
3. Finite element analysis by Corteto, Bradley and Hanriksen [76] concluded that the stress field ahead of the crack tip in an orthotropic material decays far more slowly than in an isotropic medium. Thus, if the stresses are more evenly

distributed ahead of the crack tip then the stress at the crack tip will be reduced, increasing the toughness.

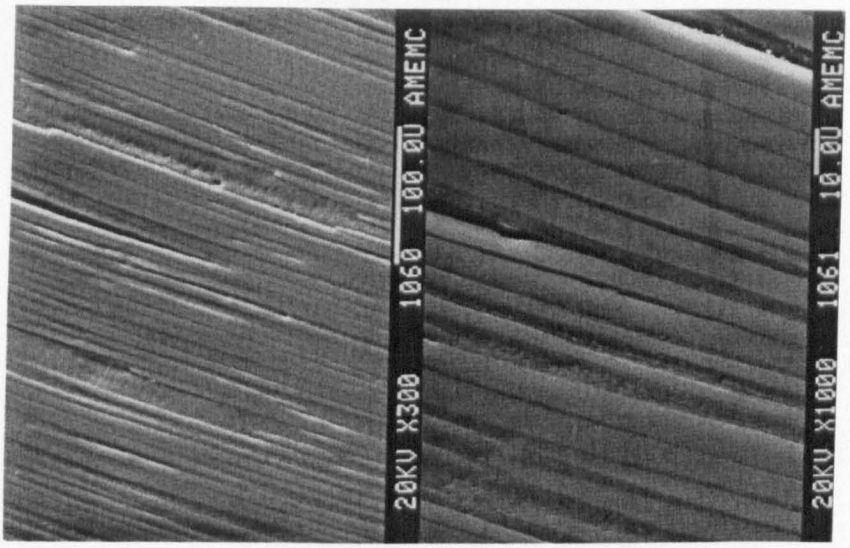

Figure 2-25 Crack growth in T300/BP907 [75].

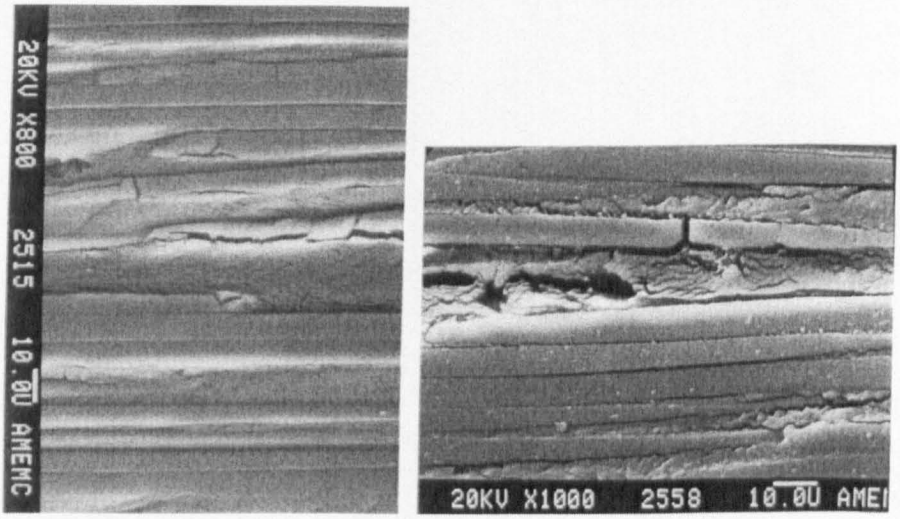

Figure 2-26Crack growth in C6000/HX205 [75].

In the next sample (Figure 2-26), a greater degree of matrix yielding was observed. Some interfacial bonding was also present. The improved bonding in this system allows crack growth within the matrix to occur more readily. This means that the enhanced toughness of the resin is exploited. The fracture toughness of this specimen was G_{IC}=0.455 kJm^{-2}.

The toughness of the resin is further increased, in this case by increasing the cross-link density and by including rubber particles (Figure 2-27). The failure mechanisms is still a mixture of fibre de-bonding and matrix cracking. The amount of a matrix cracking is increased and in this specimen, very fine micro cracks were observed. The toughness of this composite was measured as G_{IC}=0.55 kJm^{-2}.

Finally if the toughness of the resin is increased drastically, thus the toughness of the composite is now G_{IC}=2.0 kJm^{-2}, matrix yielding effects are very prominent (Figure 2-28). The deformation zone in this sample is much larger than in the other specimens. The damage extends further than the resin rich layer between the plies to the resin beyond the plies. Thus, the crack tip blunting effect is significant. In this sample there was virtually no interfacial de-bonding.

In conclusion, transverse fracture toughness can be closely linked to the toughness of the matrix combined with the interfacial strength of the fibre/matrix. A logical conclusion was to plot the composite fracture toughness vs. the fracture toughness of the resin. Figure 2-29 shows a close correlation between the properties. A direct correlation was drawn between these two parameters. As a rule they concluded that the composites toughness is roughly 40% of the resins toughness.

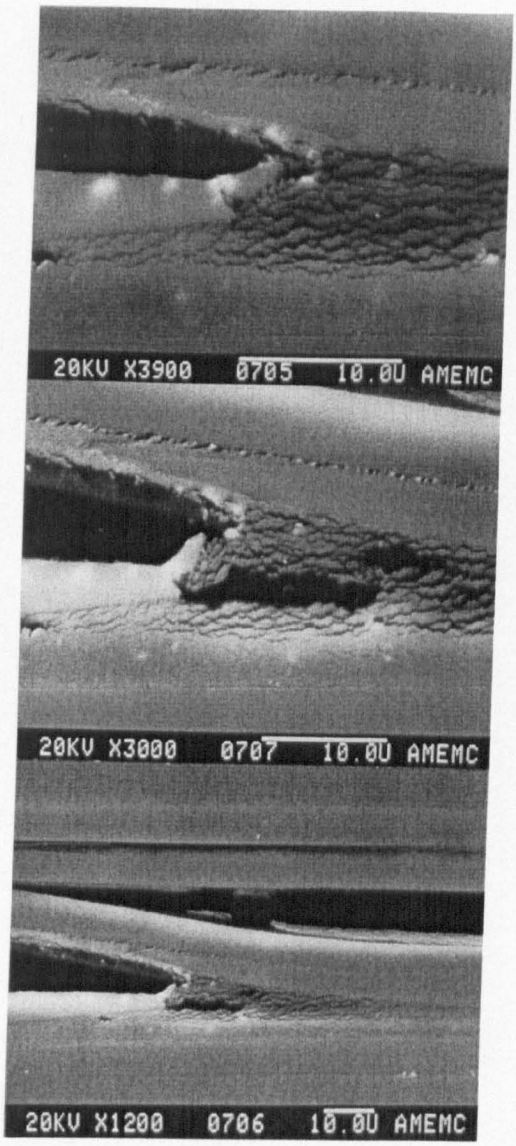

Figure 2-27 Crack growth in T6T145/F155 [75].

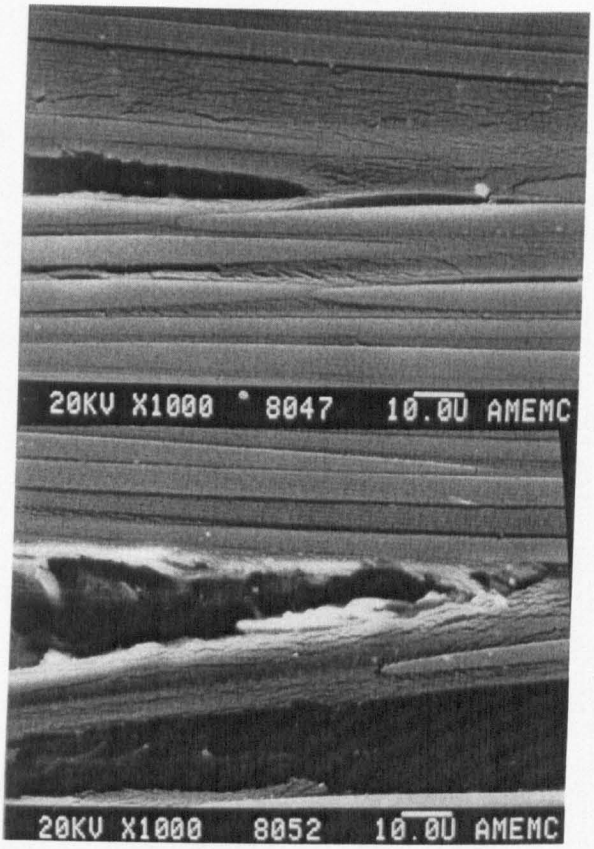

Figure 2-28 Crack growth in T6T145/F185 9 [75].

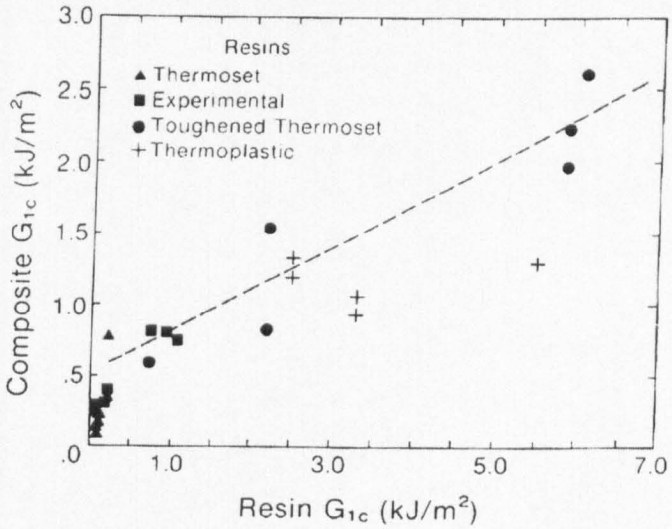

Figure 2-29 Composite Strain energy release rate vs. Resin strain energy release rate [75].

2.6 Lifetime Prediction

Virtually all industries are controlled by regulatory governing bodies. The function of these is principally orientated to towards safety. To this end these governing bodies will require equipment to be fully tested and guaranteed before a device may be ratified for use within the industry. In cases where it is not possible to test a components full lifetime, it is usually possible to convince the authority the device will be safe for a given lifespan if a suitable prediction has been presented.

To predict the life of a component, several different approaches may be used. These are usually governed by the expected failure mechanism. For the purposes of this thesis the materials are regarded as brittle, thus it is reasonable to assume that failure will occur from crack propagation from an inherent flaw. This crack propagation may be initiated by the material properties (K_{IC}) changing over the lifespan of the component. A possible mechanism for this would be influence by the service environment. An example of this would be stress corrosion when GFRP is exposed to aqueous environment [56]. Alternatively, it is possible that a crack will grow very slowly, not effectively imparing the performance of the component, until a critical crack length is reached, where the component will fail by fast fracture.

In both cases the dominant factors assessing the failure of the component is the inherent flaw size. The critical size of this defect will be determined by a number of factors, principally the stress level and distribution. Other factors such as the time period, any fatigue condition or viscoelastic effects may also play a role in the calculation of the defect size, however so long a suitable test programme may be conducted to establish these effects, simple analysis may be used to predict the lifetime of a component. Weibul [84] developed ideas that related the probability of a component failing (F) to the probability of finding a defect of a given size. In essence he managed to relate the volume of a component to the probability of finding a defect of a specified size in it.

$$F = 1 - e^{\left[-\left(\frac{V}{V_0}\right)\right]}$$

Where V=volume

V_0=volume per defect.

Thus, this expression may be used if enough information is known about the defects, i. e. how time, stress, temperature effect the calculated critical defect size.

With particular reference to composites, methods have been developed using damage mechanics. Rowatt [89] has developed models predicting life of components subjected to fatigue loading using the theory of damage evolution on composite laminates. Essentially the model is base upon a strength and stiffness reduction, which is continuously calculated with the number of loading cycles. Thus, chains of loading sequences may be analysed with progressive damage accumulation taking place. Experimental work was conducted to correlated the number of cycles and the stress level to the prediction of the occurrence of the critical cycle. Thus, life prediction may be made on these materials if the service conditions are known.

2.7 Existing Flywheel Programmes

The design and development of composite flywheel have been considered for many decades now. W.E. Dick [3] was perhaps one of the first to outline the benefits and the practical advantages of the use of composites for flywheels. Principally he illustrated the superior energy density capability of the composite rotor.

These ideas along with others led to considerable research during the late 20th century. Projects involving NASA and a number of US based institutions were developing flywheels for transportation activities. The most publicised research in this field was Chrysler development of a gas turbine powered racing car, called Patriot, which utilised a large flywheel to store energy (Figure 2-30). It was found during testing and development that the gyroscopic precessional forces that resulted as the car circulated the test track played havoc with the cars handling, the car behaved exceptionally well in left handed corners, but terribly in right handed ones. Chrysler engineers ultimately concluded that in order to complete cancel out the effects of the precessional forces, 6 flywheels were required. 2 along each of the 3 principal axis of the car, and these

would have to spin in opposite directions. This arrangement was deemed too complex. The project resulted in over 60 patents for Chrysler covering the integration of various aspects of energy handling in automobiles. Although commercial vehicles do not require the same handling limits as racing cars, the same restrictions apply. Thus, the possibility of larger scale industrial units were considered.

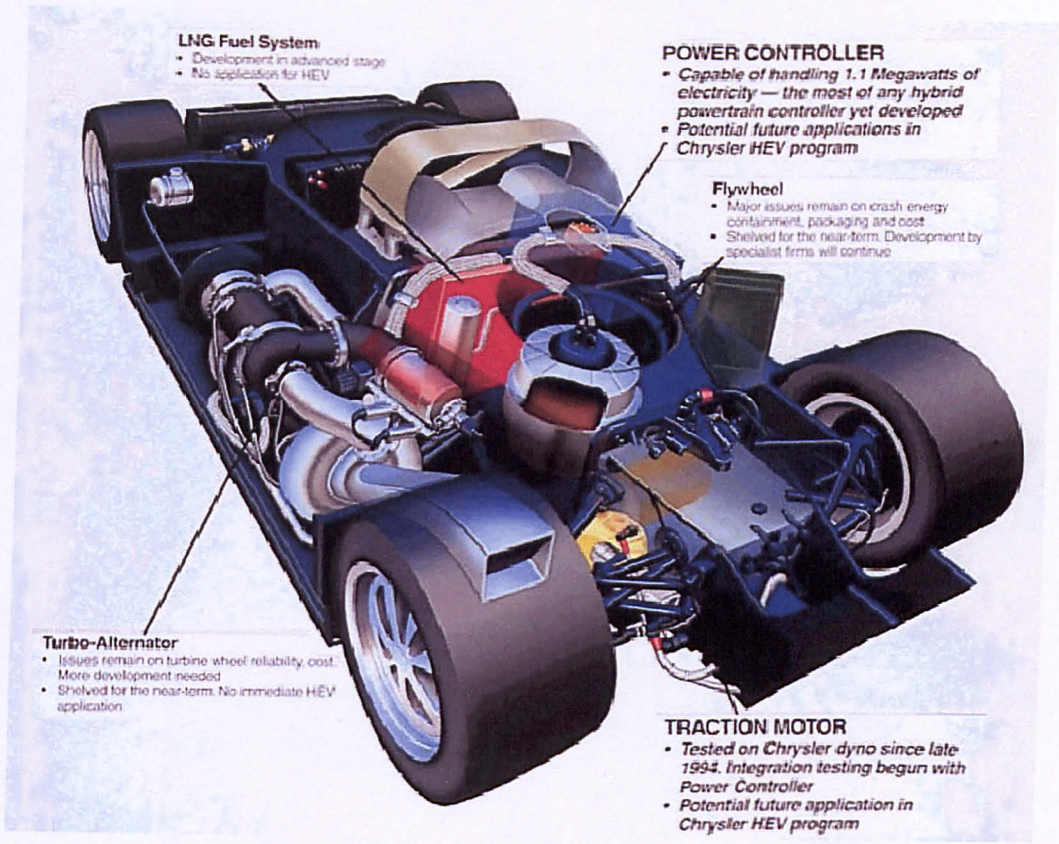

Figure 2-30 Schematic of Patriot Prototype.

In 1992 Ries and Kirk [4] published a proposal covering the design and manufacture of a flywheel energy store. The novel aspect of this work was the idea of using layers of different composite, manufactured separately and using interference fitting to build in significant compressive pre-stresses to the rotor. The advantage of the in-built pre-stresses was the ability to extract a greater maximum speed of the rotor, without changing the fibre used. The rotor was constructed entirely from carbon fibre in an epoxy matrix.

Perhaps the most eminent work on flywheels in recent years is work conducted by Bakis and his colleagues. They have researched many aspects of flywheel design and development. They have published many papers which broadly cover all aspects of flywheel design [93]. Principally the disk design has been investigated. To evaluate the stresses in the rotor, mathematical modelling was utilised. It was found that radial failure was a concern. As a result they proposed the following solutions to reduce the radial stress in a spinning disc:

- Use one or more denser and/or less stiff materials in the inner layers to provide outward pressure as the speed increases.
- Use press fit multiple rings to superimpose a compressive radial stress field in the outer layers.
- Use compliant radial inter-layers to relive radial stress transfer from one ring to another.

Bakis investigated three types of flywheel design. Rotor Y is a multi-ring interference fitted flywheel, while rotors Z1 and Z2 are simple monolithic composite rotors using elastomeric materials for the matrices. These were manufactured and tested. The two monolithic rotor designs illustrated a simple safe flywheel design. These two rotors performed well with theoretical maximum speeds of 6457 $rads^{-1}$ for rotor Z1 and 7969 $rads^{-1}$ for Z2. The rotor could not be tested to the maximum speed because of limitations with the testing facilities. Rotor Y admirably demonstrated the radial stress management concepts outlined. It had a theoretical maximum speed of 10800 $rads^{-1}$.

Other programmes have built upon these results however, to date only the Urenco design utilises a cylinder design rather than a disc as its principal failure management mode (Figure 1-2). Although this does pose a new set of difficulties, as previously highlighted, with the axial stress levels. The effects of the axial stresses in the rotor are the concern of this thesis.

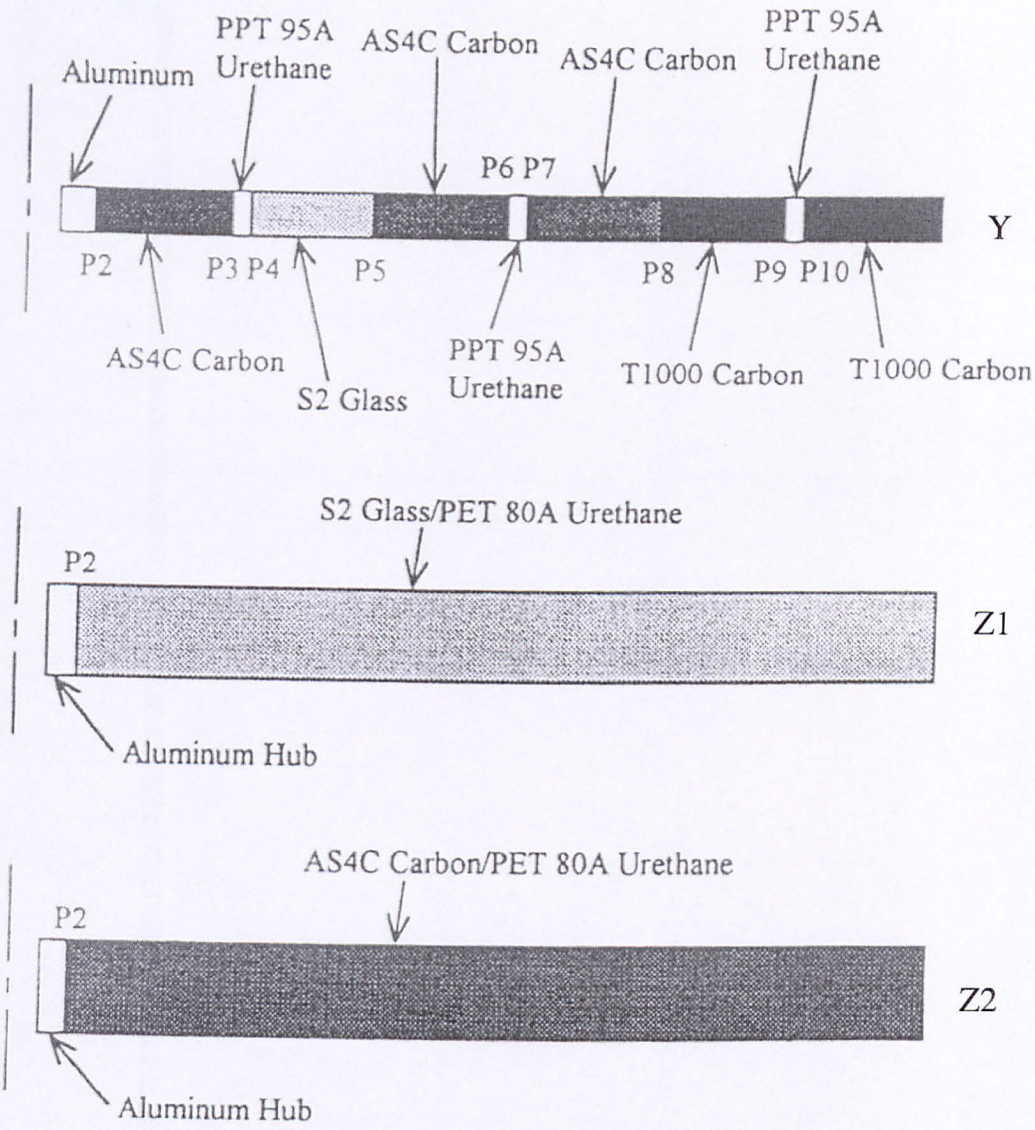

Figure 2-31 Structure of Bakis Flywheels [93].

2.8 Other Factors

There are further considerations that must be addressed in order to build a complete picture of the flywheel research. For the purposes of this study the majority of these factors have been assumed to have little or no effect on the life of the rotor.

2.8.1 Effect of vacuum

When composites are exposed to high vacuum conditions, most commonly in pressure vessels and in space applications, the most pronounced effect is material out gassing. This out gassing is commonly very rapid and leads to dimensional and mass changes in the component. Kwang [53] found that these mass changes are of the order of 0.3%, with extended thermal cycling(-70°C to 100°C) this figure rose to in excess of 1.2%.

Typically the out gassed products are moisture and other low molecular weight volatiles, such as solvents. Figure 2-32 illustrates the major out gassed products, as expected water is the most prolific while nitrogen and solvents are also present.

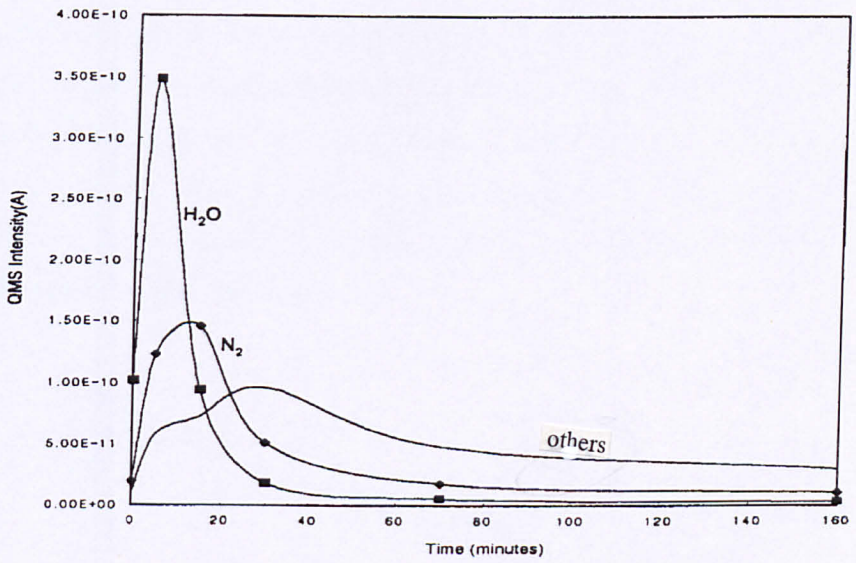

Figure 2-32 Major out gassed products of graphite/epoxy [53]

More specifically Shirey and Bakis [77] have studied the effects directly on material intended for flywheel use. The tests they conducted exposed material, both GFRP and CFRP to vacuum of 10-30 mtorr for a minimum of 85 days. They were unable to ascertain any significant mass change or dimensional change. The bulk of the testing that was then completed involved fatigue tests in the fibre direction. However, the bulk properties were also measured. In this case the vacuum conditioning was found to have no major influence on either the modulus or the ultimate tensile strength. This

in contrast to the earlier work which illustrates significant property change. This must be attributed to the thermal cycling rather than the vacuum.

2.8.2 Temperature effects [82,83].

There are considerable temperature effects in composites. Broadly these concern the resin system. As the temperature of a composite is increased the resin will soften. Thus, those parameters that are most readily affected by the behaviour of the resin will be most susceptible to temperature variations. It has already been shown that the transverse properties are highly resin dependant, both in terms of elastic properties, strength and fracture behaviour.

In GFRP, at elevated temperatures, the primary degradation process is oxidation. The rate of oxidation obviously increases with the amount of oxygen present. It is said that the fibre matrix interface acts as the transport for this process. Thus, loss of interfacial strength results. This is most obviously characterised by discolouration of the material. In figure 2-33 the dependence of tensile strength on temperature of unidirectional GFRP can be seen.

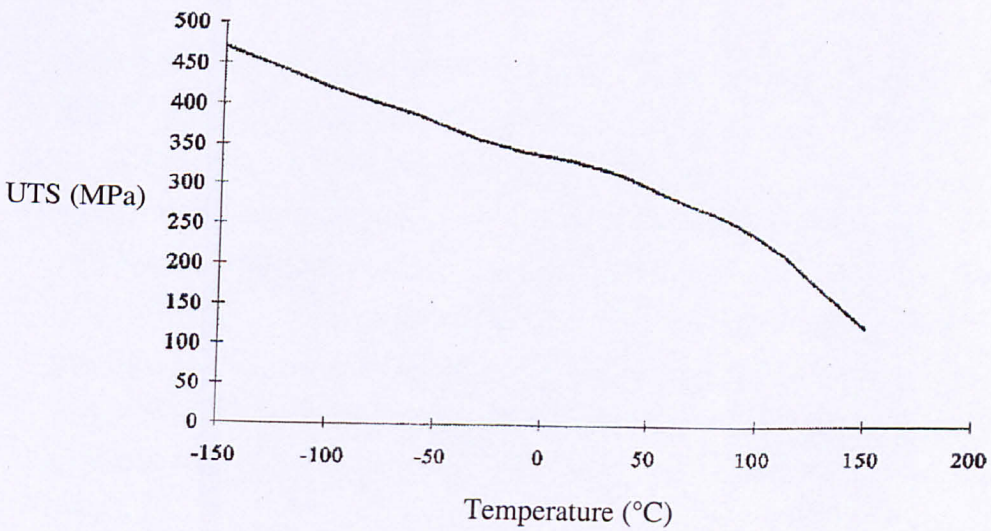

Figure 2-33 Tensile strength vs. Temperature [78].

Ilcewicz [80] researched the effects of temperature on unidirectional CFRP composites. He used IM7/8551-7 material and recorded stiffness, strength and toughness properties (Table 2-6). The longitudinal modulus was also measured, however, contrary to effects noted by Sims, no effect was seen on this property. Again, as with the GFRP, those properties most directly affected by temperature are those which are highly resin dependant.

Table 2-6 Temperature effects on unidirectional CFRP.

Temperature (°C)	E_2 (GPa)	G_{12} (GPa)	σ_{UTTS} (MPa)	G_{IC} (kJm^{-2})
-60	9.2	5.2	84.4	0.496
20	-	-	70.3	0.513
80	6.7	4.0	60.9	0.462

2.8.3 Fatigue.

It has been stated that for simplification purposes, the rotor speed does not cycle during its lifetime. In reality the rotor speed will change, thus, the rotor will experience some fatigue loading.

Neat glass and carbon fibres have excellent fatigue resistance. Fibres which have a higher modulus will exhibit improved fatigue resistance in the fibre direction, for a given stress level and volume of fibres. In these cases, the induced strain in the resin will be lower, hence, the rate of damage occurring at the interface will be lower. In unidirectional composites, glass fibres generally exceed the strain limits of the matrix, with carbon fibres the maximum strain falls significantly below the strain limit of the resin. This is the case even when the stresses are approaching the tensile strength of the material. Thus, in GFRP composites failure from fatigue will occur as a result of progressive damage in the material. In CFRP the material will fail as per static failure tests.

Sims [81] produced data which combined fatigue and temperature tests (Figure 2-34). It was found that GFRP laminates could withstand higher fatigue loads when the

temperature was reduced. With reference to the flywheel rotor, the difference in material performance between room temperature and +60°C is noticeable. For this thesis this has been neglected, but is worthy of a mention.

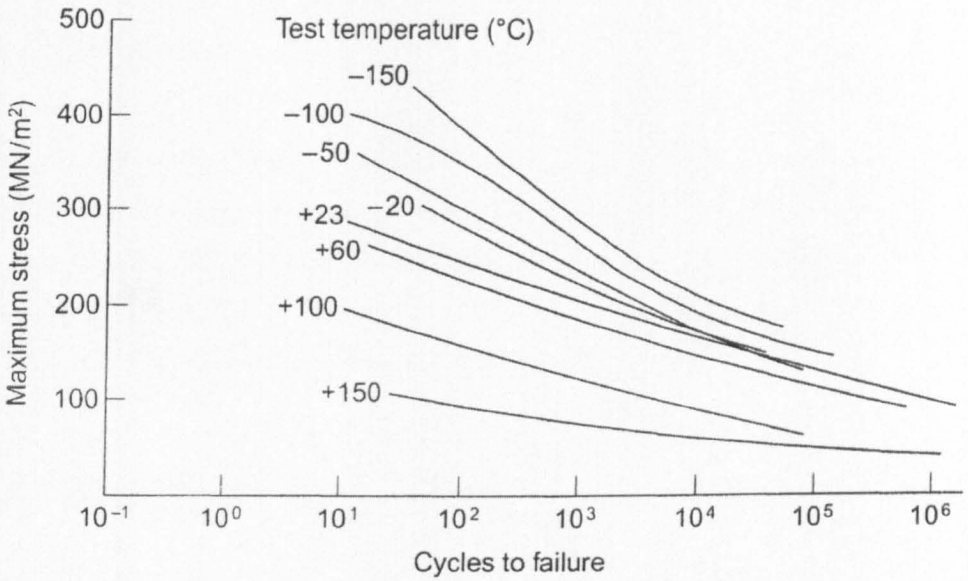

Figure 2-34 S-N curve for GFRP at different temperatures [81].

3 MATERIALS AND MANUFACTURE OF THE URENCO FLYWHEEL.

3.1 Introduction

This section covers the raw materials for the Urenco flywheel rotor along with a description of the manufacturing route. The quality of the resulting composite is analyzed with particular emphasis on void content, size and distribution. The volume fraction of the material is also determined. Also explored is the manner in which specimens were extracted from the flywheel rotor and prepared.

3.2 Material Supply

The rotor materials were not constant throughout the project. Approximately a year into the research Urenco switched to a new glass fibre manufacturer. This decision was based upon close "in house" analysis of the materials properties and the quality of supply. Concerns had also been raised following our research, since by this time, some work had already been completed with regard to determining the volume fraction (Table 3-2) of the composites. It was observed that the fibre diameter of the original glass fibre was extremely variable (Figure 3-1). The fibre diameters ranged from 6μm to 25μm, with an average of 18μm.

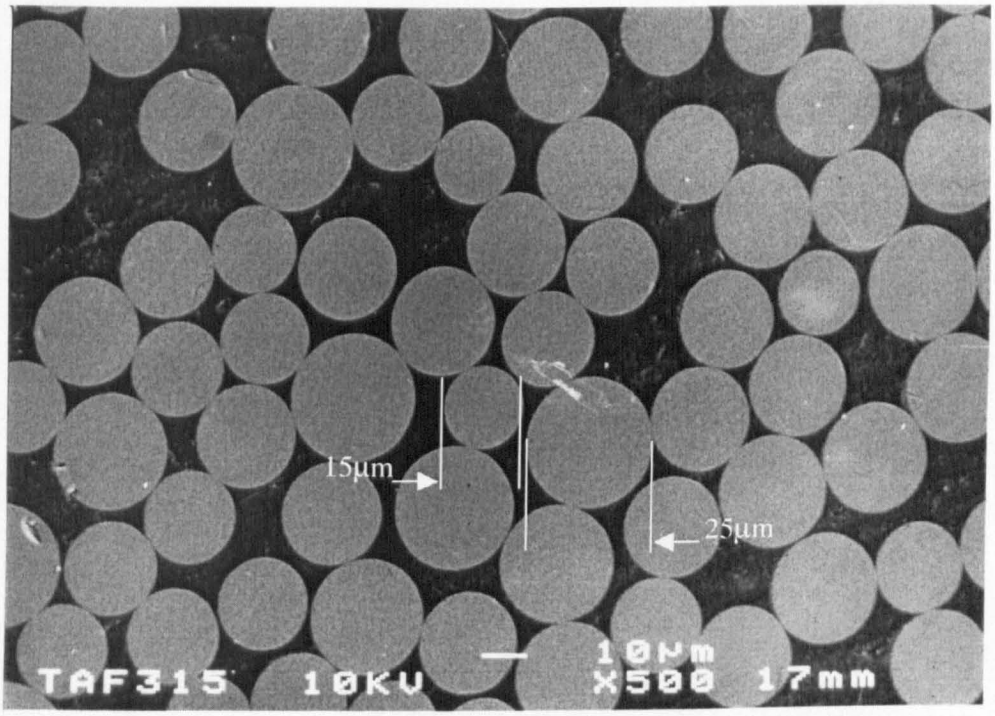

Figure 3-1 SEM of original E-glass fibre

3.3 Raw materials

The flywheel rotor, as stated is a GFRP/CFRP hybrid with an inner layer of GFRP containing additional NdFeB filler. The glass fibre is an E-glass fibre and the carbon fibre is T700 Pan-based intermediate modulus carbon fibre. The matrix is an epoxy based resin. The layer consisting of the GFRP with NdFeB filler has a fibre content of 45% by volume and a powder content of 20% by volume [61]. The middle GFRP layer has a volume fraction of approximately 65%. The outer CFRP has a slightly higher volume fraction, approximately 68%.

3.4 Manufacturing

3.4.1 Filament Winding.

The rotor is produced by the filament winding route. This method has been used for many years in various industries. Urenco [9] has considerable experience with this technique as a result of the production of centrifuges. The fibres are pulled through a resin bath under tension and then wound onto a former, known as the mandrel.

The rotor is wound at room temperature. The processing path first involves winding a single layer of GFRP onto the mandrel. The NdFeB powder is then introduced into the resin and a further 16 layers are then wound, resulting in a layer thickness of 8mm. The resin bath is then changed and the full thickness (46mm) of GFRP is wound. Upon completion of the GFRP layer the CFRP is wound. This layer is wound to a thickness of 25mm.

During the winding the winding angle is very carefully controlled and adjusted, but is always approximately 89°. Other manufacturing parameters that effect the final composite, such as fibre and roving tension are also continuously monitored and adjusted. Changes to process settings are dependant upon the material being wound and the radius. Once completed the mandrel and rotor are then transferred to the oven for curing.

3.4.2 Curing.

Since the rotor is such a thick composite, with a wall thickness of 80mm, the curing process is not straight-forward. With such a thick composite structure, the ability to predict and control the behaviour of the exothermic reaction upon curing, is critical.

The Urenco developed cure cycle controls the behaviour of the exotherm, very carefully (Figure 3-2). The rotor is first heated to 80°C, at which point resin gelation begins. The oven is then kept at a constant temperature for some time. Lastly the rotor is heated to 160° C and final curing takes place. Upon cooling, the mandrel shrinks more than the rotor, this allows easy removal of the rotor.

Figure 3-2 Rotor cure cycle

3.4.3 Post- Cure Processes.

The magnetic layer is then polarised using a large magnetic field. This is done in such a manner that patterns to produce the rotors magnetic bearing and motor generator are formed. The rotor is complete at this stage.

3.5 Material Characterisation.

Basic information such as volume fraction and void content on the materials is required for successful interpretation of the mechanical properties. This information is also crucial with regard to the lifetime prediction work, see later.

3.5.1 Optical specimens.

Pre-cut slices of rotor were supplied by Urenco. Typically these slices were "hoops" of material, 20-60mm thick. From these slices, very thin perpendicular cross sections

were produced to form the optical specimens (Figure 3-3). They were initially machined on the diamond mill (section 3.6) and ground down using wet and dry papers. The sequence of the papers was 800, 1000, 2000 and finally 4000 grit. Following this the specimens were polished using 5μm and 1μm diamond paste. Between every step of the preparation, the specimens were cleaned and checked under the microscope.

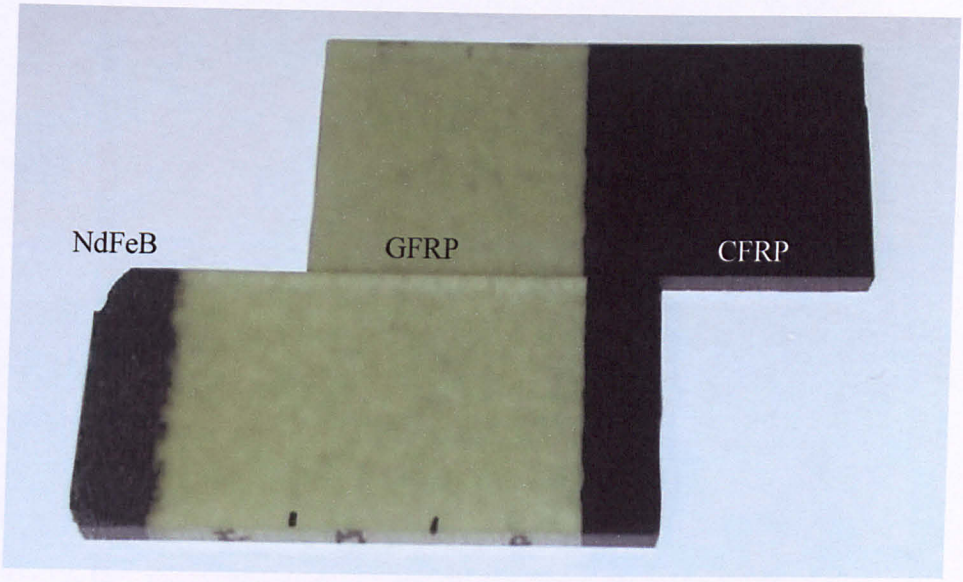

Figure 3-3 Example of optical specimens.

3.5.2 Volume fraction analysis

The volume fraction of the various layers of the rotor was determined using optical techniques. The system used involved a stereo microscope (Olympus BX60 maximum magnification x60) coupled to a PC with a digital imaging system. This allowed rapid production of micrographs needed for volume fraction evaluation.

Image Pro Plus [62] analysis processing software was then subsequently used, where it was possible to analyse the micrographs. The software was used to quantify the volume fraction of the composites, since for a unidirectional (UD) composite material the volume fraction is simply a ratio of the areas of fibre to matrix. The procedure involved randomly selecting a section of rotor in the desired region. An image was then created of this area. The image analysis software was then used to compare the

light and dark areas (Figure 3-1). This process was the most subjective step of the entire procedure, since it involved determining the boundary between fibre and matrix. However, once set, this was not altered for the duration of the analysis. Since the boundary is clear the results may considered as accurate. The sensitivity of the measurement to the setting is low since the boundaries were clearly defined

The consistency of the results were high (Table 3-2), as with any well processed composite. The volume fractions were high as expected with this type of UD composite and manufacturing route. The CFRP has the highest volume fraction. (v_f= 69%). In the GFRP layer the volume fraction was found to change with radial position. Although, this change was not significant (v_f=57.5 to %v_f= 61.5%) it has some influence on local mechanical properties.

The change of glass fibre manufacturer and subsequent refinement of the manufacturing process, did not have a pronounced effect on the volume fraction. However, it had improved the uniformity of the composite illustrated by the lower standard deviations. With the old glass fibre, standard deviations varied from 4.6 to 8.4%, while with the new fibre the values and range was smaller at 3.4 to 5%.

3.5.3 Radial and axial packing.

Another phenomenon investigated within the rotor was the packing of the fibres between the radial and axial directions. This was measured very simplistically. Micrographs of the rotor were taken in the four selected regions, 3 GFRP and the CFRP layer. 40 tests were conducted for each region. The pictures were then cropped to a square format, thus, an equal amount of radial and axial material was represented. The numbers of fibres were then counted in the two directions (Figure 3-4). The ratio of these two directions was then recorded and averaged (Table 3-1). This investigation was only conducted on the new rotor material.

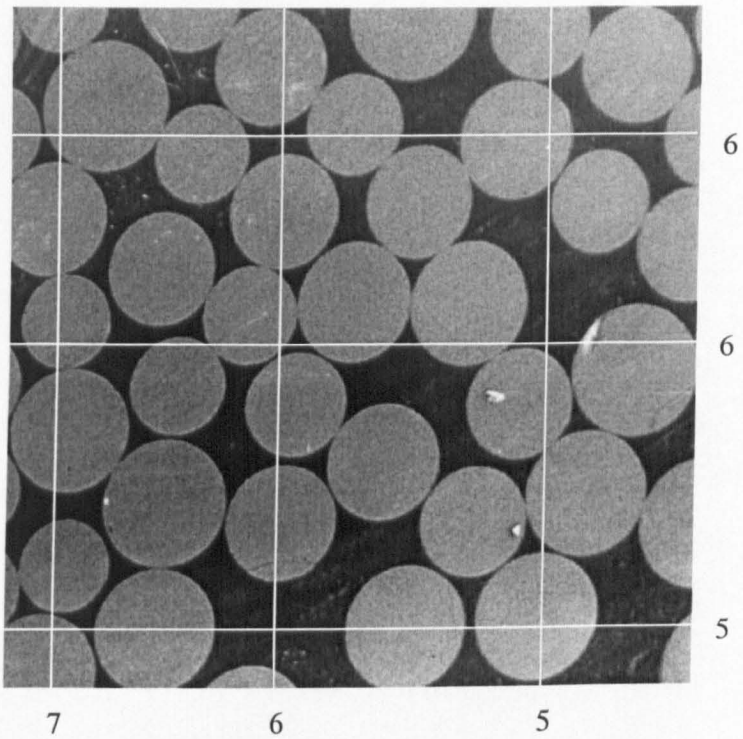

Figure 3-4 Example of radial and axial packing image and sampling. (r/a=0.94)

Table 3-1 Radial and axial packing results.

Material	Ratio (radial/axial)
GFRP Inner	0.968
GFRP Middle	0.976
GFRP Outer	0.973
CFRP	0.953

The results show that the axial packing is consistently higher than the radial packing. The difference is most obvious in the CFRP layer where there are 4.7% more fibres in the axial direction compared with the radial. In the GFRP the difference is typically 3%. This difference may be attributed to the relative contractions, upon curing. The radial thickness of the rotor is 80 mm, the contraction experienced in this direction is smaller than that experienced in the axial direction when the rotor is cured.

Table 3-2 Volume fraction data.

Material	Batch 1	Batch 2	Batch 3	Batch 4	Batch 5	Batch 6	Batch 7	Batch 8	Batch 9	Batch 10	average	standard deviation
CFRP old	0.667	0.708	0.676	0.722	0.71	0.709	0.683	0.694	0.696	0.689	0.6954	0.0171
CFRP new	0.652	0.674	0.668	0.736	0.717	0.694	0.696	0.672	0.683	0.655	0.6847	0.0267
GFRP new inner	0.652	0.594	0.574	0.614	0.581	0.69	0.594	0.568	0.64	0.631	0.6138	0.0391
GFRP new middle	0.645	0.599	0.618	0.58	0.595	0.592	0.523	0.621	0.639	0.615	0.6027	0.0348
GFRP new outer	0.582	0.613	0.574	0.537	0.517	0.687	0.586	0.516	0.589	0.549	0.575	0.0509
GFRP old inner	0.644	0.641	0.655	0.621	0.616	0.657	0.482	0.608	0.653	0.481	0.6058	0.0677
GFRP old middle	0.622	0.601	0.407	0.571	0.707	0.539	0.635	0.556	0.68	0.549	0.5867	0.0844
GFRP old outer	0.541	0.585	0.64	0.581	0.612	0.573	0.557	0.549	0.677	0.65	0.5965	0.0463

3.5.4 Void content

The same optical system, as described for the volume fraction work, was used for determining the void content. Characterization of the size and quantity of the defects present was required. The data collected on the voids in the rotor was fundamentally important since, ultimately, it might determine the probability of failure of the rotor.

The data presented here was obtained using the same principles as that of volume fraction. The principal difference being the boundary level between light and dark area was further increased to ignore the fibre boundary and only distinguish the very dark voids and material. Thus, the void fraction is measured by the ratio of areas between voids and material.

It is possible to make this assumption since every slice of the rotor is statistically equal to any other in possessing the same percentage of voids. Therefore, each slice analysed represents a snapshot of the overall void content in the rotor.

For further characterisation of the voids, 100 defects were found and analysed in each distinct layer of the rotor (Table 3-4). The primary measurement recorded was the longest dimension of the defect.

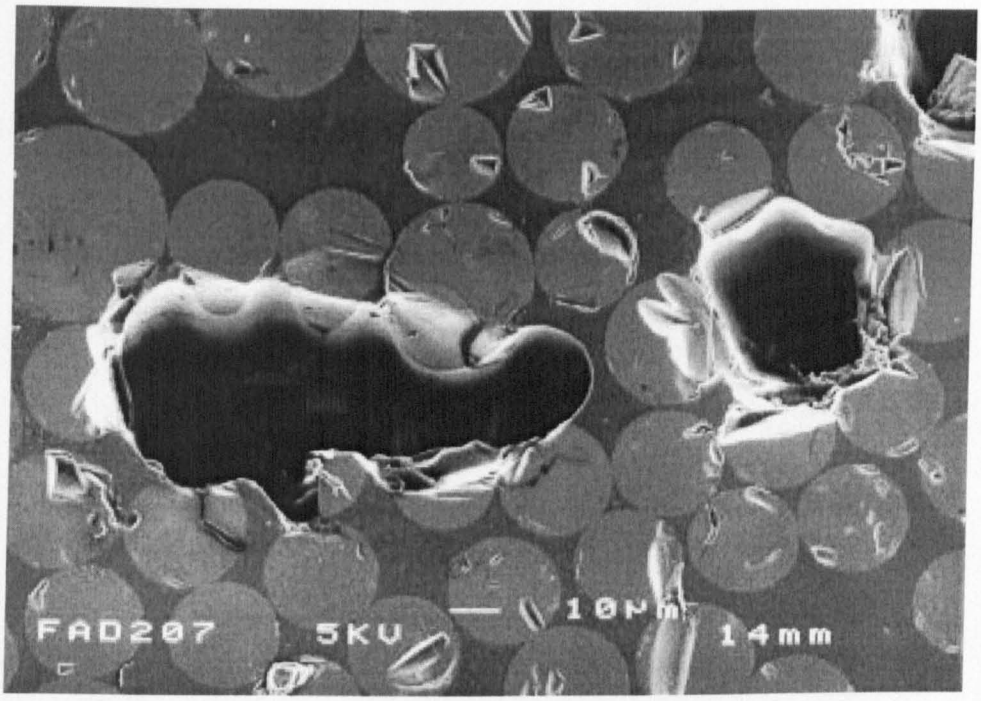

Figure 3-5 SEM of defect in the rotor.

The amount of voidage is quite high at 4.5% This however is due to the manner in which this value is calculated. The defects are assumed to be represented in the same way as the fibres in the volume fraction work.

In the NdFeB layer, the voidage is higher due to the filler disturbing the packing process allowing more bubbles to be included in the resin during winding. The filler also interrupts the movement of the fibres as subsequent layers are wound. Thus, the voids are not readily compressed. Evidence that compression by the outer layers being wound reduces the void size in the inner layers, exists in the new GFRP data illustrated in table 3-3. The void content in the GFRP layer grows from 3% next to the NdFeB layer to 4.5% adjacent to the CFRP layer. The voidage in the CFRP layer is higher than expected. From the area fraction data (Table 3-2), the smaller diameter fibres pack more efficiently. Hence, this translates into smaller voids.

Table 3-3 Void Fraction Data.

Material	Batch 1	Batch 2	Batch 3	Batch 4	Batch 5	Batch 6	Batch 7	Batch 8	Batch 9	Batch 10	average	standard deviation
CFRP old	0.062	0.067	0.081	0.086	0.1	0.044	0.076	0.086	0.061	0.101	0.0764	0.0181
CFRP new	0.031	0.036	0.056	0.044	0.058	0.041	0.029	0.021	0.063	0.048	0.0427	0.0137
GFRP new inner	0.029	0.018	0.013	0.022	0.043	0.036	0.022	0.021	0.045	0.05	0.0299	0.0128
GFRP new middle	0.034	0.079	0.023	0.056	0.025	0.038	0.022	0.061	0.039	0.061	0.0438	0.0194
GFRP new outer	0.031	0.065	0.041	0.031	0.065	0.017	0.062	0.04	0.084	0.056	0.0492	0.0205
GFRP old inner	0.013	0.043	0.028	0.063	0.079	0.029	0.052	0.04	0.024	0.049	0.042	0.0197
GFRP old middle	0.054	0.035	0.059	0.02	0.031	0.058	0.042	0.016	0.079	0.038	0.0432	0.0194
GFRP old outer	0.056	0.05	0.036	0.016	0.052	0.074	0.065	0.025	0.028	0.121	0.0523	0.0303
NdFeB old	0.022	0.052	0.038	0.088	0.086	0.068	0.064	0.073	0.033	0.017	0.0541	0.0257
NdFeB new	0.056	0.012	0.079	0.064	0.075	0.034	0.09	0.026	0.032	0.041	0.0509	0.0258

Table 3-4 Void size Analysis, mean, median, mode, range, maximum and minimums in μm.

CFRP		*GFRP outer*		*GFRP inner*		*NdFeB*	
Mean	18.365	Mean	28.731	Mean	24.221	Mean	29.723
Standard Error	1.116078	Standard Error	1.589975	Standard Error	1.238627	Standard Error	1.30145
Median	14.55	Median	26.65	Median	22.25	Median	27.2
Mode	10.3	Mode	11.6	Mode	27.1	Mode	19.6
Standard Deviation	11.16078	Standard Deviation	15.89975	Standard Deviation	12.38627	Standard Deviation	13.0145
Sample Variance	124.5631	Sample Variance	252.802	Sample Variance	153.4197	Sample Variance	169.377
Range	54.6	Range	64.6	Range	55	Range	56.9
Minimum	4.6	Minimum	5.1	Minimum	3.8	Minimum	11
Maximum	59.2	Maximum	69.7	Maximum	58.8	Maximum	67.9
Count	100	Count	100	Count	100	Count	100

3.5.5 Void size analysis.

The void size analysis data may be presented using histograms to illustrate how the void size is distributed. The data would be expected to be best represented by a normal distribution, however it does not quite fit this type of pattern. Even when a distribution may not be exactly normal, it may still be convenient to assume that a normal distribution is a good approximation (see later). In reality, the distributions are stacked towards smaller voids. In this case the distribution is said to be positively skewed rather than normal. Consequently, it is reasonable to assume, based upon the histograms (Figure 3-7), that the void size data fits a slightly positively skewed distribution .

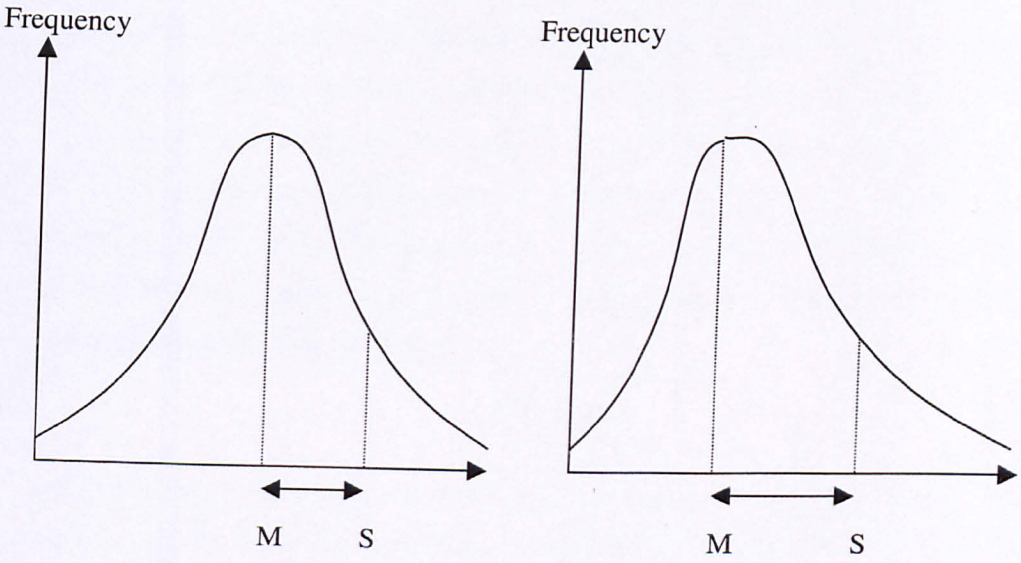

Normal distribution.

Positively skewed distribution.

Figure 3-6 Schematic of Distribution types

The normal distribution is specified by a mathematical rule presented in statistical texts **[58]** and once plotted, a characteristic bell curve is generated. The symbols M and S are the parameters that define the distribution. M is a regarded as the mean, mode or median of the distribution, and S is the standard deviation. It can be shown

[58] that a good estimate for M, in a positively skewed distribution, is the mode of the observed values, whereas in a normal distribution the estimate is the mean. Likewise, an estimate for S is the standard deviation. One test for a positively skewed distribution is that the median should lie between the mode and the mean. This is the case for all distributions, except that for the GFRP inner, whose mean lies outside of this band. The level of "skew" was then measured using a simple mathematical formula:

$$\text{skew} = \frac{3(\text{mean} - \text{median})}{S}$$

The definition of theses term is: In a set of values, the mode is the most frequently occurring value; the median is the middle value; and the mean is the average value. The resultant level of skew was low enough to simplify any analysis by way of assuming standard normal distribution charts for the defect data. As the level of skew tends to zero, the distribution becomes more normal. Thus, for the defect data, the NdFeB and GFRP layers all have a level of skew equal to ~0.5. It is acceptable to treat these as normal distributions. The only real exception was the CFRP data which is more skewed than any other (skew=1.02). Since this layer plays no real role in rotor failure (see later), the defects may also be assumed to be normally distributed. Thus, using these distributions the probability of finding a defect of a given size may be calculated using the following formula:

$$z = \left(\frac{a - a_M}{S} \right)$$

In this case the a, values refer to defect sizes, desired and mean, and S is the standard deviation. Once a value for z has been calculated, it may be converted using table into a probability (Appendix D).

3.5.5.1 Summary

The void sizes observed in the material are consistent with comparable filament wound composites [59]. The voids seen in the CFRP section of rotor are consistently smaller than those observed elsewhere. This fact may be attributed to the reduced fibre diameter, which results in smaller resin rich areas for void formation, although they occur more frequently. Generally, the largest voids are in the NdFeB layer, this is due

to the inclusion of the particulate filler. Since the NdFeB particles are quite large and irregular in shape, the effect they have on the viscosity of the resin is pronounced. This effect coupled with the packing of these particles (Figure 1-5), means that the layer is more susceptible to defects. The sharp edges of the filler and its interference with the fibre packing promotes void formation in contrast to the GFRP inner layer which lies adjacent. This theory is borne out by the decrease in void fraction from 5% in the NdFeB layer to 3% in the GFRP inner layer (Table 3-3).

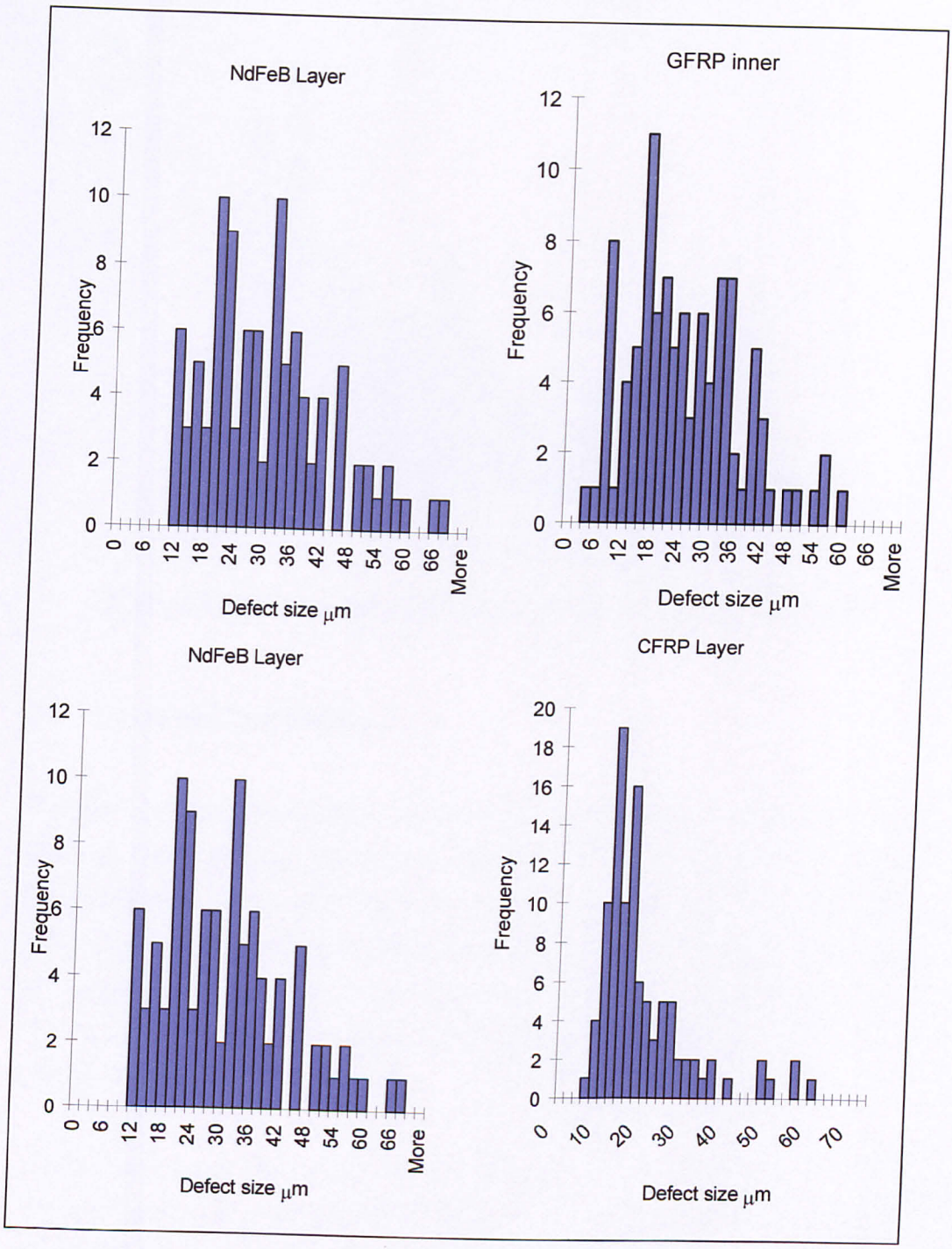

Figure 3-7 Void size and distribution (greatest dimension measured).

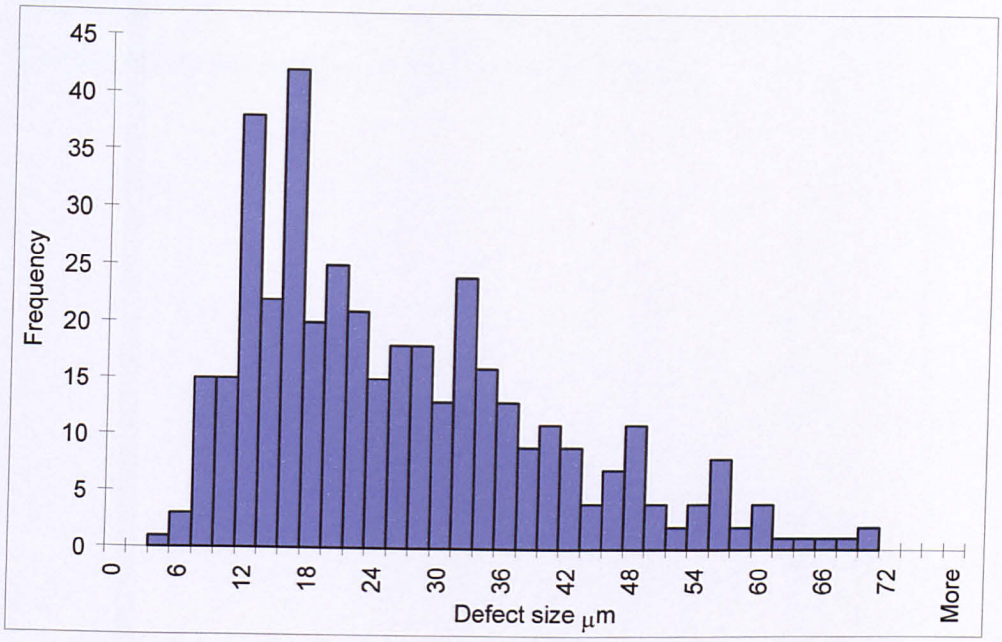

Figure 3-8 Histogram for all void data (greatest dimension measured).

3.6 Specimen Preparation

The rotor was supplied as either complete rings with a thickness of 20-30mm, or as segments whose thickness varied from 40-80mm. The complete rings were sectioned into manageable sizes, typically quarters or eighths. This procedure was conducted on a large band saw. It was recorded that upon cutting of the complete rotor ring when the carbon areas were reached, the rotor had the tendency to "grab" the saw blade. This is due to the significant residual cure stresses in the hoop direction, see later, (Figure 6-3).

The specimens were then marked up and cut out crudely on a circular diamond saw. The specimen blanks were ground down slowly on a mill equipped with a diamond wheel. The blanks were fastened to a flat steel plate using molten wax to set them in position. The use of the molten wax meant that the surfaces on the specimen were not damaged by clamping grips. This is of considerable relevance in through thickness testing where edge effects can have a major effect on the results. The rate of material removal was kept to a vertical rate of 0.5mm per pass. This rate was reduced to nearer 0.05mm per pass, as the required thickness was reached. The mill feed rate was set to

92mm/min. This combination was found by trial and error to give very good results. The dimension accuracy for all specimens was ±0.05mm.

4 STATIC TESTING

4.1 Introduction

Accurate measurement of the elastic properties of the composite rotor was fundamental to the successful completion of the research. The principle reasons for the high degree of accuracy required was due to the fact that the numerical models would be based upon these results. Hence, this data would then ultimately govern all the lifetime predictions.

4.2 Elastic properties.

The static tests were the first to be conducted during the research program. For the determination of the elastic properties, simple tests are all that are required (section 2). Although a simple straight sided block type specimen would be adequate for the evaluation of these properties, enhancement of this test might lead to a very adaptable test method. Thus, the same specimen design could be used for the fracture toughness and creep rupture tests. This was desired since it would simplify specimen manufacture and testing.

4.3 Through Thickness Test Design

4.3.1 Background

The literature survey studies (section 2.3) revealed that no fixed standard exists yet to quantify the through thickness properties of composite materials. Many of the methods discussed use very complex specimen geometries, which are expensive and time consuming to machine. As a result, the decision was taken to develop an entirely proprietary test.

The ideal was to produce a test method that could be used to generate both short and long term data, notched and un-notched with a minimum amount of specimen machining.

Short term un-notched tests for measuring through thickness tensile strength have been developed by a number of institutions. Most of these are either based on blocks of material with some wasting or on curved specimens. In order to use material cut directly from the flywheel rotor, a block type specimen was favoured.

If possible a straight sided block specimen was preferred, this was primarily due to the ease of manufacture and to reduced machining costs and time. It was also shown that Kim [46] produced very good modulus and strength results from the simplest straight sided specimens.

If a specimen such as this could be evolved for fracture toughness determination, this would be beneficial. Thus, the use of the same straight sided block, into which a slot type notch could be cut was evaluated. It was also desirable that, for long term tests, the growth of a crack was to be achieved under conditions of constant crack tip stress intensity. This simplifies any subsequent analysis and allows reliable data on K versus crack growth rate to be produced. This data would then be used for lifetime prediction. In order to achieve a constant crack tip K, specimens are usually tapered such that the crack tip compliance does not change as the crack grows. In our case it was decided to achieve this by the use of tapered end tabs which would be bonded to the straight sided block. A number of simple steel end tabs could be produced in this way and re-used with a large number of test specimens. This also had the advantage of removing gripping problems from the specimen design, as the test blocks would secure to the testing machine via pins through the metal end-tabs.

4.3.2 Specimen design

The initial design of the specimens and end tabs was largely constrained by:

- The need to be compatible with existing creep rupture test rigs.

- Compatibility with static testing in tensile test machines.
- A specimen geometry that could remain relatively thin, whilst still being completely representative.
- Quick and easy specimen production, especially for fracture toughness specimens.

The design chosen for further development was a straight sided specimen to which tapered steel end tabs would be bonded. The design of this end tab is shown in figure 4-1. For fracture toughness testing, a simple notch was introduced into the specimen.

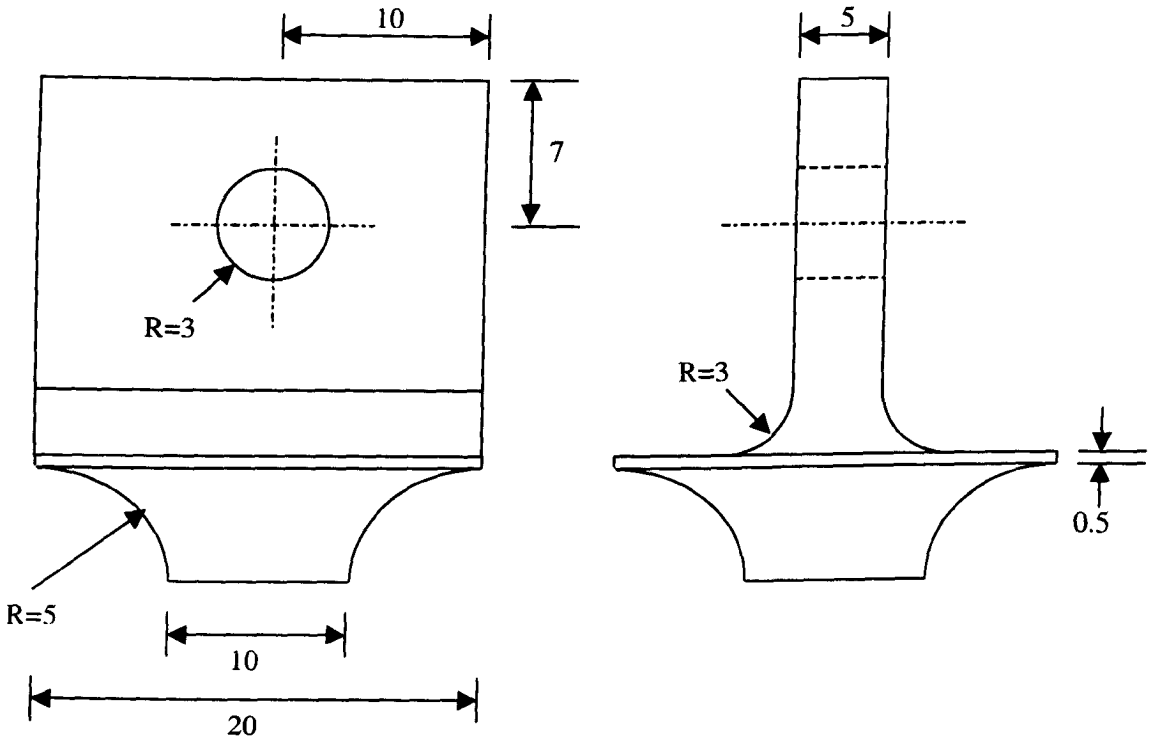

Figure 4-1 End Tab design. Dimensions in mm.

4.3.3 Modelling

Prior to manufacturing, the material and the end tab design was ratified by analytical methods. Finite element analysis was conducted using ABAQUS [10], and the entire specimen and end tab assembly were modelled in 3-D. To determine the mesh

sensitivity for the specimen, a simple 3-D block was modelled. Initially this block consisted of a single element. The block material was steel. This block was then deformed axially with a nominal displacement of 1mm. The reaction force was subsequently outputted. The number of elements was then increased and the process repeated.

The results may be plotted as force vs. density (Figure 4-2). As the element density increases the accuracy of the output also increases, although by very little ~1%. After 1 element per mm, the accuracy does not increase significantly further. This level of element density also simplifies the construction and handling and processing of the models.

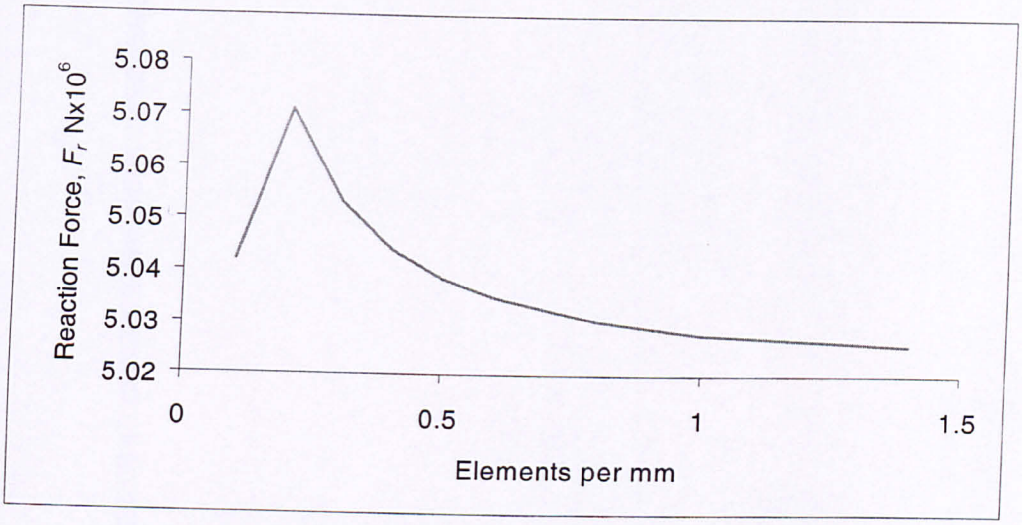

Figure 4-2 Reaction force vs. element density, for a 3d model.

With an adequate sensitivity determined, the models of the specimens were constructed. The input deck for this model may be found in appendix A1. The composite was modelled using the properties of a high volume fraction, unidirectional high strength CFRP. The models were used to study various specimen gauge lengths.

The result of the analysis indicated that the minimum specimen gauge length for no interference with the adhesive interface was 15mm. For the majority of the testing a specimen length of 20mm was chosen for a few reasons.

- Material supply was not an issue and the rotor could be supplied in any thickness required. The rotor has an axial thickness of 900mm, but the radial direction is smaller thus, shorter specimens.
- The accuracy of strain gauge placement was simplified, although every care was taken to precisely locate the strain gauges.

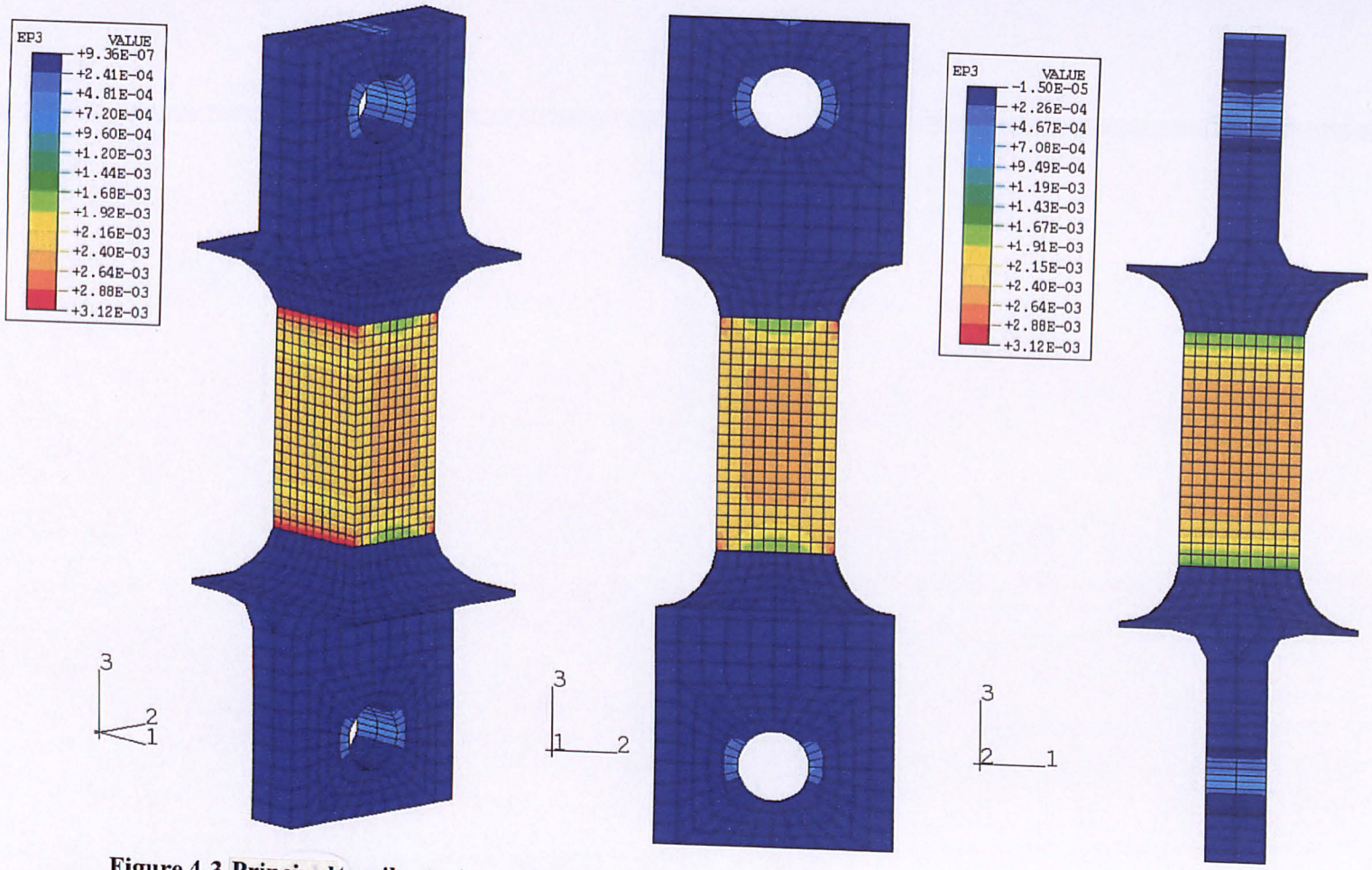

Figure 4-3 Principal tensile strain on through thickness specimen in axial direction with 1.8kN applied.

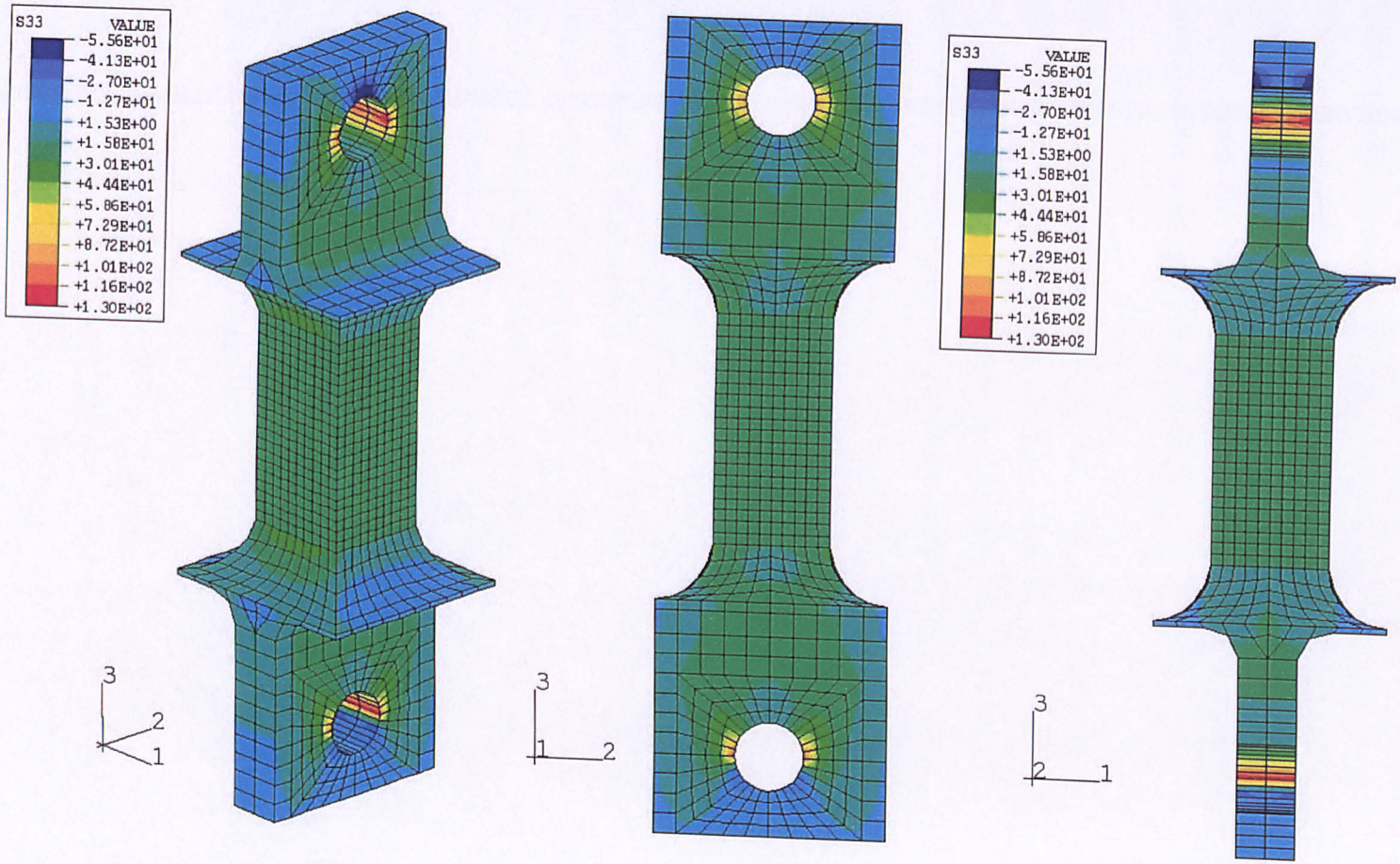

Figure 4-4 Principal tensile stress on through thickness specimen in axial direction with 1.8kN applied.

Figures 4-3 and 4-4 show the results of the modeling exercise. The specimen had an axial load of 1.8kN applied. In each figure, an isometric view is shown coupled with cross sectional views through the specimens, taken at the mid-plane. The presented models have a gauge length of 20mm. It can be seen that the strain state within the specimen is uniform. Figure 4-4 illustrates the stresses in the axial direction in the model. Again, the centre of the specimen has a uniform distribution, with stress concentrations at the CFRP/steel tab interface.

The stress concentration effect of the tab-specimen interface was of obvious significance. The concentrations produced effects on the stress/strain state which extended approximately 2mm into the specimen. This was found to be dependant upon gauge length, although the effect was very small.

4.3.4 Adhesive layer.

With this type of specimen, the performance under test would be largely dependant upon the quality of the bond between the end tab and the composite. The test was initially designed to produce a very constant stress and strain field in the composite. However, it later became apparent after private communication with an adhesives expert [11], that perhaps a simpler end tab configuration could produce a better stress state in the adhesive layer. The principle behind the next evolution of end tab would be to force a large proportion of the resin at the interface into a shear loading condition. This would be achieved by reducing the thickness of the end tab. The only concern would be that perhaps a greater gauge length of specimen would be required to achieve a uniform stress state. Unfortunately, this development was only discovered toward the end of the research programme.

However, this was obviously of no concern to the fracture toughness work, but it might allow the same specimen geometry to be used for strength determination if a highly toughened adhesive was used. Although, the use of this test geometry for strength tests would not be recommended. When conducting the elastic property tests to failure, approximately half the specimens failed away from the bond line (Figure

4-5). The specimens were observed to break approximately across the region where the stress concentration effects of the adhesive layer were seen to fall to zero. The models however did not include the "blobs" of resin on the sides of the bonded specimen that can be seen. These will have a small positive effect on the stress state, since they improve the load transfer from end tab to specimen.

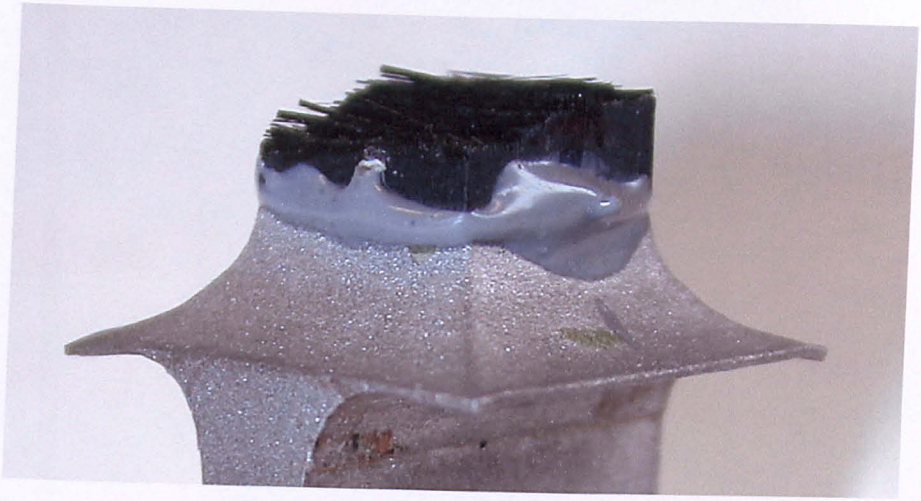

Figure 4-5 Close-up of failed specimen.

4.3.5 Alignment jig.

With this type of bonded specimen, alignment will always be an issue of concern. In the literature review several authors suggested the manufacture of an alignment jig when using bonded block type specimens. Thus, a small jig was manufactured to allow the correct specimen/end tab assembly (Figure 4-6). The jig can accommodate two specimens at a time. The jig was used for all specimen assembly.

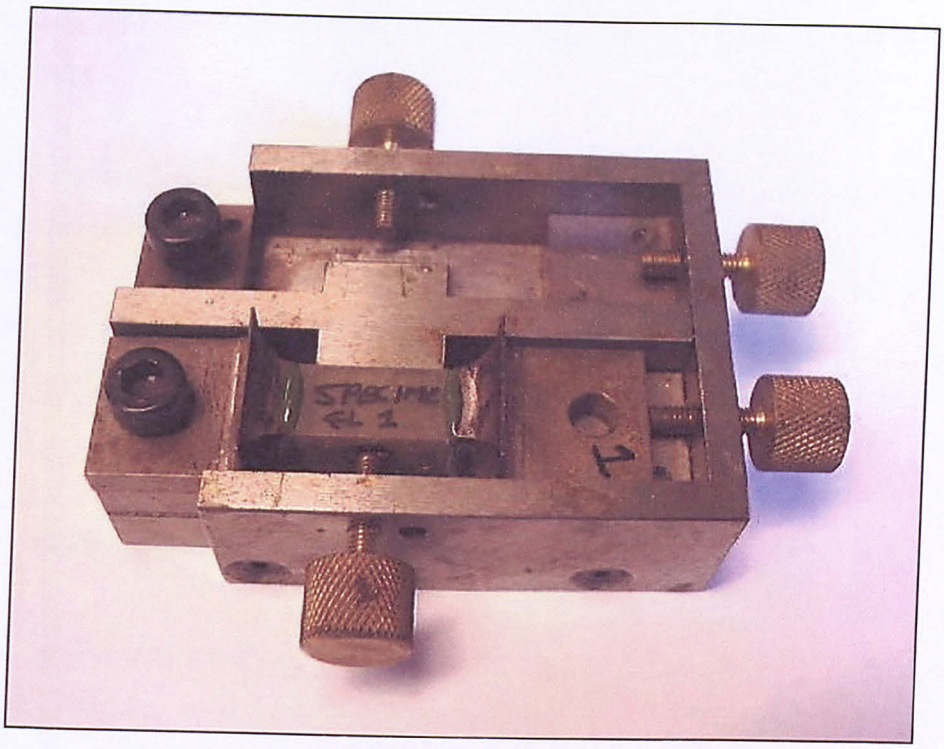

Figure 4-6 Specimen Alignment jig.

4.3.6 End tab attachment.

The resin system used was Hysol EA932, which was cured at 80°C for one hour. Glass beads of 100μm diameter were introduced into the resin to control the bond line thickness. This has been shown to have a pronounced effect on the strength on the joint [63], as stress concentrations can result from changes in bond line thickness.

4.3.7 End tab recycling.

The end tabs were recycled many times. The procedure involved, initially detaching the specimen block from the end tabs. This task was completed by using a vice and pliers to twist the specimen away from the end tabs. In the case of the pure block type specimens, used for determination of elastic properties, with care the specimen could be reused if necessary in the future so long as the adhesive layer failed easily (rare). With the specimens used for static fracture toughness and long term tests, the

specimen were destroyed at this stage due to the very weak nature of the cracked specimen.

Following the removal of the specimen, the remaining resin was burned from the end tab surface using a blow torch. Upon completion of the resin removal, the end tabs were grit blasted to prepare the surface for re-bonding. Finally, the end tabs were then cleaned using acetone and the surface of the end tab was checked for damage and flatness, in readiness for the next specimen to be attached.

4.4 Testing Machines

Static tensile tests were conducted on Instron universal testing machines. Several different machines were used for the various types of test. Table 4-1 gives a summary of testing machines used and the relevant settings.

Table 4-1 Summary of testing equipment.

Instron Model	Load Range kN	Cross head speed mm/min	Test
1195	5	0.2-0.5	Elastic testing.
6025	100	0.005-0.1	Crack Growth Studies.
1105	5	0.1-0.5	Compliance calibration.
Hounsfield	25	0.1	UTS measurements

The testing machines were calibrated before each testing series using the in-built calibration function. Where possible this was checked by the use of dead weights. The machines were then rechecked at the end of testing sessions to make sure that no settings had drifted.

4.4.1 Environment

The entire testing program was conducted at room temperature and the tests were exposed to normal atmospheric pressure and humidity. In contrast the real scenario presents elevated temperatures and a sealed vacuum. The principle reasons for the omission of these environmental parameters was due to the preliminary nature of the research, and hence the need to keep the programme simple. The effect of temperature in terms of visco-elasticity and humidity are well documented for composites [64]. Future work is needed in this area to correctly assess these environmental influences on the rotor.

4.5 Strain Measurement

The most accurate method of measuring strains on the composite specimens is through the use of bonded strain gauges. The strain gauges were used to not only measure the longitudinal and transverse strains on specimens, but also to measure the crack opening displacement, and hence compliance of some of the notched specimens. This was achieved by bonding the strain gauge across the crack opening. As the specimen was loaded, the strain in the composite was known, so the strain and hence crack opening could be reverse calculated.

4.5.1 Strain Gauge Details and Installation

All strain gauges were manufactured by TML [65],[12]. Table 4-2 shows the characteristics of the strain gauges used. The gauges are foil backed and were bonded onto the specimens using a cyanoacrylate based adhesive. The output performance of the strain gauge is dependant on the quality of the bond to the specimen. To this end the specimens surface was abraded and degreased to improve bonding.

The alignment of the strain gauges is not particularly critical. The strain gauge documentation indicated that off-axis angle of 5° results in only a 3% change in the strain value [65]. Notwithstanding this fact, the strain gauges were attached very carefully.

Table 4-2 Strain guages used

Strain Gauge	Measurement	Length (mm)	Use
FLA-6-11-1L	0°	6	Elastic Modulus
FCA-2-11-1L	0°/90°	2	Elastic Modulus and Poisson Ratio
FLA-10-11-1L	0°	10	Crack Opening displacement

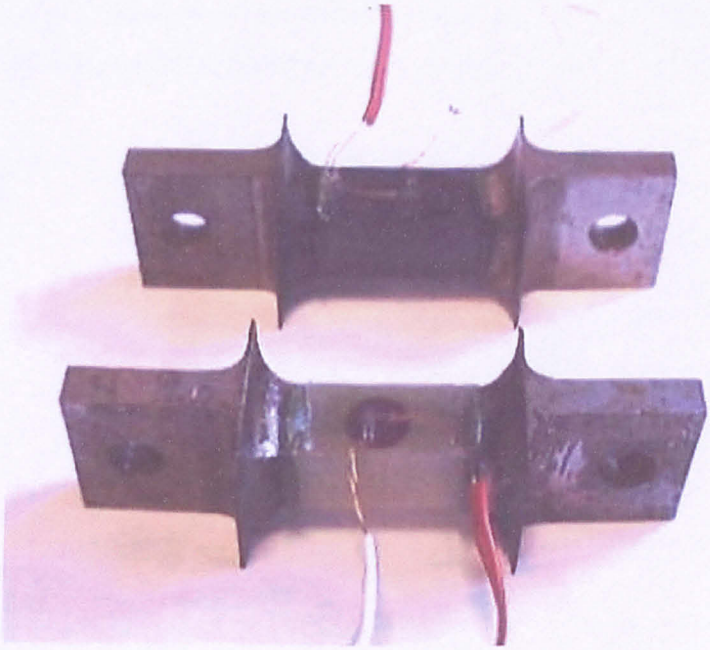

Figure 4-7 CFRP and GFRP Specimens with bonded strain gauges

4.5.2 Strain Translation

The strain gauge signal was amplified through a strain gauge amplifier (CIL Electronics SGA 800), whose electronics were based upon the Wheatstone bridge principle. The signal was then recorded through a data acquisition card mounted in a computer. The computer also simultaneously recorded the load, outputted from the tensile test machine.

A simple data translation program was installed on the PC. The program was written in basic. It calculated the tensile stress and strains, which was outputted as a data file. These files were then imported into Microsoft Excel, which was used to create the appropriate graphs (Figure 4-8).

Throughout the testing phase of the project, it was noted that some interference was present. This interference can be seen in figure 4-8. It takes the form of a sinusoidal wave superimposed over the signal. The inference has since been traced back to the electronics that control the load translation from the test machines to the computer. The effect of this interference on the modulus and Poisson ratio values is negligible.

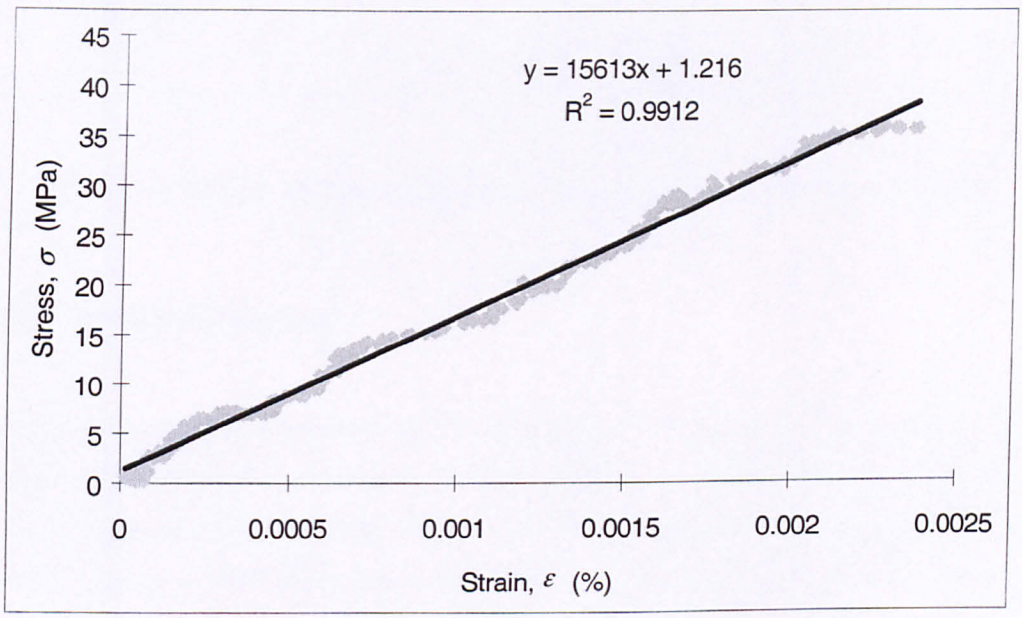

Figure 4-8 Sample stress vs. strain curve (GFRP mid-section)

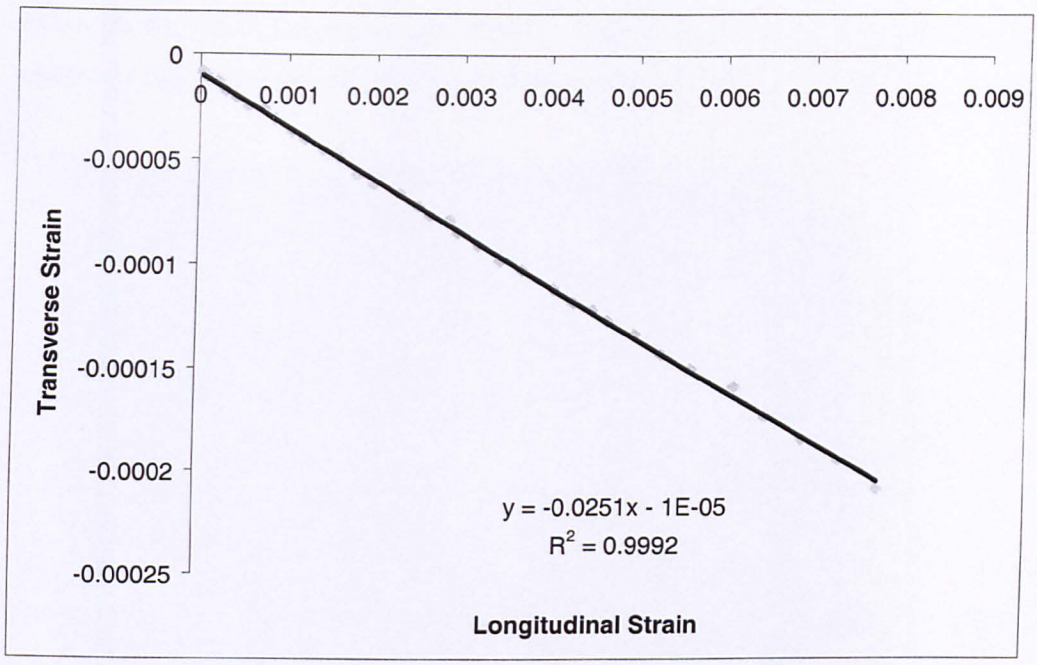

Figure 4-9 Sample Poisson ratio contraction graph. (CFRP radial direction)

4.6 Elastic Properties.

Cross strain gauges were used for the determination of the elastic properties. These allow the simultaneous measurement of longitudinal and transverse strains and thus the calculation of Poisson ratio (Figure 4-9). As stipulated there was no interference effect noticed on the Poisson ratio charts. Since the interference was related solely to the load channel.

4.6.1 Hoop direction

The test method developed was never intended to be used for testing the material in the hoop direction. This is due to the fact that testing fibrous composites in the fibre direction requires excellent transfer of load from the testing machine to the specimen. This is normally achieved by using end tabbed specimens where the end tabs are bonded to the specimen such that the adhesive layer is placed in shear. With the adhesive layer in the through-thickness method in tension, very low strains to failure

are inevitable. These tests were attempted for completeness of the property map. The results of these tests were not used in any further calculations.

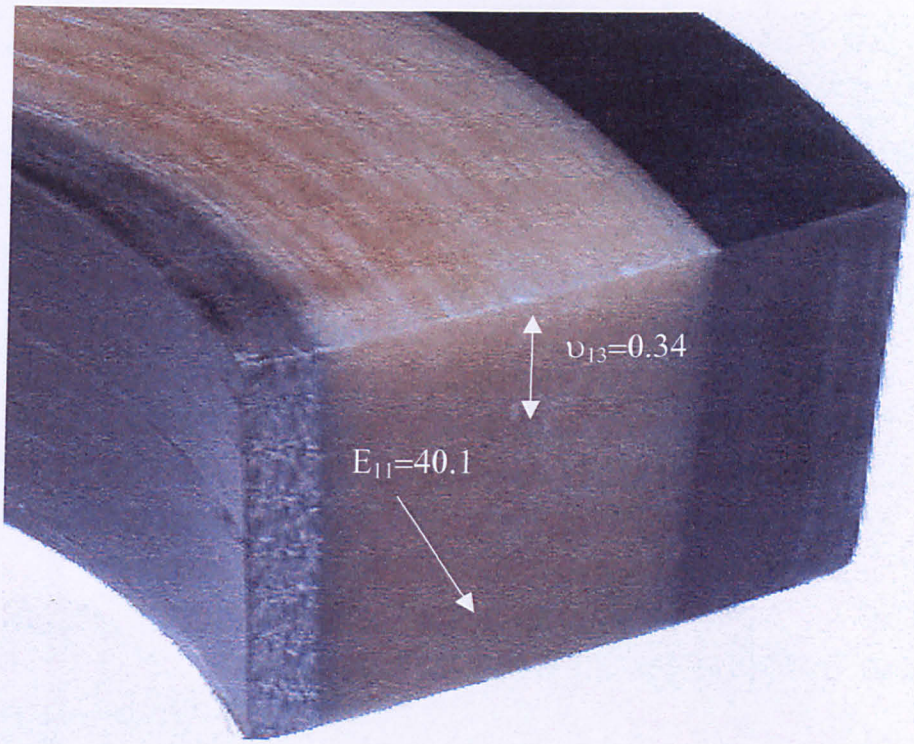

Figure 4-10 Elastic properties for hoop direction, all modulus values in GPa

Table 4-3 Hoop direction results. (Modulus values in GPa)

Material	Quantity	Mean	Standard deviation	C_v %
GFRP	E_{11}	40.1	7.83	18.1
	υ_{13}	0.34	0.072	21.1

The NdFeB layer was not thick enough to cut a suitable specimen. The CFRP layer was tested, however due to the very high modulus of this material no significant deformation could be exerted onto the specimen before the adhesive layer failed. This resulted in no practical stress/strain curve.

Hence, the results for the test in the hoop direction were only valid for the GFRP layer. The results are reasonable, if a little on the low side, when compared with other

published values for unidirectional E-glass composites [73]. The variance is not unreasonable considering the unsuitability of the test.

4.6.2 Radial Direction.

The materials were tested extensively in the radial direction. The NdFeB layer again could not be tested due to the thickness of this layer. In the GFRP layer, the first effects of the v_f of the glass fibres on the elastic modulus were noticed. The same trend was observed with the axial results and are discussed later in section 4.6.3. No perceivable difference can be seen in the υ_{23} ratios, when comparing the data to the v_f of the layer. As expected the υ_{21} values are very small due to the high stiffness of the fibre in this direction. The values obtained for both modulus and υ are reasonable for all layers when compared with published data in the literature review.

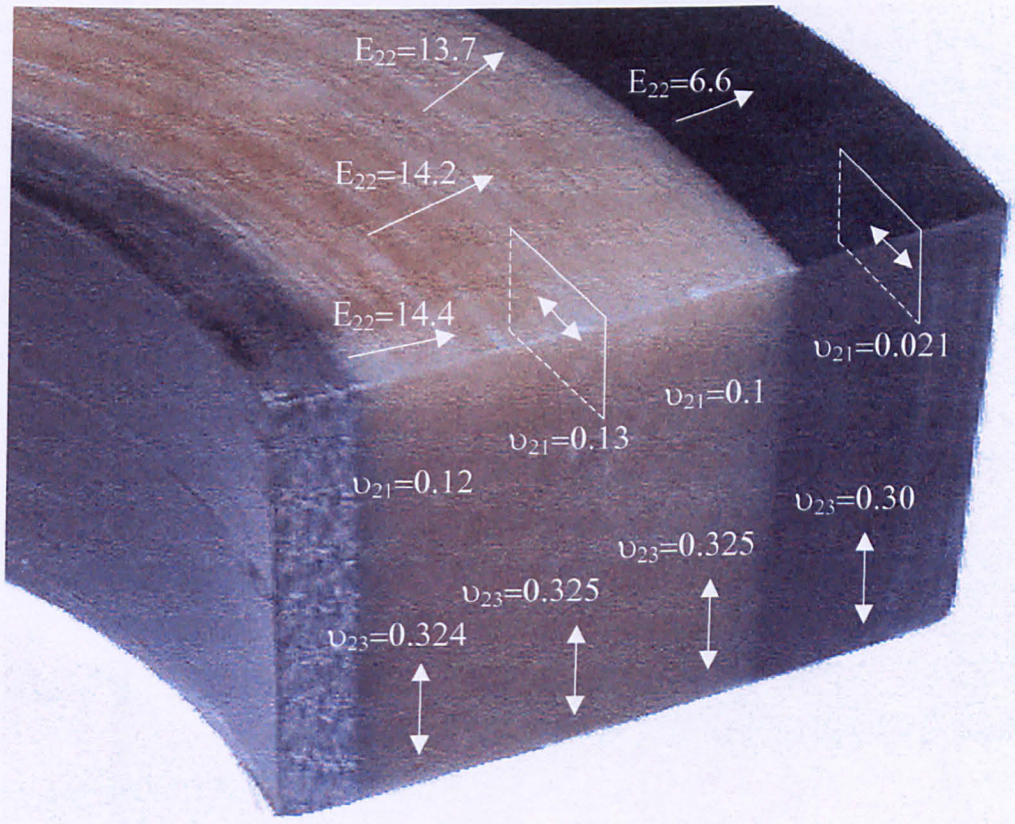

Figure 4-11 Elastic properties for radial direction, all modulus values in GPa

Table 4-4 Radial direction results.(Modulus values in GPa)

Material	Quantity	Mean	Standard deviation	C_v %
GFRP-inner	E_{22}	14.4	2.61	18.1
	υ_{21}	0.12	0.015	12.5
	υ_{23}	0.324	0.057	17.7
GFRP-middle	E_{22}	14.2	2.02	14.2
	υ_{21}	0.13	0.021	16.1
	υ_{23}	0.325	0.041	12.5
GRFP-outer	E_{22}	13.7	1.67	12.2
	υ_{21}	0.1	0.009	9
	υ_{23}	0.325	0.060	18.4
CFRP	E_{22}	6.6	1.04	15.8
	υ_{21}	0.021	0.008	38.1
	υ_{23}	0.3	0.025	8.3

4.6.3 Axial Direction

The results for the axial direction disappointingly show a high degree of variance. The sections were re-tested but the second set showed the same trends and thus were combined to form this table (Table 4-5).

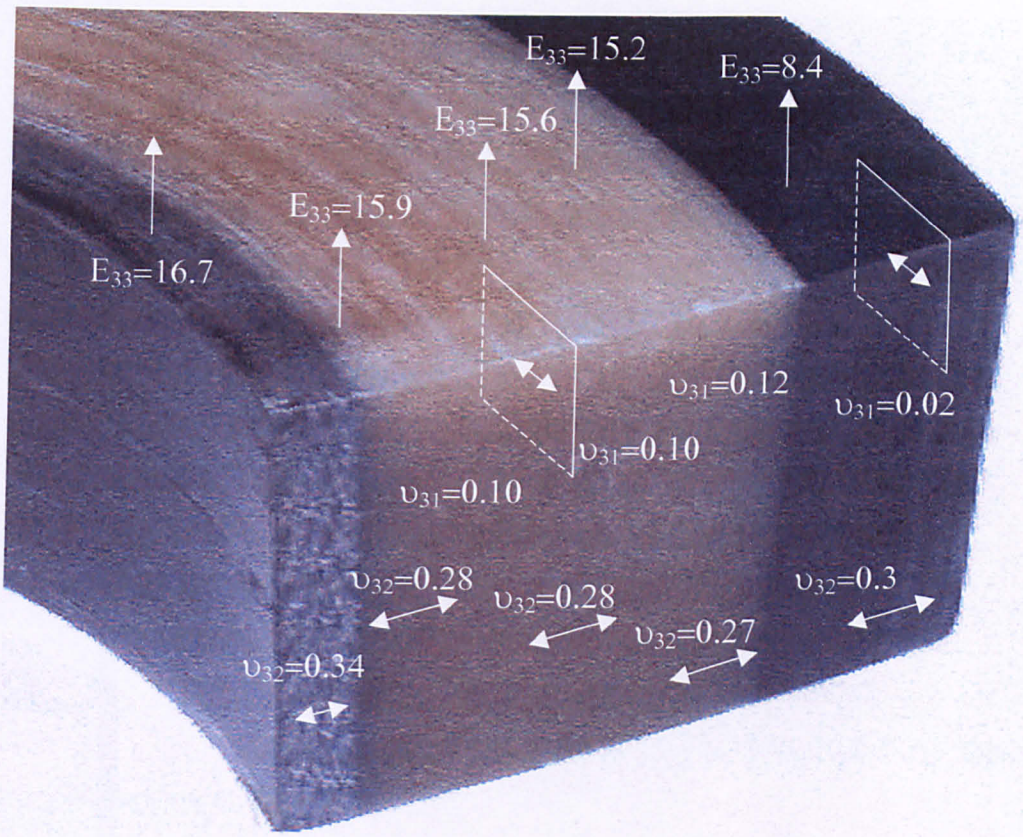

Figure 4-12 Elastic properties for Axial Direction, all modulus values in GPa

E_{33} for the NdFeB layer is higher than that for the unfilled GFRP. This is due to the high content (20% by volume) of the particulate metallic filler which has a high modulus. Thus, it is assumed to contribute to the modulus of this layer.

The CFRP layer has a higher modulus in the axial direction than in the radial. This confirms the fibres pack differently in these directions. This also applies to the GFRP layer. This correlates well with the work in the earlier section (3.5.3).

Although the variances are high, a difference in the mean values was observed across the GFRP layer. This difference is small ~ 4.5%, the difference in v_f across this region is ~ 4%. Using a numerical model, it is possible to predict the change in modulus for this volume fraction change. Halpin-Tsai model described in section 2.2.3, predicts a rise of 7.4% for a 4% increase in v_f from 57.5%.

Table 4-5 Axial direction results. (Modulus values in GPa)

Material	Quantity	Mean	Standard deviation	C_v %
NdFeB	E_{33}	16.7	1.54	9.2
	υ_{32}	0.34	0.024	7
GFRP-inner	E_{33}	15.9	1.29	8.1
	υ_{31}	0.1	0.011	11.1
	υ_{32}	0.28	0.03	10.7
GFRP-middle	E_{33}	15.6	1.9	12.2
	υ_{31}	0.1	0.005	5
	υ_{32}	0.28	0.041	14.6
GRFP-outer	E_{33}	15.2	2.02	13.3
	υ_{31}	0.12	0.017	14.0
	υ_{32}	0.27	0.039	14.4
CFRP	E_{33}	8.4	1.18	14.1
	υ_{31}	0.02	0.079	3.5
	υ_{32}	0.3	0.041	13.6

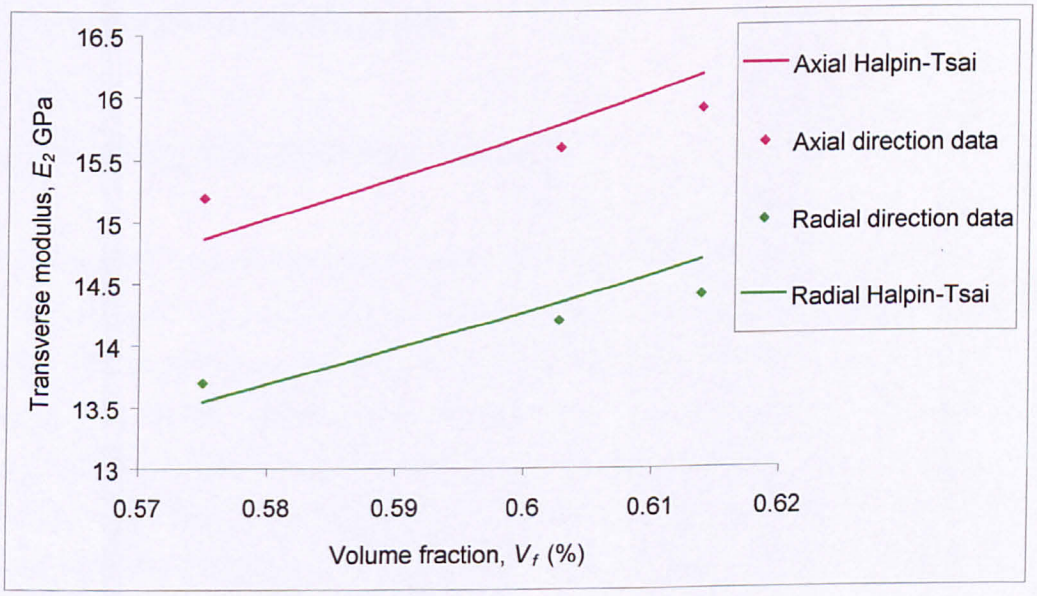

Figure 4-13 Comparison of Halpin-Tsai and experimental data

In order to fit the Halpin Tsai model to the experimental data, the adjustable parameter was set to the following levels: in the radial direction ξ=0.17 and 0.44 in the axial direction. It may be concluded that this difference in this parameter was also related to the packing of the fibres in the radial and axial directions.

4.7 Transverse Strength Measurements.

4.7.1 Introduction

The through thickness test method developed for the measurement of the transverse elastic properties was not regarded as reliable enough to measure the UTTS of the materials. It has earlier been shown that the specimens have failed away from the bond line (Figure 4-5), indicating that it may be possible to use the method for strength determination. Besides, preceding research [41] has illustrated that direct tensile testing usually results in low strengths and relative strains. These observed low values were attributed to the effects of the inherent defects within the materials, although this is not a proven theory. The test method has been used extensively by other researchers [41] and has produced reliable results.

4.7.2 Testing to ASTM D790M –92 [42]

The simplest form of strength measurement follows the ASTM standard outlined in the literature review, and is based on a bend test on a rectangular specimen. The tests used a three point bend jig. Thus, tests were conducted using a three-point bend set-up, as per ASTM standards. This standard allows the calculation of the UTS of a material, assuming that overall failure originates from a tensile failure in the outer layers at mid-span. This method is less sensitive to flaw sizes, since only a small amount of the specimen is actually loaded in tension. Hence, the method results in a more accurate representation of the materials transverse strength. [41]

Specimens were cut from the material to the dimensions constrained by the standard, figure 4-14. Upon completion of the machining, all the faces of the test specimens were polished to minimise any edge effects. The specimens were then tested in the Hounsfield tensile testing machining at a displacment rate of 0.2mm/min, as stipulated by the standard.

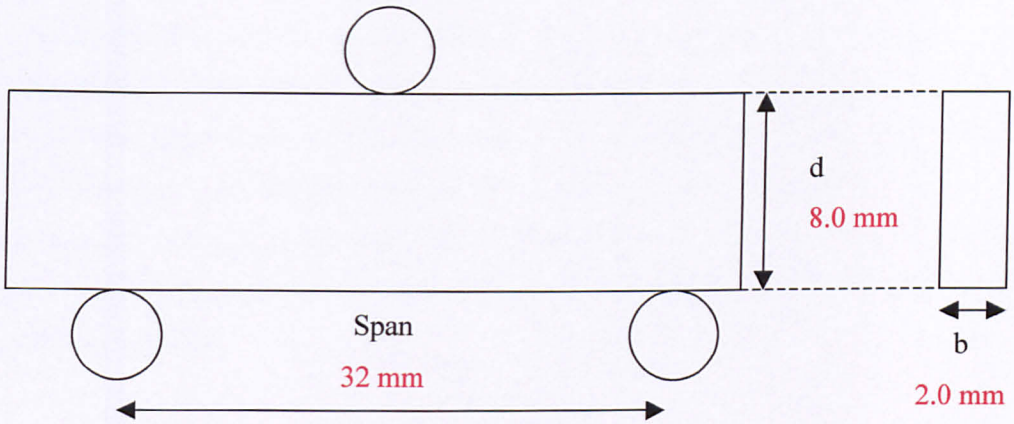

Figure 4-14 Strength specimen dimensions.

4.7.3 Calculation.

As defined in the standard, the transverse UTS, S, is given by.

$$S = \frac{3PL}{bd^2}$$

and the strain to failure, r, is defined as:

$$r = \frac{6Dd}{L^2}$$

Where: S=Stress, MPa
P=load, N
L=support span, mm
b=width of test specimen, mm
d=depth of test specimen, mm
r=strain, mm/mm
D=mid-span deflection, mm

4.7.4 Results

As one would expect, the force deflection plots for the various specimens showed normal elastic behaviour to the point of failure. (Figure 4-15).

The results for strength (Table 4-6) are consistent in terms of spread of data. With coefficient of variations of the order of 10% or less, the level is acceptable for composites testing. Interestingly, the inner layers of the GFRP perform considerably better than those in the outer. In part, this can be explained by the increased v_f (Table 3-2). However, an increase of just 4% volume of fibres does not justify a 23% increase in strength. In literature [78], [83], it can be seen that the transverse strength of GFRP is not very sensitive to v_f. thus, that the strength remains constant across a wide range of v_f.

The strains to failure are even more inconsistent. The variation is similar, again of the order of 9%, except the NdFeB layer whose variation is low. The failure in the NdFeB layer is initiated by the magnetic filler. The evidence to support this lies in the lower strength values, since this layer is considerably weaker than the unfilled layers. The only difference between these layers is the powder and lower number of fibres. If these the strength values are compared with literature, direct tensile testing by DERA [49] yielded higher results for CFRP with a similar variance. When compared with indirect tests[31] the GFRP values are broadly similar. The very high values of 87MPa were also not unreasonable when compared with some research [28], however no mention is given of the v_f of those composites tested.

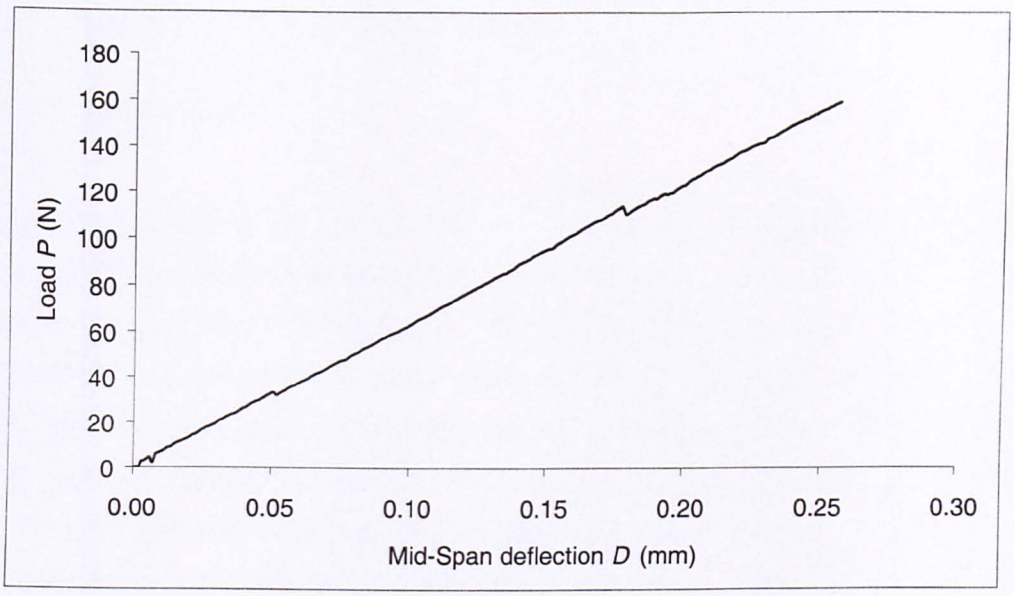

Figure 4-15 Load deflection trace for CFRP specimen, as outputted by Hounsfield tensile testing machine.

Table 4-6 Transverse strength test results.

Material	Strength (MPa)	Standard deviation	C_v %
CFRP layer	56.63	5.38	9.5
GFRP outer layer	70.52	6.75	9.6
GFRP inner layer	87.20	6.99	8.0
NdFeB layer	57.32	5.53	9.7

Table 4-7 Transverse Strain data.

Material	Strain to failure %	Standard deviation	C_v %
CFRP layer	1.360	0116	8.5
GFRP outer layer	1.212	0.117	9.7
GFRP inner layer	1.404	0.141	10.1
NdFeB layer	1.070	0.081	7.5

4.8 Fracture toughness determination.

4.8.1 Introduction.

The determination of the through-thickness fracture was the cornerstone of the life time prediction work. The accurate measurement of K values would lead to the development of the simplified model. The greatest difficulty with composites is the high degree of scatter within results, particularly where loading is not in the fibre direction, as already seen in the elastic properties results. This is due to the variable nature of the composite properties, which in turn is based upon fibre distribution, volume fraction and quality of the interfacial bonding. To further compound this, introducing a notch into the specimen adds a further variable since the notching process is not 100% accurately repeatable.

4.8.2 Testing to ASTM E399-83 [18]

The standard accepted for isotropic materials was initially used because no fixed standard exists for establishing the through thickness fracture toughness for composite materials. The applicability of this test to composites was questioned, principally due to the high degree of anisotropy that composites exhibit. However, since the specimens were very quick to machine, the tests were considered suitable for a first estimate of the transverse toughness.

The configuration of the test specimens were a single notched edge beam (SNEB). The dimensions of which are illustrated below. (Figure 4-16)

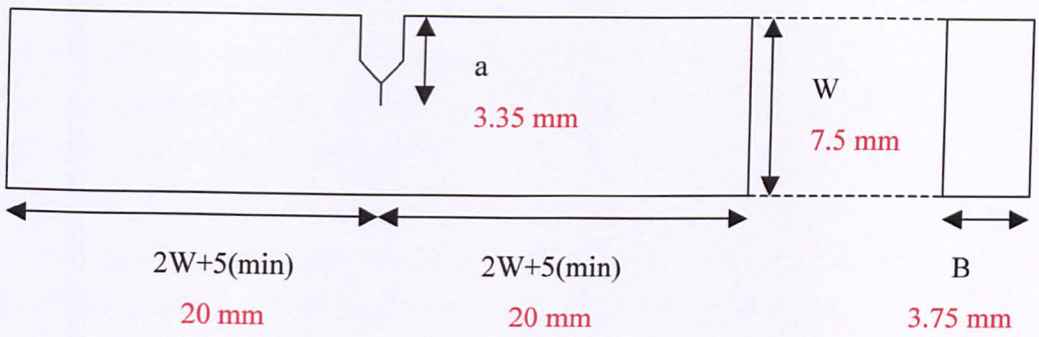

- ASTM dimensions.
- Machined dimension.

Figure 4-16 ASTM E399-83 standard specimen geometry for single notch edged beam.

The specimens were orientated in the rotor such that the toughness in the 23 plane (i.e. the crack would grow in the radial direction) would be determined. Specimens were cut from all three sections of the rotor. The test for the magnetically loaded layer would remain as the only toughness data obtained for this region. Since all subsequent test methods used a minimum specimen thickness of 10mm.

The specimens were machined in the normal fashion, as described in section 3.6 to a tolerance of 0.05mm. It was regarded unnecessary to polish the surfaces on these specimens, since the failure would be dictated by propagation of the crack.

The notches were introduced into the specimens using a slotting machine fitted with a silicon carbide slotting wheel. The thickness of the wheel was 0.25mm. Once notched, the crack tip was sharpened using a razor blade to create a crack tip with the minimum radius possible.

A further investigation was conducted into the method of sharpening the crack tip. With conventional DCB testing, literature exist that indicates the importance of the profile of the crack tip [71]. However, creating a fine crack tip is relatively

straightforward when manufacturing the composite. In this case the composite specimens were machined from the rotor. Thus, the dilemma existed with regards to the most effective method of notching the specimens. Two methods are commonly used for introducing notches into this type of specimen. Both utilise a razor blade and were tested using spare SNEB specimens. Figure 4-17 shows the force/displacement data for two specimens with crack sharpened by 1) swiping the razor blade thorough the notch and 2) by striking the blade with a small force. The graph shows that using the striking method produced a sharper notch, as no obvious transition can be seen between crack growth initiation and stable propagation.

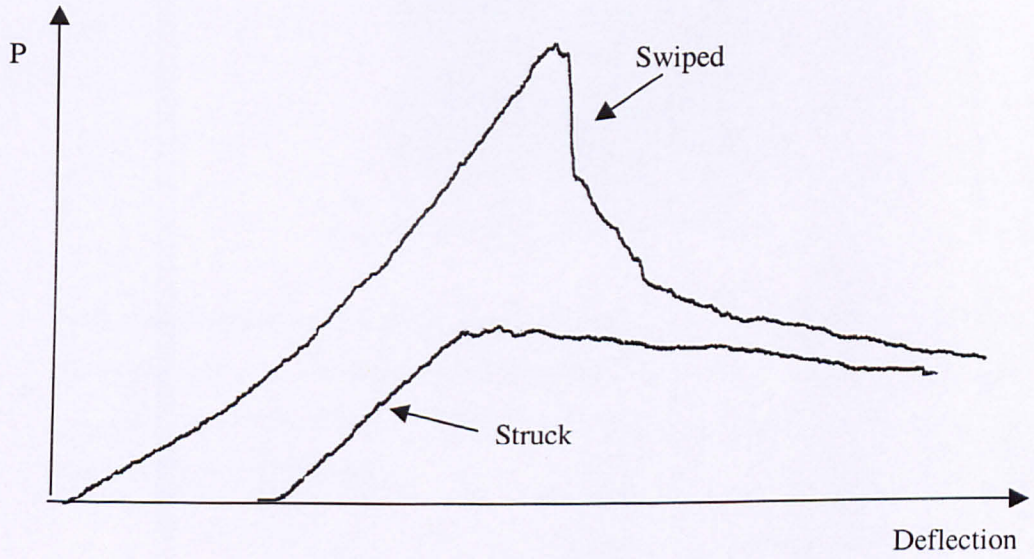

Figure 4-17 Load/deflection traces for swiped and struck specimens.

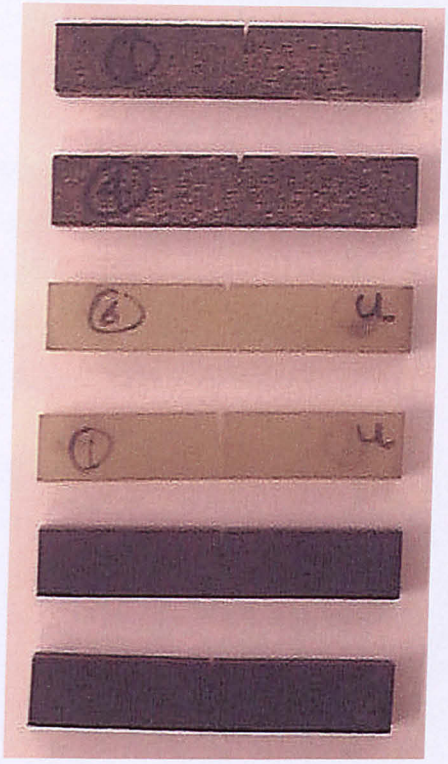

Figure 4-18 SNEB specimens.

A standard 3-point bend jig was used in conjunction with the Instron 1195 fitted with the 5 kN load cell. Since the failure loads were going to be very low, a smaller range load cell would have been more appropriate but was unavailable at the time. The displacment rate was kept at 0.1mm/min.

4.8.2.1 Results

To calculate fracture toughness values, the specimens were accurately measured and the failure loads recorded. The crack length, a, was measured using a travelling microscope. The calculation for fracture toughness is defined in the standard as:

$$K_{IC} = \frac{P}{BW^{\frac{1}{2}}} Y_1$$

Where: P= failure load, N

B= Breath, mm

W=Width, mm

and Y_1 = A constant based on an empirical formula given in the standard using the aspect ratio of the crack length and specimen width. [14]

If Y_1 falls outside the prescribed limits for the aspect ratio (a/w), which only a few specimens did, then the expressions developed by Srawley [16] for correcting for this were used. When these values were used for those specimens whose aspect ratios fell outside the standard tolerance, the Y_1 value changed significantly but the final calculated K was consistent with those that fell within the standards tolerances.

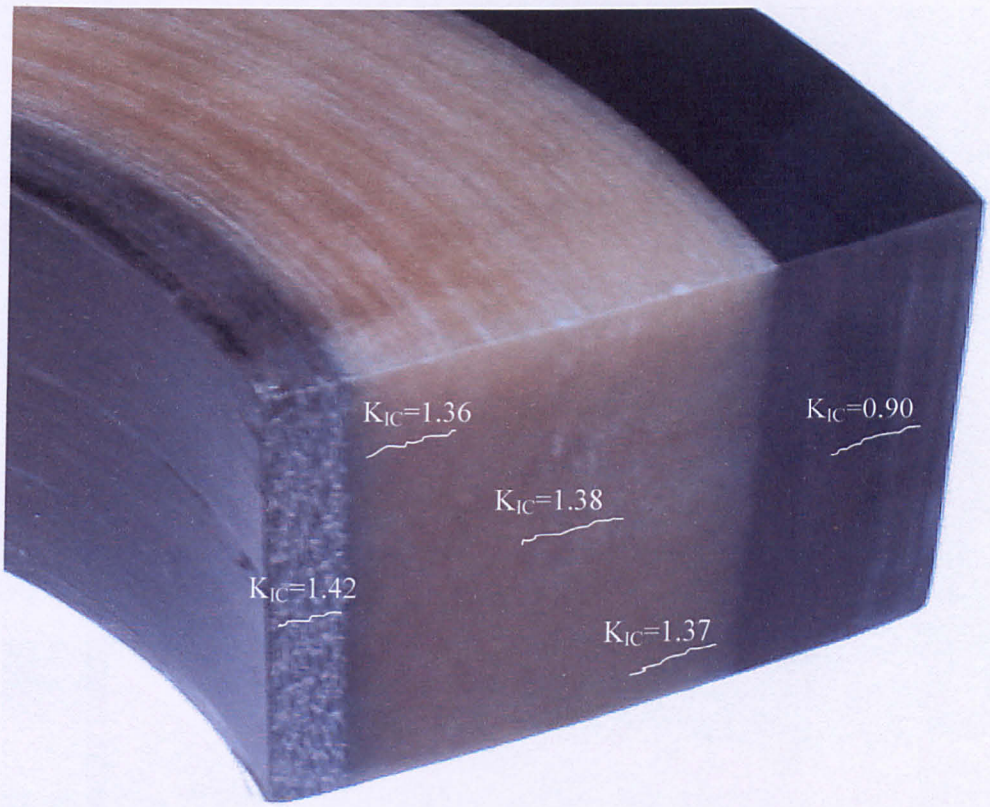

Figure 4-19 Schematic of ASTM fracture toughness results.

Table 4-8 ASTM results.

Material	K_{IC} (MPa $m^{1/2}$)	Standard deviation	C_v %
NdFeB	1.418	0.157	11.1
GFRP-inner	1.357	0.054	3.9
GFRP-middle	1.379	0.213	15.4
GRFP-outer	1.367	0.087	6.3
CFRP	0.900	0.070	7.7

4.8.3 Compliance calibration method

As described in the literature (section 2.5.5), any specimen architecture may in theory be used for determining the fracture toughness of a material, so long as the deformation and crack growth characteristics can be monitored. Hence, from the outset modified transverse tension specimens would be used to determine the static and long term fracture behaviour of the various layers.

4.8.3.1 Introduction

The specimens were machined in the same manner, to a pre determined size, for the vast majority of this research programme conventional 10x10x20mm blocks were used.

The specimens were then notched using the same method previously outlined. The notches were cut in increasing lengths typically starting at 2mm and finishing at 7mm in length. Once the notch had been introduced into the specimen, it was then subsequently sharpened with a razor blade. Based on the previous experiences, the preferred notching method was striking the razor blade. The crack tip was check after the sharpening had taken place. No obvious extension in crack length was observed, but, it is reasonable to assume that some small extension of the crack length must have taken place.

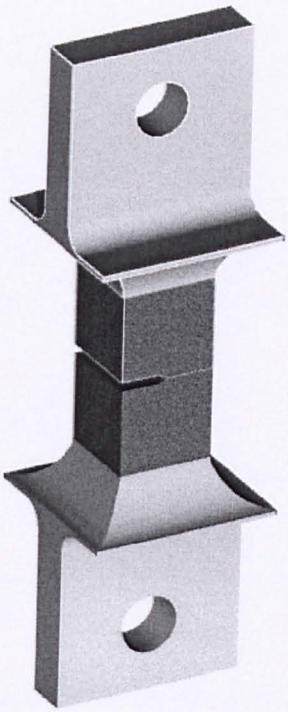

Figure 4-20 Schematic of a notched specimen.

Again the steel end tabs were then bonded to the blocks using the epoxy adhesive. With the end tabs in place the strain gauges were then bonded to the blocks. The location of the strain gauge was important for this work, since it needed to be accurately placed across the crack. The assumption was then made that the strain in the specimen block was negligible compared with the crack opening displacement. Figure 4-21 illustrates the process. The actual magnitude of the difference in stiffness is acute. For example, in the GFRP, the introduction of a 2mm notch into the specimen reduces the stiffness by 30% of the un-notched value. Thus, it can correctly be assumed that strains recorded are purely those connected to the crack opening, and hence compliance.

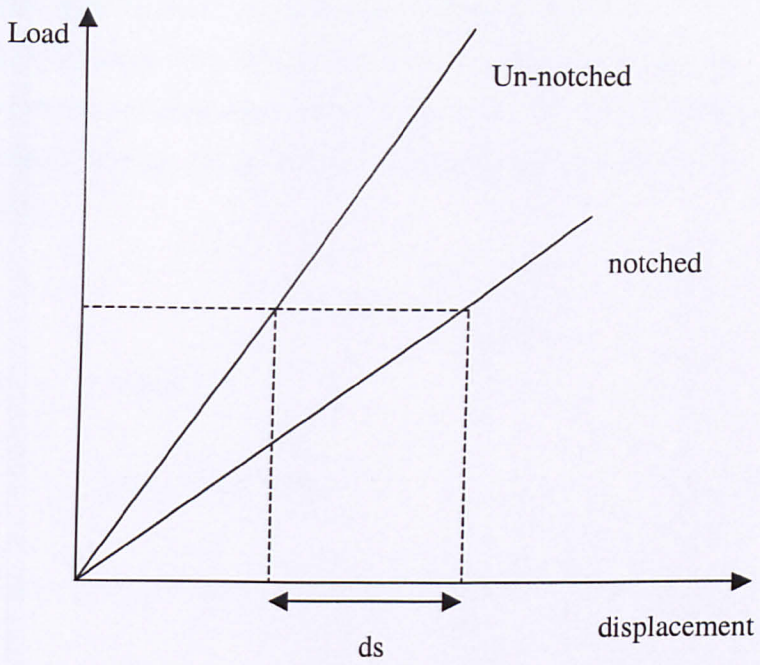

Figure 4-21 Schematic of crack opening displacement correction process.

The tests were then conducted on Instron testing machines, the displacment rate was fixed at 0.1mm/min. This velocity was chosen in order to minimise any additional matrix cracking that may have taken place during testing. The data acquisition computer was again used to monitor load and crack opening displacement (strain). The programme used to measure these parameters was a stripped down version of the code developed for measuring the elastic properties.

From this data, graphs of load vs. crack tip opening displacement could be constructed from which the material stiffness was deduced and hence, compliance was calculated. With this data now present in an excel spreadsheet, manipulation of the results was straight forward. A graph of compliance vs. crack length was plotted. From this a line of best fit was calculated. Differentiation of this equation allowed determination of the relationship $\frac{dc}{da}$.

The strain energy release rate G was then calculated using the formula explained in the literature review (section 2.5.5). These relationships are valid in the exercise, since

although these expressions have been evolved to cater for isotropic materials, these simple relationships are valid here (section 2.5.3). This is because the materials may be considered as transversely isotropic. In reality it has been shown that they are not quite equal, due to the difference in fibre packing between the radial and axial directions.

$$G_{IC} = \frac{P^2}{2\ b}\left(\frac{dc}{da}\right)$$

Where: P=Load

b= specimen width.

Once G had been determined a value for K can be found using:

$$K_{IC} = \sqrt{\frac{G_{IC}E}{1-\nu^2}}$$

Where: E=Young's Modulus

υ=Poisson Ration

4.8.3.2 Results

Using the SNEB tests as a guideline the GFRP layer was tested as a single entity rather than defining inner and outer sections. This is because the fracture toughness and strain energy release rate are predominantly resin controlled properties.

A third order polynomial was fitted to each of the compliance calibration data. The differential of this expression gives $\frac{dc}{da}$ at any crack length.

For GFRP (Figure 4-22) :

$c = 0.6978a^3 - 0.0024a^2 + 7E\text{-}07a + 2E\text{-}08$ with $R^2 = 0.9915$

$$\therefore \quad \frac{dc}{da} = 2.0934a^2 - 4.8\times10^{-3}a + 1\times10^{-6}$$

Table 4-9 Fracture toughness results for GFRP layer

Property	Mean Value	Standard deviation	C_v %
G_{IC}	235.9 J/m^2	37.7	16.0
K_{IC}	1.994 MPa m$^{1/2}$	0.157	7.9

Similarly for CFRP (Figure 4-23)

$c = 1.6935a^3 - 0.0107a^2 + 3E\text{-}05a + 3E\text{-}09$ with $R^2 = 0.9905$

$$\therefore \quad \frac{dc}{da} = 5.0805a^2 - 2.14\times10^{-4}a + 3\times10^{-5}$$

Table 4-10 Fracture toughness results for CFRP layer

Property	Mean Value	Standard deviation	C_v %
G_{IC}	216.0 J/m^2	41.0	19.0
K_{IC}	1.391 MPa m$^{1/2}$	0.134	9.7.

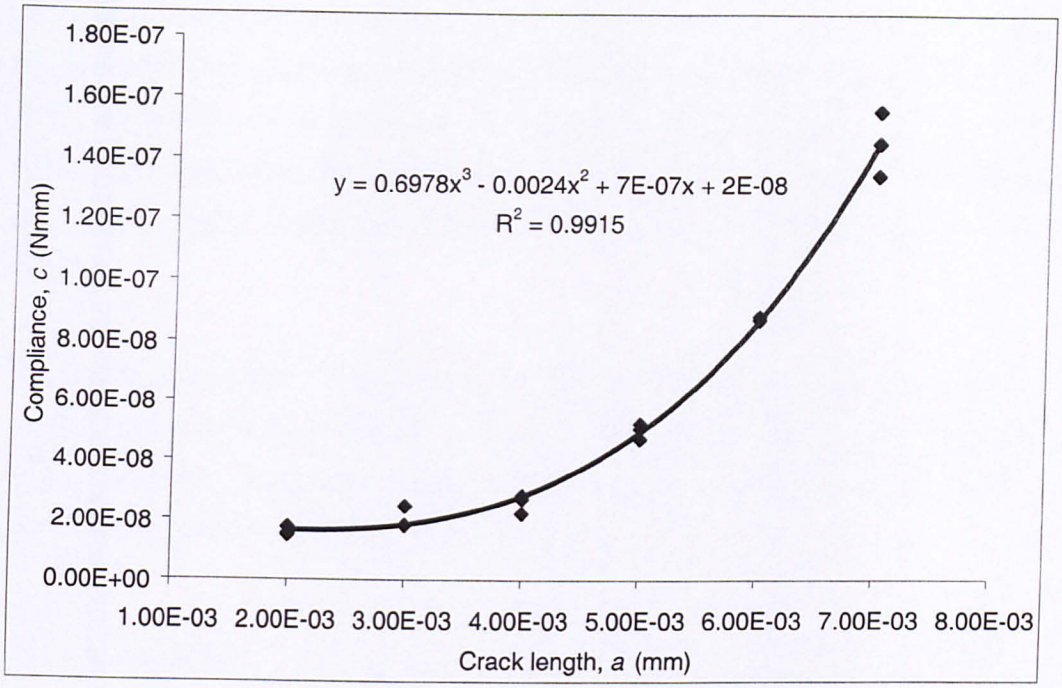

Figure 4-22 Compliance (c/Nmm) vs. crack length (a/mm) for GFRP.

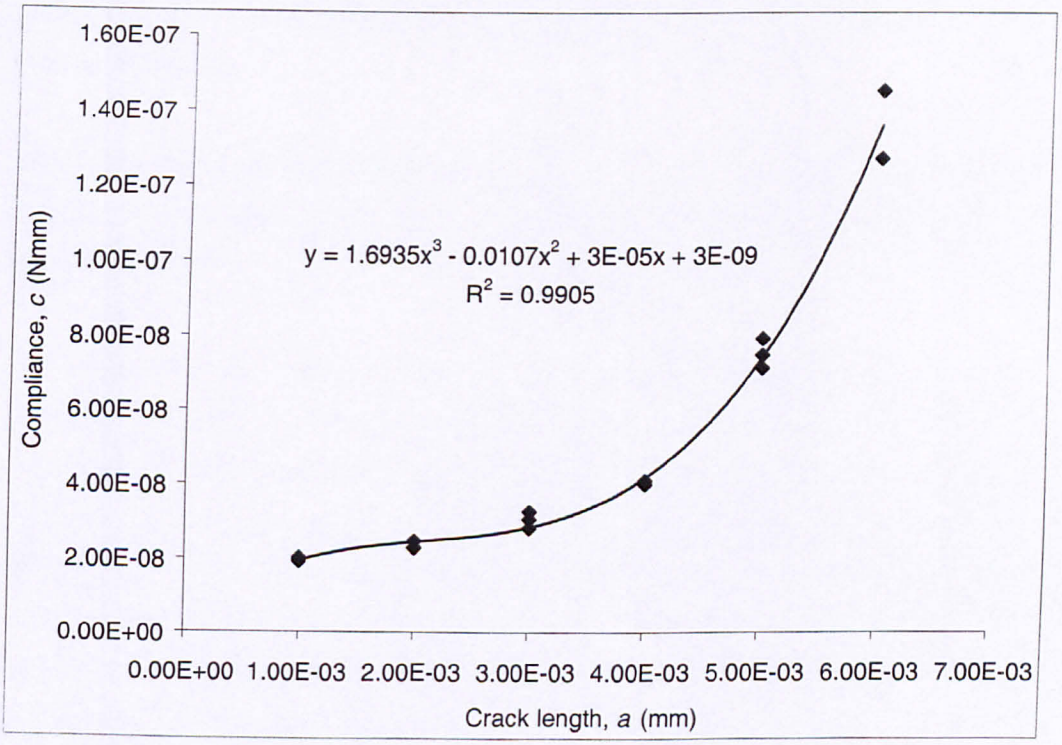

Figure 4-23 Compliance (c/Nmm) vs. crack length (a/mm) fro CFRP.

Since the K values are derived from the G values, the variance for the G value is of greater importance. Again this variance is high. The mean G values for the CFRP and GFRP are within 10% of each other. This suggests that the fibre type has very little effect on the transverse toughness in these materials. The factor that sets the K values apart is the higher transverse modulus, due to the glass fibres themselves being isotropic.

The values generated for G and K compare well with those reviewed in the literature, for example those tests conducted on GFRP by Kunmar quoted G_{IC}= 264 Jm^{-2}. The CFRP results are below those tested using UD composites in ASTM 5528 [50], at . G_{IC}= 216 Jm^{-2} compared to G_{IC}= 400 Jm^{-2}

4.9 Discussion

The evaluation of the elastic properties of composite materials always involves a large degree of scatter. Surprisingly, this scatter is no more pronounced when evaluating the fracture behaviour.

The development of the through thickness test method has been successful. The design of the end tabs has resulted in a quick and easy method for evaluating the elastic properties.

The values for these elastic properties of the various composite layers are all reasonable, even if the variances are high. As stated, the results in the hoop direction are reasonable for the test method. In the radial and axial directions the test method performed well, meeting its design targets. It was found that the radial modulus of the GFRP, varies with the radial position that the specimen was cut from. These differences in modulus are due to the changing volume fraction across the radius of the rotor. This relationship is illustrated in table 3-3. This correlation between V_f and Modulus can be compared with numerical models (Figure 4-13). The experimental data fits the Halpin Tsai model well. Thus, it was also found that the moduli of the various layers varied between the radial and axial directions. This is a result of the differing volume fractions in theses directions.

5 LONG TERM TESTING

5.1 Introduction.

With a minimum lifetime requirement of 20 years for the rotors, the long term behaviour of the material was of considerable importance. Studies of the behaviour of composites, with prolonged exposure to stresses in the transverse direction, are scarce. The definitive evaluation of these properties was fundamental for the successful completion of the project, However, although it was assumed, that with the elevated temperatures, the materials visco-elastic behaviour would probably increase the rotors resistance to cracking. creep effects were regarded as outside the scope of this study. Consequently evaluating the rotor materials crack growth characteristics was the primary long term concern.

5.2 Long term creep rigs.

The creep rigs used for the long term testing were originally designed and manufactured by ICI [13]. The rigs were supplied and used at QMW, prior to this project producing reliable data. Thus, they have not been modified in any capacity and the test method was designed to be entirely compatible with them.

The rigs are based upon a simple cantilever beam principle, (Figure 5-1). The ratio of the moment arm is 10:1. The use of the counter balancing mass allowed precise amounts of load to be applied to specimens. An Excel spreadsheet was used to calculate the magnitudes of the required forces on the various specimen, given the initial crack length and hence K value. The results of these calculations were outputted as a mass on the hanger and a position for the counter mass.

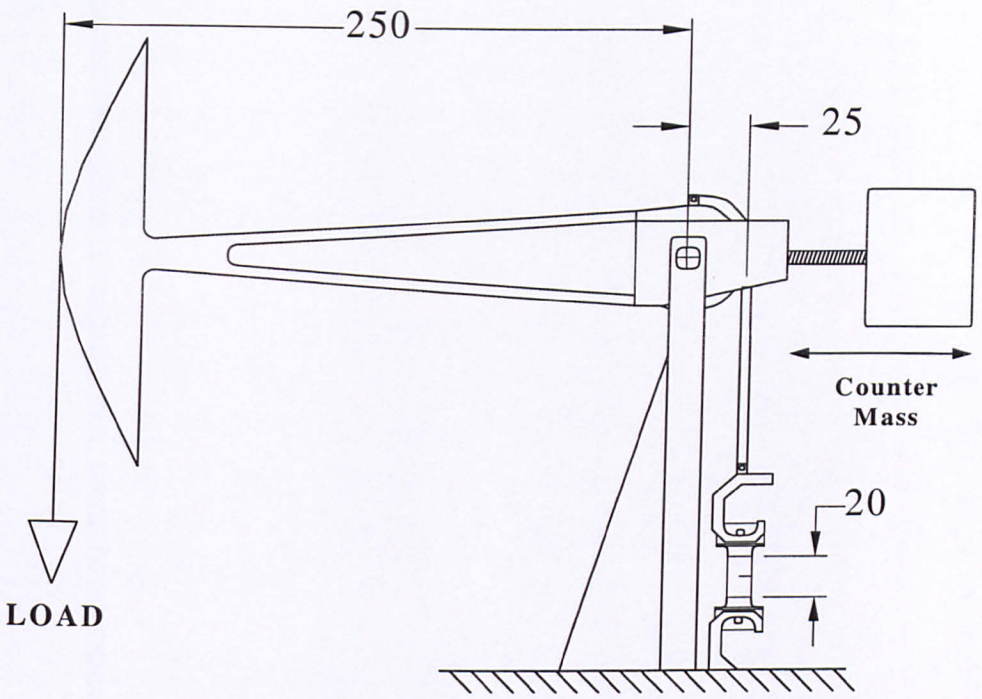

Figure 5-1 Schematic of Creep rig (dimensions in mm)

5.2.1 Experimental methods

The experimental method involved using the same notched specimens as the static compliance calibration tests. With the test conditions known the time to failure was monitored. This produced suitable results for the bulk of the subsequent analysis. However, it was deemed desirable to measure the crack growth rate. Since no long term crack growth monitoring system existed a couple of ideas were proposed.

Effectively two competing methods emerged as possible solutions. Firstly the use of crack growth strain gauges either broken contact type or simple gauges bonded across the crack opening (i.e. compliance calibration method), was considered. In competition with this was an imaging system whereby the crack length would be monitored by way of a series of images taken over a set time period.

The relative advantages and disadvantages of the two proposed solutions were considered. The principle advantage of the strain gauge system was the higher

reliability when compared with the imaging system. The crack tips in the material were very fine and some concerns were raised over the ability of a digital camera to detect these faint lines. Research and tests on a number on camera types showed that it was possible to detect the crack tip. The camera also allowed the discrete measurement of the crack length and this could be remotely recorded.

A major drawback for the strain gauge system was the reliance on a large number of amplifiers which were not readily available and the cost of these was very high. However, an advantage of the strain gauge system would be that since a computer would monitor all the crack behaviour it would also be possible to use the computer to record the final time to failure. With the digital imaging system this time would have to be recorded manually.

The imaging option was chosen for the following reasons.

- Acceptable accuracy.
- Fixed costs, i.e. cost is constant irrespective of number of specimens tested.
- Ease of use.

A digital camera was chosen primarily due to the zero processing costs. The camera chosen was a Polaroid PDC-2000 with a very high resolution (1600×1200 pixels). This worked in combination with a series of macro lenses that were tested with the assistance of Polaroid UK [72]. The culmination of this work resulted in digital images of the specimen (Figure 5-2), with acceptable resolution around the crack tip, (Figure 5-3).

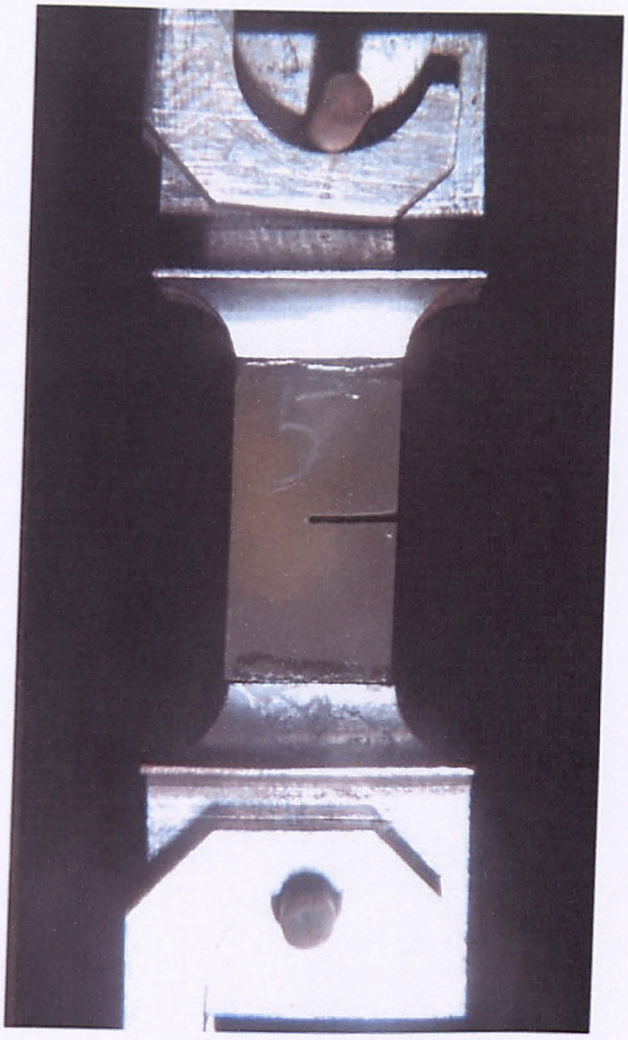

Figure 5-2 Sample camera output.

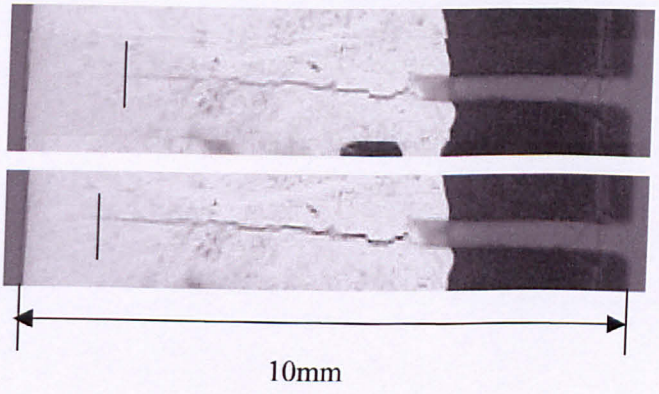

Figure 5-3 Series of crack images.

5.2.2 Camera jig.

A camera jig was designed to minimise the set-up time for the camera on the rigs. The desired design of the jig was such that it would allow the camera to be easily moved between creep rigs. It was also required to align itself automatically after every move.

The initial design involved mounting the camera on the jig itself. However, analysis of the rig geometry meant that it was not physically possible to achieve this. Since the jigs were accurately arranged in two continuous banks, the next best solution would be to mount the camera of the adjacent rig, using the knowledge that the position of each rig is fixed in relation to the others. Thus, mounting the camera on the neighbouring rig would allow these parameters to be accomplished.

The final design uses these design criteria and the fact that the creep rigs incorporate various constant reference planes to mount the jig from (Figure 5-4).

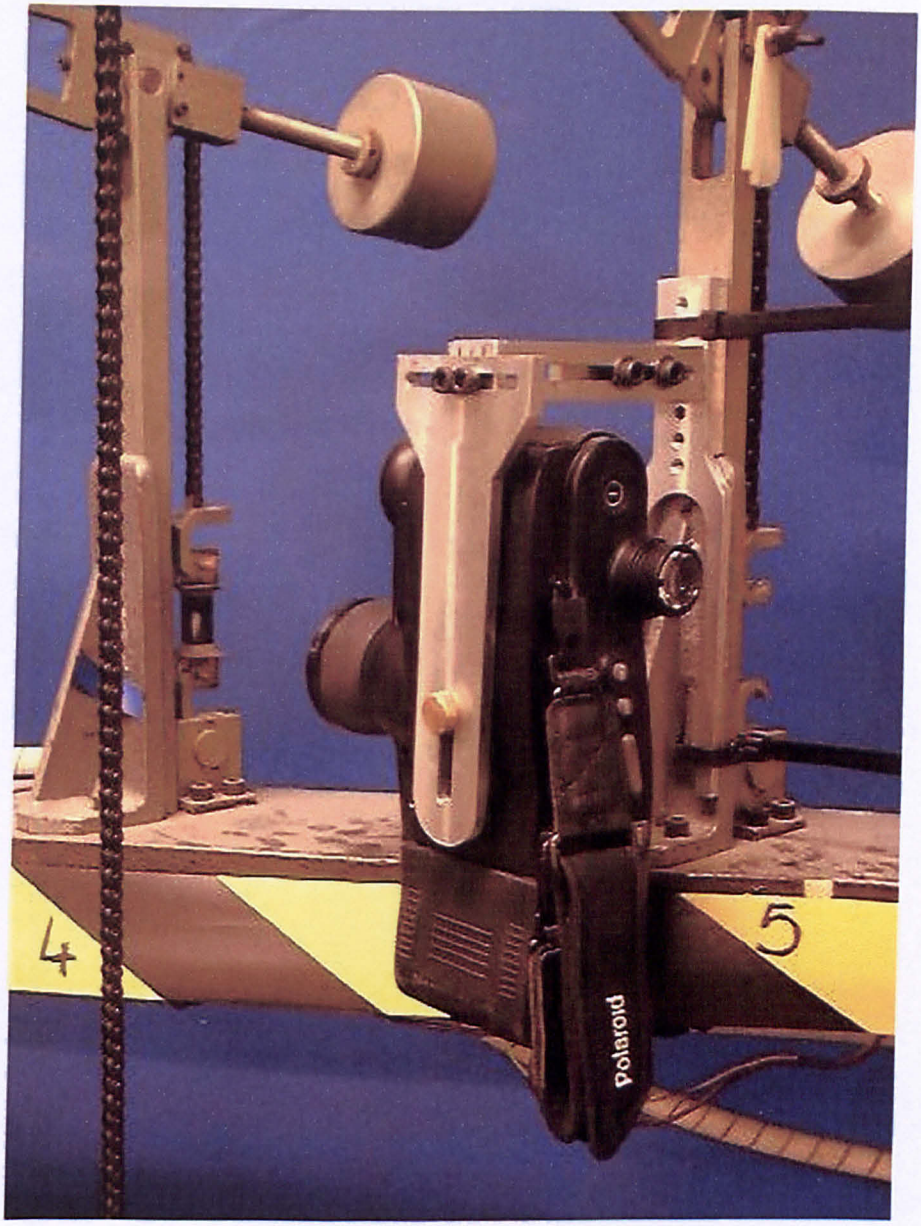

Figure 5-4 Camera jig in operation.

5.3 Results.

The results were recorded as time to failure for the specimens with a corresponding set of digital images in some cases.

To enhance the contrast of the crack, the sides of the specimens were marked with a white paint and the photos were converted to black and white.

5.3.1 Processing.

The load applied on the notched specimens was recorded, as was the time to failure. The time to failure was defined as the time elapsed for the specimen to completely crack into two separate pieces. This raw data is represented in figures 5-5 and 5-7. It can be seen that as one would expect, the lower the load on the specimen the longer the time to failure. Conversely, the greater the initial crack length, the shorter the time to failure for a given load.

The fracture toughness for the long term data was calculated using the same principles as the static tests (section 4.8.3.2). i.e. the original master compliance calibration curves for the materials were used (Figures 4-22 and 4-23). This allowed the initial K values to be plotted against time to failure (Figures 5-6 and 5-8)

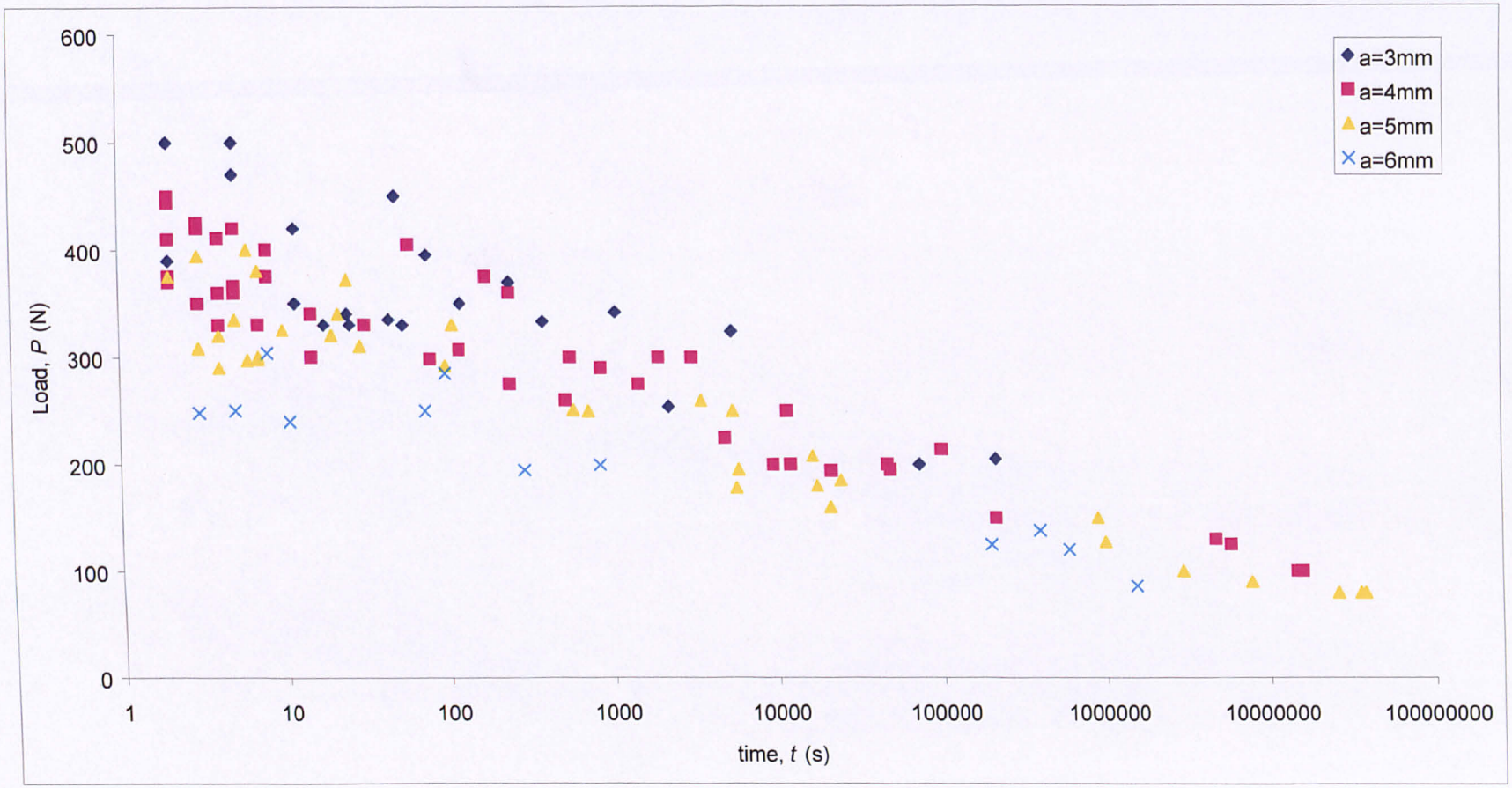

Figure 5-5 Load (N) vs. time (s) for GFRP Layer.

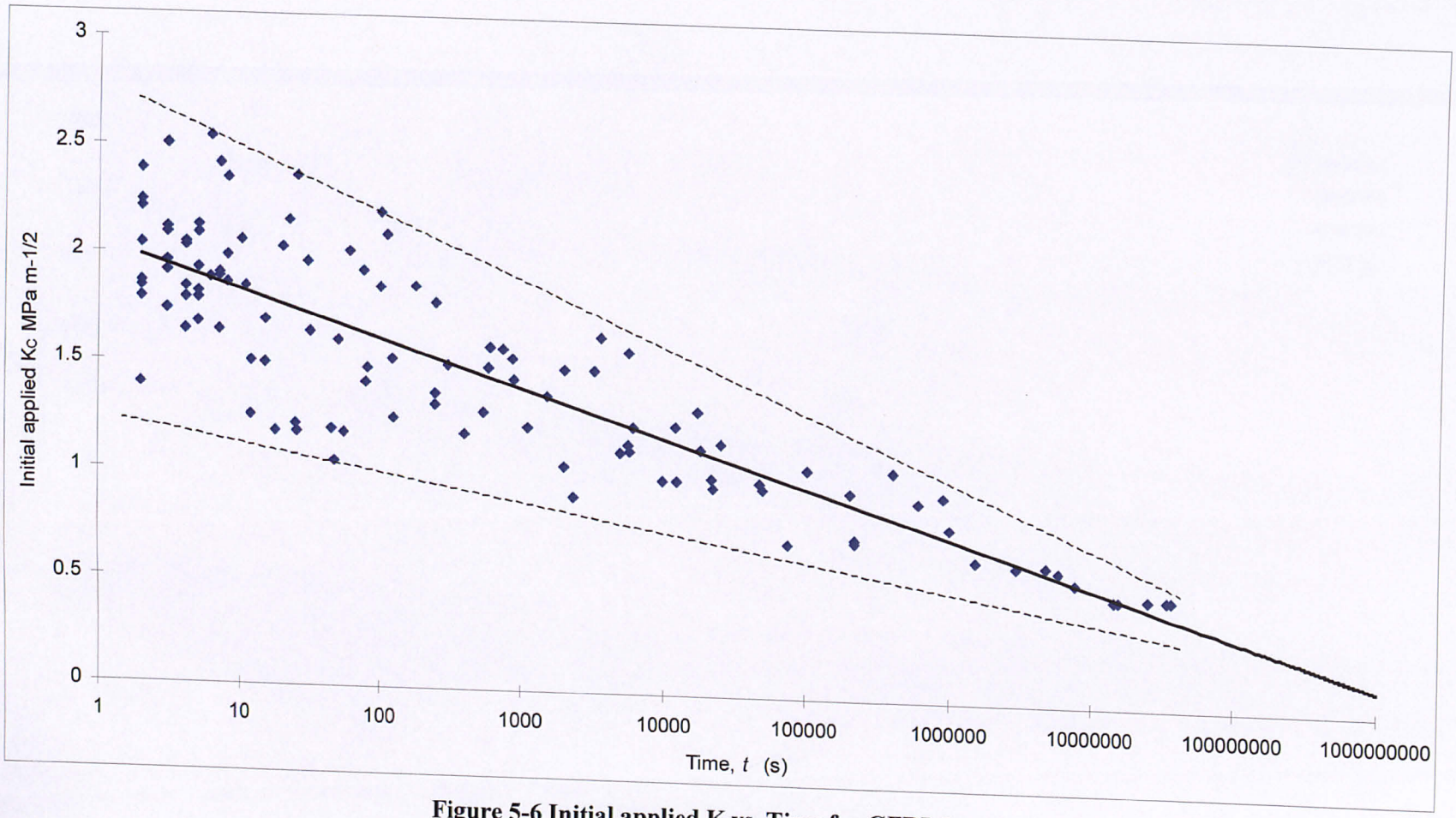

Figure 5-6 Initial applied K vs. Time for GFRP Layer.

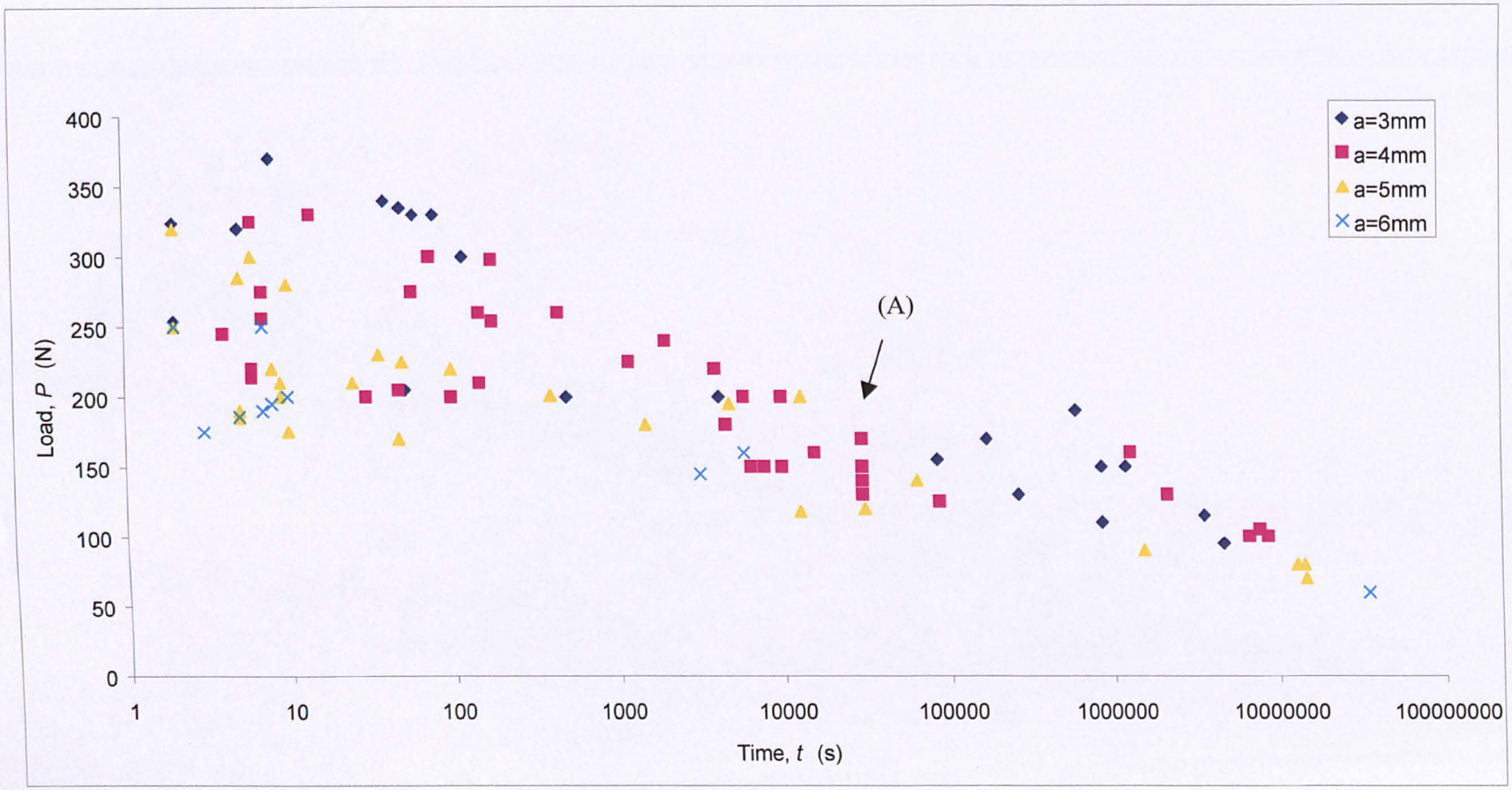

Figure 5-7 Load (N) vs. time (s) for CFRP Layer.

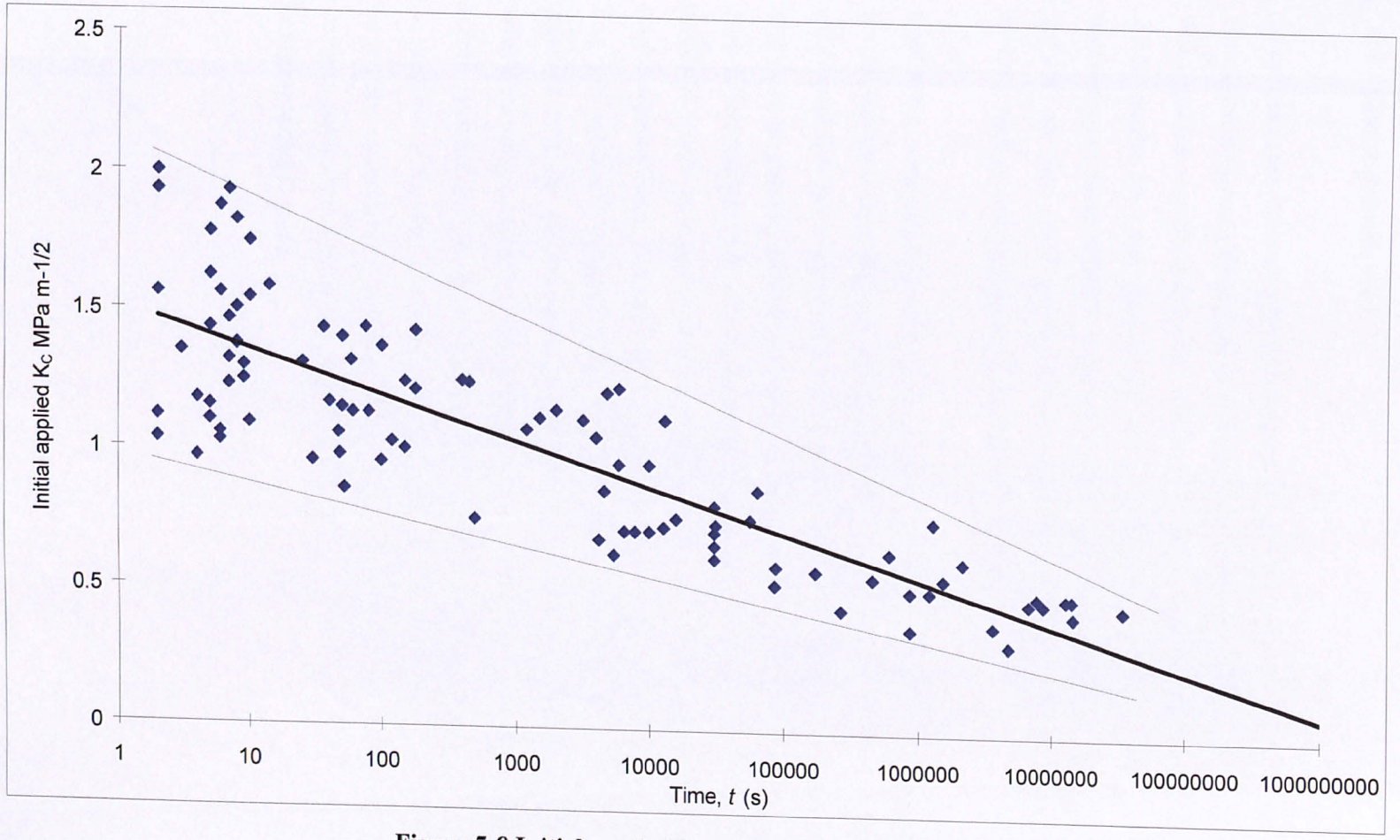

Figure 5-8 Initial applied K vs. Time for CFRP Layer.

5.4 Crack growth rate.

In certain cases the crack growth rate was directly measured. This was achieved using the digital imagining system, as described in the previous section. The premise behind this approach was that the notches will experience slow crack growth before failure. In all 50 results for crack growth rate were recorded, 25 for GFRP and 25 for CFRP notched specimens. In both cases more specimens were produced but some of these showed no slow crack growth. It was assumed that those specimens that did not exhibit crack growth had poorly sharpened crack tips.

Specimens were notched with either a 3 or 4 mm initial crack length. This crack length was used to avoid any specimens failing by end tab de-bonding. Since it was anticipated that some specimens would be lost through unsuitable crack tips, it was important to guarantee those specimens that were good, then failed by slow crack growth The notches were then sharpened in the conventional manner. A typical set of results is shown in figure 5-9, these specimens were all GFRP and had an original crack length of 4mm. The rate was measured by determining the gradient of each line. This was relatively straightforward for most cases where linear crack growth was observed over the greater extent of the crack length and was determined manually rather than using a computer. The crack growth rate would always be biased towards a steeper gradient and thus more rapid crack growth if there was any doubt regarding the gradient of the line. It can be seen from the sample curves that the crack growth rate is quite constant for a particular batch of specimens. Also included on this chart is a sample curve from a three day test. This failed at a lower final crack length due to the higher initial K value.

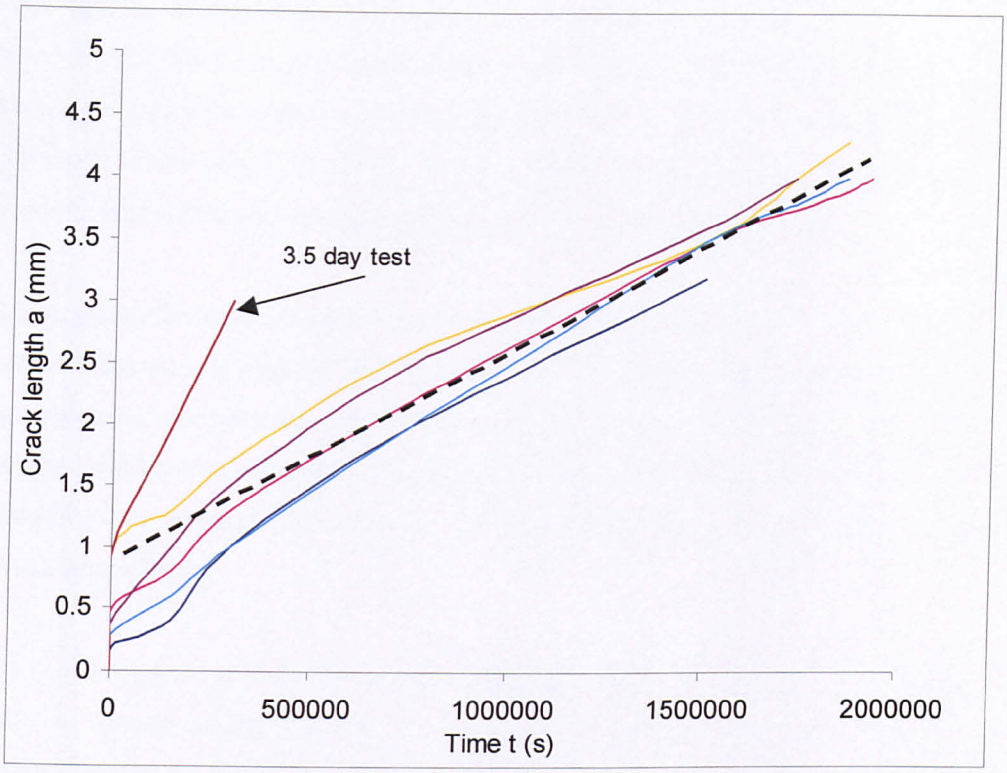

Figure 5-9 Approximately 1 month to failure crack growth rate raw data for several specimens.

When the crack growth specimens were loaded, this loading was conducted very carefully, although obviously it was not a controlled as per a tensile test machine. Thus, in the first few seconds of the tests the true crack growth rate was not observed. It is believed that some visco-elastic effects are having an influence on the crack growth. Thus, there was an initial crack growth response of anywhere between 0.3 and 1mm. No real correlation could be drawn between this initial crack length and load. While every care was taken to introduce the load onto the specimen as carefully as possible, this was still a manual task. Thus, it was prone to variability. This is in contrast to the static compliance calibration tests where the specimens are loaded up very slowly and constantly to reduce any visco-elastic effects.

Final K values were calculated at failure using the simple fracture mechanics expression.

$$K_{IC} = Y\sigma(\pi a_c)^{1/2}$$

The various specimens were all found to fail at similar K levels. The Y value was taken as that for a compact tension specimen, whose a/w ratio lies outside prescribed limits [16]. For the GFRP specimens the fracture toughness was approximately 1.72 $MPam^{1/2}$, while only 1.24 $MPam^{1/2}$ for the CFRP. However, these are averages and it must be stated that a large degree of scatter existed (Variances=25%+).

Thus, using this data coupled with the assumption that there is 0.6 mm (on average) instantaneous crack growth, it was possible to calculate the apparent growth rate of all the specimens, not just those from these tests. This was achieved since the initial crack length was known, as was the final crack length, the initial visco-elastic response could be accounted for, thus, then this crack length divided by time yields an apparent crack growth rate.

By plotting crack growth rate vs. time (Figures 5-10 and 5-11), the crack growth rate may be related to the original K_I value. In these charts the direct crack growth measurements are represented by the red triangles, and the derived crack growth rates are the blue diamonds. The best fit line of this data takes the form:

$$\frac{da}{dt} = AK_I^n$$

Presenting the data in this manner is useful since it allows the crack growth rate to be represented as an equation. This is extremely convenient when predicting the service life of components (see later).

For GFRP $$\frac{da}{dt} = 2.31\times10^{-7} K^{9.85} \qquad R^2 = 0.841$$

For CFRP $$\frac{da}{dt} = 3.96\times10^{-6} K^{9.93} \qquad R^2 = 0.806$$

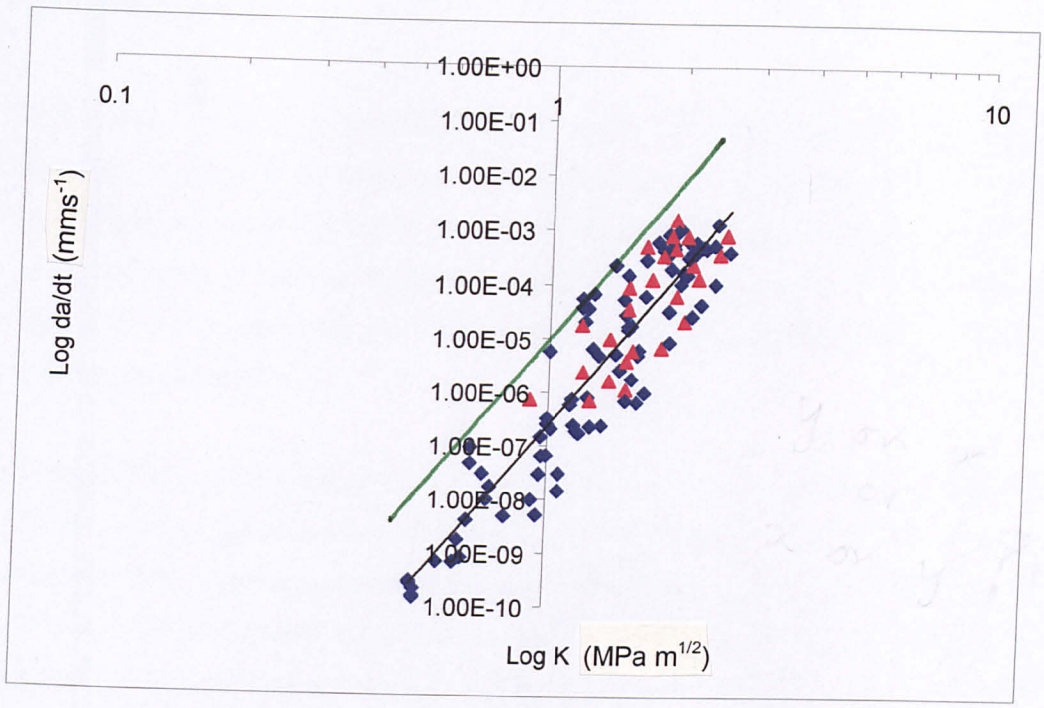

Figure 5-10 log crack growth rate (da/dt) vs. log time for GFRP.

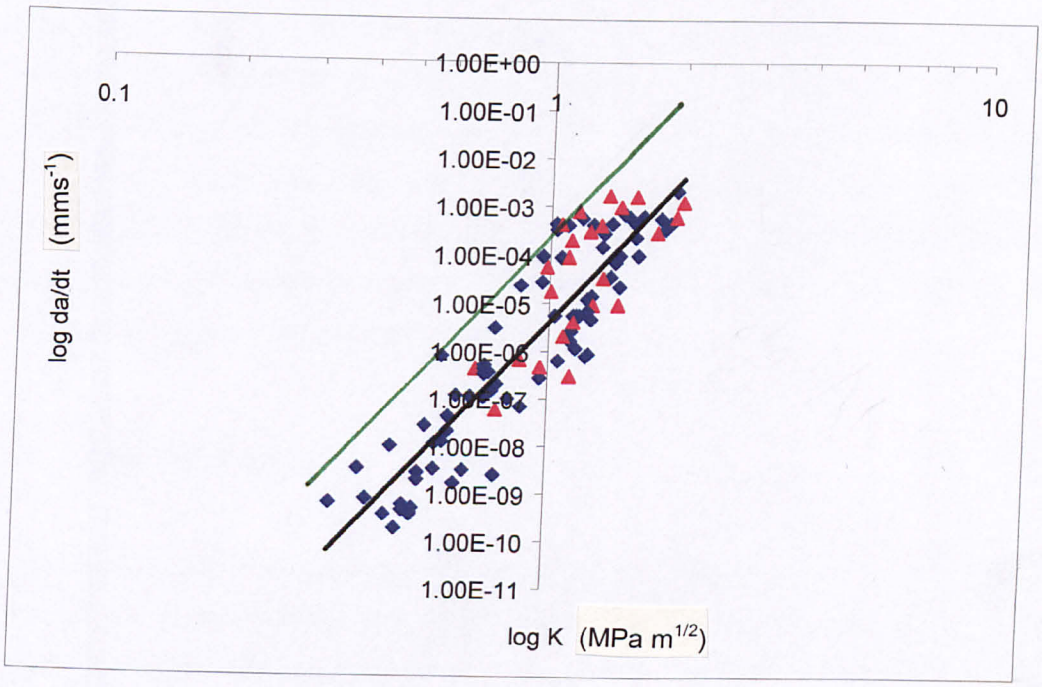

Figure 5-11 log crack growth rate (da/dt) vs. time for CFRP.

Addendum: The green line represents a 95% confidence line, see page 261.

5.5 Discussion.

The results for the static tests, both elastic and fracture toughness, exhibited large amounts of scatter. This scatter has been carried through to the long term tests. The high degree of scatter is expected to some extent with this type of test. By nature the testing of fracture behaviour in composite materials is very variable, and when this is combined with other parameters such as crack tip sharpening, large variances in the results were expected.

In figure 5-7, an event occurred (A), that caused simultaneous failure of a number of samples. It was presumed that this was caused by one specimen failing. When a specimen failed, the moment arm would swing back violently due to the counter mass. When the arm hit its travel stop, it sent a shockwave through the whole rack of rigs. A simple weight catching system was crafted from polystyrene to combat this. No similar events occurred after its installation.

The direct crack growth rate measurements are reasonable, although no direct comparisons could be found in the literature, the rates are faster than those measured by Hogg [39] in GFRP laminates. In this case the fibres were perpendicular to the crack front, which would account for the slower crack growth rate. However the material was exposed to an aggressive environment. The derived values of crack growth rate are comparable to the actual measured ones, although a large amount of scatter was present throughout these tests.

5.6 Fracture Surfaces

The fracture surface morphology was analysed using scanning electron microscopy (SEM). No specimen preparation was conducted other than coating of the specimen with gold and installing a conductive strip to the side of the specimen. The acceleration voltage was between 10-15kV.

The specimens examined were sets of those exposed to long term loads as well as a batch that had been tested statically. Both CFRP and GFRP samples were examined. Both sets had the same initial crack length (5mm).

When comparing the static and long term GFRP specimens at low magnification (Figures 5-12 and 5-13, crack growth is in the direction of the arrow.), the most obvious difference between static and long term tests is the amount of fibres that have been pulled away from the surface and the manner in which they have been pulled off.

With the crack direction marked, it can be seen in figure 5-13 that in the long term test, a period of slow crack growth has occurred. Here, virtually no fibres have been pulled away from the surface. This was followed by very rapid crack growth characterised by the muddled fibres at the bottom of the picture. In the long term specimens at low load it can be seen that the slow crack growth has occurred across a far larger area of the fracture surface.

Time dependant mechanisms in the matrix can be seen at high magnification (Figures 5-14 and 5-15). The depth and quantity of the striations in the matrix, are much smaller in the static test specimen. It is postulated that is primarily due to brittle cracking ahead of the advancing crack tip. These striations will have a small amount of plastic deformation associated with them. These are probably the marks that can be seen in the static samples.

As expected the CFRP specimens behaved in a very similar manner. This lends weight the earlier findings that suggest the fibre type has little influence on the fracture behaviour of composites in this direction. Thus, the interfacial bond strength also appears to have little effect on this property, since GFRP is known to have a higher interfacial strength, yet its toughness values are not significantly higher.

Figure 5-12 GFRP, Static Test. (magnification ×50)

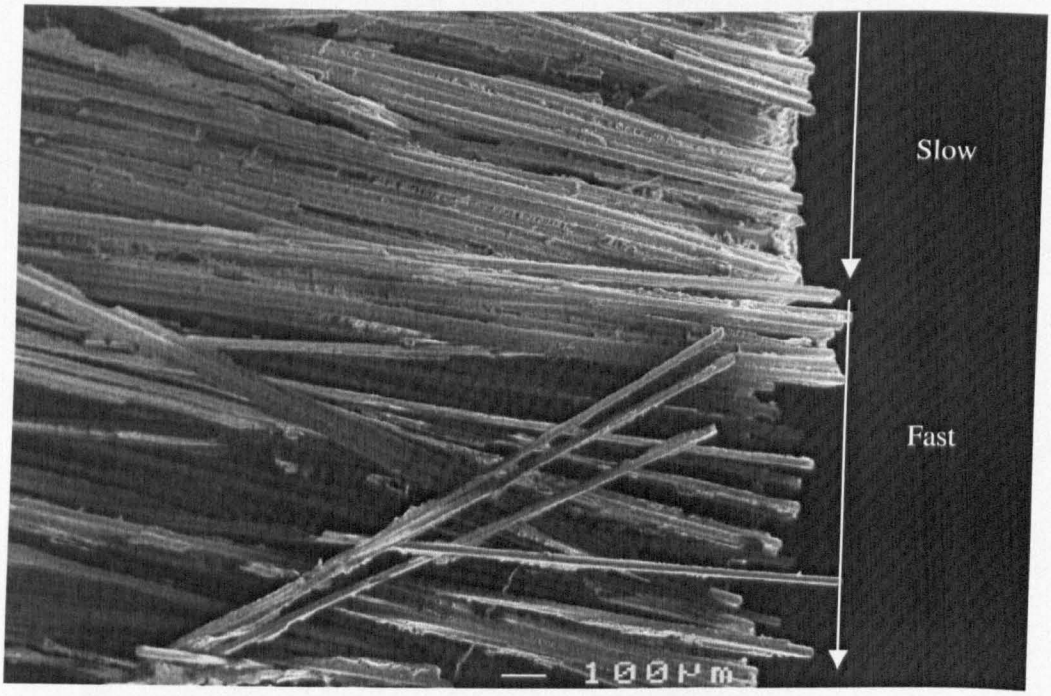

Figure 5-13 GFRP after 9 months. (magnification ×45)

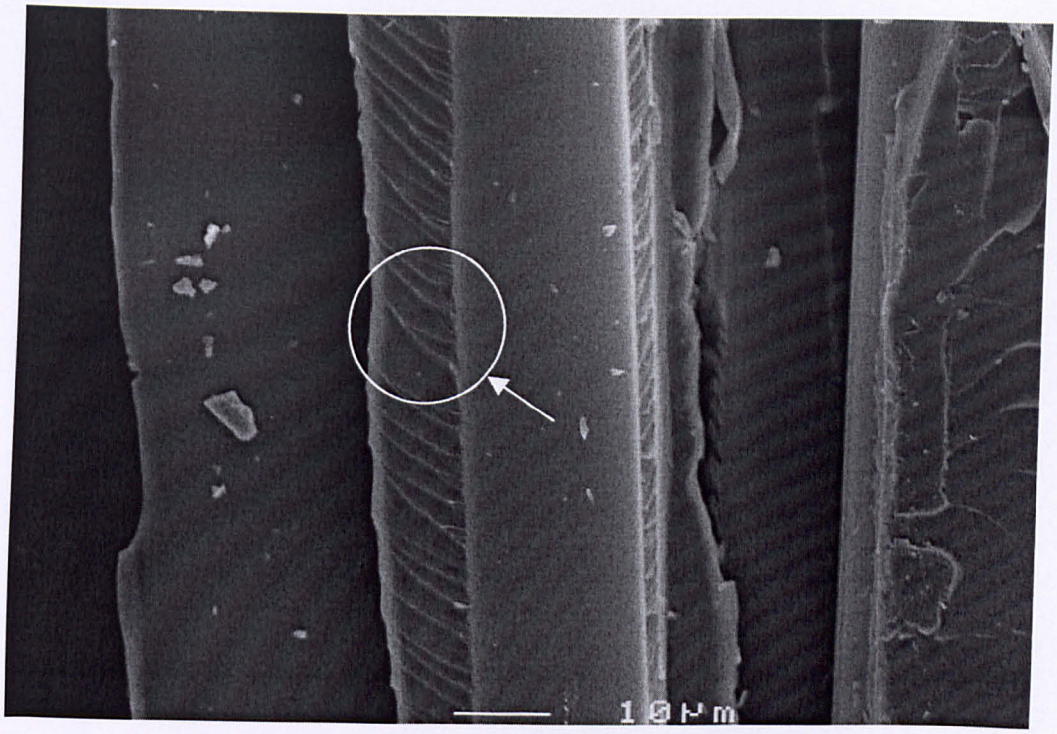

Figure 5-14 GFRP Static test. (magnification ×1100)

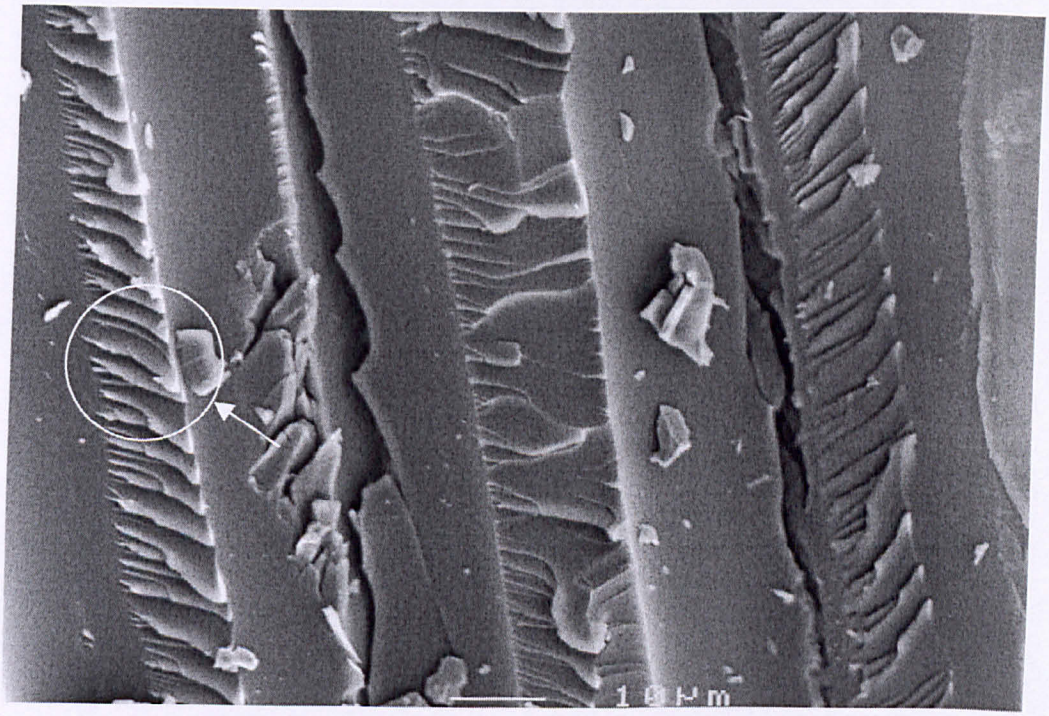

Figure 5-15 GFRP after 9 Months. (magnification × 1100.

6 STRESS STATE WITHIN THE ROTOR.

6.1 Introduction.

The actual physical stress state within the rotor as a result of the manufacturing process and under normal operating conditions is complex. The maximum angular velocity of the flywheel is 700 Hz. With a flywheel exposed to this dynamic situation, the resultant forces within the composite rotor will be of considerable magnitude and must be studied in great detail. Since instrumenting a flywheel rotor is very difficult, numerical modelling is the only practical method to evaluate these forces and displacements. This approach is widely accepted in the field of flywheel research,[3,4,7,9,74].

When conducting dynamic as opposed to static analysis using FE techniques it is necessary to calibrate all the dimensional units to ensure the outputted values are correct. This procedure is illustrated in Appendix B.

6.1.1 Input data for model and loading conditions.

The un-deformed model (Figure 6-1) shows the element geometry used to evaluate the stress state This model was based upon the flywheel geometry supplied by Urenco (Table 1-3). The entire rotor was modelled and it was found easiest to simplify it to an axi-symmetric model. This did not detract any accuracy from the results since the rotor is symmetrical in the cylindrical plane. The mesh density was increased in the centre of the rotor, to obtain a more accurate prediction. Through the centre section the element density is increased to one element per mm. This is the same mesh density as previously used. This was again found to produce suitable results. ABAQUS [10], was set up to extrapolate a mean stress value to the centre of each element. Element sets were created along the centre lines of the rotor, both in the axial and radial directions (Figure 6-1). The input deck for the flywheel rotor may be found in Appendix A2. The greater extent of the node and element data has been removed due

to space constraints. However, the important input variables in terms of boundary and loading conditions are all present. The output options are also shown, the results from these options were then exported and processed using Microsoft Excel.

The material properties for the model are summarised in table 6-1. This table also illustrates the origin of the data used. All longitudinal modulus, thermal contraction and density values were measured and supplied by Urenco. It would be possible to calculate more exact values for thermal contraction if the thermal data for the constituents was known. Since the moduli values differed with direction (E_{22}, E_{22}) it follows that the thermal contraction (α_{22}, α_{33}) should also change. However, the magnitude of this difference will be very small, and thus the effect upon the cured stresses in the rotor would have been negligible.

No specific boundary conditions were applied to the model. This was due in part to the fact that during curing the rotor was gently rotated while still on the mandrel and air heated. The rotor cures away from the mandrel and end plates. Thus, no external forces were exerted on the part, other than the rotor's own mass, as it lay on the rotating mandrel. To apply boundary condition to copy this behaviour was regarded as unnecessary and overly complex. The curing cycle (Figure 3-2) was simplified. It is assumed that at 110°C, a zero global stress state exists within the rotor. The model used this condition. Curing was initiated at this temperature and cooled down to 40°C. This was the chosen operating temperature. In the FE analysis, this curing process was completed as the first step of the model, with a single increment.

The dynamic loads are exerted on the rotor by specifying the rotational acceleration. Thus, the angular acceleration was inputted in $rads^{-2}$. This coupled with the various densities of the constituent materials induced the stresses and strains in the rotor. The analysis was again unconstrained, since during operation the rotor is held in place by a magnetic bearing and no other external forces apply. This analysis was again completed in a single step with seven increments, each increment representing an increase in angular velocity of 100Hz.

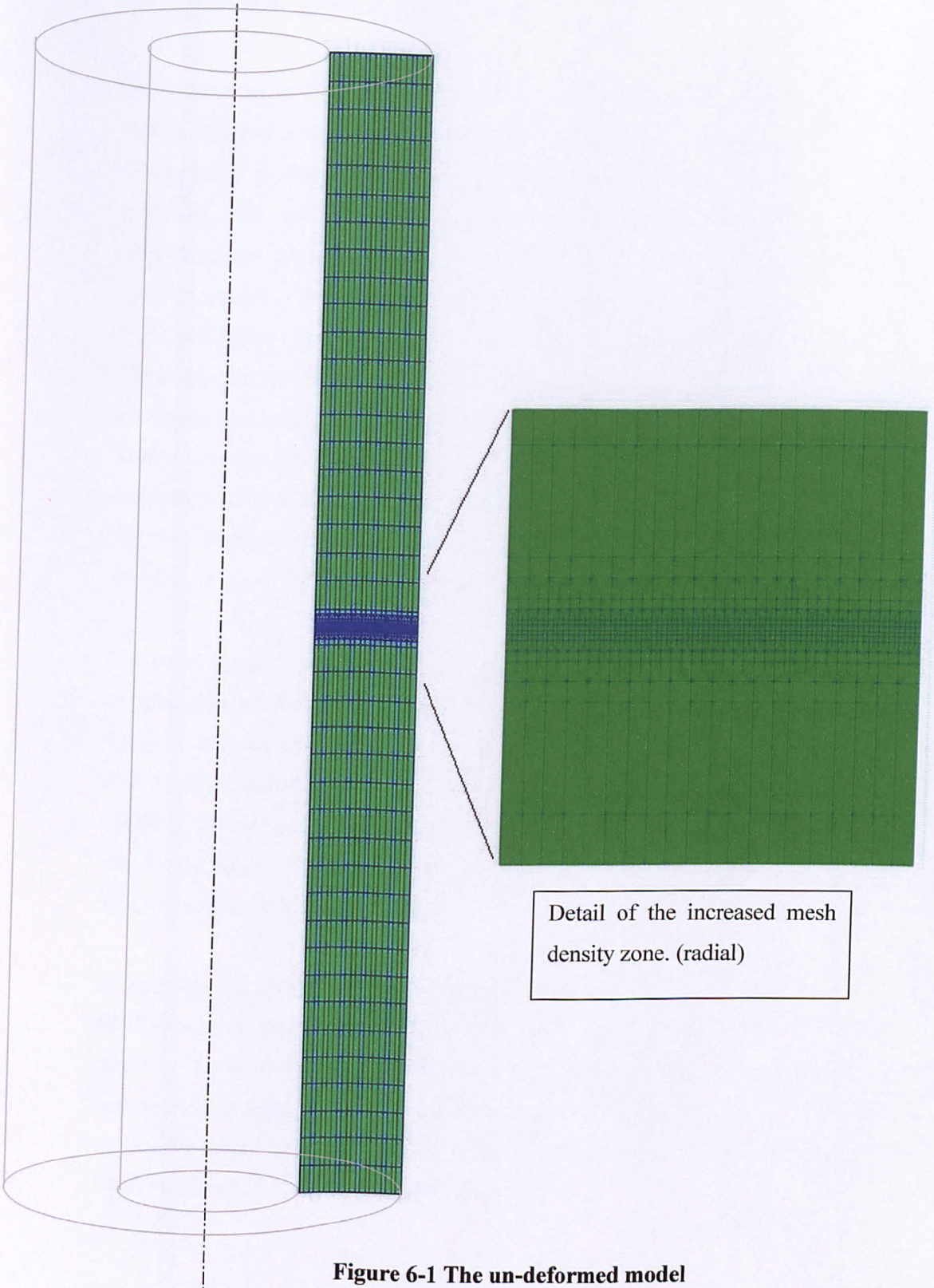

Detail of the increased mesh density zone. (radial)

Figure 6-1 The un-deformed model

6.2 *Residual stresses and strains.*

Since the rotor is a hybrid of materials with differing thermal properties, cooling will induce residual stresses and strains in the rotor. These stresses and strains are also compounded by the fact that the rotor has a large thickness. Thus, in the post cure condition, the rotor has significant residual stress levels (Figure 6-3). Most importantly, in terms of designing for maximum energy storage, the CFRP layers have been designed to contain large compressive stresses in the hoop direction. These range from 39.9 MPa at the interface with the GFRP layer up to 76.1 MPa at the rotor' edge. Thus, the corresponding hoop strains are also low, the negatively strained outer layers are again advantageous for increasing the energy storage capacity of the flywheel. This allows the flywheel to run faster as the stresses in the hoop direction govern the maximum speed of the rotor. The remaining GFRP and NdFeB layers are in tension in the hoop direction. The radial stress varies in a parabolic manner, reaching a peak of 10 MPa, at the CFRP/GFRP interface.

The axial stress in the NdFeB layer is constant at 3.6 MPa. The GFRP layer is in compression, while the CFRP has a maximum residual tensile axial force of 4.6 MPa. These values are too low to cause any cracking at this stage. The axial and radial strains show contraction, as expected. The uniform axial strain is unusual, due to differing thermal contractions, some variation in this strains was expected. However, the output model data is across the mid-plane of the rotor and thus any contraction will be symmetrical around this plane.

In practice, the residual hoop stresses and strains are caused by contractions in the fibre direction, however the fibre direction is not perfectly aligned in the hoop direction. Since, the rotor is manufactured by filament winding, at an angle ~89° (see manufacturing section 3.4), the resultant residual hoop stress is off-axis. This is clearly illustrated by figure 6-2, which shows a distorted section. The section was cut 5mm thick and after cutting buckled out of shape.

The overall dimensional changes of the complete rotor, as a result of the curing process, show a radial shrinkage of 8.3886×10^{-2}mm (0.10%) and an overall axial shrinkage of 2.09mm (0.23%).

Figure 6-2 Distorted rotor section.

Table 6-1 Input data for FE Models

Material	Property	Data Origin		Quantity	Model Units
		Urenco	QM		
NdFeB Layer	Longitudinal Modulus E_{11}	✓		35.0	MPa
	Transverse Modulus E_{22}		✓	13.7	MPa
	Transverse Modulus E_{33}		✓	16.7	MPa
	Poisson Ratio υ_{13}		✓	0.13	
	Poisson Ratio υ_{12}		✓	0.13	
	Poisson Ratio υ_{23}		✓	0.32	
	Coefficient of Thermal Contraction α_1	✓		8×10^{-6}	$°C^{-1}$
	Coefficient of Thermal Contraction $\alpha_{2,3}$	✓		32×10^{-6}	$°C^{-1}$
	Density	✓		3209.15	Mg/mm^3
GFRP Layer	Longitudinal Modulus E_{11}	✓		48.0	MPa
	Transverse Modulus E_{22}		✓	13.7	MPa
	Transverse Modulus E_{33}		✓	15.6	MPa
	Poisson Ratio υ_{13}		✓	0.13	
	Poisson Ratio υ_{12}		✓	0.13	
	Poisson Ratio υ_{23}		✓	0.3	
	Coefficient of Thermal Contraction α_1	✓		8×10^{-6}	$°C^{-1}$
	Coefficient of Thermal Contraction $\alpha_{2,3}$	✓		26×10^{-6}	$°C^{-1}$
	Density	✓		2141.16	Mg/mm^3
CFRP Layer	Longitudinal Modulus E_{11}	✓		154.1	MPa
	Transverse Modulus E_{22}		✓	6.6	MPa
	Transverse Modulus E_{33}		✓	8.4	MPa
	Poisson Ratio υ_{13}		✓	0.021	
	Poisson Ratio υ_{12}		✓	0.021	
	Poisson Ratio υ_{23}		✓	0.3	
	Coefficient of Thermal Contraction α_1	✓		0.4×10^{-6}	$°C^{-1}$
	Coefficient of Thermal Contraction $\alpha_{2,3}$	✓		36×10^{-6}	$°C^{-1}$
	Density	✓		1612.33	Mg/mm^3

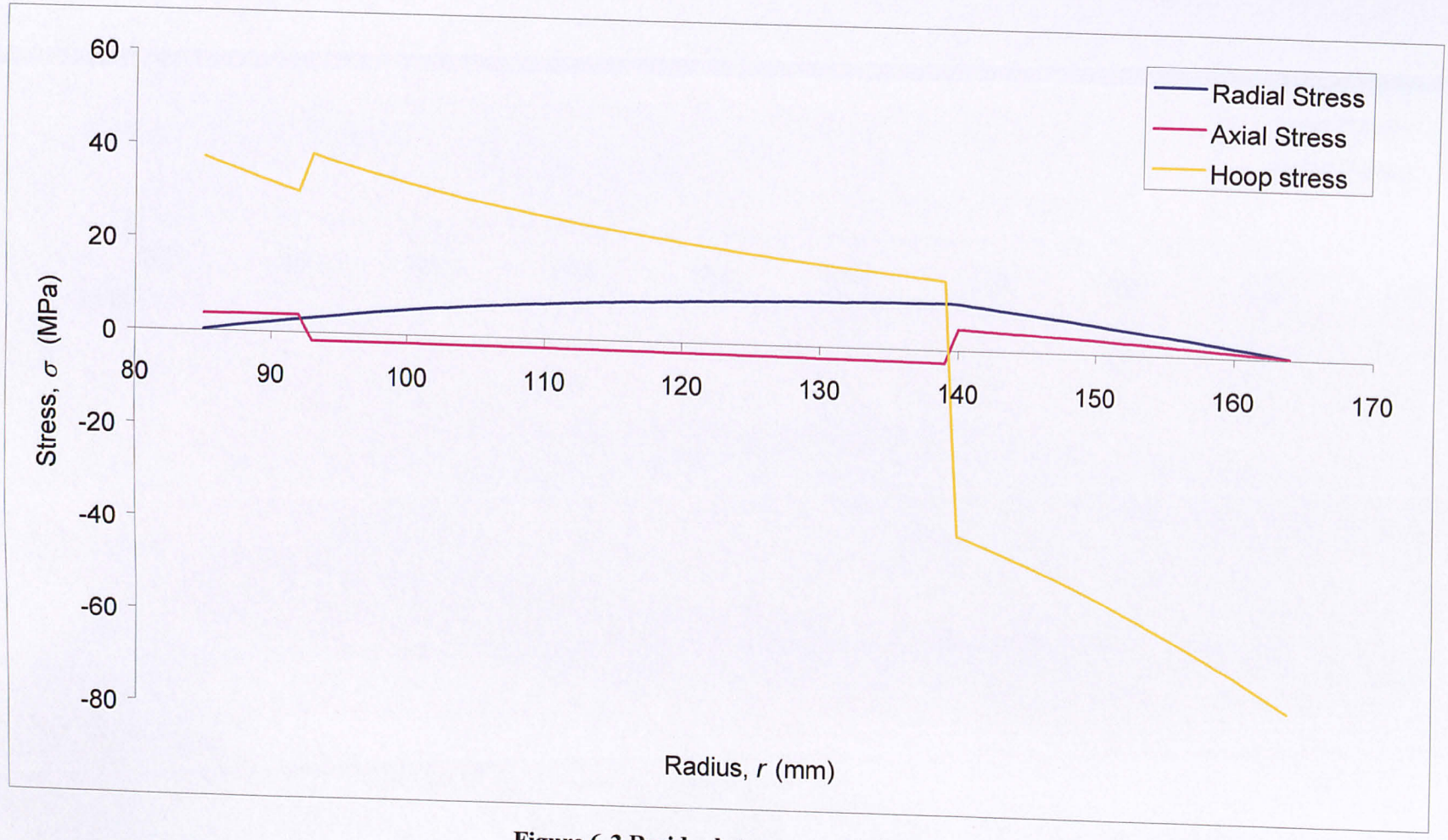

Figure 6-3 Residual stresses vs. radius

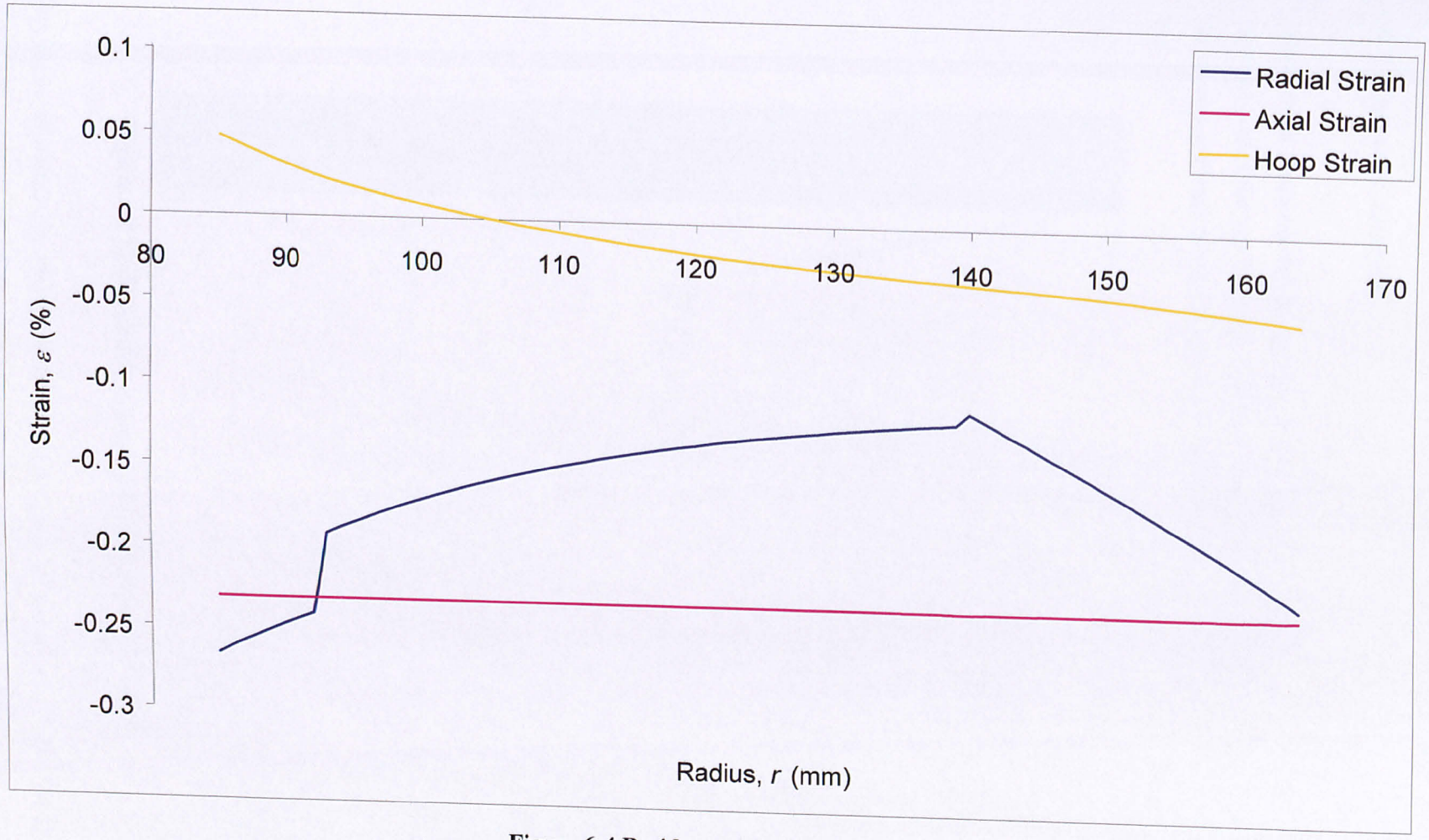

Figure 6-4 Residual strains vs. radius.

6.3 Dynamic Analysis

As the rotor accelerates to its operating speed range (300-700Hz), the stress and strain patterns within the rotor change. The magnitude of the stresses and strains increase to far more significant levels. The result of these angular velocities can be seen in figure 6-5

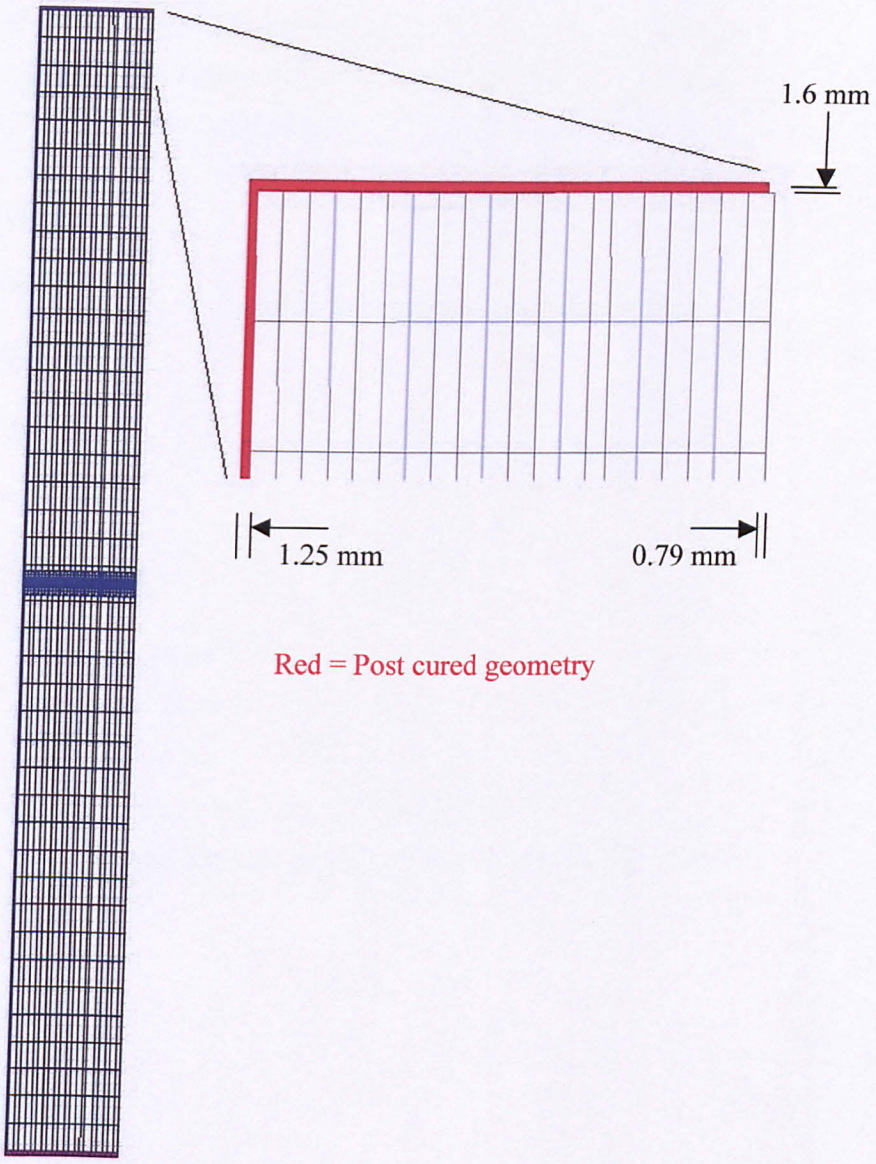

Figure 6-5 FE Prediction of rotor displacements at 700Hz

This figure illustrates the change from cured geometry, to running at 700Hz. As the rotor accelerates up to its maximum speed, the entire structure shortens by some

3.2mm (0.35%). This reduction in axial length is accompanied by an expansion in the inner and outer radii of the rotor. The inner radius increases by 1.25mm (1.47%), while the outer radius expands by 0.79mm (0.47%). The inner radius increases more than the outer due to the NdFeB and GFRP layers being pushed up against the CFRP layer as the rotor spins. Hence, the wall thickness of the rotor also changes, it reduces by 0.46mm (0.58%).

The relationship between hoop stress and rotor speed can be seen in figure 6-6. All the stresses in the rotor follow this type of relationship (x^2) between stress and speed figure 6-7. (note, for position of maximum stresses see later.)

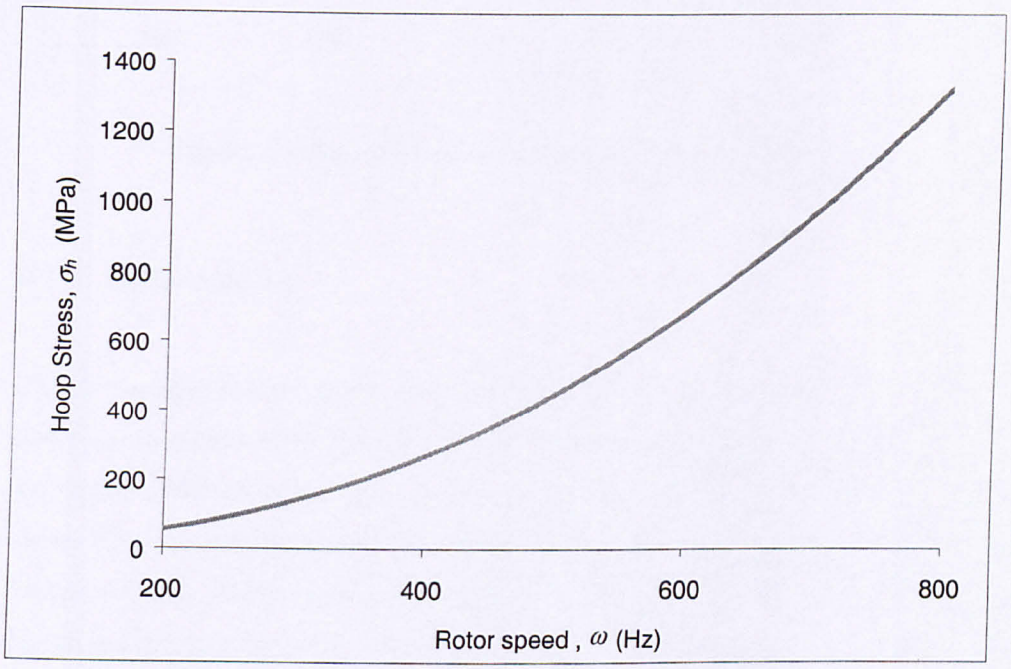

Figure 6-6 Hoop stress (MPa) vs. rotor speed (Hz).

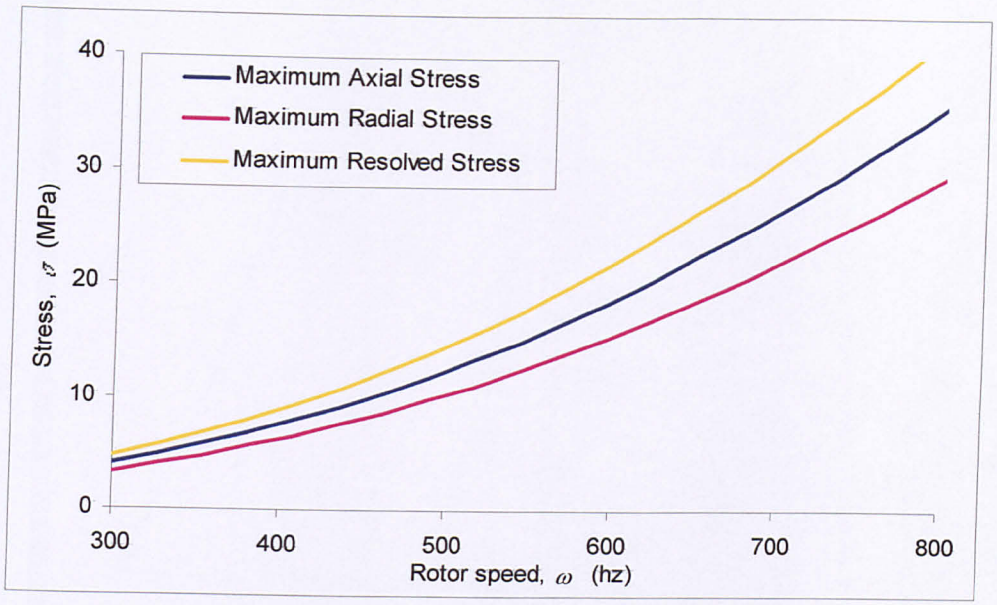

Figure 6-7 Transverse stresses (MPa) vs. Rotor speed (Hz)

6.3.1 Hoop Loading

Clearly the maximum stresses the rotor would experience in service are in the hoop direction, by nature of the flywheel theory (Figure 6-8). The maximum stress occurs at the GFRP/CFRP interface with a peak at a value of 1042 MPa. This is still within the capabilities of unidirectional T700 carbon fibre in this matrix. The reason the stress level climbs so dramatically at the interface is because the CFRP has a considerably higher hoop modulus and is supporting the GFRP layer. This is compounded by the greater density of the GFRP. The GFRP alone could not withstand this angular velocity. The stress in the CFRP at the outer edge has fallen to 774 MPa. The strain is also at its lowest point here.

The maximum stress in the GFRP occurs again at the interface, this time between the NdFeB and GFRP layers. Again, the lower modulus and higher density of the NdFeB layer mean the GFRP has to support it.

The hoop strains are greatest in the NdFeB layer with a value of 1.51%. This decays very smoothly to a minimum value of 0.5% at the CFRP layers edge.

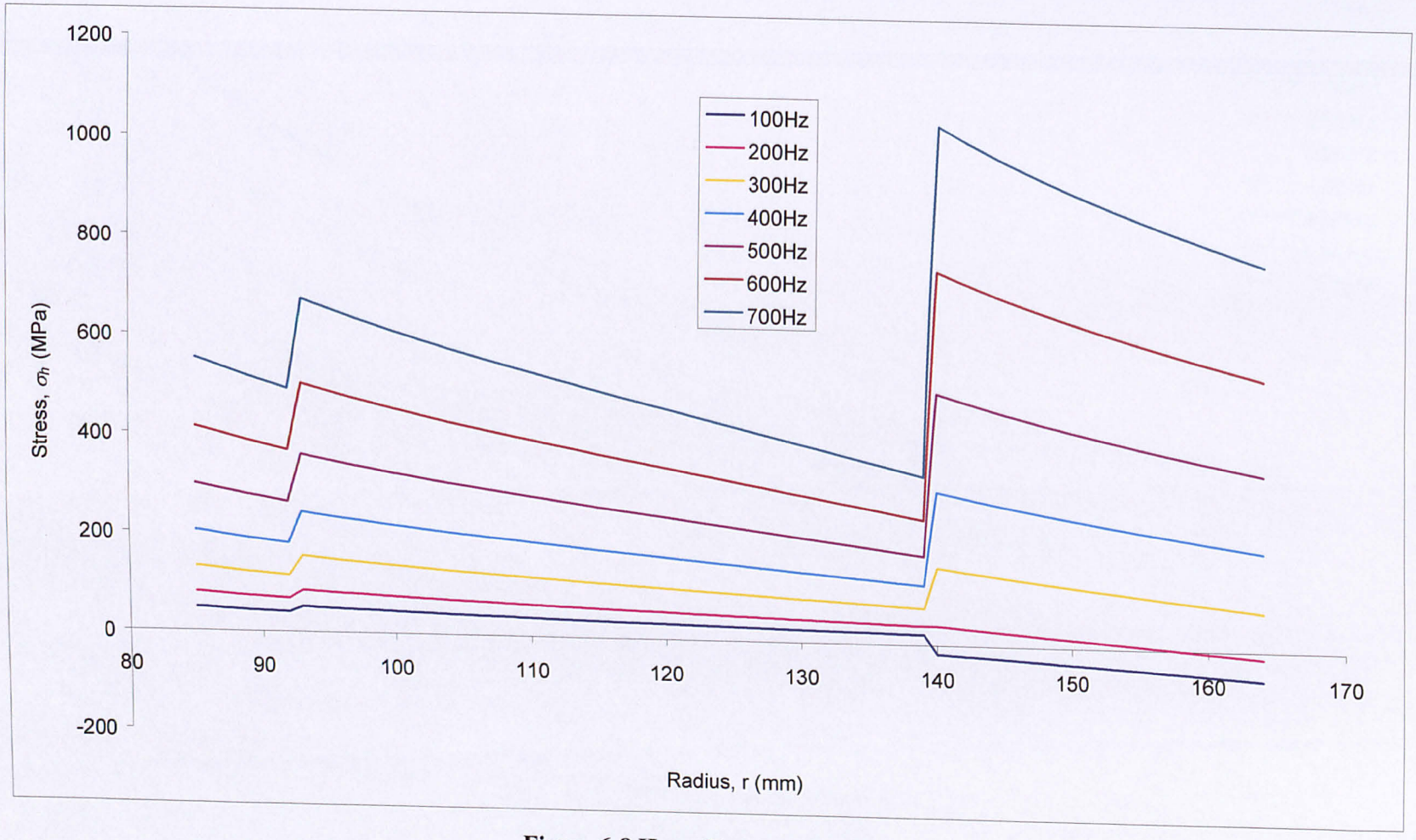

Figure 6-8 Hoop Stress vs. Radius

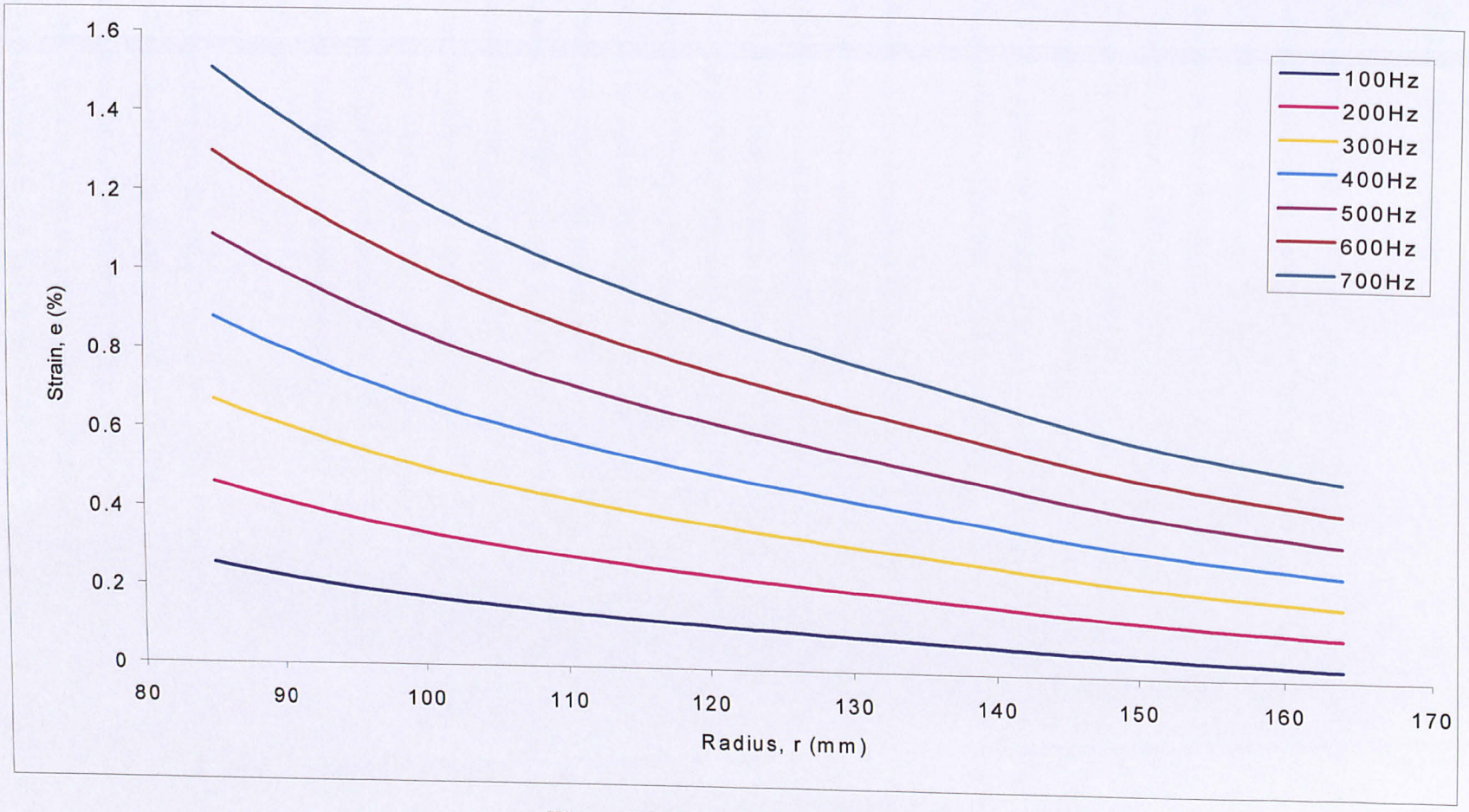

Figure 6-9 Hoop strain vs. Radius

6.3.2 Radial Loading

Interestingly, both tensile and compressive stresses are present in the radial direction during operation. At low speeds tensile stresses are prominent across the entire radius of the rotor. These are largely due to the residual radial stresses, however the maximum has risen slightly to 10.5 MPa and more importantly, the distribution has changed (Figure 6-10). The maximum now occurs in the centre of the GFRP layer. As discussed earlier, the lower hoop modulus of the NdFeB layer, due to the lower volume of fibre, means the GFRP has to support the NdFeB, in the same way the CFRP supports the GFRP. The tensile stresses arise from the stretching of the GFRP layer between the NdFeB interface and the CFRP.

As the speeds increase so do the magnitudes of the radial stresses and the pattern that the stresses take, also change (Figure 6-10). The deformations due to differing moduli become far more exaggerated. The tensile stresses increase, with a maximum value of 26.1 MPa. This maximum occurs at a radius of 109mm, or 16mm into the GFRP layer from the NdFeB/GFRP interface. The considerably higher hoop modulus of the CFRP puts the GFRP layer into compression at this interface. The behaviour of the GFRP pushing up against the CFRP can be easily visualised. However, the tensile forces are developed across this region due to the GFRP being restricted from compressing against the CFRP as much as it wants to. Thus, the inner GFRP layers are loaded in tension even though the net strain is negative due to the Poisson contractions resulting from the positive hoop strains. A stationary point exists in the GFRP layer at a radius of 125mm, where the stress is always 10.3 MPa, regardless of rotor velocity. Since, it is known that the wall thickness of the rotor reduces during operation by 0.58%, it follows that the overall resultant strains in the radial direction must be negative which they are.

Changes between the residual strain and the operating strains are again evident. The NdFeB layer has a lower residual strain than the GFRP. However, as the rotor accelerates the GFRP deforms less, this increases the compressive strain in the GFRP at this interface. Again the pushing of the GFRP layer on the CFRP loads the CFRP in high compressive strain. This is the CFRP supporting the GFRP as explained earlier.

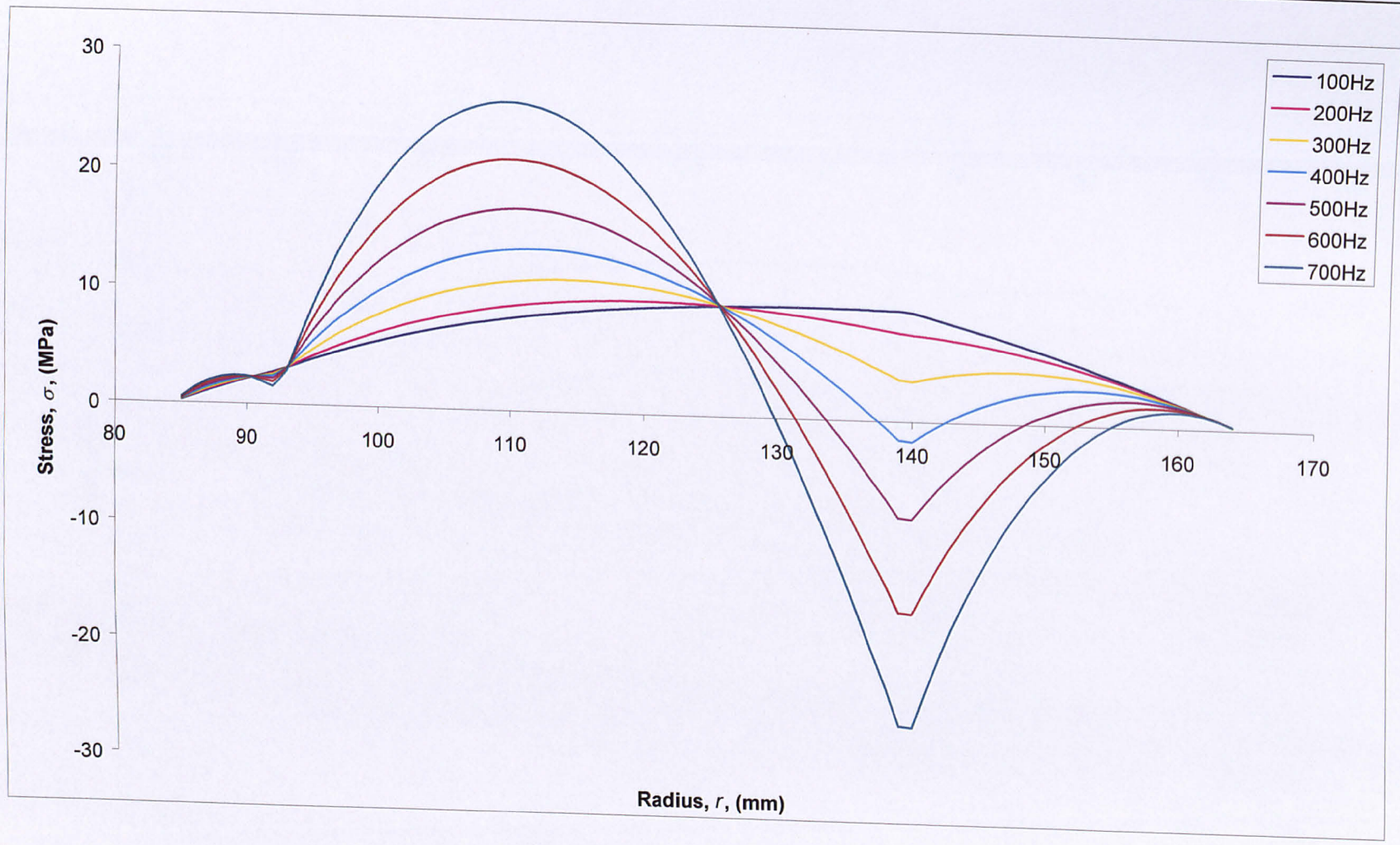

Figure 6-10 Radial Stress vs. Radius

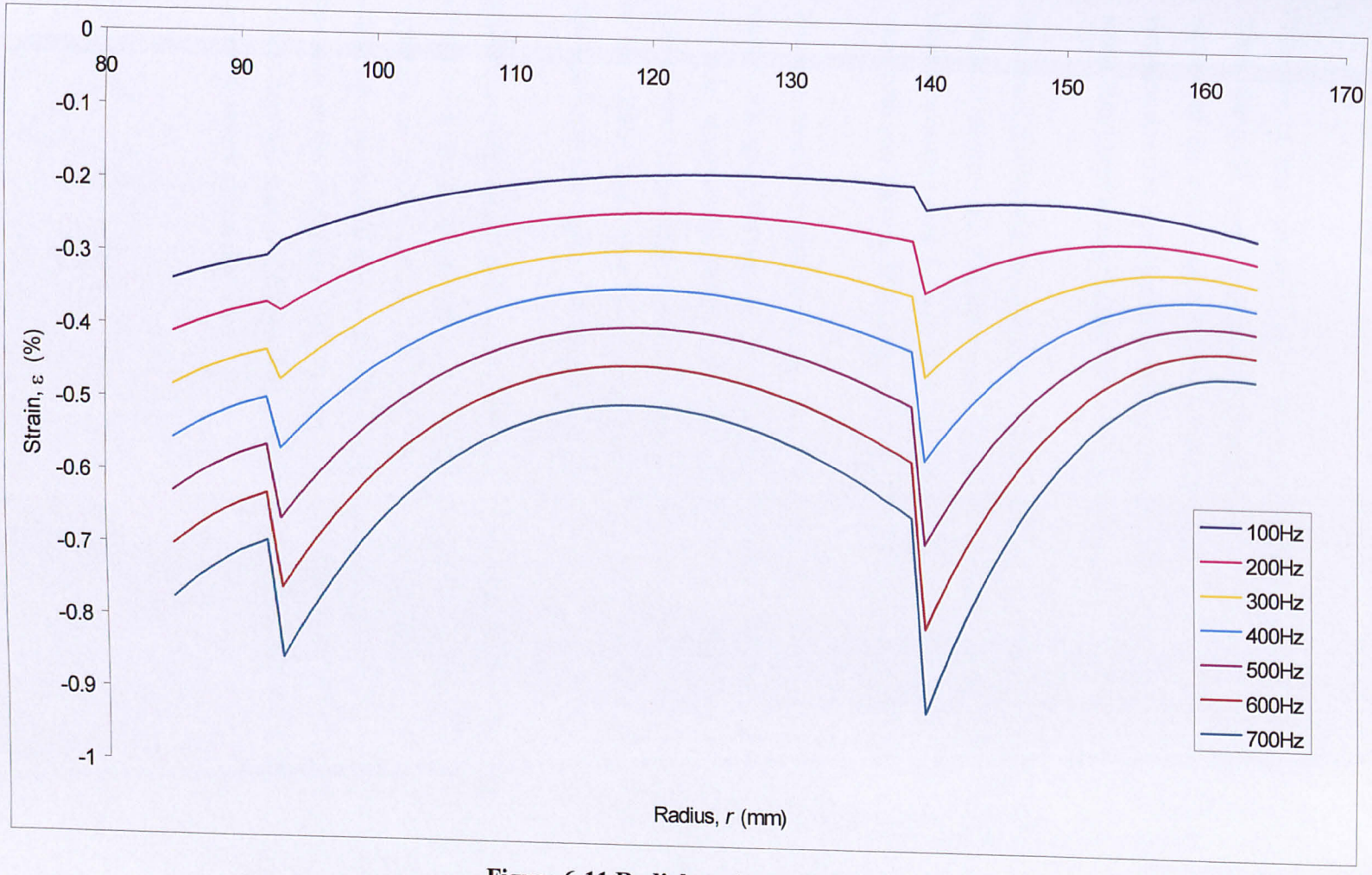

Figure 6-11 Radial strain vs. Radius

6.3.3 Axial Loading

The aim of this research was to investigate the possibility of transverse cracking. Thus, the axial stress is of greatest importance. The stress level through the GFRP section of the rotor varies from a tensile force of 27.7 MPa, at the NdFeB/GFRP interface down to a compressive stress of 24.5 MPa at the GFRP/CFRP interface. This stress state exists across the majority of the axial length of the rotor.

The stress distribution along the axial length was analysed using the information from the axial element set. The stress rose from zero at the ends of the rotor to a constant value reasonably over a small distance (Figure 6-14). The distance over which the stress rose was 200mm. This length is approximately the overall radius of the rotor.

The high tensile stresses are caused by the load exerted on the GFRP by the NdFeB layer. Once again, the reasons for this were exactly the same as in the radial direction. The axial stress on the NdFeB layer were reasonably low, peaking at 13.8 MPa, this level of stress in not high enough to cause concern. However, the stress that is induced in the GFRP layer was of concern (27.7 MPa). Thus, the possibility of crack propagation in this region was theoretically significant.

Understandably, the axial strain condition was interesting in that it showed uniform compressive strain across the entire width of the rotor. This pattern remained regardless of rotor speed. It was also obviously independent of material and no observable interface effects were evident. This condition may well be different at the free ends on the rotor where some deviation in strain between material layers may be evident but this was not investigated. These results were taken from the node set across the centre axis of the rotor.

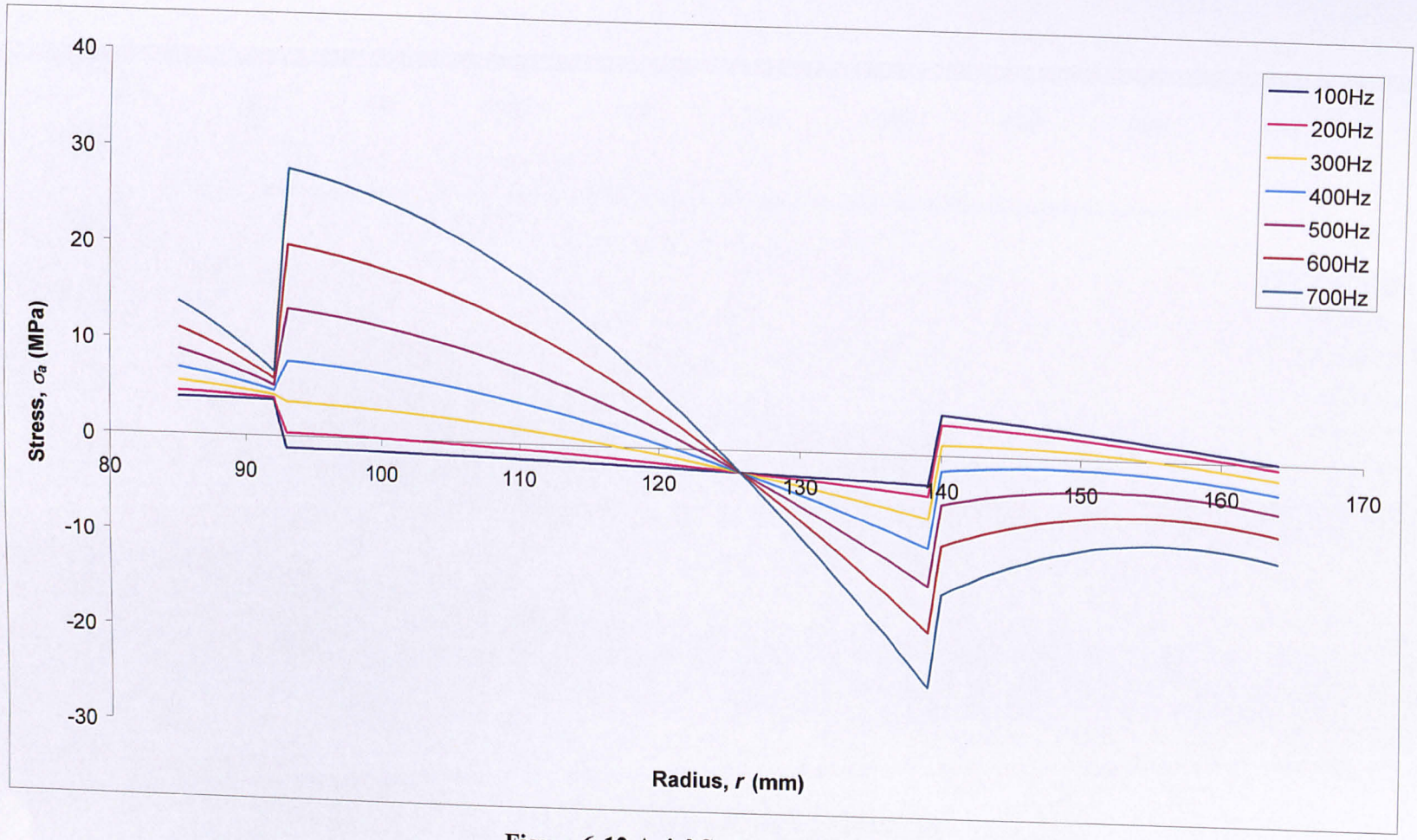

Figure 6-12 Axial Stress vs. Radius

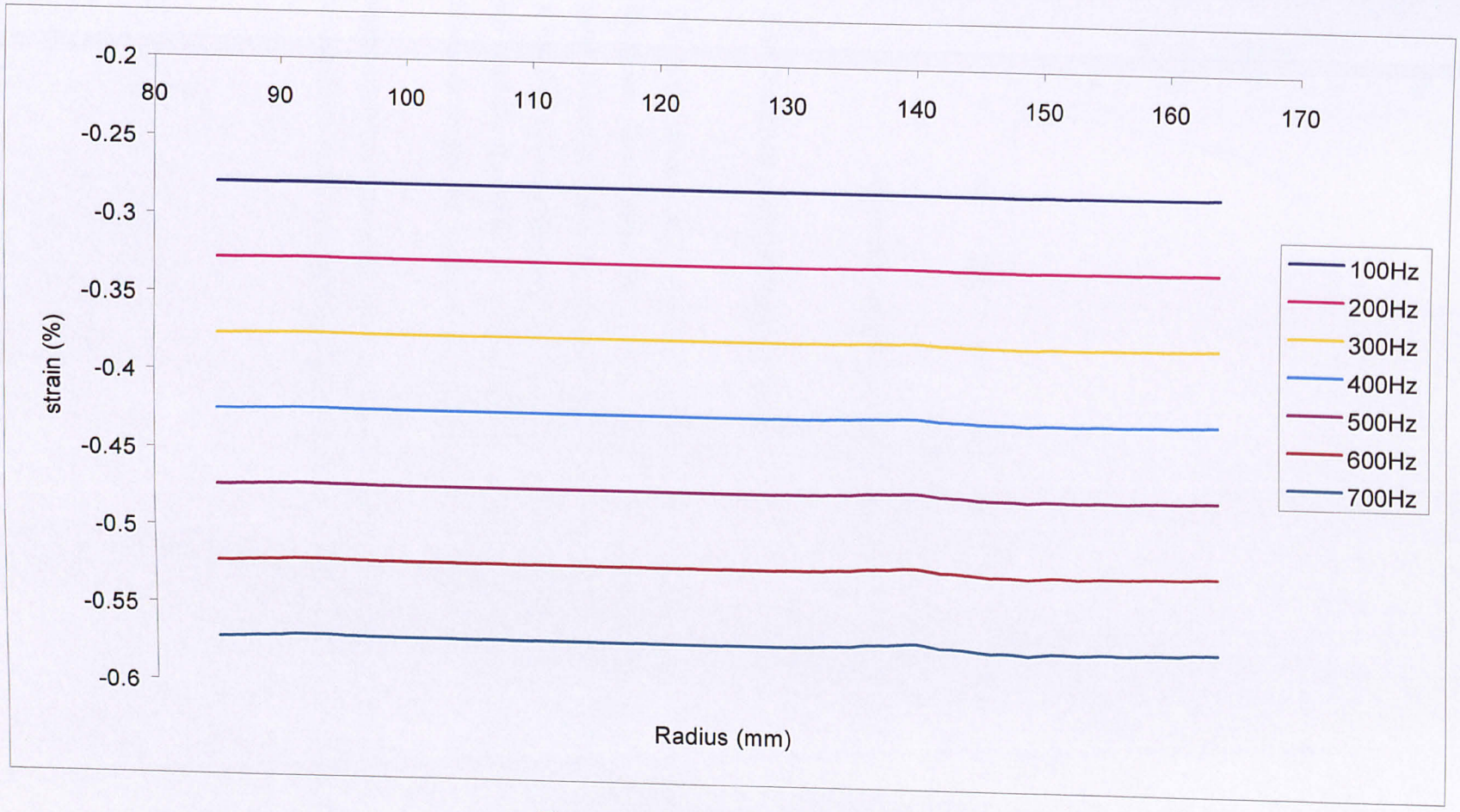

Figure 6-13 Axial Strain vs. Radius

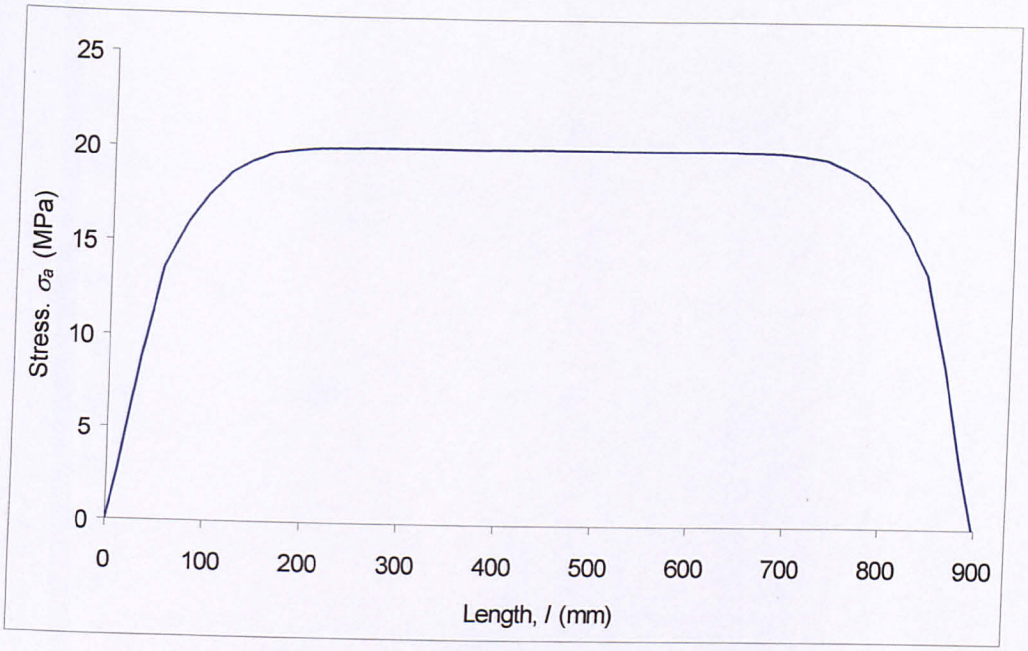

Figure 6-14 Axial Stress vs. Rotor Length at r=109mm

6.4 *Summary of QM Rotor model*

The hoop stress was the primary influence on the stress state of the rotor in all directions. These hoop stresses induce all the subsequent behaviour in the radial and axial directions. Since the magnitude of these hoop stresses was large, the levels of stress they in turn project onto the radial and axial directions, was small in comparison but crucially significant. In practice, it may be the radial and axial stresses that will finally determine the maximum speed of the rotor and rotor life.

High transverse stresses are only evident in the inner section of the GFRP layer. These are attributed to the increased density and lower hoop modulus of the NdFeB layer.

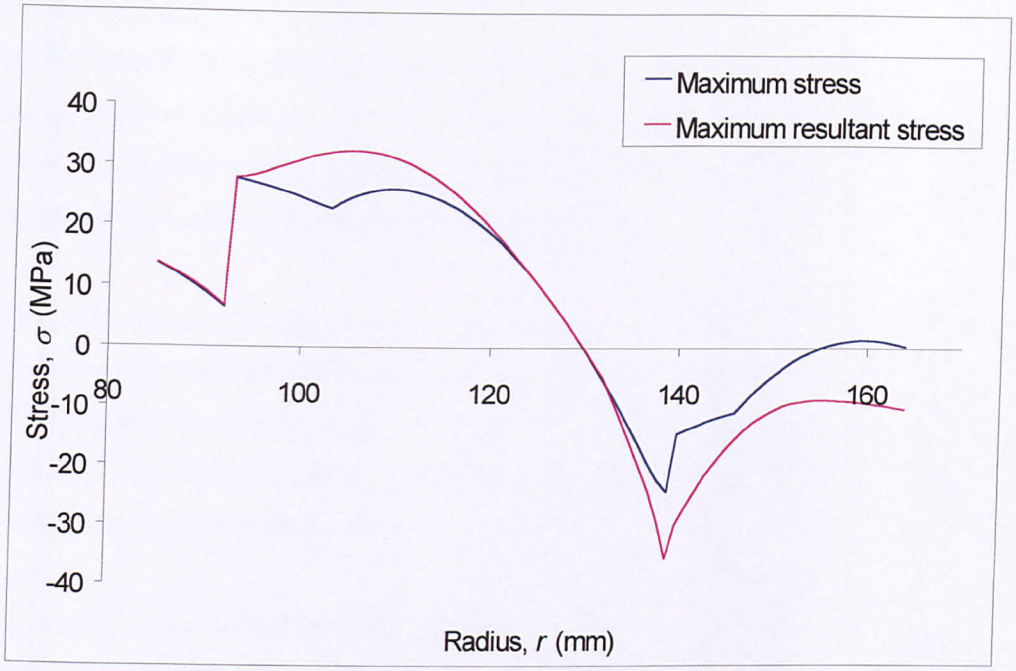

Figure 6-15 Maximum transverse 'as resolved' stresses vs. radius at 700Hz

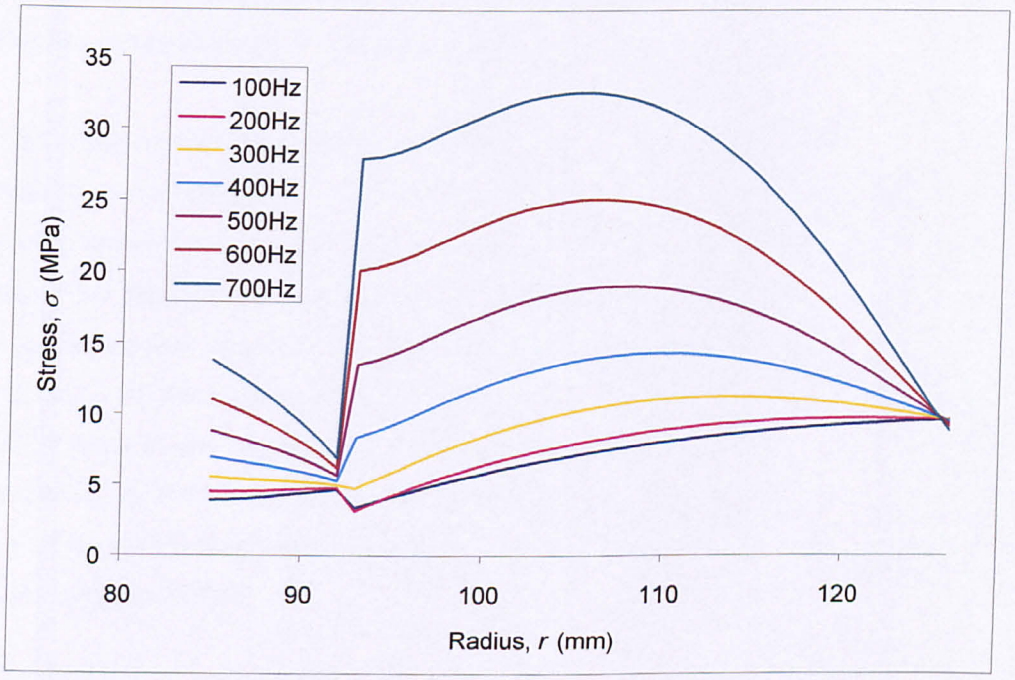

Figure 6-16 Resolved stress vs. radius at different rotational frequencies.

When the results of the radial and axial stresses were studied, tensile stresses were exerted in both these directions, in the same location. Thus, by combining the radial and axial stress results, the maximum transverse stresses were plotted (Figure 6-15). These forces were resolved by using Pythagoras theorem. This is the simplest form of resolving forces, but gives the best results in this case.

With reference to the graph and its two constituents, at a radius of 103mm, the transverse stress was 22.8 MPa, in both directions. This results in a biaxial stress state, whose highest resultant stress occurs at a radius of 105mm and has a value of 32.5 MPa. This was the region of the rotor that was of greatest concern with regard to crack propagation from an in plane defect.

The model indicated that there was no cause for concern with regards to transverse crack propagation in the CFRP layer. This is because the maximum occurs below the operating range of the flywheel, and the maximums are well below the transverse strength of the CFRP. The radial and axial stresses were low and any resultant biaxial stresses were compressive or insignificant.

As a result of the high hoop stresses, there was significant Poisson contraction in the radial and axial directions, in all layers. Although, this negative strain state existed, as shown earlier. This was how the high transverse tensile stresses were produced. The reason for this was due to the different material layers. For example, the GFRP layer was constrained between the CFRP and NdFeB layers. The different mechanical properties of these layers, namely moduli, had the effect of initially stretching the GFRP next to the NdFeB and then bunching up next to the CFRP. In the axial direction, the NdFeB pulled the GFRP into tension, which decays to compression at the CFRP interface due to the large contraction in the CFRP, as a result of the CFRP supporting the GFRP.

6.5 Comparison of Urenco and QM models.

The results outlined so far cover a model run using the static results. These results would form the basis for all lifetime calculations. However, Urenco used their own data for flywheel analysis using ANSYS and Matlab modelling packages.

The values for hoop modulus were supplied by Urenco and thus these values were the same in both models. The Poisson ratios measured were also the same as those generated at QM. The transverse moduli were different, table 6-2. The QM values were lower. Urenco assumes that the material is transversely isotropic. This secondary modelling also allows an insight into the effect of modulus changes has on the overall stress state in the rotor.

Table 6-2Comparison of Urenco and QM data.

	NdFeB Urenco Modulus values (GPa)	NdFeB QM Modulus values (GPa)	GFRP Urenco Modulus values (GPa)	GFRP QM Modulus values (GPa)	CFRP Urenco Modulus values (GPa)	CFRP QM Modulus values (GPa)
Longitudinal Modulus E_{11}	35.0	35.0	48.0	48.0	154.1	154.1
Transverse Modulus E_{22}	16.0	13.7	18.0	13.7	9.0	6.6
Transverse Modulus E_{33}	16.0	15.7	18.0	15.6	9.0	8.4
Poisson Ratio υ_{13}	0.13	0.13	0.13	0.13	0.021	0.021
Poisson Ratio υ_{12}	0.13	0.13	0.13	0.13	0.021	0.021
Poisson Ratio υ_{23}	0.28	0.32	0.28	0.28	0.28	0.3

The differences in transverse modulus values did not have a profound effect on the overall stress state. It was important to note that the subtle changes were worth consideration, since high variations were recorded in the mechanical testing sections. As expected the primary stresses are still the hoop stress induced by the rotation. The effect of the lower transverse moduli in the QM model was to reduce the hoop stresses in the CFRP layer (Figure 6-17), but increase those in the GFRP and NdFeB.

The radial stresses have increased in the QM model (Figure 6-19). In the GFRP layer the maximum tensile stress is 26.5 MPa. The radial strains had also increased due to the lower stiffness.

The axial strains had also increased by a small amount. The axial stresses in the NdFeB layer had reduced significantly in the QM model. As a result there was an increase in the tensile stress on the GFRP layer. Even if the Urenco model is considered more accurate the stresses predicted in the NdFeB layer are still well below the transverse strength (57.3 MPa) of the material.

Critically, the most important consequence of the lower moduli in the QM model was the increase in transverse tensile stress in both the radial and axial directions (Figures 6-19 and 6-21). Thus, the resolved stress also increased. This was the area of most concern and all following calculations would use the QM model predictions since it represented a more severe transverse loading scenario.

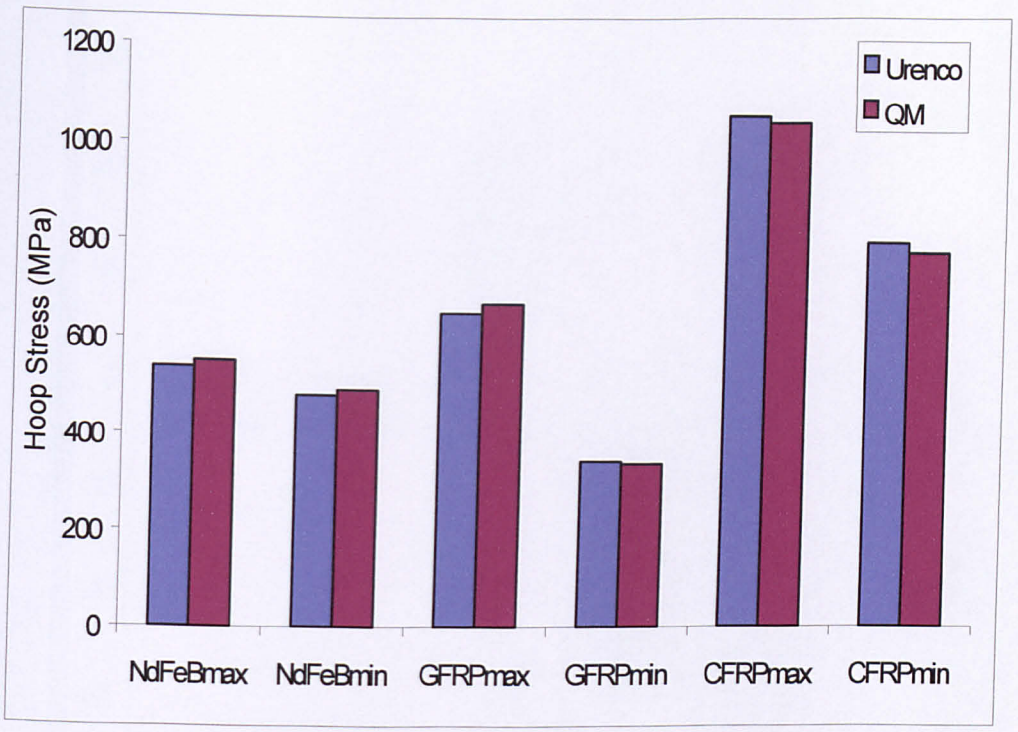

Figure 6-17 Comparison of Urenco and QM data models, hoop stresses at 700Hz

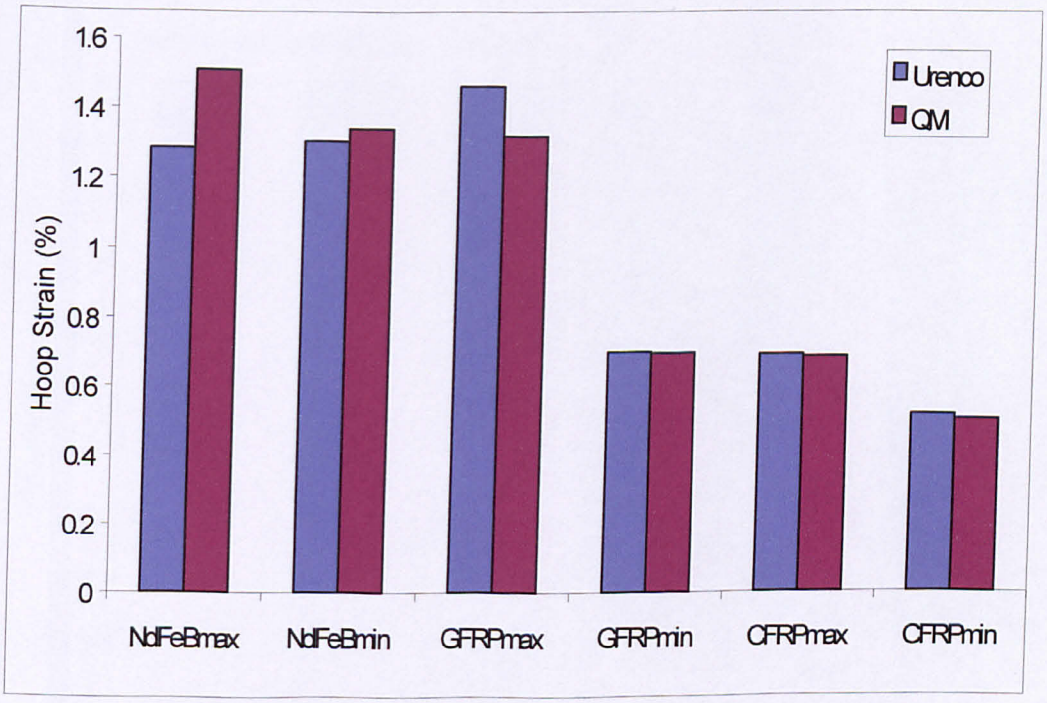

Figure 6-18 Comparison of Urenco and QM Data models, hoop strains at 700Hz

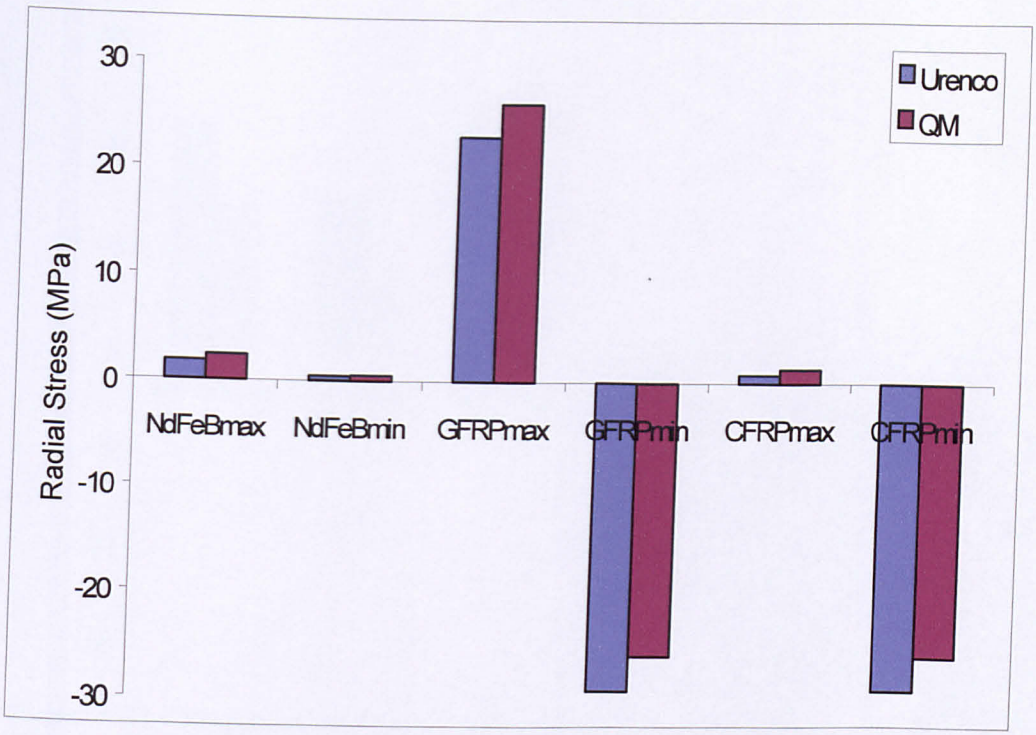

Figure 6-19 Comparison of Urenco and QM data models, radial stresses at 700Hz

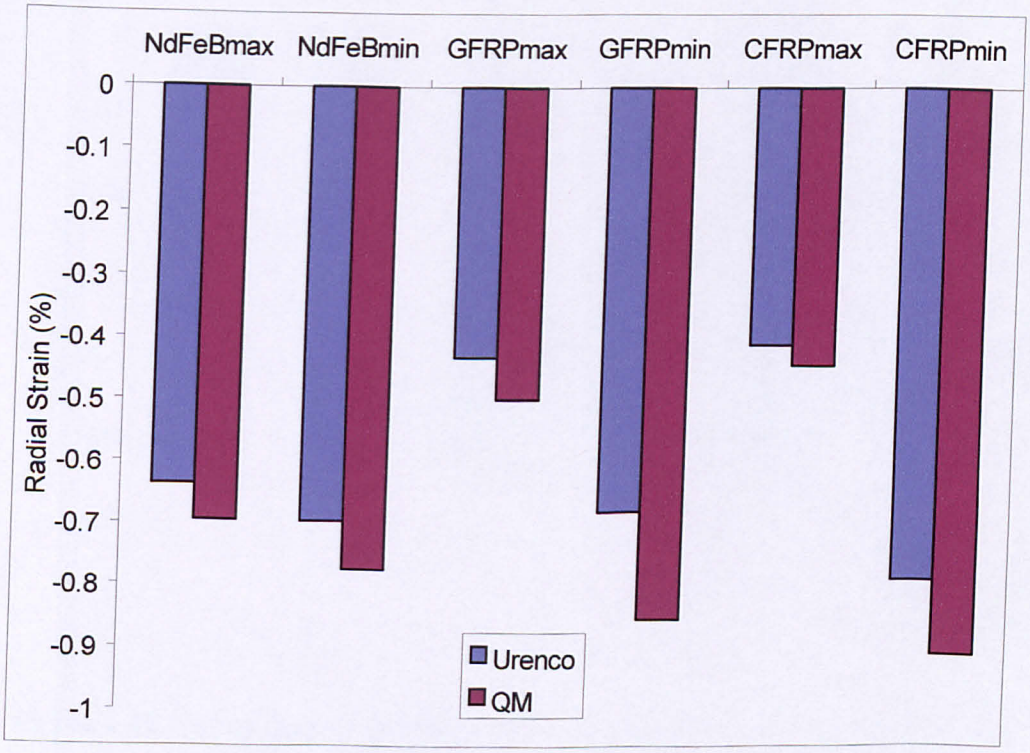

Figure 6-20 Comparison of Urenco and QM data models, radial strains at 700Hz

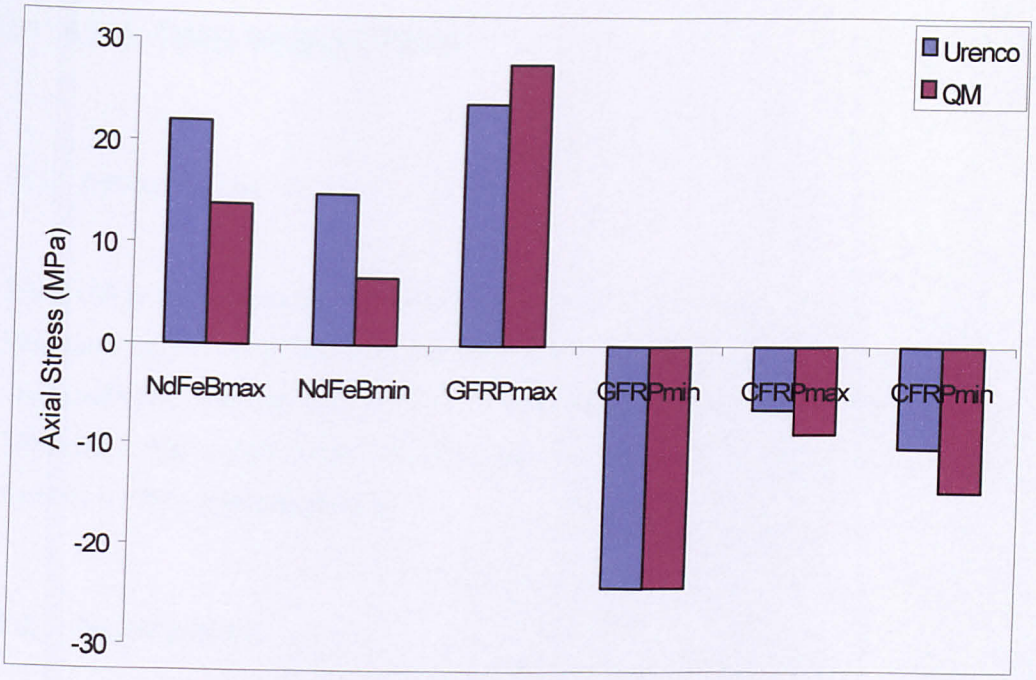

Figure 6-21 Comparison of Urenco and QM data models, axial stresses at 700Hz

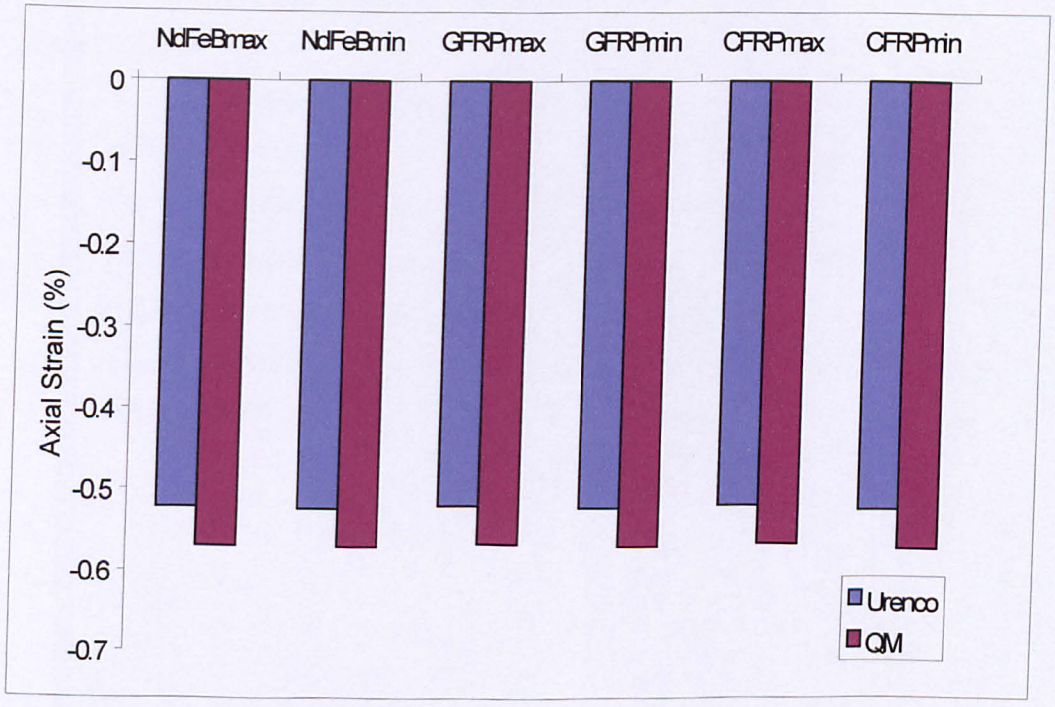

Figure 6-22 Comparison of Urenco and QM data models, axial strains at 700Hz

7 LIFE TIME PREDICTION

7.1 Introduction.

From the outset the primary goal for this body of work was the ability to predict the long term behaviour of the flywheel rotor. Thus, the culmination of the experimental and modelling research was to form a suitable methodology to fulfil this objective. Ultimately, the model would be based upon simple fracture mechanics influenced directly by the experimental data.

7.2 Assumptions.

In reality the flywheel rotor is exposed to a very complex service life pattern and conditions. For the purposes of this thesis assumptions had to be made to simplify this scenario. These were:

- The rotor is assumed to remain at a constant velocity. i.e. the effects of fatigue have been ignored.
- The temperature of the rotor is static throughout the lifetime
- The vacuum condition was ignored.
- The defects within the rotor are regarded as sharp cracks.
- Any effect that the hoop loading may have upon the material behaviour has been neglected. I.e. A biaxial and not triaxial stress state exists.

7.3 Theory.

Using basic fracture mechanics outlined in the literature (section 2.5.1), consider a sharp crack in an infinite body (Figure 7-1).

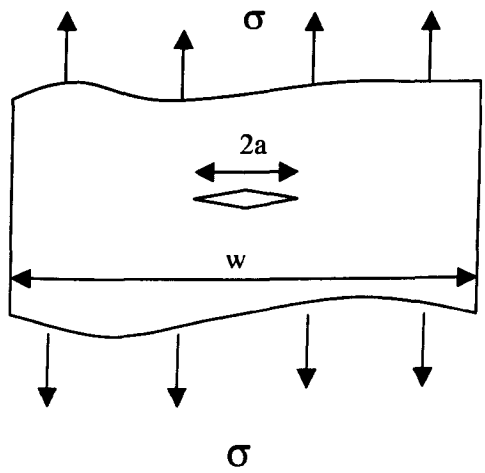

Figure 7-1 Schematic of sharp crack, where a<<w.

In this situation we know that.

$$K_{IC} = Y\sigma(\pi a_c)^{1/2}$$

Where Y= a constant based upon the specimen geometry.

Rearranging the previous expression to solve for crack length

$$a_c = \frac{1}{\pi}\left(\frac{K_{IC}}{Y\sigma}\right)^2$$

In this expression all the parameters are known or have been determined experimentally. The only unknown quantity is Y.

7.3.1 What is Y?

The geometric factor (Y) is based upon the specimen geometry and takes into account the fact that the crack is not situated in an infinite plate. In the case for lifetime

prediction, the specimen is the entire flywheel rotor. In order to derive the correct value for Y, complex mathematical functions need to used. Ideally using FEA techniques the stress fields around the crack tip at any given location in the rotor, could be generated. Using this information coupled with the displacement data of the crack opening, a weight function could be developed to relate Y to crack length [66]. This is the theory, however the problem is further compounded by a number of other influences. Primarily, the greatest challenges are the highly discontinuous prevailing stress field and the layered structure, each with differing behaviour. Thus, cracks that extend across these boundaries will be exposed to different stress fields on either end of the crack. To date, fracture mechanics has not attempted to solve Y for this type of very specific condition.

As a result, the procedure to accurately determine Y falls outside the scope of this thesis and so a simpler solution was found. A software program [17] was used to evaluate a variety of different worked solutions that were deemed relevant in some manner to the flywheel rotor (Table 7-1). The Y values were calculated assuming a 0.5mm crack length in the rotor. This is considerably bigger than actual envisaged cracks.

After consideration and consultation with the programmes author [82] the circumferential crack in a tube with a tensile stress was regarded as the closest scenario to the flywheel. This situation also yielded the highest value (Y=1,117) which means all calculations are conservative.

Table 7-1 Candidate Geometry Factors. [17]

Scenario	Accuracy	Y	Reference.
INTERNAL RADIAL CRACK: ROTATING DISK ANGULAR VELOCITY	99%	0.874	[18]
CENTRE CRACKED RECTANGULAR SHEET: UNIFORM UNIAXIAL TENSILE STRESS	>99%	1	[19]
A PENNY SHAPED CRACK: UNIFORM STRESS ON THE CRACK	Exact	1	[20]
INTERNAL EDGE CRACK IN A TUBE: INTERNAL PRESSURE	99%	1.11	[21]
EXTERNAL CIRCUMFERENTIAL CRACK IN A TUBE: TENSILE STRESS OR TORQUE	99%	1.117	[22]

7.4 Inherent flaw size.

Assuming the calculated transverse strength and toughness values are reasonable, which they are when compared with published values, we can derive the inherent flaw size of the materials, using the expressions outlined in the previous section. If we take a mean value for the GFRP strength of 78.5 MPa and 56.6 MPa for the CFRP layer (Table 4-6) and the fracture toughness for the layers as 1.994 and 1.391 MPa $m^{1/2}$ respectively (Tables 4-9 and 4-10) then the flaw sizes are 165 and 1520μm. It is also worth remembering that this is calculated as a sharp defect

Since we know that defects of this magnitude are extremely rare in the rotor, then it poses the question of the validity of the fracture mechanics relationship to these materials. Since the relationship between sharp and actual defects is unknown, then this may account for a sizeable amount of this discrepancy. The overall concern lies not with the accuracy of the calculation, however it poses the question of whether fracture mechanics may be applied across a wide range of specimen sizes. We shall see that for the very long lifetimes of the rotor, defect sizes of the order of tens of microns are predicted, i.e. one or two glass fibre diameters. The consequences of these calculations will be dealt with in the next chapter. For now we must assume that no

size effects exist for conventional fracture mechanics, thus they may be used to predict the defect sizes.

7.5 Approaches.

Assuming that fracture mechanics is scalable across a various sizes, it is possible to predict the critical defect sizes for the rotor over a variety of lifetimes. Two distinct approaches were taken. These are diagrammatically summarised in figure 7-2.

The first was to assume that the crack does not grow over the life of the rotor. Rather the fracture toughness changes with time. This information was recorded in figures 5-6 and 5-8. Thus, the critical defect size may be predicted for a given lifespan. This approached was called the dormant defect method.

In contrast to this rather simplistic approach, a more rigorous analysis was performed. This assumed that cracks will propagate from the defects in the rotor. It is possible to calculate the initial critical defect size, i.e. time=0, K_{IC}=measured static value. Then with these values and the knowledge of the crack growth rate it would be possible to calculate the time taken for a defect to grow to this size. This type of analysis was known as the active crack growth method.

Figure 7-2 Next Page. Lifetime prediction approach development.

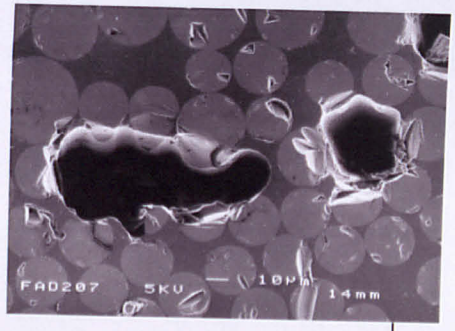

V_f, a_0, %a

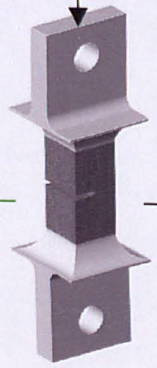

E_{xx}, υ_{xx}

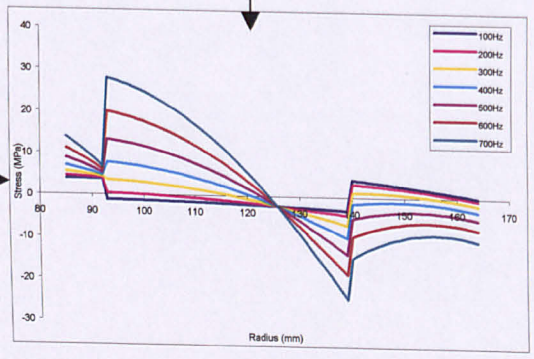

σ_{xx}, ε_{xx}

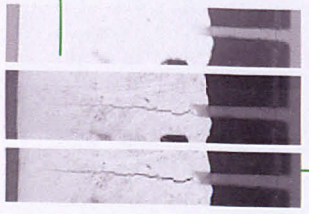

K_{IC}, Initial applied K_{IC}

Dormant Defect Method

$\frac{da}{dt}$

Active Crack Growth Approach

7.6 *Dormant defect method.*

Using the simple fracture mechanics relationships presented at the beginning of this chapter, bound by the assumptions outlined, it is possible to calculate the size of the critical defect at any given stress level, if the value of K_{IC} is known. In addition, the relationship between the initial values of K_{IC} and time has been determined. Combining this information allows charts to be produced linking rotor lifetime to defect size (Figures 7-3, 7-4 and 7-5). These assume the stress in the rotor exists in one direction only. The maximum values have been used for both axial and radial conditions.

Example: in the GFRP section, what would have been the critical defect size in the rotor if it was run at 700Hz and survived for 1 minute?

For t=60 seconds , K_{IC}=1790000 Pa $m^{1/2}$. (Figure 5-6)

And, ϖ=700Hz, therefore σ=27760000 Pa. (Figure 6-12)

$$a_c = 2\times\frac{1}{\pi}\left(\frac{1790000}{1.117\times 27760000}\right)^2$$

$a_c=2.121\times10^{-3}$ m

$a_c=2121$ μm

7.6.1 Axial stress

In the axial case, a defect was assumed to lie at the NdFeB/GFRP interface region, but still within the GFRP layer (r=93mm). From figure 6-12, it can be seen that the highest axial stress exits within the GFRP lying next to the NdFeB interface. Thus, this location represented the "worst case" position for a defect to be lying. Although, the stress distribution in this area was highly discontinuous, it was assumed that since defects of less than 100μm were common, the local stress field was quite uniform in comparison. Defect size charts have also been constructed purely for the NdFeB and CFRP layers (Figures 7-3 and 7-5). However, the stresses in these layers were significantly lower. In the case for the NdFeB layer, a defect was assumed to lie at the

inner surface of the rotor, where the stresses are highest. In the CFRP layer a defect was assumed to lie in the CFRP layer but adjacent to the GFRP interface. The axial tensile stresses in the CFRP layer are relatively inconsequential since the peak stress occurs at only 100Hz.

7.6.2 Radial stress

For the radial scenario, the maximum tensile stress was midway through the GFRP layer (r=110mm). Thus, the defect was assumed to lie within this region. The stress field at this point was more constant than for the axial case, although the value was slightly lower at 26.1 MPa, compared with 27.7 MPa. Hence, with such a small difference in stress between the directions, the same chart may be used for predictions in the radial direction. Again, the same plots could be used for the NdFeB and CFRP layers, since the variations in stress levels were as small.

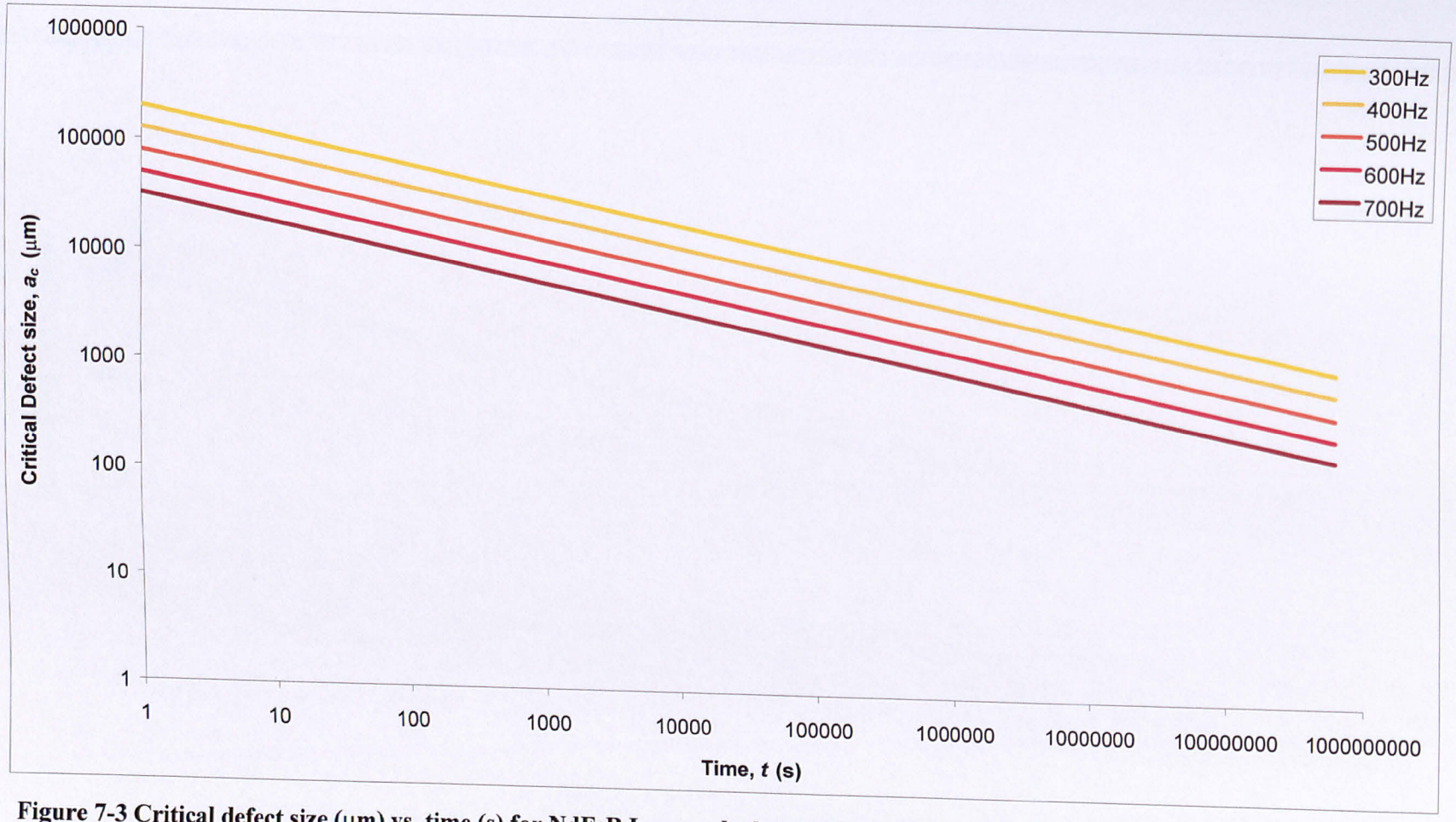

Figure 7-3 Critical defect size (μm) vs. time (s) for NdFeB Layer calculated via the dormant defect route (maximum axial stress used).

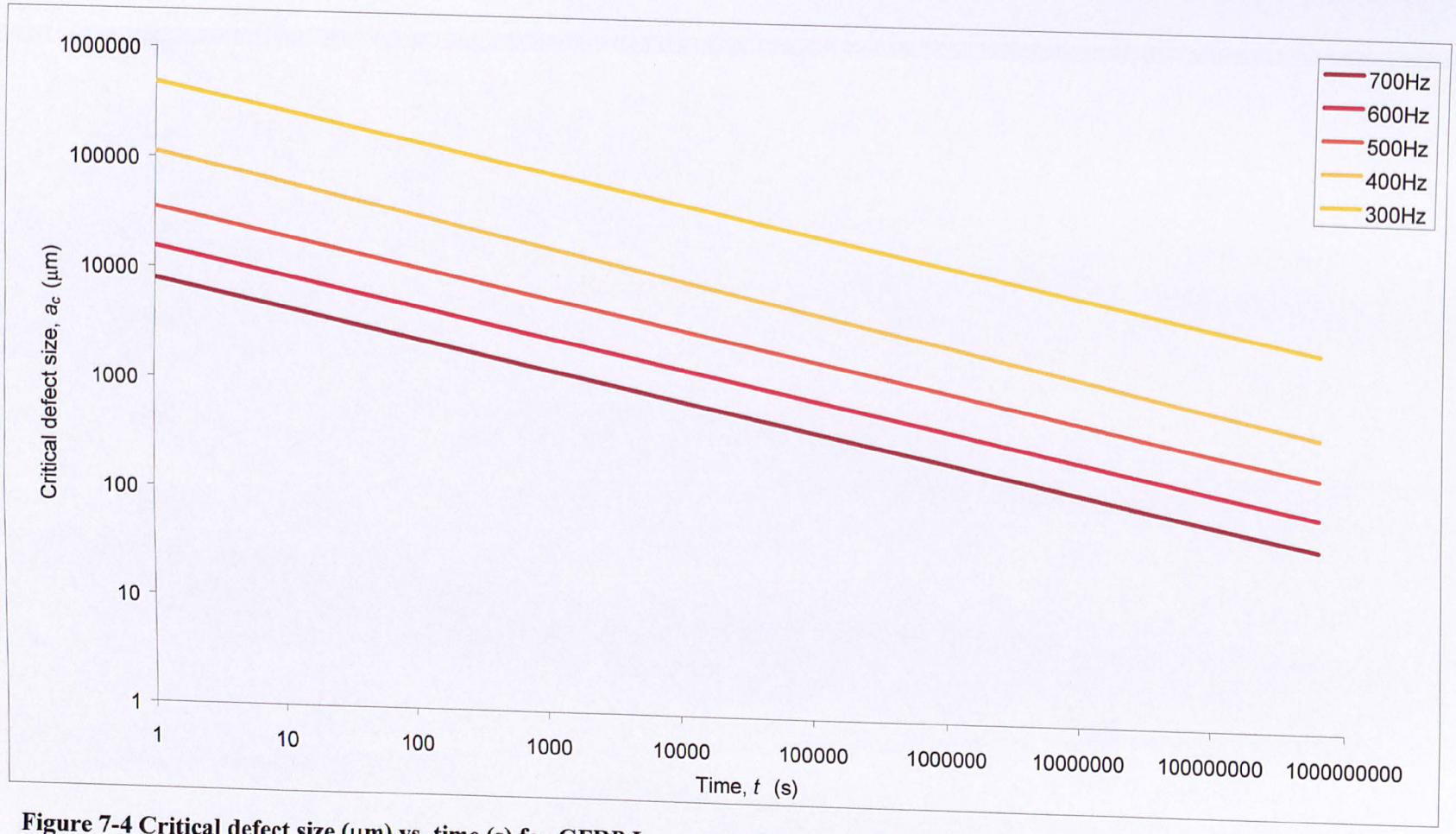

Figure 7-4 Critical defect size (μm) vs. time (s) for GFRP Layer calculated via the dormant defect route (maximum axial stress used).

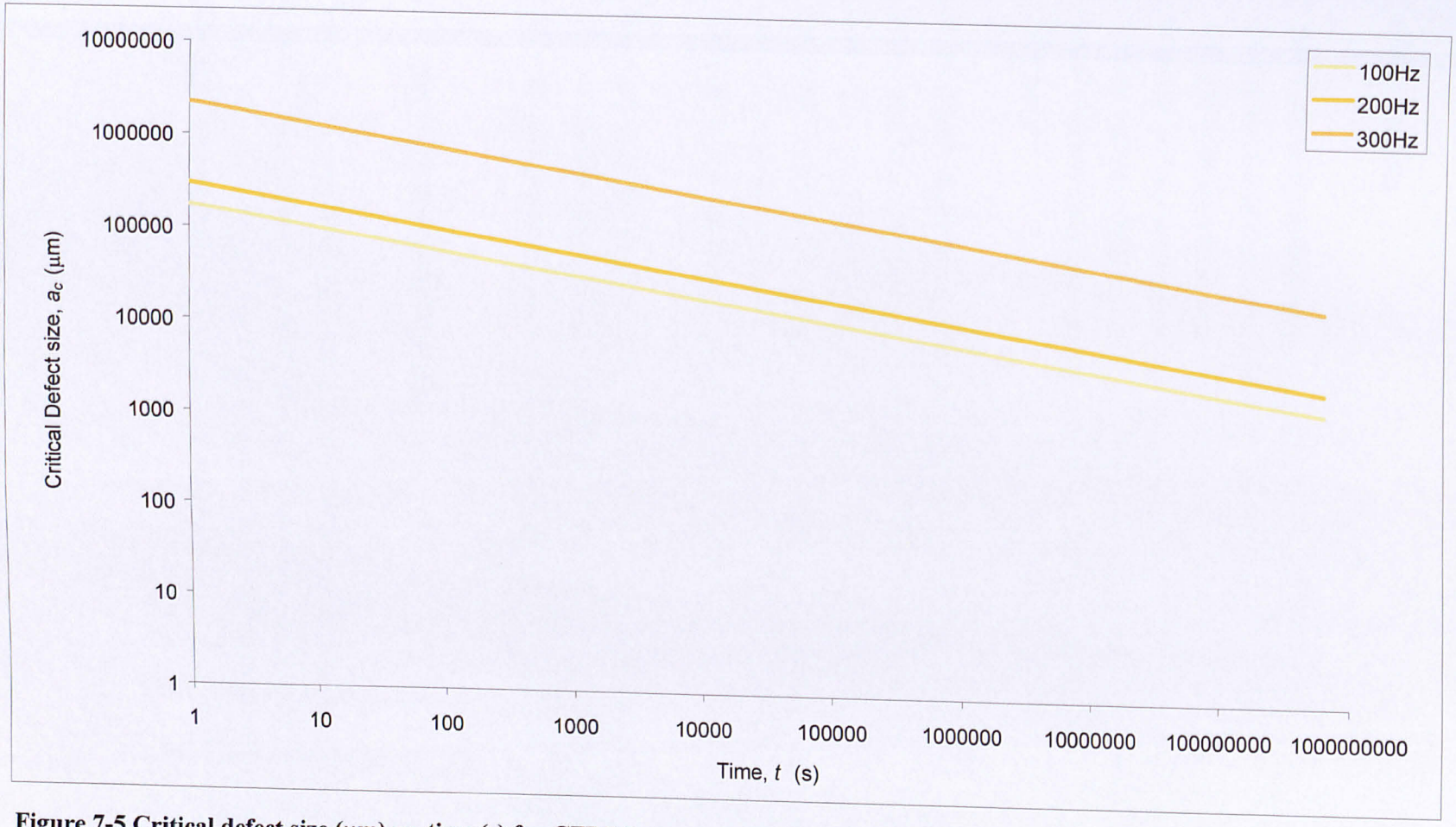

Figure 7-5 Critical defect size (μm) vs. time (s) for CFRP Layer calculated via the dormant defect route (maximum radial stress used.).

7.6.3 Results.

When the stress distributions for the CFRP are studied (Figures 6-10 and 6-12), it can be seen that tensile transverse stresses are only developed at very low speeds. At these low speeds the stresses are very small. Thus, analysis of these charts showed there was no cause for concern regarding failure in the CFRP layer. At the lowest end of the operating range (300Hz), a defect of 700mm would be required to cause failure in 20 years! This was due to the very low applied tensile stress rather than the toughness of the material.

In the NdFeB layer, for a similar lifetime, a 300μm crack was predicted. The largest defect detected was 67.9μm and it did indeed occur in this layer. This defect size was well below the danger level predicted and as such the NdFeB layer could not be considered an immediate threat. If the Urenco model is considered accurate then the defect size for this lifetime would be 120μm. Although the defect size has reduced significantly, it is still nearly double the large defect measured.

The GFRP layer was of greatest concern. The highest transverse stress occurred in this layer and therefore the smallest defect sizes were predicted. A defect of 60μm was calculated for a 20 year lifespan. Defects of this magnitude are a distinct possibility.

7.7 Resolved stress predictions.

Thus far the predictions had been based upon the stress distribution in a single direction. The evidence highlighted in figures 6-15 and 6-16, illustrated that a biaxial stress state existed, acting over a greater proportion of the rotor. Therefore, the life predictions must be amended to allow for this condition.

7.7.1 The NdFeB layer.

The NdFeB layer required no further prediction beyond the simple axial case. The maximum resolved stress was 13.79 MPa compared to a 13.78 MPa maximum for the unresolved stresses. Thus, the same chart may be used.

7.7.2 The GFRP layer.

The conditions within this, the most critical layer, have changed significantly. The location of the maximum stress level has moved outward to be more centrally located (r=105mm). The maximum stress level has also increased significantly, by 17% to 32.5 MPa. The consequences of these changes were primarily that the defect size would of course reduce, but more significantly the geometric factor (Y) would become simplified. The same value for Y is used in this analysis, regardless. However, since the crack would be lying purely in one material, and not across an interface, calculation of the true Y would be easier. However, the stress field is still highly discontinuous, in fracture mechanics terms.

The increase in stress and subsequent reduction in critical defect size had been calculated out for the case of 700Hz. Figure 7-6 illustrated the effects of these changes upon the defect size. The critical defect sizes had reduced by 28%, to just 40μm.

7.7.3 The CFRP layer.

The defect size prediction had also been recalculated for the CFRP at 100Hz where the biaxial stresses were most prominent. The critical defect sizes for this layer had fallen significantly, but still do represented a danger to the operation of the flywheel.

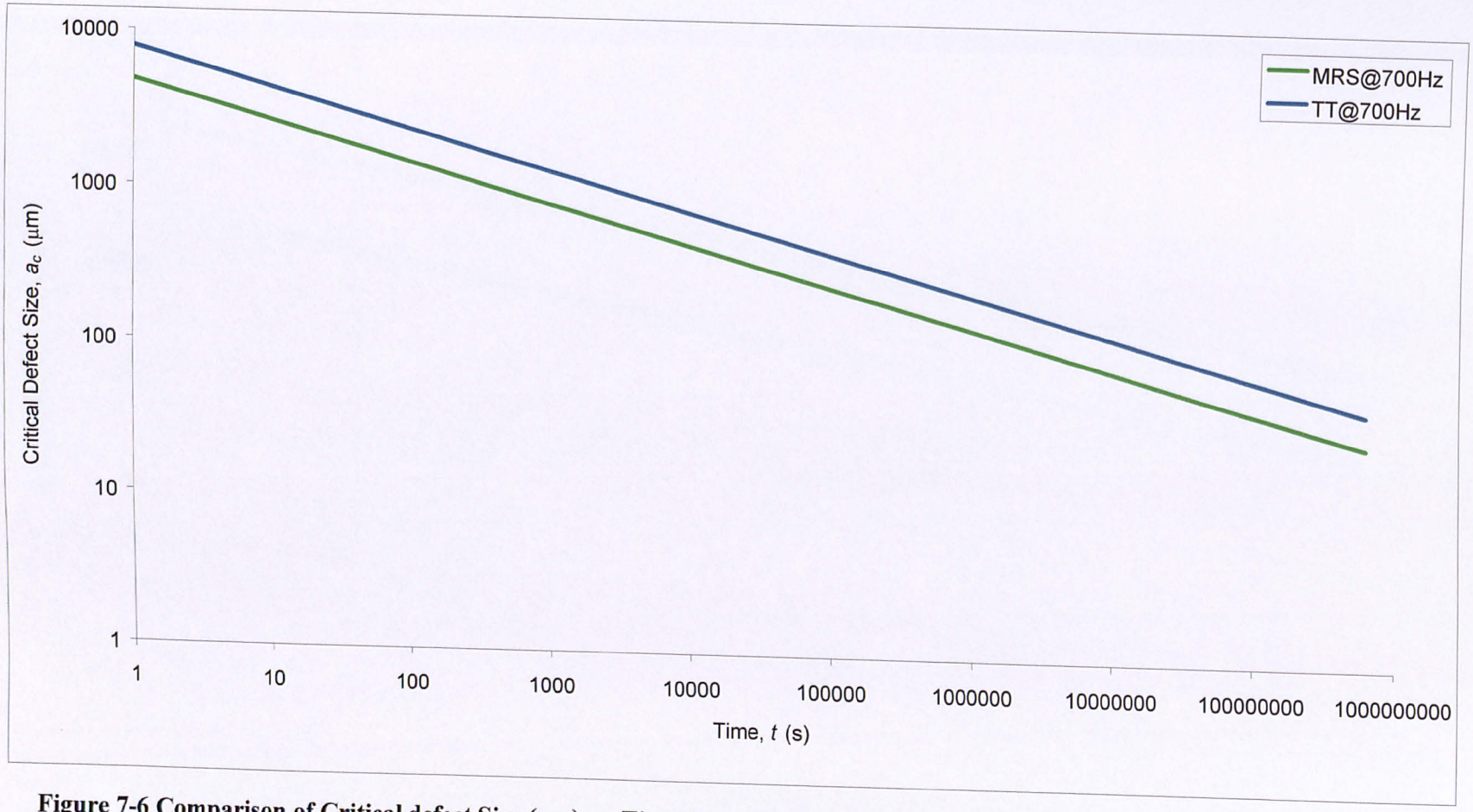

Figure 7-6 Comparison of Critical defect Size (μm) vs. Time for GFRP layer calculated for maximum transverse tension(TT) and Maximum Resolved Stress(MRS) at 700Hz via the dormant defect route.

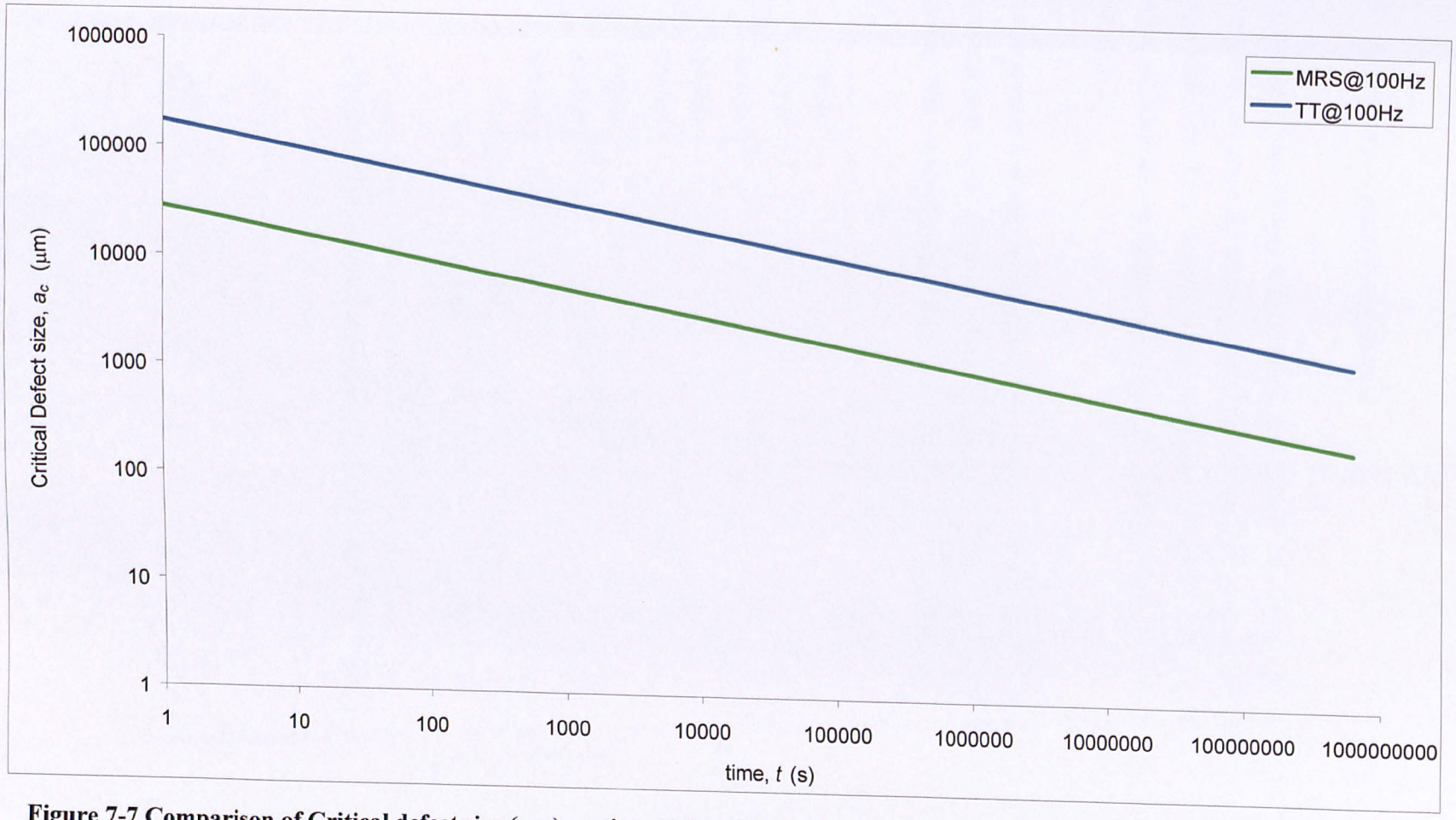

Figure 7-7 Comparison of Critical defect size (μm) vs. time (s) for CFRP layer calculated for maximum transverse tension (TT) and Maximum resolved stress (MRS) at 100Hz via the dormant defect route.

7.8 Active crack growth approach.

As previously highlighted, it was found that cracks can grow slowly. Hence, the assumption now must be made that the fracture toughness of the material does not change with time. Thus, if the K remains constant and the cracks grow slowly, it was possible to calculate the initial defect size by working back from the known final defect size.

The relationship between final defect size and rotor speed can be plotted for the various material layers (Figures 7-8 and 7-9). These charts were produced using the measured static values for K_{IC}, using the simple dormant defect method.

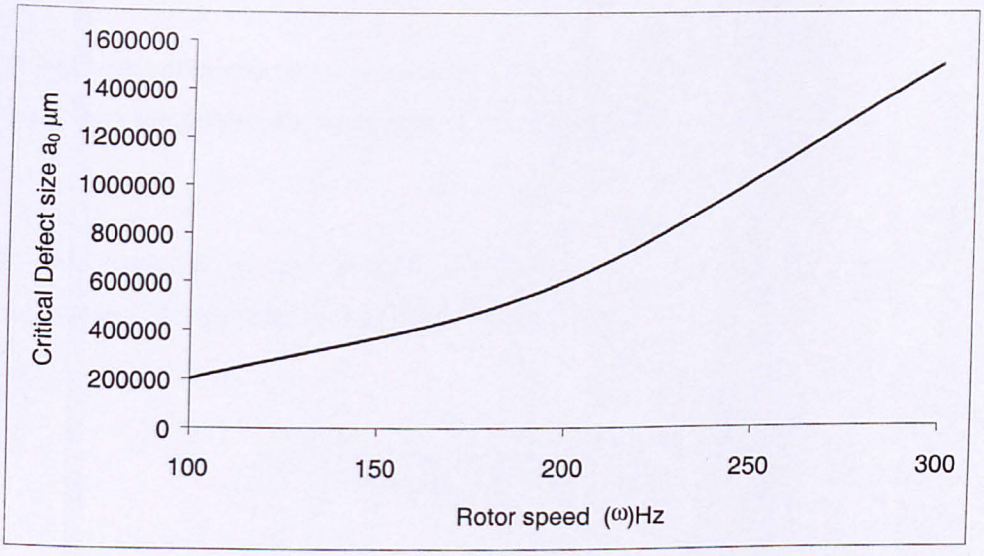

Figure 7-8 Rotor speed vs. critical defect size for CFRP layer.

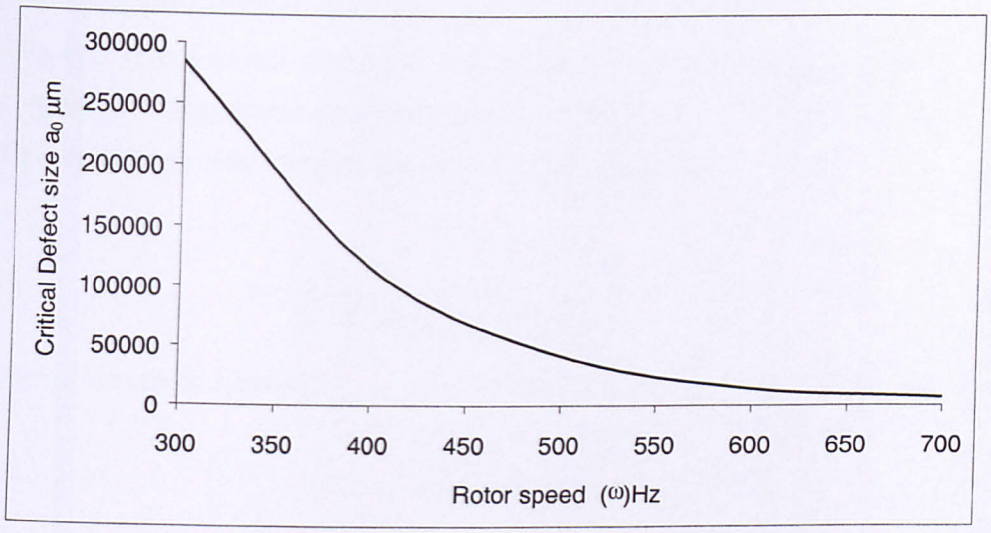

Figure 7-9 Rotor speed vs. critical defect size for GFRP layer.

The next step with this type of analysis is to calculate the starting defect size. This achieved by integrating the crack growth rate expression:

$$\frac{da}{dt} = AK^n$$

The full workings of this integration may be found in Appendix C. With this resultsknow. The lifetimes may now be calculated using:

$$t = \frac{2}{2-n} \cdot \frac{1}{A\left(Y\sigma\sqrt{\pi}\right)^n} \cdot \left[a^{1-\frac{n}{2}} \right]_{a_0}^{a_{crit}} + C$$

Using figures 7-8 and 7-9, the final critical flaw size is known. Thus, if values are substituted in for starting flaw size (a_0) then the time to failure may be calculated. In contrast to the dormant defect method, using this technique, we predict lifetimes for given initial flaw sizes. Thus, to establish the flaw size for a set lifetime it is an iterative process inputting initial flaw sizes in the equation.

Example: What is the time to failure in the GFRP layer with the rotor running at 700 Hz, if an initial flaw size (a_0) of 20 µm exists in the rotor at the "worst case" location.

We know that the critical crack length (a_{crit}) for failure in the GFRP section at this speed, using the maximum resolved stress level is 1913 μm. Thus, by substituting in the various values we can obtain the time for the defect to grow from a_0 to a_{crit}. Since the crack growth equations were derived with the units of K in $MPam^{1/2}$, we must use MPa and m for the stress levels and crack lengths respectively.

$$t = \frac{2}{2-n} \cdot \frac{1}{A\left(Y\sigma\sqrt{\pi}\right)^n} \cdot \left[a_{crit}^{\,1-\frac{n}{2}} - a_0^{\,1-\frac{n}{2}} \right]$$

From earlier charts, specified, $A=2.31\times10^{-7}$ (Figure 5-10)

$n=9.85$ (Figure 5-10)

$\sigma=32.5$ MPa (Figure 6-16)

$$t = -0.2547 \cdot 6.6458\times10^{-12} \cdot \left[4.6694\times10^{10} - 2.7762\times10^{18}\right]$$

$$t = 4.69\times10^{6}\ s$$

Thus, Graphs may again be constructed to show the critical initial flaw size vs. time. The same guidelines that applied to the previous set of graphs apply again here. The axial stress level has been used for the NdFeB and GFRP layers, whereas the radial stresses have been used for the CFRP layer.

In the cases, where applicable, the MRS stress prediction was included on the lifetime charts as a red line. No MRS prediction has been included in the NdFeB layer, since the resolved stress level is almost identical to the maximum axial stress. It is also assumed that the crack growth rate in the NdFeB layer is the same as in the GFRP layer. Accepting that this is almost certainly not the case the analysis has been completed as an estimation rather than a definitive prediction of defect size.

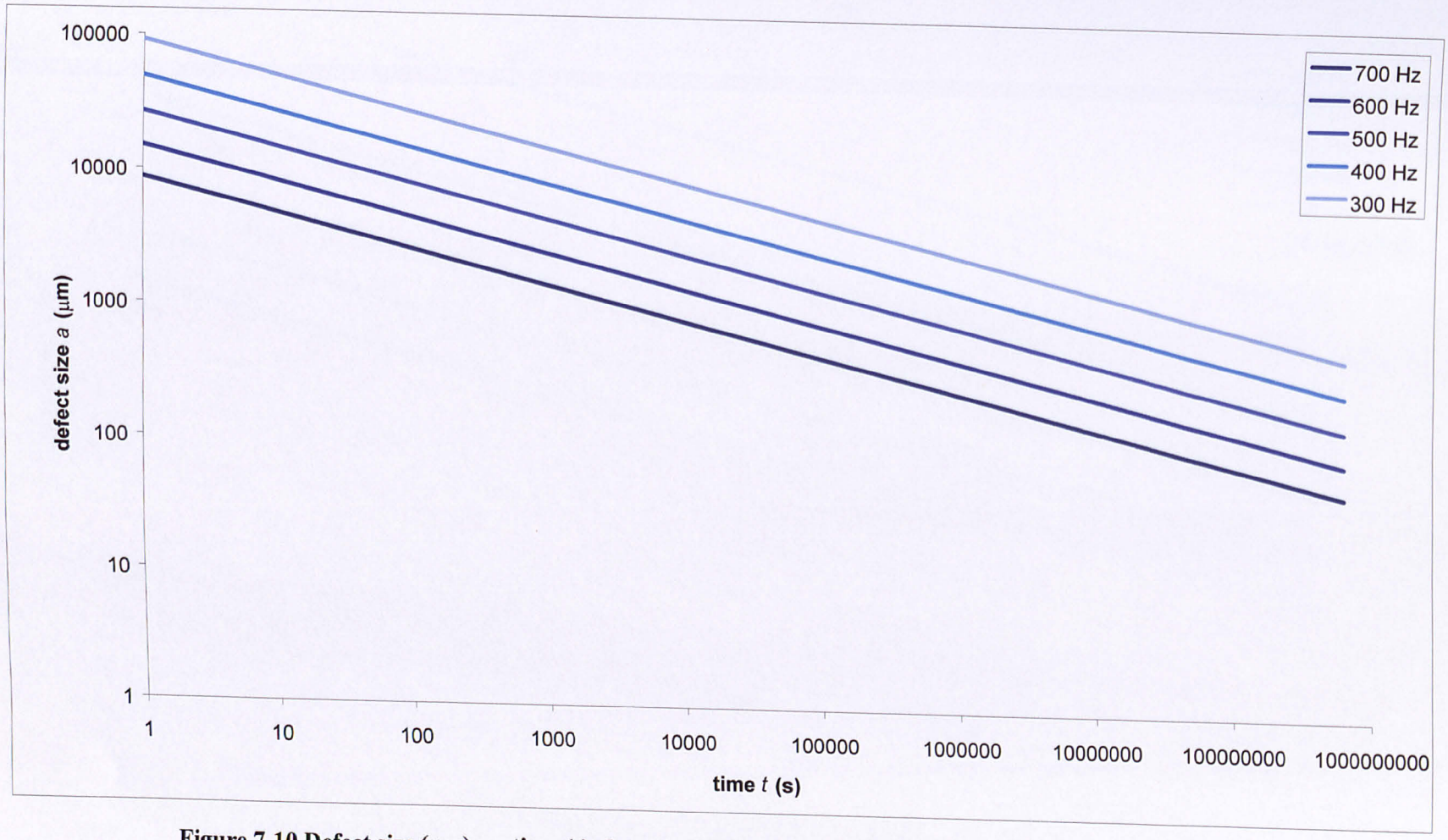

Figure 7-10 Defect size (μm) vs. time (s) chart for NdFeB layer calculated via active crack growth route.

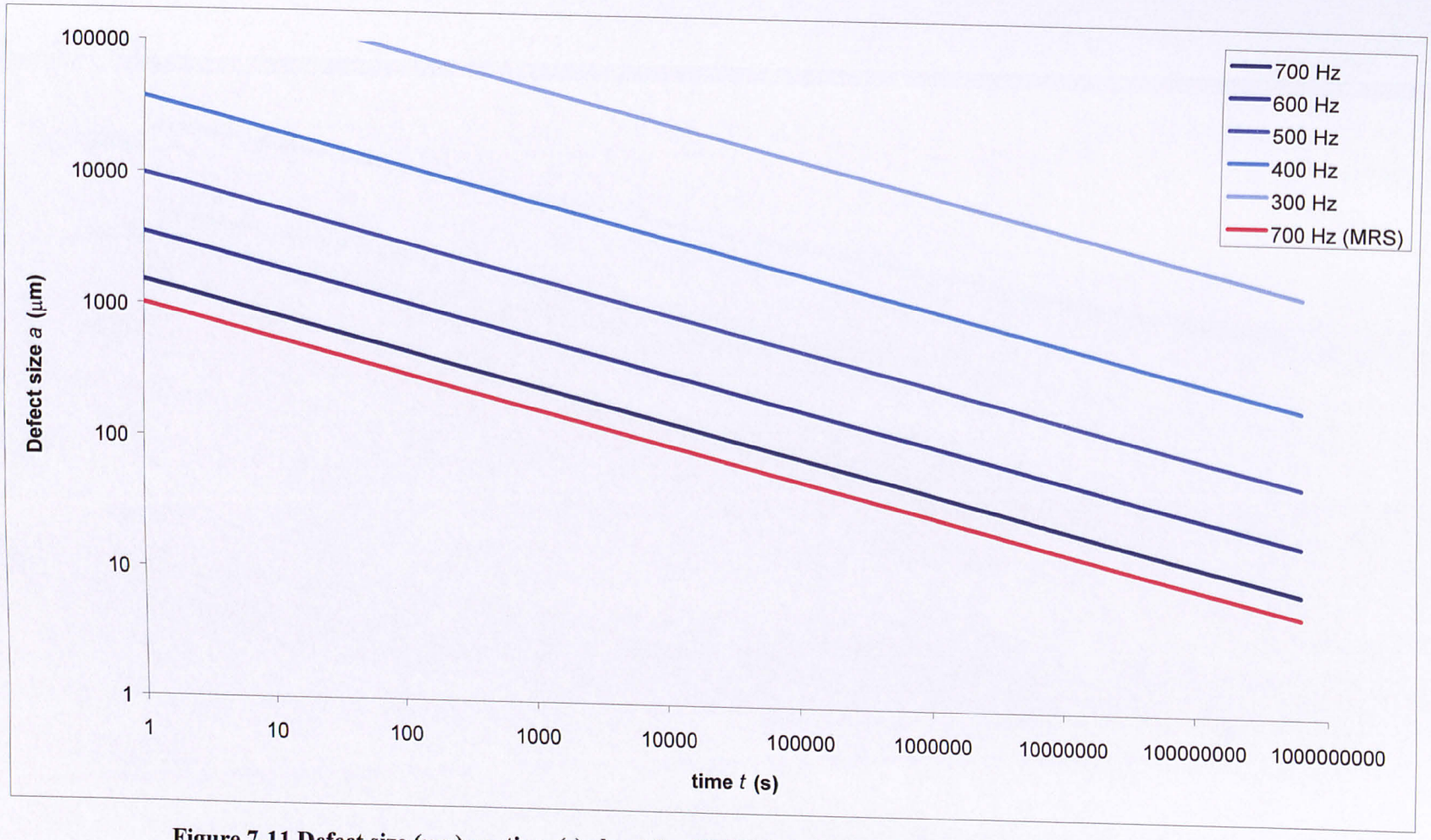

Figure 7-11 Defect size (µm) vs. time (s) chart for GFRP layer calculated via active crack growth route.

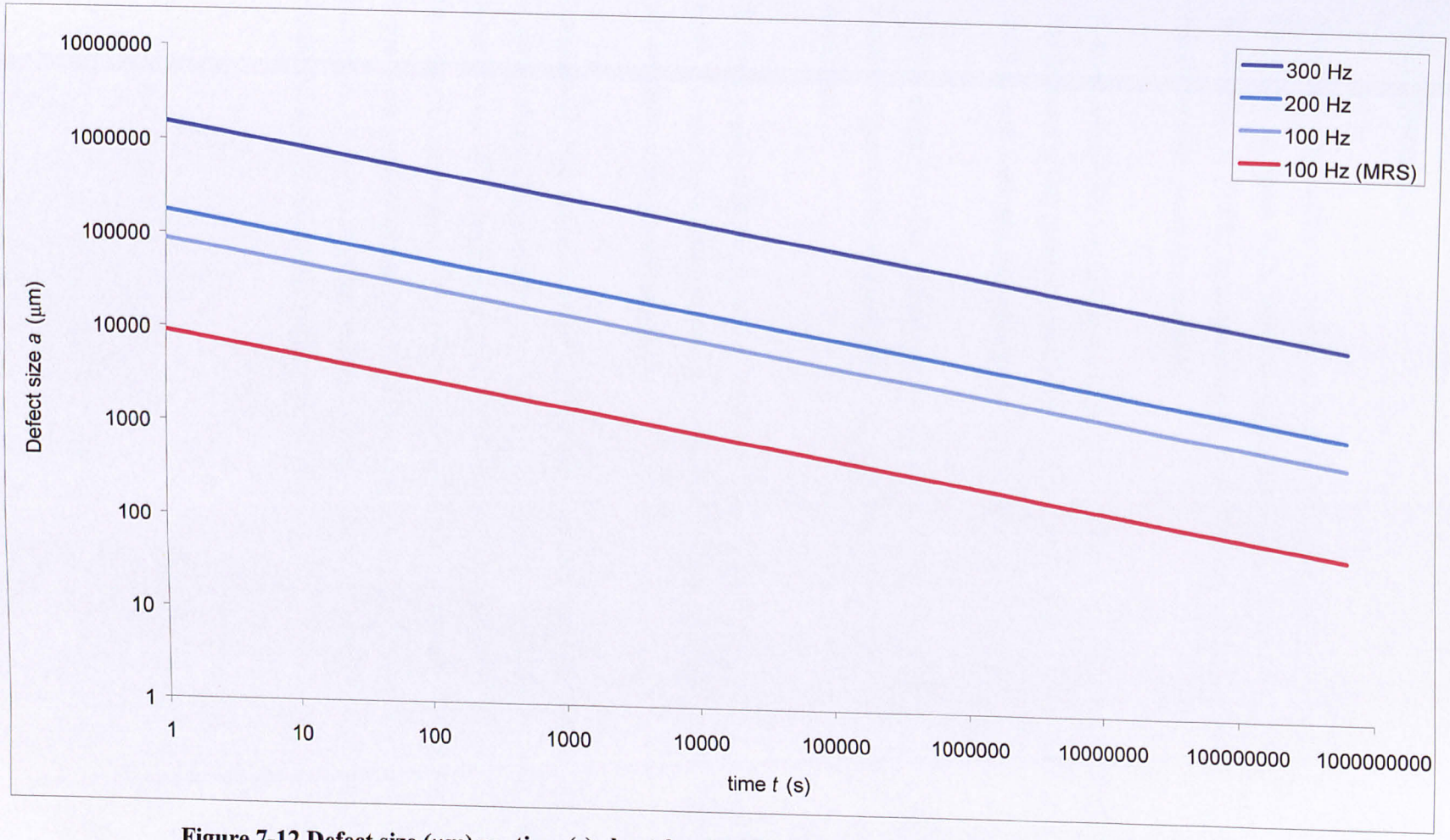

Figure 7-12 Defect size (µm) vs. time (s) chart for CFRP layer calculated via active crack growth route.

7.8.1 Discussion.

The two approaches to crack growth give similar results. These methods are illustrated in figure 7-13, which compares the results of the two approaches for the GFRP layer at 700Hz. In addition we may also look at given cases and compare the results between prediction methods.

1, Rotor speed=700 Hz, Lifetime =10 seconds. Failure to originate in the GFRP layer. For dormant defect method a defect size of 5000μm is forecast, whereas for the active crack growth method a critical defect size of 1000μm is predicted.

2 Rotor speed =700 Hz, Lifetime =6 months. GFRP layer failure. The two approaches predict 140μm for the dormant defect approach, and 40μm for the active crack growth approach.

3, Rotor speed =700 Hz, Lifetime =20 years. Again failure to originate in the GFRP layer. The two approaches predict 40μm for the dormant defect approach, and 10μm for the active crack growth approach.

Simplistically the active crack growth method predicts far smaller defects. Since the science behind this predictive method is more accurate, these should be relied on more heavily. When comparing cases 2 and 3 it can be seen that it will take 19.5 years for a defect to grow from 10 to 40μm, but then just 6 month to grow to 1000μm. This is due to the significantly smaller initial K on the crack, increasing as it grows, until it reaches K_c at a crack length of 2000μm at which point the rotor fails. This sequence should occur in the final 10 seconds of the rotor life.

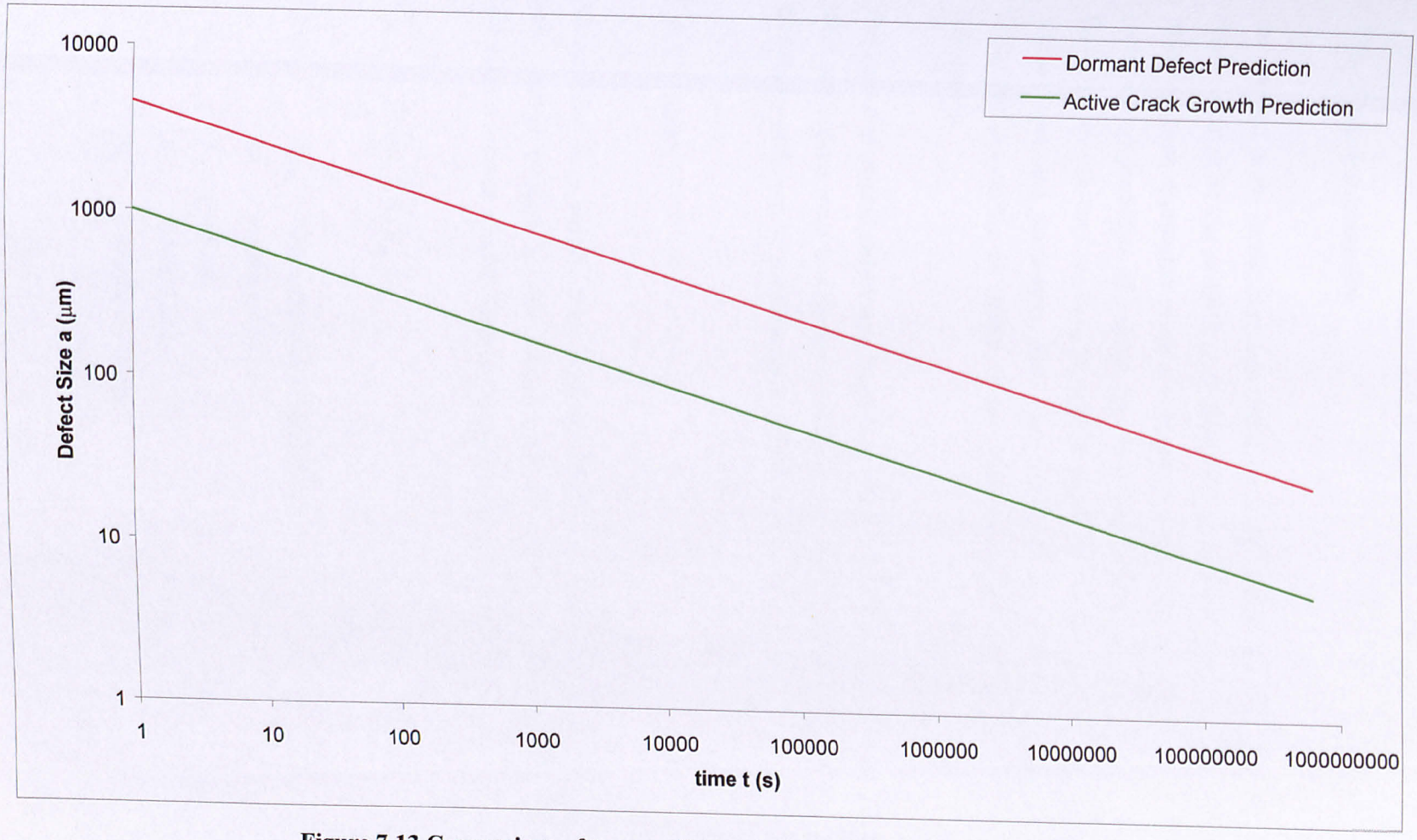

Figure 7-13 Comparison of two predictive methods for GFRP layer at 700Hz.

7.9 *Failure probability*

As outlined in the literature review, there are many approaches that may be taken in order to calculate the probability of failure of a component for a given service life. Many of these approaches relate a wide range of operational parameters in order to make a final prediction of service life. Traditionally these approaches are complex. However, in this case we have completed experiments and analysis that relates the primary operating parameters, time and speed, with a critical starting defect size. Thus, the probability of failure of the rotor is solely related to defect size and distribution.

The spread of critical defect sizes have been predicted by separate methods, however these predictions must be combined with the measured defect data to determine the probability of failure for the rotor for any given lifetime.

7.9.1 Theory

Assumptions have already been made to simplify the analysis. These assumptions were carried through to this section and with these in place the probability calculations become simpler. Essentially, the problem can be defined:

$$F_{rotor} = fn(\omega, t, a, v_a)$$

Where:

F_{rotor}	=Probability of rotor failure.
ϖ	= rotor speed.
t	= time.
a	= defect size.
v_a	=volume of defects.

In essence failure of the rotor is governed by a function of speed, time, defect size and quantity of defects. Thus, for a given scenario (i.e. rotor speed and time are constant), the probability of failure is purely a function of defect size and occurrence. The relationship between ϖ, t and a has already been formed via two separate routes. The two methods project different critical defect sizes. The defect sizes are different enough to present different solutions to the probability of failure calculations.

The two sets of charts for defect size vs. time are used to specify the initial starting defect size (Figures 7-8 and 7-9). These charts calculate the magnitude of the critical defect size for a given operating condition. This means that for a given scenario, ϖ and t can be treated as constants, thus defining that particular critical defect size. Consequently to estimate the probability of failure, we must establish the likelihood of a defect of this magnitude or greater existing within the rotor.

In this case the simplest solution by Weibull [84] is suitable. This solution predicts the probability of the occurrence of a critical defect in a solid of volume V. As outlined, advanced methods of lifetime prediction use many other parameters such as the stress levels, lay-up method and environment. In this case, the flywheel, those other factors have either been calculated or an assumption has been made, i.e. stresses, time are already incorporated into the defect size charts. Thus, an adapted version of the Weibull theory may be used to calculate the probability of failure of a rotor.

Since we can calculate the probability of the occurrence of a critical defect (Section 3.5.5), this will equate to the probability of failure of the rotor, since failure can be purely related to defect size. Thus, the probability of failure is:

$$F_{rotor} = 1 - e^{\left[-\left(\frac{V}{V_0}\right)\right]}$$

Where V=volume of the rotor

V_0=mean volume per defect.

The mean volume per defect data in this case is not accurate. The parameter here must be mean volume per dangerous defect. The size of this defect was calculated from the

charts in sections 7.6-7.8. Since the defect data is taken at random locations throughout the rotor, statistically each measurement was representative of the entire rotor. I.e The distribution of voids was assumed to be independent of radius. In reality it was found that the void size and distribution does change with radial position, however, the effects were slight. In future a more comprehensive study of the voids should be undertaken.

7.9.2 Defect data

In previous sections (3.5.4) the defects were analysed in detail. Histograms, figure 3-7, were formed to show the distribution of the measured void sizes for all the material layers and the associated distributions were allocated. All the defect data was combined into figure 3-8.

Thus, the probability of finding a dangerous defect may be determined using these distributions.

7.9.3 Calculations.

At this point the scenario we were asked to investigate, must be outlined. Using the original guidelines outlined by Urenco. A flywheel life of not less than 20 years was required. The angular velocity was set at an upper limit of 700Hz. This is the same as case 3 outlined earlier. Thus, for the dormant defect method, figure 7-6 stated the maximum permissible flaw size in this case was 40μm. This assumed the failure would originate in the GFRP layer. The maximum resolved stress level was used since this had the highest magnitude.

Using a simple statistical calculation, based upon the measured defect data, it is possible to determine the probability of a given defect being present. The background for the expression is highlighted in section 3.5.5.

$$z = \left(\frac{a - a_M}{S} \right)$$

The z value may be converted to a probability (P_{danger}) using statistical tables [58], Appendix D.

Where P_{danger} =probability of a dangerous defect being present.

a =defect size

a_M =mean defect size.

S =standard deviation.

z =this is a measure in terms of standard deviations of the probability.

Thus, the probability could be determined using the data for the GFRP inner layers (Table 3-4). This example required the probability of finding a defect ≥40μm, which related to a z value=1.28. This equated to a probability of 10.03% for finding a dangerous defect out of the defects measured in the GFRP layer.

To allow the predictions to be made, these probabilities were converted into mean volume per dangerous defect. This was achieved using the void fraction data (Table 3-3), which represented the voidage of the composite in terms of % volume. Since all rotors are exactly the same size and the measurements on voidage were defined in percentage terms. If the entire volume of the rotor is regarded as 1, then the product of the %voidage and the probability of finding a dangerous defect, resulted in the volume of dangerous defects, measured in complete rotors. The reciprocal of this gave us the number of rotors per dangerous defect (V_0). The final required parameter.

Again using the "worst case" scenario, in terms of voidage in the GFRP layer (4.9%), V_0=203.5 rotors

Thus, using the Wiebull expression, the probability of failure of a rotor (case 3) via dormant defect method is 0.49%.

Using the same analysis, but for the more severe active crack growth approach, where the critical defect size is 10μm. then the probably of a defect of this sizes occurring amongst the voids is 87.3% as opposed to 9.6% for a 40μm defect. Surprisingly, the effect this has on the overall lifetime is small, although it has increased by a factor of 10, the probability of failure has only risen to 4.2%.

The reasons that this change in overall probability is small is that the change in critical defect size effects a small part of the overall probability. I.e. 90% of 5% instead of 9% of 5%.

Addendum: Extra probability has been calculated, see page 261.

7.10 Lifetime Guarantee.

The fact that it is possible to predict that 4.2% of manufactured rotors will fail is useful. However, this is of little consequence to Urenco, the manufacturer, who need to be able to guarantee the life of every rotor produced.

7.10.1 Introduction.

Thus far it had been possible to predict the time to failure and the probability of failure of the flywheel rotor under simplified loading conditions, if the initial flaw size were known. However, we were still constrained by the defect size. This was the variable parameter and ultimately the only free variable. Thus, to guarantee the lifetime of the rotor one must either:

- Be able to directly measure every defect in the rotor. (NDT)

Or

- Perform a test upon the rotor which indirectly measures the size of every defect. (Proof stress)

7.10.2 Non-destructive techniques.

The use of non-invasive techniques to measure the quality of the rotor had been considered. Although the use of non invasive techniques have been employed on composite structures in many industries, to detect damage and voids, in general they are unsuited to small defects. Defects of the order of 40μm in size are practically undetectable let alone 10 μm [60]. Another concern was the thickness of the rotor (80mm). This coupled with the inherent problems posed by the cylindrical geometry and the ability to produce a reliable transmission trace, meant that the possibility of developing an NDT test for the rotors was low.

Notwithstanding these concerns, a section of rotor was C-scanned, figure 7-14. The results showed that the transmission of the signal was independant of radius. The peak transmission signal occurred at the GFRP/CFRP interface. This trace for signal intensity was compared with the plots for residual stress levels (Figure 6-3). However, no correlation could be drawn other than the maximum signal intensity coincided with the greatest change in residual hoop stress levels. Thus, the C-scan was insensitive to defects, but does seem to give an indication of the residual stress state. Further investigation into this phenomenon was not conducted.

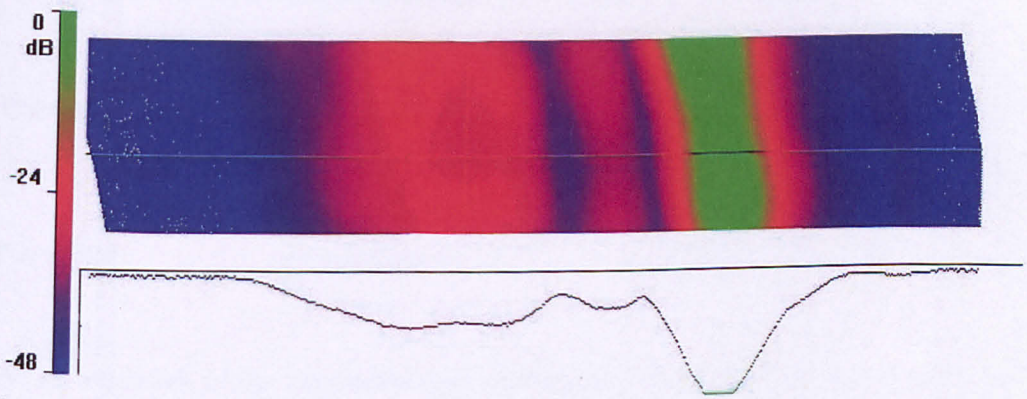

Figure 7-14 C-scan of rotor. (NdFeB left to CFRP right)

7.10.3 Proof Stress Method.[39]

The proof stress method involved the use of the fracture mechanics data with suitable testing conducted upon the structure. The assumption is that failure results from the growth of a crack originating from a defect. If a component is assumed to fail at a given stress, it is possible to calculate the size of the inherent defect in the material using the relationship between applied stress, fracture toughness and crack length. If a component survives the application of the same stress level, then the inherent defect size calculated when failure was assumed, this becomes the maximum permissible defect size in the component. The higher the stress level the component survives, the smaller the maximum possible defect size becomes. The consequence of the survival of such a test at such stress levels, is that the life of the component could be guaranteed with a high degree of confidence.

7.10.3.1 Method.

Since the rate of crack growth for the various materials had already been determined and was known to take the form:

$$\frac{da}{dt} = AK_I^n$$

Where A and n are constants determined previously (Figures 5-10 and 5-11):

For GFRP $$\frac{da}{dt} = 2.31\times10^{-7}K^{9.85} \quad R^2 = 0.841$$

For CFRP $$\frac{da}{dt} = 3.956\times10^{-6}K^{9.93} \quad R^2 = 0.806$$

As an extension of the simple fracture mechanics[39]the following expression could be used to relate the minimum time (T_{min}) to failure with the operating stress, in terms of a_0, which was the maximum possible flaw size.

$$T_{min} = 2\left(\frac{\sigma_p}{\sigma_a}\right)^{n-2} \cdot \frac{1}{(n-2)A\sigma_a^2 Y^2 K_{IC}{}^{n-2}}$$

Figures 7-15 and 7-16 illustrate the product of this expression in terms of generic proof stress diagrams for thick transverse UD composites. Here T_{min} has been plotted against σ_a for a variety of stress ratios (1.5→10). The red line plotted represents an upper limit to the proof stress. I.e. this is the transverse strength of the composites. These values were based upon those generated in the static testing section.

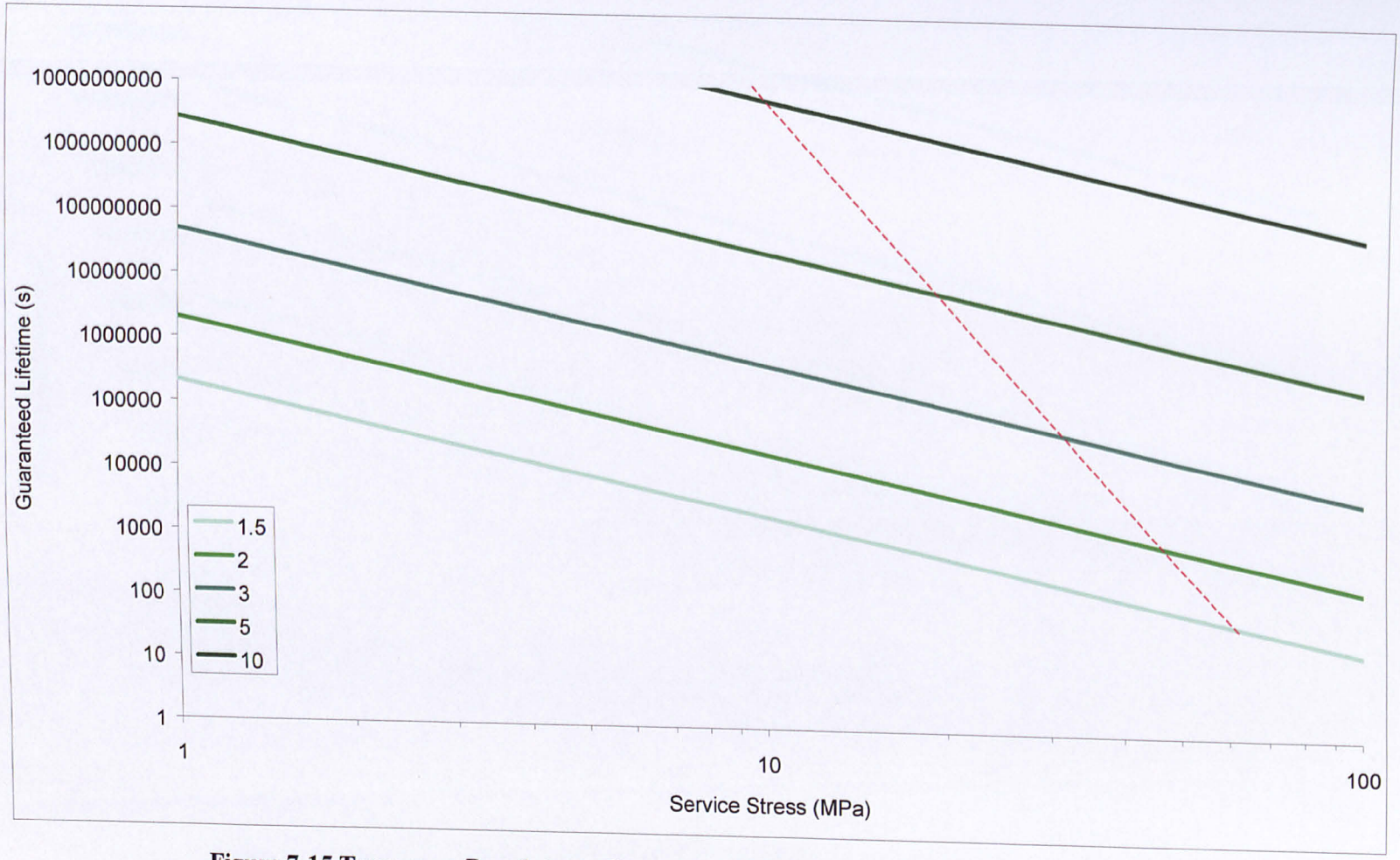

Figure 7-15 Transverse Proof stress diagram for GFRP composites, stress ratios in legend.

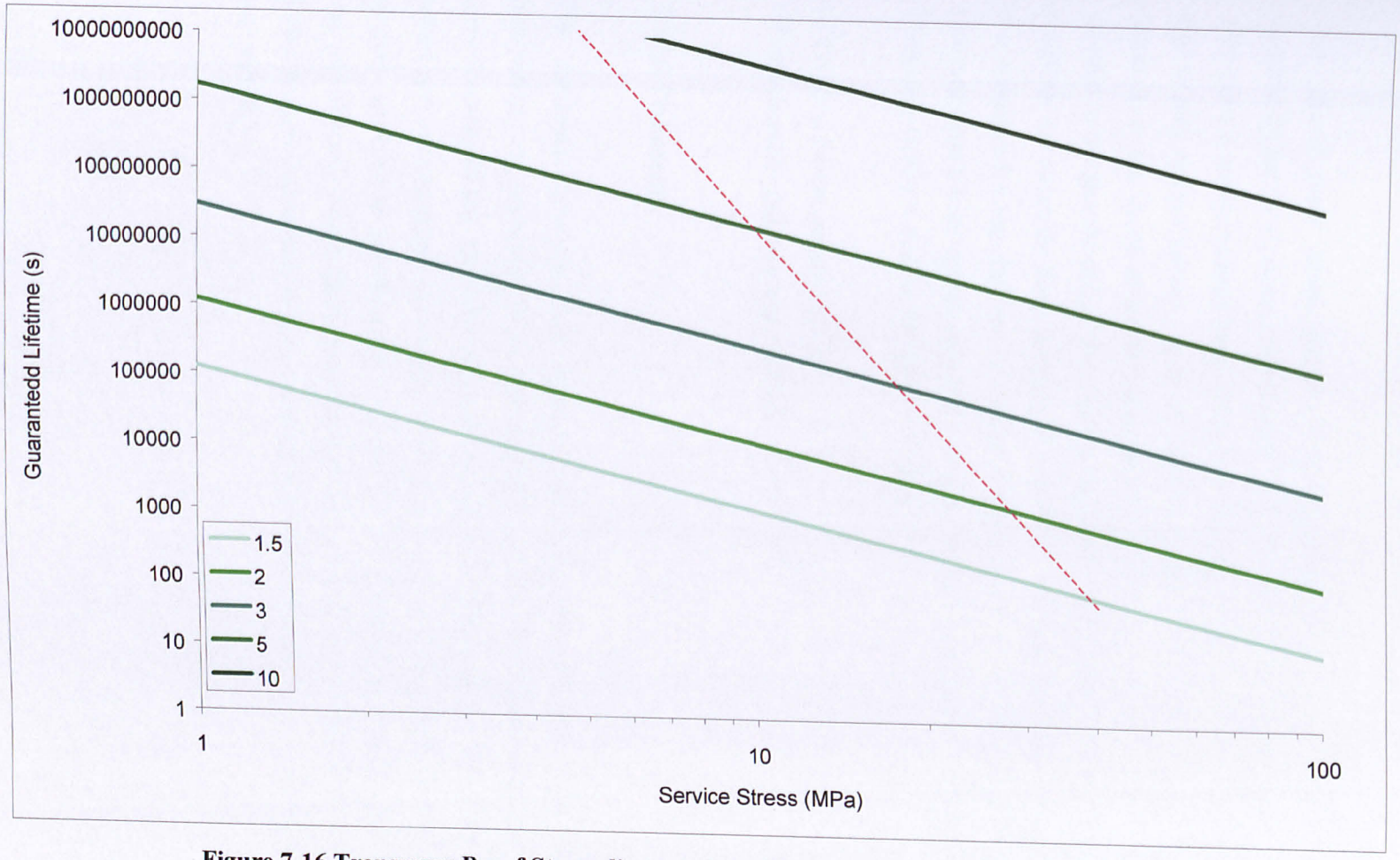

Figure 7-16 Transverse Proof Stress diagram for CFRP composites, stress ratios in legend.

7.10.4 Proof Stress for flywheel rotor.

The generic proof stress data may be represented as a proof stress diagram, specifically for the flywheel rotor (Figure 7-17). This chart was based upon the GFRP data since it has previously been determined that the other layers have no significant role to play in rotor failure. Again the red line denotes the upper bound of the proof stress. I .e. the speed at which instantaneous failure of the rotor would occur. In contrast to the generic charts, this line is not based upon the transverse strength of the materials but rather the hoop strength of the CFRP. The hoop strength of the material was calculated using the rule of mixtures (section 2.2.1). This strength was then converted into a rotor speed using figure 6-6. In theory, failure will occur in this layer marginally before it does in the transverse direction.

CFRP hoop failure speed=1106Hz
GFRP transverse failure speed=1175Hz

7.10.5 Comments.

The maximum predicted safe lifetimes are very short, 6 months at 700Hz. Interestingly the predicted defect size to cause failure in 6 months, from case 2 is approximately 40 μm. the void size analysis has shown that a void of this magnitude would not be considered uncommon in the rotor, with a 9 % chance in any given section. However, as the discussion will show this is based upon a highly simplified case and although this analysis proposes that the flywheel is not stable at this speed, further thought is required to give a clearer picture of the actual likely lifetimes, see next section.

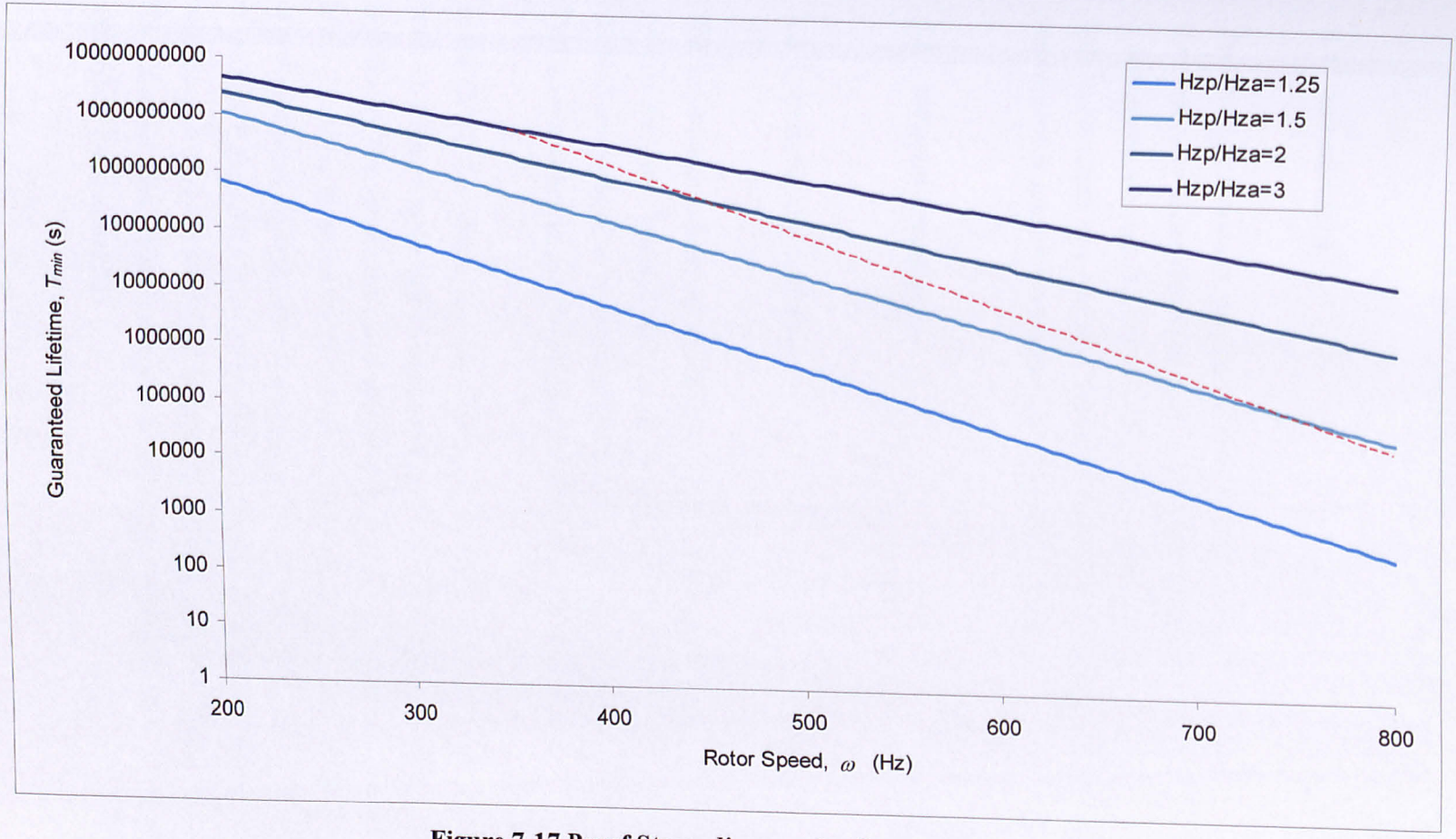

Figure 7-17 Proof Stress diagram for flywheel rotor.

8 DISCUSSION AND ANALYSIS.

8.1 Introduction.

The aim of the research project has been to ascertain the long term durability of the flywheel rotor under simplified operating conditions and predict its survivability over a designated lifespan. To this end the various materials were characterised and these will be discussed here initially. The stress state will be briefly reviewed, then all this information is related to the behaviour of flywheel system.

8.2 Material Properties.

8.2.1 Volume and void data.

The material properties of the various layers of the rotor were determined using various methods. Initially the volume fraction of the layers was determined. This allowed comparisons to be made with other research. The volume fractions were high. This was expected. In the CFRP layer the v_f was approaching 70%.

In the GFRP the volume fraction (Table 3-2) was found to vary with radial position, from 61.4% next to the NdFeB layer down to 57.5%. This is not a huge variation but a significant. The prominent cause of this variation is the significant thickness of this layer. The inner layers of the GFRP are packed more tightly due to the large amount of material being layered onto it, supplying extra compression, i.e. the full thickness of the GFRP and CFRP layers. This theory is supported by the void fraction data. The void fraction of the inner GFRP layers is lower than the outer layers by nearly 2%. The statistical data for the voids also illustrates that the voids that are present in the inner layers are also smaller.

Obviously the NdFeB layer has a lower v_f (not measured) due to the 20% filler included in the matrix. However, on the basis of the above theory the NdFeB layer should have the smallest voids, since it is the first layer to be wound and thus, the entire rotor is then wound onto it. This is not the case and in reality it has the largest voids present in the rotor. This effect is attributed to the interference that the filler particles has upon the viscosity of the resin and subsequent manufacture.

A difference was also recorded between the axial and radial volume fractions. It was found that the axial direction was more tightly packed than the radial. This was attributed to the contractions during the curing process. Since the axial dimension is far greater then the radial one, more contraction takes place, increasing the V_f.

8.2.2 Elastic properties.

Although an attempt was made to measure the hoop modulus of the various layers the test method was not designed to perform this type of measurement. Only values for the GFRP layer were recorded, this is due to the lack of material of the NdFeB layer and the very high hoop modulus of the CFRP. The results for the GFRP are reasonable. Compared with similar composites a modulus of 40.1 GPa is acceptable. The variance of 18.1 % may be attributed to the unsuitability of this test method. Thus, in general this test method would not be recommended for this type of test due to the reasons outlined in section 4.6.1.

The values for transverse modulus are comparable with those in the literature (CFRP [46] [49], GFRP [23],[78]). The variances measured are also similar. Possible reasons for the higher than desired variances was the interference experienced by the data logging system, perhaps compounded with inaccurate strain gauge placement. The Poisson ratios are also broadly inline with published values. In the CFRP layer those Poisson ratios recorded in the hoop direction show very high variances. This was attributed to the very high stiffness of the material in this direction, coupled with the limit of the data logging system being reached in terms of very small strains.

When the radial and axial GFRP data is considered, the first effect of the changing volume fraction can be observed. The moduli in these directions changes with radial position. In both directions higher moduli were recorded for the inner GFRP layers. The variances of the radial tests are high, although they improve as the radius increases. No reason can be offered with regards to this change in variance. In the axial direction the opposite occurs, the variance improves as the radius decreases. Similar variances are recorded for the various Poisson ratios.

The Poisson ratio of the radial direction is constant across the radius. In the axial direction the value is also constant, however lower at 0.28 compared to 0.325. This difference in Poisson ratio again strengthens the argument that the materials are not transversely isotropic. The ratio of Poisson ratio is 0.86, this compares with a ratio of 1.1 for the moduli. These findings correlate well with the results that show the fibres are more densely packed in the axial direction.

The same trend is evident in the CFRP layer where the axial modulus is higher than the radial by a ratio of 1.3. This relationship could not be established for the NdFeB layer since no data was recorded for the NdFeB in the radial direction. The axial modulus of the NdFeB layer is higher than that of the glass fibre alone. The modulus of the filler material is high and assuming the adhesion between the filler and resin is good, then the modulus should increase.

8.2.3 Strength Measurements.

The strength measurements conducted using the flexural test method yielded good results. This method only places a small volume of the specimen in tension. Thus, the well documented volume effects of the composite must be considered. With this in mind is reasonable to assume that the "true" strength of the composite had been measured. When compared to similar tests the strengths are reasonable. The v_f effect was again evident in the GFRP layer. The difference between the inner and outer sections is very pronounced. This is due to a combination of the v_f effect potentially exaggerated by the increase in the voidage and void sizes.

The results indicate that the GFRP has a better interfacial strength than the CFRP. In the NdFeB layer the low strength is caused by the filler. Although the adhesion between filler and matrix is good, the filler is still effectively acting as voids in the material, creating large stress concentrations at the sharp edges of the powder.

8.2.4 Fracture toughness.

The results for the two different test methods did not compare well. The ASTM was not designed for testing composite materials in this manner and as such the poor results may be attributed to this. The tests did, however, justify themselves by demonstrating the most effective crack tip sharpening technique. The variances of these tests were low, for fracture tests. This indicated that indeed they were representative if the material behaviour even if the results were low. Thus, they demonstrated the changing v_f of the GFRP layer had no significant effect on the fracture behaviour of this layer.

Those tests conducted upon the NdFeB using this method would remain the only results for this region. According to these results the NdFeB layer had the highest fracture toughness of all layers. A probable cause of the increased toughness is the resistance the powder offers to crack growth coupled with the increased volume fraction of matrix. We know from the strength tests that in this situation the powder acts as voids. However, here it acts as a toughening medium, almost like a short fibre in the matrix. This is only conjecture since the variances are large enough to dispel this theory.

The compliance measurement data yielded more representative values for fracture toughness. Only the CFRP and GFRP layers were tested using this method. The strain energy release rate values recorded were very similar to each other. Thus, it is reasonable to assume that the strain energy release rate is closely related to a factor that is constant in both materials, the matrix. The notion that the transverse toughness of fibrous composites is a highly resin dominated property is not new. Other research had shown that this is the case. These results merely help to confirm these theories [75]. Another primary factor that is known to have an effect on the fracture properties

of the materials is the interfacial strength. However, without appropriate tests it is not possible propose any relationship here. It is however known that in theory the interfacial strength of the GFRP layer should be higher than the CFRP layer. This may in part explain the greater G_{IC} value for the GFRP.

The K values differ because the transverse moduli of the two materials are very different, and modulus is used in the calculation. The generated values for both G and K are respectable, and are inline with other published data [78]. They compare well with the DCB and other methods examined in the literature.

8.2.5 Creep rupture.

The scatter in the data for the long term tests is somewhat higher than in the pure static test. This is due to the added variable of time. Since the time dependant mechanisms of the materials were not constant this added to the variability. The suggestion must be made on the evidence of the SEM work that the long term behaviour of these materials is largely dependant on the resin. The amount of matrix yielding evidence supports this. However, again the interfacial strength of the materials, and its dependence upon time must also have an influence on this property, but without qualification it is not possible to make a definitive proposal.

Except the magnitude of the numerical values for the differing materials, there was no fundamental distinguishable difference in the long term CFRP and GFRP behaviour.

8.3 Stress state.

The stress state within the rotor is complex. It is however, worth noting various overall points from this section.

The various materials with different properties result in various high stress gradients. In some cases these are advantages. I.e. the compressive transverse stresses in the CFRP which should act as a barrier to crack growth. Consideration must also be given

to the fact that any improvement in the transverse modulus decreases the hoop stresses during operation but broadly increases the radial and axial stresses. The increase in radial and axial results in higher resolved transverse stress. This stress is crucial for lifetime prediction.

8.4 Flywheel Behaviour.

The consequences of the material data on the performance of the flywheel was widespread. Since the flywheel is destined for a multitude of roles, each with its own specific design variables, only the simplest of cases, i.e. power back-up was investigated. Even with the reduced uses in mind, specific conditions were applied rather than studying every possible scenario, due to the complexity of the task. The principle guidelines were

i. Static loading condition, i.e. rotor velocity remains constant.
ii. Constant temperature (40°).
iii. Omission of the vacuum condition.
iv. The third (hoop) dimension stresses are ignored.
v. All defects in the rotor have sharp edges.

These conditions were all assumed to be constant throughout the working life of the flywheel rotor.

8.4.1 Theory Assumptions and Consequences.

The effects of these constraints on the prediction made in this thesis are widespread. The notion that the rotor is subjected to a constant speed during its lifetime is highly idealised. In practice the flywheel rotor does not even need to be "topped up" with energy very often, due to the highly efficient design the rotor only losses a couple of Hz every few months. Thus, the assumption is reasonably safe. However, it is anticipated that many flywheels will be used for power smoothing, or similarly backing up supply on a daily basis, in which case the units will be continuously

changing speed. This introduced a fatigue element to the prediction, which has been ignored at this stage.

Even so the assumption has been that the velocity does not change whatsoever. Thus, we could expect creep within the rotor, in all directions, although this has been assumed to be negligible for this project. In addition the temperature of the rotor is expected to be very constant, regardless of installation location. However, to compound the issue it is expected to be somewhat higher (c. 60-80°C) than the originally designated 40°. The effect on the composites of elevated temperatures and constant loading will certainly lead to significant creep within the rotor in the transverse directions. The temperature effect will be beneficial since it should increase the toughness of the material due to the increased visco-elastic effect. However, the transverse strength of the materials will reduce, but this does not effect the lifetime calculations presented.

The omission of the vacuum condition poses some interesting issues. Polymer materials are known to outgas rapidly under vacuum. Typically the out gassed products are moisture and other low molecular weight volatiles, such as solvents. Studies [67], [53] have shown that the reduction in mechanical properties can be quite severe when this vacuum is combined with stresses. Thus, the rotors are degassed by Urenco prior to installation.

The huge stresses in the hoop directions are not taken into account when the testing was conducted, neither were the radial stress, however, these have been partially corrected for in the lifetime prediction graphs. Conversely any effect of the residual stresses in the rotor were also neglected during the testing phase, but were included in the lifetime prediction work.

The hoop stresses are ignored, it was assumed that this loading condition has no effect on the transverse behaviour of the material. The extent of the effects that this may have are unknown, but could be very significant. Some researchers [41] have published information suggesting that the effects are very pronounced. The triaxial loading in the rotor can be very significant, for example at a r=100mm the GFRP is being loaded at in excess 70% of its UTS in all directions.

It has been observed that the perimeter of the defects present within the rotor are rounded in virtually all cases, a product of the filament winding manufacturing route. In addition the winding manufacture will produce defects that are not symmetrical in every plane, i.e. it is expected that the defects will run around the circumference of the rotor, as highlighted earlier. The primary assumption for LEFM is that all cracks are sharp cracks (i.e. stress concentrations with a tip radius of curvature of atomic dimensions). As a result, although the predicted critical defect sizes will be accurate, the magnitude of the effects of crack shape are unknown. It is, however, reasonable to assume that the estimation will be conservative due to local stress intensity required to propagate a crack from a blunt defect will be greater than that for a sharp one. The magnetic filler with its sharp edges may be considered as a defect. If this is the case then the LEFM is a good fit. To offset this argument, the size of the magnetic filler is considerably larger then the predicted defect sizes and it will carry load through it and thus will not have the same stress intensity as a hole in the material. However, it is reasonable to assume that as the resin shrinks around the NdFeB particles during cure, significant stresses will be built up in the resin around the particles edge. With this situation present, it is prudent not to neglect the role the filler may have on the life of the rotor.

One other cause of in accuracy is the assumption made for Y. As stated, to accurately determine this for the rotor is a complex task. However, without this no prediction can be truly accurate. The influence this will have on the lifetime is unknown since it cannot even be guessed as to which way Y will tend towards. It is safe to assume that the overall effect this will have will be relatively minor since Y is typically equal to 1 for most cases.

The validity of the fracture mechanics relationship to the materials has also been raised as an important concern. This concern lies not with the accuracy of the calculation, however it poses the question of whether fracture mechanics may be applied across a spectrum of specimen sizes. If the static fracture toughness and strength tests are accurate, for which there is no reason to believe they are not. Then, we must question why the inherent defect size and the directly measured defect data are so different. In reality only the calculation can be at fault. It has been widely

regarded that conventional fracture mechanics may be used [75], however further investigation is ideally required into to the situation specifically, i.e high volume fraction unidirectional composite with transverse cracking.

8.4.2 Influence on lifetime predictions.

The outlined assumptions will of course have an effect on the calculated lifetimes and probabilities. It is impossible to state what the definitive results of these assumptions are. However, table 8-1 shows the anticipated trends these assumptions may have on the life of the rotor.

Table 8-1 Consequences of the assumptions.

Assumption	Effect on stress state	Effect on Fracture toughness	Effect on lifetime
Constant rotor velocity	0	0	+
Constant temperature (40°)	N/A	-	+
Omission of vacuum	0	-	+
Unknown Y value	N/A	±	±
Defects are sharp (LEFM)	0	+	+
Triaxial stress state	N/A	-	-

8.5 Failure scenario.

Thus far the probabilities of failure has been established. However, in the event of all the assumptions being wildly inaccurate, what is the likely failure event.

Realistically we can disregard any suggestion that failure will be initiated in the CFRP layer. The defects here were relatively small and the axial stress levels predicted for the CFRP are very low or non-existent, within the normal operating range (300-700Hz). The CFRP will only see tension below a velocity of 400Hz, with a maximum of 3.5MPa at 300Hz. In reality for failure to be started in the CFRP layer, one would expect this to be due to failure in the hoop direction. However, this is outside the scope of this thesis.

The NdFeB layer potentially contains a large amount of defects in terms of voids and the magnetic filler. This filler with its sharp edges can cause stress concentrations which may act as a very good crack initiator. The NdFeB/GFRP layers interface also experiences very high axial stresses. These are lower than the MRS values found in the GFRP layer but combined with the proximity of the filler particles this location must be regarded as more dangerous than just a large manufacturing defect in the GFRP layer.

Thus, a large defect or a particle of magnetic filler at this location is the most likely point of crack initiation in the transverse directions. If this was the case what could we expect the crack to do as the rotor accelerates?

8.5.1 To crack or not to crack?

We know that cracks will grow through the material, however, it is unknown if the cracks will propagate in a negative prevailing strain field.

As a simple preliminary investigation, a modified FEA model was used to predict the extent of crack growth. This model had a much finer mesh in the radial direction, which acts as the crack path. Elements of the fracture behaviour were included. These values were based upon the experimental results. A defect 0.25mm was introduced at the NdFeB/GFRP interface, this was achieved by removing two elements. This is not the ideal method for modelling crack propagation but was regarded as adequate for this simple study. The model was run to 700Hz.

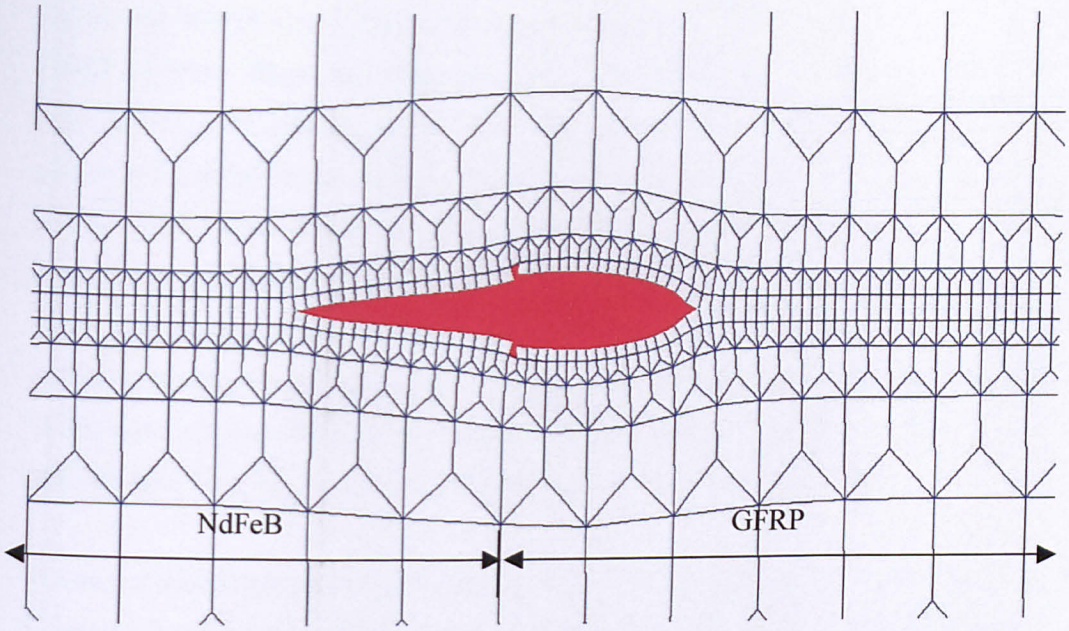

Figure 8-1 Crack propagation from a 0.25mm void, located at the NdFeB/GFRP interface. (×40 deformation magnitude.)

The results of this model are interesting. In figure 8-1 it can be seen that the crack has propagated into both the NdFeB and the GFRP layers. The effect of the higher toughness and lower axial stress of the NdFeB layer can be seen in the smaller crack opening. The amount of crack propagation is relatively balanced, even though the side of the crack in the GFRP layer is exposed to higher stress levels. The FEA did confirm that the introduction of this type of crack resulted in no deterioration of rotor performance.

Unfortunately this model does not represent the true failure of the rotor. The crack growth in the FE model is restricted to a single growth direction. This is predetermined in the input deck. At this stage it is not possible to introduce a number of crack paths and determine the actual growth direction.

In reality as proposed the biaxial stress (MRS) plays a very important role in the fracture of the rotor. Figure 8-2 shows how an actual rotor has failed. It is believed that the crack started at the NdFeB/GFRP interface, however, as the rotor span and the crack propagated into the GFRP layer the crack turned through 90°. Sensibly was reasonable to conclude that the crack was following the line of maximum transverse tensile stress. Once it had reached this maximum (r=109mm) it began to turn back in

toward the NdFeB layer. This is due to the stress level rapidly falling off towards the CFRP interface. Thus, the only option for the crack has is to either continue in the axial direction or make this turn. It is then reasonable to assume that as the crack grows in this stress state, the stress state in the rotor changes such that it is preferential for the crack to turn back in this direction. Once the crack front reaches the NdFeB layer the process reoccurs and the crack began to propagate out into the GFRP layer again. The process continued until the crack extended throughout the entire rotor. In reality since the two "halves" of the rotor are very well keyed together, the functioning of the rotor is not actually compromised. However, with the considerable axial torques that the rotor may see, this situation could quickly deteriorate.

It must be stipulated that this cracked rotor was a prototype for a rotor that could exert a greater electrical flux. As such it had a higher powder loading in the NdFeB layer. The powder grain size was also considerably bigger, of the order of 1000μm. This loosely fits in with case 2 in the prediction section that indicated that a 1000μm defect should case failure at approximately 10 seconds at 700 Hz. These factors associated with the powder were thought to have been the cause of failure, which occurred at approximately 550 Hz upon the first run of the rotor. It must also be noted that the time period from crack initiation to the total rotor beingcrackedwas very rapid, less than 1 second. The indication would be that a far larger defect was present in the rotor.

Figure 8-2 Cross section of actual failed rotor.

9 CONCLUSIONS AND RECOMMENDATIONS.

9.1 Conclusions

- Simple fracture mechanics relationships can readily be used for composites in the transverse directions. However care must be taken when more rigorous analysis is required.
- The fibre volume fraction of the rotor is high and comparable with other filament wound structures.
- The fibre volume fraction of the GFRP layer decreases with increasing radius, by 4%.
- The void content in the GFRP layer increases with increasing radius.
- There is correlation between the transverse moduli and the volume fraction of the materials. I.e the modulus decrease with decreasing v_f (radius).
- The NdFeB filler increases the axial modulus of the GFRP (no radial data measured).
- Halpin-Tsai gives a good approximation for transverse modulus.
- The fibres are packed more tightly packed in the axial direction. The ratio between radial to axial packing is approximately 0.97
- The transverse strain energy release rate is independent of fibre type.
- Time dependant mechanisms are active in the matrix.
- There is a rapid visco-elastic effect when loading long term specimens. This is usually accounts for an initial 0.3-1mm of crack growth.
- The cracks grow very predictably once this initial visco-elastic effect is overcome.
- Slow crack growth may be characterised by a relatively "smooth" fracture surface.
- Residual compressive hoop stresses are present in the CFRP layer, to augment the upper limit of rotor speed.
- Considerable stresses are exerted upon the materials in all directions during normal operation of the rotor.

- The GFRP layer is predicted to be the area most prone to transverse cracking. This is due to the high axial stress (27.7 MPa) at the NdFeB/GFRP interface and the maximum resolved stress (32.5 MPa) approximately midway through the GFRP layer.
- A reduction in the transverse modulus increases the transverse stresses in the rotor during operation, but reduces the hoop stresses.
- Transverse cracking in the CFRP layer is not foreseen as dangerous over the desired lifetime.
- The active crack growth approach to calculating critical initial defect sizes is more accurate and predicts smaller defects overall.
- Rotor failure is most likely to originate in the GFRP layers, the NdFeB/GFRP interface is of particular concern.
- The GFRP/CFRP interface should act as a barrier if a crack grows this far.
- Cracks originating in the GFRP layer will follow the path of highest resolved tensile stress, i.e. turn through an arc.
- Based upon the simple probability calculation. There is a 4.2% chance of rotor failure over 20 years at 700Hz.
- The fact that the defects are not sharp in nature builds an added safety factor in to all the calculations.

9.2 Recommendations.

- Reduce the maximum rotor speed from 700 Hz to 600 Hz. Using the probability calculations this will reduce the probability of failure over 20 years from 4.2 % to 0.1 %.
- Proof tests should be conducted on all rotors to guarantee the lifetime.
- Investigate the possibility of localised toughening of the resin, particularly in the NdFeB and inner GFRP layers. This may be taken to an extreme using elastomeric materials or additives.
- Introduce some axial reinforcement around the NdFeB interface. This could take the form of veil of fibres that could be layered onto the NdFeB layer once it has been wound. Alternatively the winding angle could be momentarily changed radically at this point to offer some strength in the axial direction.
- Initiate a further testing programme to establish a number of unknowns:
    1. Determine at what scales does fracture mechanics apply to these materials.
    2. Investigate how cracks nucleate and begin to grow.
    3. Thus, determine the time period for a defect to grow from 'nothing' to a crack size which then obeys LEFM.

10 FUTURE WORK

10.1 Introduction.

The future work that this research initiates falls into two distinct categories. The first is the continuing measurement of the composite rotors mechanical properties and behaviour under more realistic operating conditions. Secondly, The work presented thus far must be linked into contemporary composites research.

10.2 Continued Rotor evaluation.

Further study of the flywheel rotor is required, if the full commercial potential of this ingenious design is to be realised. The research presented in this thesis forms the basis for continued study of the Urenco flywheel. Figure 10-1 illustrates the current and foreseen continued research activity for the flywheel programme.

As concluded a simplified lifetime prediction model has been successfully developed Again as highlighted previously, the assumptions made allow this prediction for only the simplest case, i.e. constant rotor speed. Still assuming that this is the case, the most immediate work that needs to be conducted is the determination the creep behaviour of the composite and thus assessing how the stress state of the rotor will change over time.

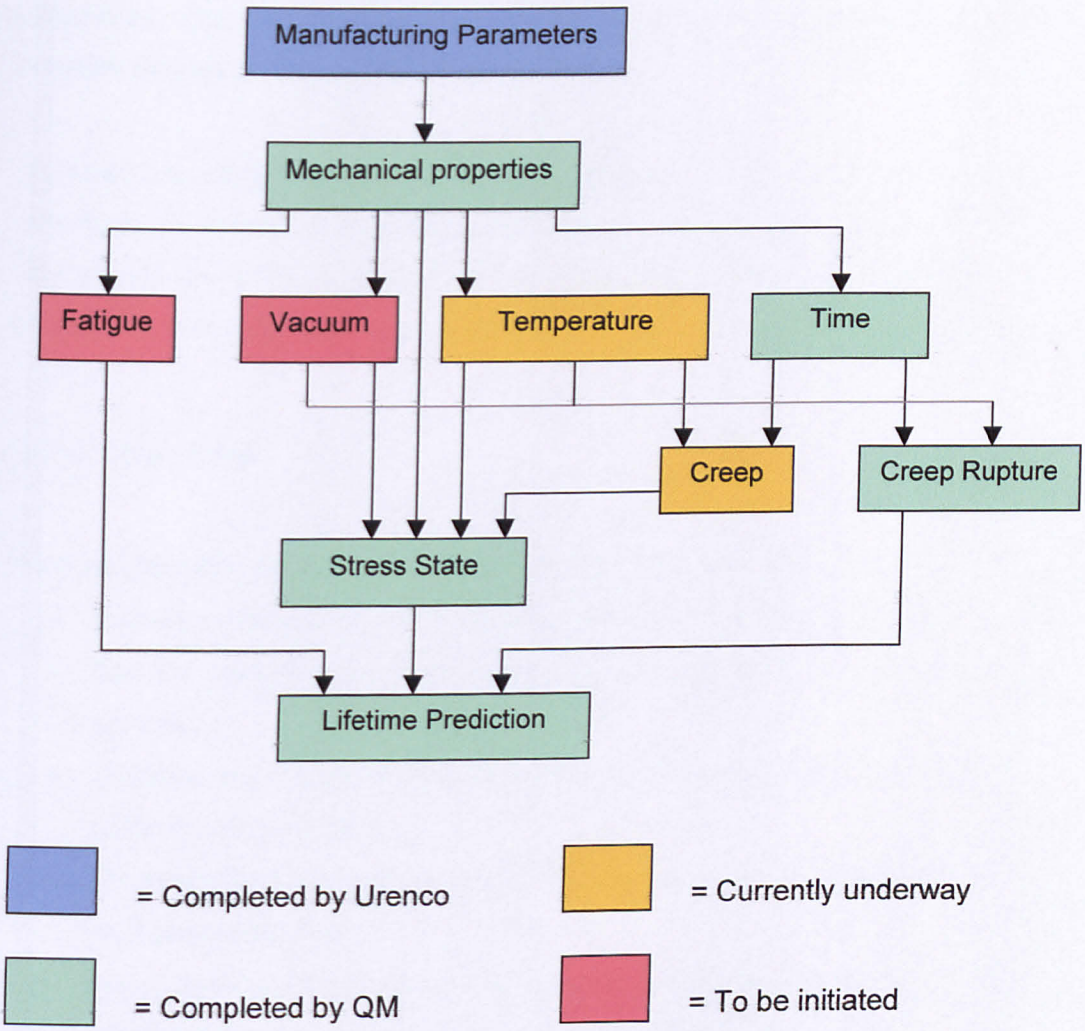

Figure 10-1 Research Overview.

In reality it is highly likely that the device will be used as frequently as a supply smoothing utility as it will an energy storage device. When using the flywheel as a current smoothing unit, the implication is that the velocity of the rotor is constantly changing. Hence, the induced stresses in the rotor will also be continuously variable. As a result the immediate continuation of research should focus on the transverse fatigue properties of the composites. The effects of fatigue loading on the transverse properties has to be determined and the subsequent influence that this will have on the lifetime predictions also needs to be determined

Moreover, the effects of the vacuum on the composite should be assessed. In conjunction with this, the composite response at the correct operating temperature should be analysed.

Although not illustrated in the figure, a programme should be undertaken to investigate the validity of conventional fracture mechanics to this composite system. This should extend to addressing the issue of crack growth initiation and thus propagation from a flaw that is not regarded as a sharp crack.

10.2.1 Other notes.

Some specific tasks should also be completed to aid the continued research:

- Redesign of the end tab for better stress distribution in the adhesive layer.
- Test the bulk resin properties to make the FE and theoretical models more accurate.
- Accurate data for the NdFeB layer in hoop and radial directions, again to refine the FE predictions.
- Determine the interfacial strength of the materials to aid the understanding of the fracture behaviour.
- Investigation of the visco-elastic effect seen in crack growth rate experiments and determine how this will influence the lifetime work.
- Accurately model the stresses around a crack tip in a negative strain field.

10.3 Overall Picture.

This thesis has looked at how macro material parameters may be linked to an application in order to obtain some insight into the durability of a structure.

With the ever increasing use of thick composite structures, the work presented here must be put into context. The design of the through thickness test method and subsequent creep rupture analysis, are valid for testing of composite materials for

other applications. Indeed, the test method has already been used to determine interlaminar properties for work connected to crush structures.

Clearly the analysis of data in this thesis is specific to flywheel rotors. However, in practice, there is no reason why the method could not be employed for other applications where the prevailing stress state is known or can be determined.

Although, as highlighted in the literature, a great deal of work has been undertaken in determining the nature of the transverse mechanical properties of composites. The majority of these studies have focused on analysing the behaviour of the materials at the micro level. The next stage of this research is to investigate the materials at the meso level.

Ultimately, the links must be formed (Figure 10-2) to complete the understanding of the transverse behaviour of composites at all levels.

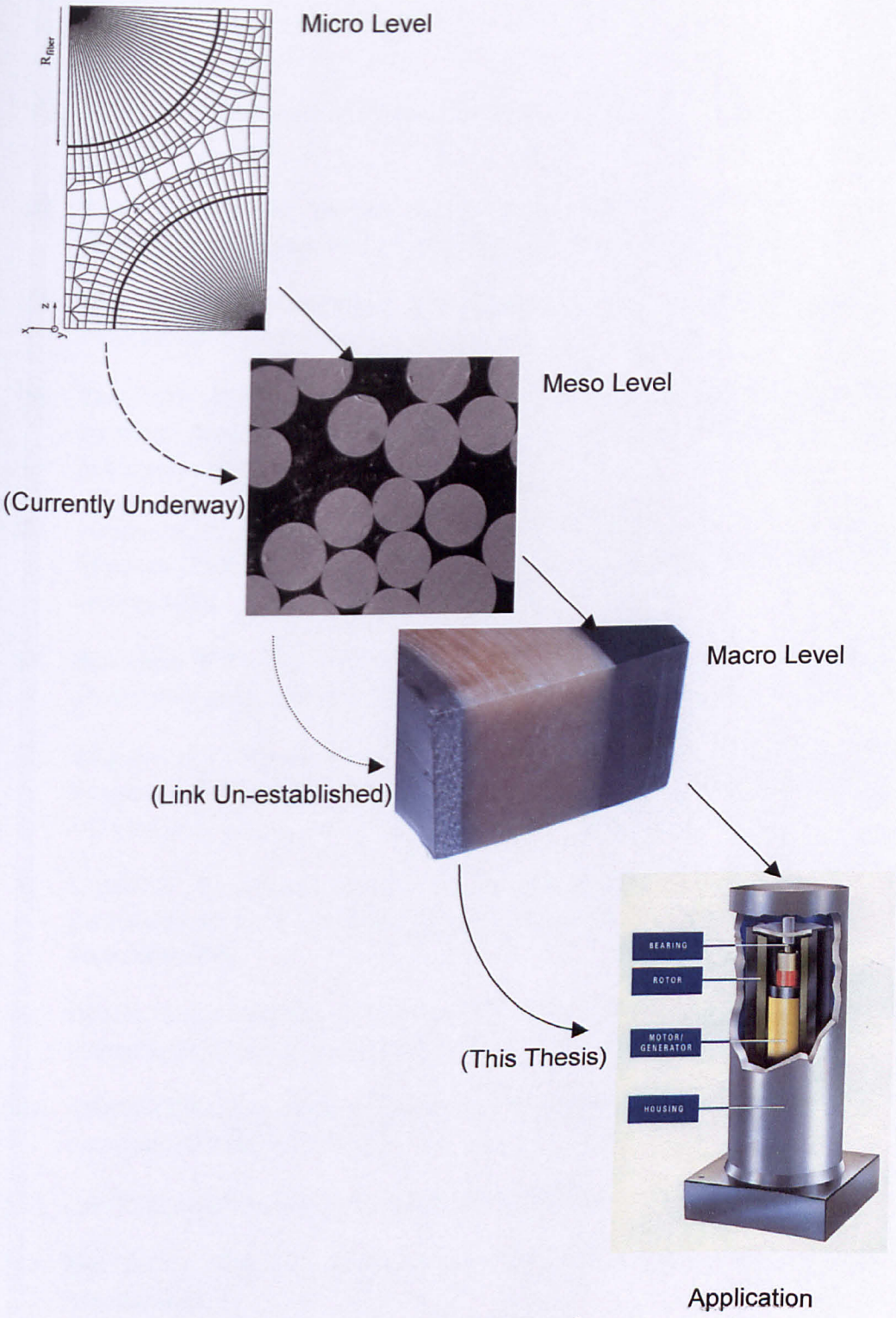

Figure 10-2 Research Levels.

REFERENCES

[1] Ashby M.F. Materials selection in mechanical design. Pergamon Press ISBN 0 08 041907 0, 1992

[2] Cambridge Material Selector. Version 2.1.1 1994-98 Granta Design Ltd. Max Watson, David Cebon, Mike Ashby, Chris Charlton, Wei Tatt Chong.

[3] Dick W.E. Design and Manufacturing considerations or composite flywheels. Proceedings of the flywheel technical Symposium pp 275. 1975.

[4] Ries D.M, .Kirk J.A. Design and Manufacturing for a composite multi-ring flywheel. Proceedings of the intersociety energy conservation engineering conference. 1992 pp 43-48

[5] Mespoulet S. Through Thickness Test Methods of Laminated Composite Materials. Ph.D Thesis, Imperial College of Science, Technology and Medicine. January 1998.

[6] Broughton W.R., Sims G.D. An overview of Through-Thickness Test methods for Polymer matrix composites. National Physics Laboratory. October 1994

[7] Ferguson R.F., Hinton M.J., Hiley M.J. Determining The Trough-Thickness Properties of FRP Materials. Composites Science and Technology 1998 pp 1411-1420

[8] Curtis P.T., Broadly B.P. A review of test methodology for the measurement of the through thickness properties of polymeric composites. DERA Farnborough. September 1993.

[9] Hudson L.A., Modelling of Pirouette™ Rotor Winding. Urenco (formerly International Energy Systems Ltd.) ES (96) pp 167. 1995

[10] ABAQUS/Standard Hibbitt, Karlsson & Sorenson, Inc. 1080 Main Street, Pawtucket RI 02860-4847

[11] Lees B. Composites Processing Accosiation workshop, 25th November 1999

[12] TM Techni Measure, Alexandra Buildings, 59 Alcester Road, Studley, Warwickshire.

[13] Imperial Chemical Industries PLC (ICI), Imperial Chemical House, Millbank, London.

[14] ASTM Standards.E399-83. Volume 02.02 pp 681-705.

[15] Hogg P.J., Price J.N., Hull D. Stress corrosion of GRP 39th Annual Conference, Reinforced Plastics/Composites Institute. 1984

[16] Srawley J. E., Wide range stress intensity factor expressions for ASTM E399 Standard fracture toughness specimens. International journal of fracture Vol. 12 pp 475-477

[17] Aliabadi M.H., Lopez J.F.L. K Database of Stress Intensity Factors. Computational Mechanics Publications 1996

[18] Rooke D. P, Tweed J. International Journal of Engineering Science., Vol. 10, pp 709, 1972.

[19] Isida M. Effect of width and length on stress intensity factors of internally cracked plates under various boundary conditions, Int. J.Frac., Vol. 7, pp 301, 1971.

[20] Collins W. D. Some axially symmetric stress distributions in elastic solids containing penny-shaped cracks, I. Cracks in an infinite solid and thick plate, Proc. Roy. Soc. London, Ser. A., Vol. 266, pp 359, 1962

[21] Bowie O. L., Freese C. E. Engng. Frac. Mech., Vol. 4, pp 315, 1972.

[22] Harris D. O. J. bas. Engng, Vol. 89, pp 49, 1967.

[23] Hull D, and Clyne T.W. An introduction to composite materials. Second edition, University press Cambridge. 1996.

[24] Timoshenko S.P, Goodier J.N, Theory of elasticity, Third edition, Mc Graw Hill, 1970

[25] Okubo H, The Stress distribution in an allotropic disc compressed diametrically, journal of mathematical physics, vol. 31, no. 1,1952

[26] Mao T. H, Owen M.J., Through-the-thickness tensile strength of fibre reinforced plastics. Composite materials: testing and design 6th conference, 1982

[27] Lekhnitskii, S. Anisotropic plates, Gordon& breach science publishers, 1968

[28] Jackson, W.C. Martin, R.H. An interlaminar tensile strength specimen. Composite Materials: testing and design. Vol. 11, 1993

[29] Kedward K. T, Wilson R.S. McLean S. K. Flexure of simply curved composite shapes. Composites, Vol. 20, no. 6 pp 527-536, 1989.

[30] Shivakumar K. N., Allen H.G., Avva V.S. Interlaminar tension strength of Graphite/Epoxy composite Laminates. AIAA journal, Vol. 32, No. 7 pp 1478-1484. 1994

[31] Heil C. C., Sumich M, Chappell D. P. A curved Beam test Specimen for determining the interlaminar tensile strength of a laminate composite. Journal of composite materials vol. 25 pp 854-868, 1991

[32] Sumich M., Manufacture of composite test specimens for delamination studies. Experimental techniques , Vol. 13 pp 20-22 1989

[33] Matthews F. L., Ellis S. C., Through thickness properties of a composite laminate. Report for 2037/392/RAE. Imperial College London. 1993.

[34] Gower, M. R. L. Through thickness tensile strength of fibre reinforced plastics. M.S.c Thesis. Imperial College London 1994

[35] Wu H. Y. T, Springer G. S. Impact induced stresses, strains and delamination in composite Plates. Journal of composite materials Vol. 22 pp 533-560 1988

[36] Hexcel Composites, Duxford, Cambridge, CB2 4QD

[37] O'Brien T. K, Salpekar S. A. Scale effects on the transverse tensile strength of graphite epoxy composites. ASTM Symposium on composites materials testing and design. 1992.

[38] Ige D. O. Rationalisation of design with composite materials. Ph.D theses, Cambridge University . U.K. 1992

[39] Hogg P.J, Price J.N., Hull D., Stress Corrosion of GRP. Reinforced Plastics/Composites Institute 39th Annual Conference. January 1984

[40] Winsom M. R, Jones M.I, Size effects in interlaminar tensile and shear strength of uni directional glass fibre/epoxy. Journal of reinforced plastics and composites. Vol. 15 No. 1, pp 2-15. 1996

[41] Govaert L. E, Schellens H. J, Thomassen H. J. M, Smit R. J. M, Terzoli L, Pejis T. A Micro mechanical approach to time dependant failure in off-axis loaded composites. Submitted to Composites, Part A. 2000.

[42] ASTM Standard D 790M. Flexural Properties of un-reinforced and reinforced plastics and elastic Insulating materials [metric].

[43] Kitching R., Tan A.L, Abu-Mansur T. M. N., The influence of through thickness properties on glass reinforced plastic laminated structures. Composite Structures. Vol. 2 1984.

[44] Roy A. K., Kim R. Y., Interlaminar Normal Stiffness and strength of thick orthotropic laminates: an experimental study. Journal of reinforced plastics and composites. Vol. 13, pp 880-98. 1994

[45] Ishai O., Gandelsman M., Strength of composite materials in the third dimension. Internal reports, technical research and development foundation ltd. Hafia, Israel. 1996

[46] Kim R. Y., Abrams F., Knight M., Mechanical Characterisation of a Thick composite Laminate. Integrated composite technology, 3rd technical conference Seattle 1988.

[47] Martin R.H., Sage G.N., Prediction of the fatigue strength of bonded joints between multi-directional laminates of CFRP. Composite structures. Vol. 6 pp 141-63. 1986.

[48] Lagrace P.A, Weems, D.B. A Through-the-thickness tensile strength specimen for composites. Test methods for design allowables for fibrous composites, Vol. 2, ASTM STP, No. 1003 Chamis conference edition. American society for testing and materials. Philadelphia 1989

[49] Ferguson R.F, Hinton M.J, Hiley M.J., Determining the through thickness properties of FRP materials. Composites Science and technology. Vol. 58 pp 1411-1420. 1998.

[50] ASTM D5528-94a Mode I Interlaminar Fracture toughness of unidirectional Fibre-reinforced polymer matrix composites.

[51] Savona S.C., Thanomslip C., Smith F., Unpublished work on Mode I fracture toughness of various composite systems.

[52] Kunmar P., Kishore N. N., Rajkumar B., Determination of interlaminar fracture toughness through an embedded crack. ICCE 7th Annual conference on composite materials. 2000.

[53] Kwang-Bok S., Chun-Gon K.,Chang-Sun H., Ho-Hyung L., Prediction of failure thermal cycles in graphite/epoxy composite materials under simulated low earth orbit environments. Composites part B. Vol. 31, pp 223-235. 1999

[54] Bubsey R.T., Fisher D.M., Jones M.H., Srawley J.E. Compliance measurement. Experimental techniques in fracture mechanics. The Iowa State University Press. Society for experimental stress analysis. pp 76-95 1973.

[55] Parhizgar S., Zachary L.W., Sun C.T., Application of the principles of linear elastic fracture mechanics to composite materials. International journal of fracture. Vol. 20. pp 3-15 1982.

[56] Sapalidis S. N. Stress corrosion of glass reinforced plastics at elevated temperatures. Ph.D. thesis Queen Mary and Westfield College. 1997

[57] Buckley J. M., Atallah. K., Bingham C. M., Howe D., Magnetically loaded composite for roller drivers. IEE colloquium on new magnetic materials. London 1998.

[58] Hannagan T.J., Mastering Statistics. Macmillan Press Ltd. 1982

[59] Emerson R. P., Orlet M. W., Bakis C. E. Fabrication and characterization of filament wound elastomeric composite materials. 42nd International SAMPE symposium. pp 342-353. 1997.

[60] Pipes R. B., Non-destructive evaluation and flaw criticality for composite materials. ASTM 696. 1978.

[61] Tarrant C., Lewis L. A., Urenco (Capenhurst) Ltd. Capenhurst, Chester CH1 6ER.

[62] Media Cybernetics, L.P., 8484 Georgia Avenue, Suite 200, Silver Spring, MD 20910 USA

[63] Cauchi Savona S., Adhesive bonding of carbon fibre to titanium, applications in highly loaded automotive components. MS.c. Thesis. Queen Mary and Westfield College. 1998.

[64] Lee B. L., Lewis R. W., Sacher R. E. Environmental effects on the mechanical properties of glass fibre/epoxy resin composites. Proceedings of ICCM/2. 1978.

[65] Tokyo Sokki Kenkyujo Co. Ltd. 8-2 Minami Ohi 6 Chome Shinagawa-ku, Tokyo 140.

[66] Basoalto H.C., Weight Function formalism applied to crack bridging problems. Ph.D thesis Queen Mary and Westfield college. London 1996.

[67] Sirley C.L., Bakis C.E., Weaver E. J. Tensile behaviour of filament wound composites in vacuum. 44th International SAMPE Symposium. pp 2110-2118. 1999.

[68] Ganley J. M., Arup K. M., Huybrechts S. Quantifying process induced residual stresses in filament wound composite parts. 44th International SAMPE Symposium. pp 2095-2109. 1999.

[69] Ha S. K., Kim D. J., Choi S. K., Optimal design of a hybrid composite flywheel rotor using finite element methods. . 44th International SAMPE Symposium. pp 2119-2132. 1999.

[70] Tarrant C. Revolutionary flywheel energy storage system for power quality. Power engineering journal. pp 159-163. June 1999

[71] Turmel, D. J. P., Szpicak J. A., Singh S., Partridge I. K. Crack initiators and pre-cracking techniques for fracture testing of polymer-matrix composites. Conference proceedings of deformation and fracture of composites 3. pp 190-199 1995

[72] Polaroid Great Britain, Wheathampstead House Codicote Road Wheathampstead, Herts AL4 8SF.

[73] Hull D., Clyne T. W. An introduction to composite materials. Cambridge University Press. Second Edition. 1996.

[74] Barnby J. T., Spencer B. Crack propagation and compliance calibration in fibre-reinforced polymers. Journal of Materials science. Vol. 11. pp 78-82. 1976

[75] Bradley W. L. Relationship of Matrix toughness to interlaminar fracture toughness. Chapter 5 in "Application of fracture mechanics to composite materials" edited by K. Friedrich. Elsevier Applied science publications. 1989.

[76] Corleto C., Bradley W. L., Henriksen M. Correspondence between stress fields and damage zones ahead of crack tips under Mode I and Mode II loading. ICCM and ECCM:Proceedings of 6th international conference on composite materials. 1987.

[77] Shirey C. L., Bakis C.E., Weaver E. J. Tensile behaviour of filament wound composites in vacuum. Proceedings of 44th International SAMPE Symposium. pp 2110-2118. 1999.

[78] Sims G. D., Broughton W. R. Glass fibre reinforced plastics-properties. National Physical laboratory, Teddington. Published in Comprehensive Composite Materials. Elsevier Science Ltd. 2000

[79] Smith P.A. Carbon fibre reinforced plastics. University of Surrey, Guilford. Published in Comprehensive Composite Materials. Elsevier Science Ltd. 2000.

[80] Ilcewicz L. B., Dost E. F., McCool J. W., Grandle D. H. Composite Materials Fatigue and fracture . ASTM STP 1110. Edited by O'Brien T. K. American society for testing and materials. pp 30-35. 1991.

[81] Sims G. D., Galdman D. G. Plastics and rubber materials and applications. Vol. 1. pp 41-48. 1978.

[82] Aliabadi M.H., Private communication. January 2000.

[83] Johnson A.F. Engineering design properties of GRP. Published by The British Plastics Federation. 1986.

[84] Wagner D. H. Statistical concepts in the study of fracture properties of fibres and composites. Chapter 2 in "Application of fracture mechanics to composite materials" edited by K. Friedrich. Elsevier Applied science publications. 1989.

[85] Endo T., Chang M., Matsuda N., Matsuura K. Creep behaviour of SiC/Al composite at elevated temperature. Metal matrix composites – processing, microstructure and properties. pp 323-8. 1991.

[86] Mclean M. Directionally solidified materials for high temperature service. Materials Society. London. 1983.

[87] Blythe S. Personal website. Department of Statistics and Modelling Science,University of Strathclyde, Glasgow. 2001

[88] Scott D. W., Lai J. S., Zureick A.H. Journal of reinforced plastics and composites. Vol. 14. pp588-617. 1995.

[89] Rowatt R.D., Spanos P.D. Markov chain models for life prediction of composite laminates. Journal of structural safety. Vol. 20. pp 117-135. 1998.

[90] Karger-Kocsis, J. Microstructure and Fracture Mechanical Performance of Short-Fibre Reinforced Thermoplastics, in Composite Materials Series; Application of Fracture Mechanics to Composite Materials, K. Friedrich, Editor., Elsevier Science Publishers. pp. 189-247. 1989.

[91] Phillips, D.C., A.S. Tetleman, The fracture toughness of fibre composites. Composites, Vol. 3. pp. 216-223. 1972.

[92] Dharan, C.K.H. Fracture mechanics of composite materials. Journal of Engineering Materials and Technology Vol. 100. pp. 233-247. 1978.

[93] Gabrys C. W., Bakis C.E. Design and testing of composite flywheel rotors. Composite materials: testing and design, thirteenth volume, ASTM STP 1242. American society for testing and materials. pp 1-22. 1997

APPENDIX A

This section contains the input decks used for the various models used in the thesis. In both cases the geometry has been removed due to space constrains. The geometry for the models may easily be constructed using the information provided in the thesis:

A1 Through Thickness Test Method Model.

```
** ABAQUS Input Deck Generated by HyperMesh Version3.0
**
**   Template:  ABAQUS/STANDARD
**
*HEADING
THROUGH THICKNESS TEST METHOD-MODELLED WITH RESIN AT INTERFACE.
*RESTART,WRITE,FREQUENCY=2
*SYSTEM
0.00000000, 0.00000000, 0.00000000, 1.00000000, 0.00000000,
0.00000000
0.00000000, 1.00000000, 0.00000000
*NODE, SYSTEM=R
       1,  2.5,  -5.0,  -18.2
       2,  5.0,  -5.0,  -18.2
       3,  7.5,  -5.0,  -18.2
       ▽▽▽data cut▽▽▽
    7972,  4.0,  10.0,  10.1
    7973,  4.0,  8.0,  10.1
*ELEMENT,TYPE=C3D8,ELSET=  sample
       2,     137,     168,     169,     136,     258,     289,
290,
     257,
       3,     136,     169,     170,     135,     257,     290,
291,
     256,
       ▽▽▽data cut▽▽▽
     4233,    5654,    1257,    1226,    5656,    5676,    1378,
1347,
    5678,
*ELEMENT,TYPE=C3D8,ELSET=  corner
    2001,     143,     142,     263,     264,    1913,      16,
15,
    1914,
    2002,     142,     141,     262,     263,      16,      18,
17,
       ▽▽▽data cut▽▽▽
    2003,     141,     140,     261,     262,      18,      20,
    5691,    7642,    7633,    7558,    7641,    7731,    7722,
7647,
    7730,
*ELEMENT,TYPE=C3D8,ELSET=   resin
    4534,    2725,    2724,    2834,    2835,    6043,    6044,
6045,
```

```
    6046,
    4535,    2724,    2723,    2833,    2834,    6044,    6047,
6048,
       ▽▽▽data cut▽▽▽
    5991,    7957,    7973,    7970,    7955,    6485,    6486,
6497,
    6496,
*NSET, NSET=      fix
    4672,    4684,    4685,    4686,    4687,    4700,    4701,
4702,
    ▽▽▽data cut▽▽▽
    5159,    5164,    5173,    5174,    5179
*NSET, NSET=    pull
    7210,    7222,    7223,    7224,    7225,    7238,    7239,
7240,
    ▽▽▽data cut▽▽▽
    7697,    7702,    7711,    7712,    7717
**
**
**
*SOLID SECTION,ELSET=sample,MATERIAL=COMP
*MATERIAL,NAME=COMP
*ELASTIC,TYPE= ENGINEERING CONSTANTS
154100,7500,7500,0.3,0.02,0.02,5320,7600,
7600
**
**
**
*SOLID SECTION,ELSET=corner,MATERIAL=STEEL
*MATERIAL,NAME=STEEL
*ELASTIC, TYPE=ISO
200000,0.3
**
**
**
*SOLID SECTION,ELSET=resin,MATERIAL=RESIN
*MATERIAL,NAME=RESIN
*ELASTIC, TYPE=ISO
4242,0.3
**
*STEP,NLGEOM,INC=999
**
**********************************************
**************loading*************************
**********************************************
*STATIC, DIRECT
1,10
*CLOAD
pull,3,30
**
*BOUNDARY
fix,1,6,0
pull,4,6,0
**
*EL PRINT, POSITION=CENTROIDAL, FREQUENCY=1, SUMMARY=YES
*NODE PRINT, FREQUENCY=1, SUMMARY=YES, TOTALS=YES
*EL FILE, POSITION=CENTROIDAL, FREQUENCY=1
S, SINV
*NODE FILE, FREQUENCY=1
U,RF
*END STEP
```

A2 Flywheel Rotor Model.

```
** ABAQUS Input Deck Generated by HyperMesh Version3.0
**
**   Template:  ABAQUS/STANDARD
**
*HEADING
3D FLYWHEEL TEST MODEL
*RESTART,WRITE,OVERLAY
*PREPRINT,ECHO=NO,HISTORY=NO,MODEL=NO
*NODE
       1,  89,  484.75
       2,  97,  484.75
       3,  97,  506.5
       4,  97,  528.25
       ▽▽▽data cut▽▽▽
    1825,  161.0,  0.0
    1827,  165.0,  0.0
*ELEMENT,TYPE=CAX3,ELSET=  carbon
      26,     462,     463,     457
      29,     468,     469,     463
      55,     516,     517,     469
      ▽▽▽data cut▽▽▽
     286,    1000,     999,    1001
     289,    1002,    1001,    1003
*ELEMENT,TYPE=CAX3,ELSET=   glass
     515,     116,     117,     111
     539,     156,     157,     117
     542,     162,     163,     157
     ▽▽▽data cut▽▽▽
    1024,     983,     982,     984
    1027,     985,     984,     986
*ELEMENT,TYPE=CAX3,ELSET=  magnet
    1465,      92,      93,      91
    1468,      98,      99,      93
    1471,     104,     105,      99
    ▽▽▽data cut▽▽▽
    1532,     960,     959,     961
    1541,     326,     323,     327
*ELEMENT,TYPE=CAX4R,ELSET=  carbon
       1,     751,    1178,    1155,     749
       2,    1178,    1179,    1156,    1155
       3,    1179,    1180,    1157,    1156
       ▽▽▽data cut▽▽▽
     489,    1776,    1777,    1815,    1814
     490,    1777,    1825,    1827,    1815
*ELEMENT,TYPE=CAX4R,ELSET=   glass
     491,     446,     694,       2,     125
     492,     125,       2,       3,     129
     493,     129,       3,       4,     155
     ▽▽▽data cut▽▽▽
    1441,    1592,    1593,    1655,    1654
    1442,    1593,    1617,    1659,    1655
*ELEMENT,TYPE=CAX4R,ELSET=  magnet
    1443,     401,     419,       1,      43
    1444,      43,       1,       5,      46
```

```
     1445,      46,       5,       7,      47
     ▽▽▽data cut▽▽▽
     1609,      81,      83,      64,      63
     1610,      83,      85,      65,      64
*NSET, NSET=     all
       1,       2,       3,       4,       5,       6,       7,
8,
       9,      10,      11,      12,      13,      14,      15,
16,
      17,      18,      19,      20,      21,      22,      23,
24,
      ▽▽▽data cut▽▽▽
    1804,    1805,    1806,    1807,    1808,    1809,    1810,
1811,
    1812,    1813,    1814,    1815,    1819,    1821,    1823,
1825,
*ELSET, ELSET=  radius
      13,      15,      17,      19,      21,      33,      35,
37,
      39,      41,      43,      45,      47,      49,      51,
73,
      75,      77,      79,      81,      83,      85,      87,
89,
      ▽▽▽data cut▽▽▽
     651,     653,     655,     677,     679,     681,     683,
685,
    1603,    1604,    1605,    1606,    1607,    1608,    1609,
1610
*ELSET, ELSET=axial
    1075,    1074,    1073,    1072,    1071,    1070,    1069,
1068,
    1067,    1066,    1065,     795,     794,     793,     792,
791,
     790,     789,     788,     787,     712,     698,     593,
581,
     ▽▽▽data cut▽▽▽
    1271,    1272,    1273,    1274,    1275,    1276,    1277,
1278,
    1279,    1280,    1281,    1282
**
**
**
*SOLID SECTION, ELSET=  carbon, MATERIAL=carbon
*SOLID SECTION, ELSET=   glass, MATERIAL=glass
*SOLID SECTION, ELSET=   magnet, MATERIAL=magnet
**
**
**
*ELSET, ELSET=rotor
carbon,glass,magnet
**
**
*MATERIAL, NAME=   magnet
*DENSITY
3.209E-9
**
*ELASTIC, TYPE = ENGINEERING CONSTANTS
13700,16700,35000,0.32,0.13,0.13,3800,5000,
5000
*EXPANSION, TYPE=ORTHO
32E-6,32E-6,8E-6
```

```
**
**
**
**
*MATERIAL, NAME=   glass
*DENSITY
2.1416E-9
*ELASTIC, TYPE = ENGINEERING CONSTANTS
13700,15600,48000,0.28,0.13,0.13,3800,5000,
5000
*EXPANSION, TYPE=ORTHO
26E-6,26E-6,8E-6
**
**
*MATERIAL, NAME=  carbon
*DENSITY
1.61233E-9
*ELASTIC, TYPE = ENGINEERING CONSTANTS
6600,8400,154100,0.3,0.021,0.021,5320,7600,
7600
*EXPANSION, TYPE=ORTHO
36E-6,36E-6,0.4E-6
**
*INITIAL CONDITION, TYPE=TEMPERATURE
all,110
**
************************************************
**************thermal shrinkage*****************
************************************************
**
*STEP,NLGEOM, INC=999
*STATIC
*TEMPERATURE
all,40
**
**
*EL PRINT, ELSET=record, POSITION=CENTROIDAL, FREQUENCY=1,
SUMMARY=YES
S, E
*NODE PRINT, FREQUENCY=0, SUMMARY=YES, TOTALS=YES
*EL FILE, POSITION=CENTROIDAL, FREQUENCY=0
S, SINV,E
*NODE FILE, FREQUENCY=0
U,RF
*END STEP
**
**
************************************************
**************rotation**************************
************************************************
**
**
*STEP, INC =     25, NLGEOM
**
**
*STATIC,DIRECT
0.1,0.7
**
*BOUNDARY
**
*DLOAD
```

```
**centrifugal acceleration specified in (rads-1)2
wheel,CENTRIF,19.349441E6,0.0,0.0,0.0,0.0,1.0,0.0
**
**
*EL PRINT, ELSET=radius, POSITION=CENTROIDAL, FREQUENCY=1,
SUMMARY=YES
S, E
**EL PRINT, ELSET=axial, POSITION=CENTROIDAL, FREQUENCY=1,
SUMMARY=YES
**S, E
*NODE PRINT, FREQUENCY=0, SUMMARY=YES, TOTALS=YES
*EL FILE, POSITION=CENTROIDAL, FREQUENCY=0
S, SINV,E
*NODE FILE, FREQUENCY=0
U,RF
*END STEP
```

APPENDIX B

The earlier FE work conducted on the through-thickness test specimen involved static analysis. In this case FE models may be simply constructed using units such as mm and N. Thus, output stresses will be in MPa. Since the flywheel is a dynamically loaded structure it is necessary to 'calibrate' the FE model for units. The problem arises since the model is constructed in mm, and is loaded with a variable (rotor speed) that has a time component. If we again require the output units of stress to be MPa, then the units of mass are now an unknown. This poses a crucial problem since the density of the materials plays a pivotal role in the resultant stresses in the component.

Dimensional analysis was used to calculate the units for mass.

M=? L=mm=m$\times 10^{-3}$ T=s

σ=Pa$\times 10^{6}$ (1MPa= 1N/mm^2)

M=Mass

a=acceleration

A=Area

F=force

$$\sigma = \frac{F}{A} = \frac{M.a}{A} \qquad (1)$$

and,

$$a = LT^{-2} \quad \text{and} \quad A = L^2 \qquad (2)$$

$$\sigma = \frac{MLT^{-2}}{L^2} = \frac{ML}{L^2T^2} = \frac{M}{LT^2} \qquad (3)$$

Substitute in actual units

$$\frac{N}{mm^2} = \frac{M}{(m\times 10^{-3})s^2} \qquad (4)$$

but $1N = \frac{kg.m}{s^2}$ and substitute into (4)

$$\therefore \frac{kg.m}{s^2.(m\times10^{-6})} = \frac{M}{(m\times10^{-3})s^2} \quad (5)$$

rearranging gives,

$$M = \frac{kg.m.(m\times10^{-3})s^2}{s^2.(m\times10^{-6})} \quad (6)$$

or

$$M = \frac{kg.m}{(m\times10^{-3})} = kg\left(\frac{m}{m\times10^{-3}}\right) \quad (7)$$

i.e.

$$M = kg\times10^3 \quad (8)$$

APPENDIX C

Integration of crack growth rate equation.

$$\frac{da}{dt} = AK^n$$

$$\frac{da}{dt} = A\left(Y\sigma\sqrt{\pi a}\right)^n$$

We require t=*fn*(a) therefore we integrate.

$$dt = \int \frac{da}{A\left(Y\sigma\sqrt{\pi a}\right)^n}$$

$$dt = \frac{1}{A\left(Y\sigma\sqrt{\pi}\right)^n}\int \frac{da}{a^{\frac{n}{2}}} \qquad \text{Let } B = \frac{1}{A\left(Y\sigma\sqrt{\pi}\right)^n}$$

Therefore

$$dt = B\int_{a_0}^{a_{crit}} a^{-\frac{n}{2}} da$$

$$t = B\left[\frac{1}{-\frac{n}{2}+1}\cdot a^{-\frac{n}{2}+1} + C\right]_{a_0}^{a_{crit}}$$

$$t = \frac{2}{2-n}\cdot\frac{1}{A\left(Y\sigma\sqrt{\pi}\right)^n}\cdot\left[a^{1-\frac{n}{2}}\right]_{a_0}^{a_{crit}} + C, \qquad \text{For } n \neq 2$$

Since it is know that when t=1 a=0.07 m. The constant C' may be determined. If the calculation is completed C'=1. Since the numbers involved are very large (i.e. lifetimes of 10^9 s) C may be ignored.

APPENDIX D

Presented here are the normal distribution tables for conversion of z value to a probability [87]. The most significant decimal of z is the first column, and the second decimal is the top row. For example, F(1.79) = 0.9633, and is lightly shaded in the figure below:

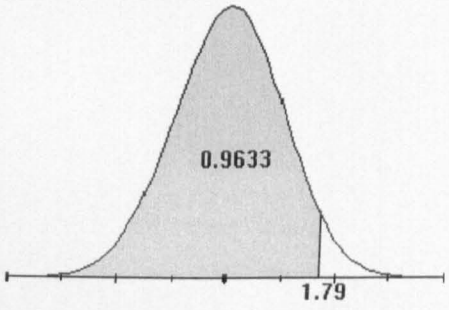

z	.00	.01	.02	.03	.04	.05	.06	.07	.08	.09
0.0	.0000	.0040	.0080	.0120	.0160	.0199	.0239	.0279	.0319	.0359
0.1	.0398	.0438	.0478	.0517	.0557	.0596	.0636	.0675	.0714	.0753
0.2	.0793	.0832	.0871	.0910	.0948	.0987	.1026	.1064	.1103	.1141
0.3	.1179	.1217	.1255	.1293	.1331	.1368	.1406	.1443	.1480	.1517
0.4	.1554	.1591	.1628	.1664	.1700	.1736	.1772	.1808	.1844	.1879
0.5	.1915	.1950	.1985	.2019	.2054	.2088	.2123	.2157	.2190	.2224
0.6	.2257	.2291	.2324	.2357	.2389	.2422	.2454	.2486	.2517	.2549
0.7	.2580	.2611	.2642	.2673	.2704	.2734	.2764	.2794	.2823	.2852
0.8	.2881	.2910	.2939	.2967	.2995	.3023	.3051	.3078	.3106	.3133
0.9	.3159	.3186	.3212	.3238	.3264	.3289	.3315	.3340	.3365	.3389
1.0	.3413	.3438	.3461	.3485	.3508	.3531	.3554	.3577	.3599	.3621
1.1	.3643	.3665	.3686	.3708	.3729	.3749	.3770	.3790	.3810	.3830
1.2	.3849	.3869	.3888	.3907	.3925	.3944	.3962	.3980	.3997	.4015
1.3	.4032	.4049	.4066	.4082	.4099	.4115	.4131	.4147	.4162	.4177
1.4	.4192	.4207	.4222	.4236	.4251	.4265	.4279	.4292	.4306	.4319
1.5	.4332	.4345	.4357	.4370	.4382	.4394	.4406	.4418	.4429	.4441
1.6	.4452	.4463	.4474	.4484	.4495	.4505	.4515	.4525	.4535	.4545
1.7	.4554	.4564	.4573	.4582	.4591	.4599	.4608	.4616	.4625	.4633
1.8	.4641	.4649	.4656	.4664	.4671	.4678	.4686	.4693	.4699	.4706
1.9	.4713	.4719	.4726	.4732	.4738	.4744	.4750	.4756	.4761	.4767
2.0	.4772	.4778	.4783	.4788	.4793	.4798	.4803	.4808	.4812	.4817
2.1	.4821	.4826	.4830	.4834	.4838	.4842	.4846	.4850	.4854	.4857
2.2	.4861	.4864	.4868	.4871	.4875	.4878	.4881	.4884	.4887	.4890

2.3	.4893	.4896	.4898	.4901	.4904	.4906	.4909	.4911	.4913	.4916
2.4	.4918	.4920	.4922	.4925	.4927	.4929	.4931	.4932	.4934	.4936
2.5	.4938	.4940	.4941	.4943	.4945	.4946	.4948	.4949	.4951	.4952
2.6	.4953	.4955	.4956	.4957	.4959	.4960	.4961	.4962	.4963	.4964
2.7	.4965	.4966	.4967	.4968	.4969	.4970	.4971	.4972	.4973	.4974
2.8	.4974	.4975	.4976	.4977	.4977	.4978	.4979	.4979	.4980	.4981
2.9	.4981	.4982	.4982	.4983	.4984	.4984	.4985	.4985	.4986	.4986
3.0	.4987	.4987	.4987	.4988	.4988	.4989	.4989	.4989	.4990	.4990

PUBLICATIONS

Certain sections of this research have been published at various conferences.

1. Long term Through Thickness properties of uni-directional composites for flywheel applications. 7th International Conference on Fibre Reinforced Composites. University of Newcastle upon Tyne. p63-67. 1998.
2. A Transverse tension creep and creep rupture test. 4th European conference on composites: Testing and Standardisation. Lisbon. p320-328. 1998
3 Through-thickness properties of unidirectional thick composites for flywheel energy storage systems. ECCM 8, 1998.

In reality to increase confidence in the final results, instead of using the mean of the crack growth rate, it is prudent to use a 95% confidence line. The equation of this new line has the same slope, but A now equals 5.724×10^{-6} instead of 2.31×10^{-7}. Consequently using this line the subsequent predictions will change. The figure below illustrates the effect this change has upon the defect size, calculated via the active crack growth approach for the GFRP layer (the only layer of the rotor of real concern to us).

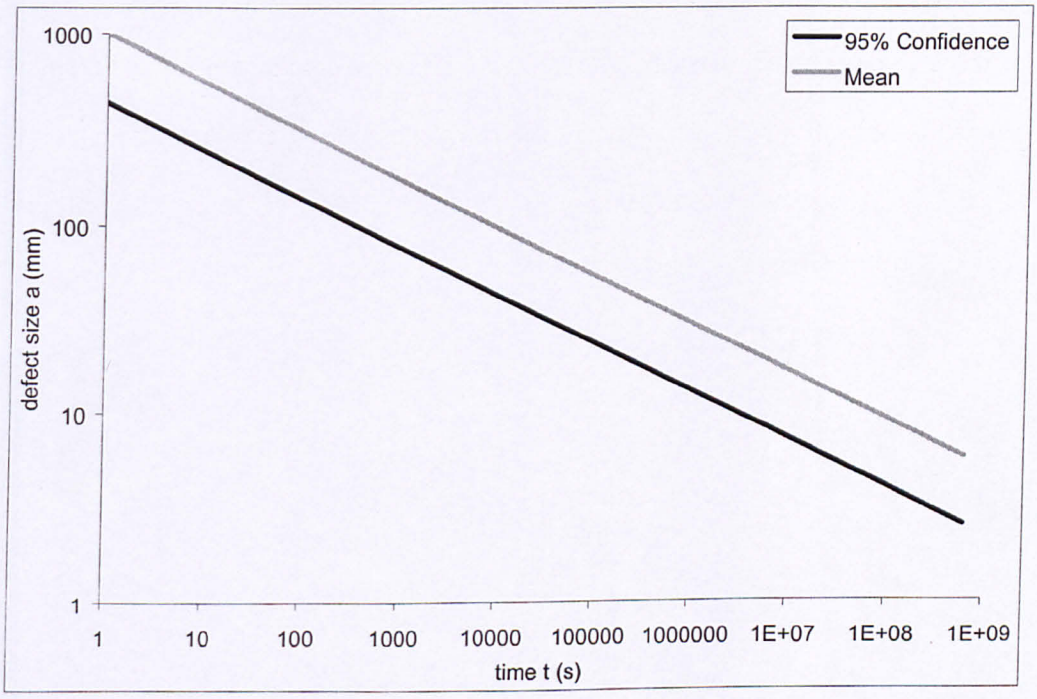

The critical defect size for a rotor with a desired life of 20 years has reduced from 10μm to 6μm. In contrast the probability of failure for the rotor has only risen from 4.2% to 4.5%. This is due to the fact that the probability of finding a defect of this size has changed from 87.5% to 93%.